EXPERIMENTS WITH ISOTHERMAL TWO PHASE FLOWS

IOANNIS HARDALUPAS
DIPL (Eng.)

Thesis submitted for the degree of
Doctor of Philosophy
in the University of London
and for the
Diploma of Membership of the Imperial College

Imperial College of Science, Technology and Medicine
(Department of Mechanical Engineering)

September, 1989

To my Parents

ABSTRACT

Velocity and flux measurements of spherical glass beads with nominal diameters of 200, 80 and 40 μm and velocity measurements of the gas phase in the presence of the beads have been obtained by phase-Doppler anemometry in a round, unconfined, fully turbulent air jet over the first 28 diameters and a round, turbulent, sudden-step expansion. The purposes of the experiments were to quantify the influences of bead diameter and mass loading on the dispersion of the beads and on the velocity characteristics of gas phase in the presence of the dispersed phase. The bead volume fraction was always sufficiently small that bead-to-bead interaction was negligible. The results were interpreted in terms of the relative timescales of the mean and turbulent motion of the carrier fluid and the inertial timescales of the beads, which were 298, 48 and 12 ms respectively.

The jet diameter was 15 mm and the exit velocity was 13 m/s giving a Reynolds number of 13000 and an exit timescale of 1.15 ms which increased quadratically with axial distance. Gravity effects were negligible. The mean centreline velocity of the jet of the 80 μm beads decayed to about one-half of the bead exit velocity by 28 diameters downstream and was independent of mass loading up to 86%. The decay rate of the mean gas centreline velocity in the presence of the beads reduced with increasing loading due to transfer of momentum from the discrete to the gaseous phase and, at least beyond 20 diameters from the nozzle, resulted in increased turbulence relative to the single phase jet. The decay rate of the mean centreline velocity of the 40 μm beads decreased with increasing loading and, in contrast to the 80 μm beads, the rate of spread decreased with increasing loading up to 80%. Although the beads were not expected to be responsive to the frequencies of the energy-containing eddies, the bead axial r.m.s. was more than twice as large as the radial r.m.s. velocity and the correlation coefficient of the cross correlation between axial and radial r.m.s. velocity was larger than that of the single phase. The large bead turbulence, anisotropy and strong correlation coefficient is explained by the superposition of bead trajectories from regions of different bead *mean* velocity, referred to as the fan-spreading effect, and is not due to acquisition of turbulent motion from the gaseous phase.

The round sudden step expansion had identical initial conditions with the jet experiment and two expansion ratios of 3.33 and 5 were examined. The 80 μm beads entered the recirculation zone for the expansion ratio of 5, but not for 3.33, which was due to the combination of a favourably long transit time along the corner recirculation zones, together with dispersion by the large eddies of the flow. Gravitational effects occured in the recirculation zone. Their dispersion rate increased with loading increasing up to 86% and the axial bead r.m.s. velocity was found larger than that of the gas phase in large part of the recirculation zone and this was an artefact of the fan-spreading effect and the bead response to the large eddies of the flow. The recirculation length of the beads was smaller than that of the single phase and increased with loading. The gas phase recirculation zone was extended and was up to 40% longer than that of the single phase for bead loading of 86%, in contrast to that of the single phase which is constant and independent of Reynolds number and the gas phase axial r.m.s. velocity was suppressed in the recirculation zone relative to the single phase. The 40 μm beads entered the recirculation zone for both expansion ratios and, in contrast to the 80 μm beads, the dispersion rate decreased and their reattachment length increased by 15, 30 and 55% relative to that of the single phase respectively for loadings 13, 40 and 80%. The axial bead turbulence was lower than that of the single phase in the recirculation zone but more than twice that of the bead radial and azimuthal r.m.s. velocity.

Reliable instrumentation was required for the preceding simultaneous size and velocity measurements and for this purpose the phase-Doppler technique was developed. The influence of the collection angle, the angular spacing of the detectors, the beam intersection angle, the aperture integration, the refractive index and the Gaussian intensity distribution of the incident beams on the linearity and slope of the calibration curves were established from analysis of light scattering based on geometrical optics. Validation schemes were proposed to reduce sizing errors. The technique could size spherical particles for large off-axis forward-scatter direction, sidescatter and maybe backscatter collection angles, was independent of the turbidity of the flow and could discriminate the gas phase seeding particles from the dispersed phase.

ACKNOWLEDGEMENTS

Being at the end of this work, I would like to share my pleasure with the people who helped me along the way and acknowledge this.

I am deeply indebted to my supervisor, Prof. J. H. Whitelaw, for his persistent interest in the investigations and his guidance which helped to keep the objectives of this work in sight and achieve them in a relatively short time.

I am also grateful to my other supervisor, Dr. A. M. K. P. Taylor, who offered generously his time and advice. His stimulating comments and suggestions created a challenging working environment and contributed significantly to the completion of this work.

I am obliged to Dr. A. R. Jones who helped with discussions on the light scattering theory and with the assistance of Dr. S. A. M. Al-Chalabi provided the Mie theory results for the comparison to the geometrical optics approximation of chapter 2.

Dr. J. Gibb with his continuous interest, as contract monitor, helped with useful discussions and inspiring questions to the progress of this work. I have also benefitted from my association with all my colleagues and particularly Dr. C. Vafidis.

I thank Dr. E. Hislop and Mr. N. Western of the Long Ashton Research Station for the use of their Aerometrics phase-Doppler instrument.

My thanks go also to Mr. J. R. Laker for the construction of the signal processing electronics, to Mr. P. Trowell for the construction of the experimental hardware and the collection optics and Messrs. B. Crew, O. Vis and J. Mistry for their technical support.

Finally, I would like to thank Evi for her understanding and support who in many ways assisted the completion of this work.

Acknowledgement has to be given to the "Science and Engineering Research Council" and to "Central Electricity Generating Board" for financing the research work, without which this thesis could not have been carried out.

TABLE OF CONTENTS

		PAGE
ABSTRACT		iii
ACKNOWLEDGEMENTS		v
TABLE OF CONTENTS		vi
LIST OF TABLES		xiii
LIST OF FIGURES		xv
GLOSSARY OF SYMBOLS		xxxiii
CHAPTER 1	INTRODUCTION TO THE THESIS	1
1.1	The flows considered	1
1.2	Previous work	2
	a) Two phase flow : theory and experiment	2
	Effects of particle inertia, crossing trajectories and volume fraction of particles on dispersion rate	2
	Particle dispersion rate in shear flows	9
	b) Instrumentation for size-velocity correlation measurements	17
1.3	The present contribution	24
1.4	Outline of the thesis	25
CHAPTER 2	DEVELOPMENT OF THE PHASE-DOPPLER TECHNIQUE	45
2.1	Introduction	45
2.2	The phase-Doppler anemometry technique	46
2.3	Theoretical foundation	47

a) Light scattered by a sphere located in a single beam 47

b) Light scattered by a sphere located at the crossing section of a laser Doppler anemometry 53

2.4 Parametric evaluation of the phase-Doppler method 58

a) Collection angle 58

Forward scatter direction (Zone I and II) 59

Sidescatter direction (Zone III and IV) 62

Backscatter direction (Zone V, VI and VII) 63

b) Beam intersection angle 65

c) Finite collection aperture 66

d) Gaussian intensity distribution 67

e) Particle refractive index 69

f) Detector angular spacing 70

g) Polarisation of the incident beams 70

h) Flow turbidity 71

2.5 Experimental verification 72

a) Calibration curve 72

b) Flow turbidity 73

c) Signal-to-noise ratio 75

d) Aerodynamic sizing - Phase Doppler comparison 75

Sizing measurements 78

Sizing 40 μm glass beads 79

Seeding measurement - cross-talk from glass beads 81

2.6 Design of a phase-Doppler instrument 84

a) Optical design 84

b) Signal processing 85

Frequency measurement 88

Phase measurement 90

2.7 Particle flux and number density measurement 91

a) Particle flux 93

b) Particle number density 93

2.8 Conclusions 95

APPENDIX 2.A Expressions for the amplitude functions of the scattered light from a sphere illuminated from a single beam 102

APPENDIX 2.B Expressions for the geometrical parameters of the scattered light theory 104

APPENDIX 2.C Influence of Doppler signal amplitude on the phase measurement in a zero crossing counter with finite threshold levels 105

APPENDIX 2.D On-line calculation of effective size of measuring volume of a laser Doppler anemometer with frequency shift 107

APPENDIX 2.E Comparison between two methods suggested for particle number density measurement 110

CHAPTER 3 AXISYMMETRIC TURBULENT PARTICLE-LADEN JET 151

3.1 Introduction 151

3.2 Materials and methods 152

a) Jet flow, bead feed and recovery 152

b) Glass beads 154

c) Phase-Doppler anemometer 156

Optical arrangement 156

Electronic arrangement 157

d) Uncertainties in the measurement of the gas in the presence of the disperse phase 157

3.3 Results 160

a) Measurements of velocity characteristics of "unresponsive" beads 161

b) Measurements of velocity and flux characteristics of "partially responsive" beads 163

Centreline development of bead velocity 164

Radial profiles of mean velocities 165

Radial profiles of r.m.s. bead velocity 166

Bead flux and concentration 167

c) Measurements of gas velocities and rate of spread at the presence of 80 μm beads 170

d) Mass flowrate and momentum flux 173

3.4 Comparison with previous experimental results 176

a) Comparison with the experiments of Shuen et al (1985) 177

b) Comparison with the experiment of Modarress and Tan (1982, 1984) 178

3.5 Discussion 179

3.6 Conclusions 186

APPENDIX 3.A Derivation of expressions for the axial variation of the timescales of the "energy containing motion" & Kolmogorov scales in a jet 193

APPENDIX 3.B Estimation of bead turbulent Stokes number in a turbulent, round jet 194

(i) Turbulent Stokes number at jet exit 194

(ii) Turbulent Stokes number as a function of axial distance in jet 195

APPENDIX 3.C Estimation of the drag coefficient of the beads in the jet 196

CHAPTER 4 ROUND SUDDEN STEP EXPANSION 231

4.1 Introduction 231

4.2 Experimental arrangement 232

4.3 Results 233

a) Velocity and flux characteristics of 40 μm beads 234

Expansion ratio of 3.33 234

i) Centreline velocities 234

ii) Radial profiles of mean and turbulent velocities 236

iii) Bead flux characteristics 237

Expansion ratio of 5 239

i) Centreline velocities 239

ii) Radial profiles of mean and turbulent velocities 240
iii) Bead flux characteristics 241
b) Velocity and flux of the 80 μm beads and the gas phase flow 242
Expansion ratio of 3.33 242
i) Centreline velocities 242
ii) Radial profiles of mean and turbulent velocities 243
iii) Bead flux characteristics 244
Expansion ratio of 5 245
i) Centreline velocities 245
ii) Radial profiles of mean and turbulent velocities 246
iii) Bead flux characteristics 248
c) Velocity characteristics of 200 μm beads 249
Expansion ratio of 3.33 249
i) Centreline velocities 249
ii) Radial profiles of mean and turbulent velocities 250
Expansion ratio of 5 251
d) Separation streamlines and zero velocity contours 251
4.4 Comparison between the centreline velocity of the free jet and the expansion flows 252
4.5 Discussion 255
4.6 Conclusions 262
APPENDIX 4.A Curvature of the separation streamline of the expansion flow 270

CHAPTER 5	CLOSURE TO THE THESIS	318
5.1	Achievements and conclusions	318
	a) Instrumentation for two phase flows.	318
	b) Physics of two phase flows.	319
5.2	Recommendations for further work.	321

LIST OF REFERENCES 324

LIST OF TABLES

TABLE		PAGE
1.1	Principal characteristics of particle-laden jets measured by laser-Doppler anemometry.	27-29
1.2	Laser non-Doppler based techniques for simultaneous particle size-velocity measurements.	30-33
1.3	Laser Doppler based techniques for simultaneous particle size-velocity measurements.	34-44
2.1	Principal characteristics of phase-Doppler anemometer used for the depth of field experiment.	98
2.2	Principal characteristics of scattering particles used for the depth of field experiment.	99
2.3	Comparison of random errors due to depth of field in sizing between phase-Doppler and visibility.	100
2.4	Principal characteristics of phase-Doppler anemometer used for the accelerating nozzle experiment.	101
3.1	Nominal properties of glass beads.	188
3.2	Principal characteristics of the phase-Doppler anemometer.	189
3.3	Estimates of systematic and random errors in quantities measured.	190
3.4	Values of centreline velocity and flux used to normalise quantities.	191
3.5	Turbulent Stokes number as a function of axial distance along a jet for three bead diameters.	191
3.6	Momentum flux of 40 and 80 μm beads.	192
4.1	Flow conditions.	264

4.2	Values for velocity and flux used to normalise quantities for the expansion ratio of 3.33.	265
4.3	Values for velocity and flux used to normalise quantities for the expansion ratio of 5.	266
4.4	Deceleration rates and mean Stokes numbers for free jet and expansion flows.	267
4.5	Stokes numbers for the expansion ratio of 3.33.	268
4.6	Stokes numbers for the expansion ratio of 5.	269

LIST OF FIGURES

FIGURE		PAGE
2.1	Phase shifted Doppler signals showing the phase shift τ_{phase} and the Doppler period τ_D.	112
2.2	The amplitude functions S_1 and S_2 of the light scattered by a sphere located in one beam according to the notation of Van de Hulst (1981); S_1 is normal and S_2 parallel to the scattering plane defined by the incident beam and the scattering direction.	112
2.3	Ray optics of a transparent sphere showing paths due to surface reflection, refraction and first internal reflection.	113
2.4	(a) Diagram is after Van de Hulst (1981) showing the scattering angle regions where paths due to surface reflection, refraction and first internal reflection across a water droplet are present; (b) classification of scattering angle into seven intervals according to the combination of ray paths across a water droplet.	114
2.5	Definitions of angles used in the theoretical analysis of the light scattered by a sphere located in the crossing region of two laser beams.	115-116
2.6	The physical meaning of the terms A and N of equation (2.25) for a Doppler signal; A is the amplitude of the pedestal and N is the modulation depth.	116
2.7	Intensity interference pattern of the light scattered by a 40 μm glass sphere located in the crossing region of the two laser beams as a function of the rotation angle; (a) pattern due to interference of surface reflection, refraction and diffraction (solid line) and due to refraction only (dashed line), (b) pattern due to surface reflection and refraction only at the plane parallel to that of the beams at an elevation angle y=30°, (c) and (d) the same as above for the plane of the beams (y=0°).	117

2.8 (a) Intensity of the scattered fringe pattern due to refraction only (solid line) and due to surface reflection only (dashed line) showing the relative amplitude of the two patterns as a function of particle diameter. Observation at a position with elevation angle of 30° and rotation angle of 5.3°; (b) Intensity of the scattered fringe pattern due to interference from refraction and surface reflection showing increased oscillations around a mean value due to the refraction only pattern when their relative amplitudes are similar. 118

2.9 Refraction only interference fringe pattern scattered by a 40 μm glass bead located in the probe volume of a LDA system which has beam intersection angle 10°. 119

2.10 (a) Oscillations in the calibration curve due to use of point apertures for a mean scatter angle of 30°. Solid line is full geometrical optics approximation and straight dashed line is the calibration curve due to refracted light only. Abscissa is Mie size parameter, $\pi d/\lambda$ and ordinate is phase difference in radians. (b) Reduction in the oscillations in figure 2.10(a) owing to inclusion of finite aperture size, 0.95° x 9.5°, in the calculations. Mie's solution is the solid curve and full geometrical optics approximation is the dashed line. 120

2.11 Variation of phase (degrees) with water droplet diameter (μm) at a mean scatter angle of 100° showing comparison between Mie's solution (solid line) and approximation based on surface reflected light only (dashed line). 121

2.12 Variation of phase (degrees) with water droplet diameter (μm) in the second rainbow, mean scatter angle of 120°, showing comparison between Mie's solution (solid line) and approximation based on surface reflected light only (dashed line). 121

2.13 Variation of phase (degrees) with water droplet diameter (μm) between the second and main rainbow angles, mean scatter angle of 133°, showing comparison between Mie's solution (solid line) and approximation based on surface reflected light only (dashed line). 122

2.14 Ray optics of a transparent sphere showing the two branches of the first internal reflection. 122

2.15 (a) Variation of phase (degrees) with water droplet diameter (μm) within the main rainbow, mean scatter angle of 150°, showing comparison between Mie's solution (solid line) and geometrical optics approximation (dashed line); (b) Comparison of Mie's solution (solid line) of figure 2.15(a) with approximation based on internally reflected light only (dashed line). 123

2.16 Effect of beam intersection angle on the size resolution of the phase-Doppler, expressed as the ratio of phase/particle diameter. The figure shows a linear dependence between size resolution and beam intersection angle up to 30°; the detectors' locations were at elevation angle of 30° and rotation angles of 5.3° and 1°. 124

2.17 Calibration curve for variation of phase difference between Doppler signals observed at two points which are at an elevation angle of 30° and rotation angles of 8° and 1° with the diameter of spherical particles smaller than 10 μm with refractive index of 1.5 for incident beam intersection angle 10°; (a) results for point aperture, (b) results for finite apertures with height of 9.5° and width 1.1°. Solid line is full geometrical optics approximation, dashed line is refraction only calculation. 125

2.18 Sketch showing the effect of the Gaussian intensity distribution of the incident beams on the relative amplitude of the refracted and surface-reflected rays scattered by a sphere crossing at the edge of the LDA probe volume. Ray "A" due to surface reflection has larger amplitude than ray "B" due to refraction. 126

2.19 (a) Phase shift calibration curves due to refraction only and surface reflection only; (b) Two calibration curves with different size resolution by using three photodetectors; (c) Phase ratio, defined in equ. (2.34) as the phase of the steeper calibration curve to that of the shallower curve, from refraction only and surface reflection shows that the refraction phase ratio can be successfully discriminated from the surface reflection phase ratio. 127

2.20 Effect of refractive index of non-absorbing spheres on the phase-Doppler calibration curve; (a) Calibration curves for refractive indices 1.3 - 1.6, (b) variation of the phase-Doppler size resolution as a function of refractive index showing that decreases with refractive index increase. Size resolution is expressed as the ratio of phase/particle diameter. The beam intersection angle was 10°, the laser light wavelength 0.6328 μm and the detectors were located at elevation angle of 30° and rotation angles of 5.3° and 1°. 128

2.21 Effect of angular spacing of the detectors on the size resolution of the phase-Doppler, showing that increases with angular spacing increase. 129

2.22 Experimental arrangement used for the verification of the theoretical calibration curve. 130

2.23 Comparison between experimental and theoretical results for beam intersection angle of 11.3° and observation locations of the detectors at elevation angle of 30° and rotation angles of 3.5° and 1.9°. 130

2.24 Experimental arrangement used for the depth of field experiment. 131

2.25	(a) Phase as a function of void fraction. Interruption in (i) transmission, 14 cm depth of field, and (ii) reception, 5 cm depth of field, paths by 40-75 μm particles. (b) R.m.s. error as a function of void fraction. Interruption in (i) transmission, 14 cm depth of field and (ii) reception, 5 cm depth of field paths with interrupting particle diameter (μm) as parameter.	131-132
2.26	R.m.s. error as a function of filter settings showing the effect of noise on the signal on the phase measurement. Interruption in transmission path (14 cm depth of field) by 14-40 μm particles at 0.05% void fraction.	133
2.27	(a) Calibration curve of phase-Doppler for droplets with refractive index of 1.5 used for the accelerating nozzle experiment. "Φ_2" is curve for phase between central and an outer detector and "Φ_1" is curve for the phase between outer detectors; (b) Tolerance of ±15% of the phase shift value applied on the calibration curve of the system.	134
2.28	(a) Refraction only and surface reflection only calibration curves for accelerating nozzle experiment with two size resolution levels. (b) Phase ratio for refraction and surface reflection curves as a function of particle diameter showing that the expected ratio due to surface reflection for a 40 μm bead is around 0.5 and due to refraction is 2.	135
2.29	Cross-section of converging nozzle used to produce acceleration of beads as a function of aerodynamic diameter.	136
2.30	Velocity probability distributions of gas phase and of nominally 40 μm diameter beads at the exit of the accelerating nozzle, showing separation due to acceleration.	136

2.31 (a) Probability distribution of ratio of phases measured on channels "Φ_1" and "Φ_2" (figure 2.27) for laser power of 300 mW showing two peaks one at 0.5, which is due to surface reflection measurements and one at 2. which is the expected value due to refraction phase shift. (b) Probability distribution of ratio of phases of figure 2.31(a) after phase validation showing only one peak near the expected value of 2. 137

2.32 Probability distribution of ratio of phases measured on channels "Φ_1" and "Φ_2" (figure 2.27) before phase validation for laser power of 60 mW showing smaller peak at 0.5 than for the 300 mW laser power (figure 2.31(a)). 138

2.33 Phase distribution of nominally 40 μm diameter beads measured on channel "Φ_1" (figure 2.27) by the prototype counter 150° ≈ 10 μm. 138

2.34 Simultaneous measurements of phase and velocity of nominally 40 μm diameter beads at the exit of the converging nozzle. 139

2.35 Graphical definitions of terms: area "A" - 40 μm phase-window; area "B" - 40 μm velocity window; F40 signifies the phase corresponding to 40 μm; V40 is the velocity-window corresponding to 40 μm, taken from figure 2.30; and V_{gmin} and V_{gmax} are the minimum and the maximum velocities of the gaseous phase, also taken from figure 2.30. 139

2.36 Velocity probability distribution of signals in 40 μm phase-window, area "A" of figure 2.35, showing small cross-talk from other diameters. 140

2.37 Phase probability distribution of signals in the 40 μm velocity-window, area "B" of figure 2.35, showing optical cross-talk into size ranges outside the 130° - 170° phase-window. 140

2.38 (a) Size distributions of atomised mineral oil seed measured by Aerometrics instrument. (b) Phase distributions of atomised mineral oil seed measured by the prototype counter : 40° ≈ 10 μm. 141

2.39 (a) Size distributions of kaolin powder seed measured by Aerometrics instrument. (b) Phase distributions of kaolin powder seed measured by the prototype counter: 40° ≈ 10 μm. (c) Phase distributions of titanium dioxide powder seed measured by the prototype counter: 40° ≈ 10 μm. 142

2.40 Velocity probability distribution of signals with both phase in the seed window and velocity less than V_{gmin}, showing cross-talk from beads; (a) the laser power was 300 mW and in (b) it was 60 mW. 143

2.41 Schematic of a droplet in a laser beam showing the angular width of droplet α which reflects light into the aperture of a photomultiplier of angular width β. Scales have been exaggerated for clarity. 144

2.42 Sketch showing the geometry of the receiving optics. 145

2.43 Sketch of the probe volume of the phase-Doppler showing the image of the spatial filter of the receiving optics; its width limits the length of the probe volume and determines the area of the measuring volume. 146

2.44 Amplitude and frequency validation timing diagram. 147

2.45 Phase measurement 1-2 timing diagram. The low threshold pulses are generated only if the sequence between the high and low threshold of the amplitude validation of figure 2.44 is correct. 148

2.46 Percentage of number of 500 MHz clock pulses of 8 Doppler periods tolerance ε_f used for the frequency validation as a function of the Doppler frequency. Constant (0.015) tolerance (circles) and variable tolerance such that the difference between the number of clock pulses of the Doppler period based on the measurement of eight periods and that of five periods is 1 (square) or 2 (triangle). 149

2.47 Phase error due to the uncertainty of 1 pulse of a 500 MHz clock as a function of the phase and the Doppler frequency. Figure shows the 12.5% of the real phase shift error line. At the region above this line the error is lower. 149

2.48 Cross section of the probe volume of the phase-Doppler anemometer showing the fringes, which can be used to provide a length scale in the probe volume which can be used to measure on-line its size as the fringe spacing f is known. 150

2.49 Dependence of cross section of measuring volume of phase-Doppler intersection region as a function of particle size with the frequency shifting parameter, $S = [\ |U_i| / (U_{shift}+U_i)\ ]$ (appendix 2.D). N_0/N_f = 8/10. 150

3.1 Experimental arrangement. 198

3.2 Size distributions of the 40 μm beads used in the experiment; (a) volume (%), (b) number of counts (%). 199

3.3 Size distributions of the 80 μm beads used in the experiment; (a) volume (%) of new beads, (b) counts (%) of new beads, (c) counts (%) after half year use. 200

3.4 Size distributions of the 200 μm beads used in the experiment; (a) volume (%) and (b) counts (%) of new beads. 201

3.5 40 μm beads viewed by a scanning electron microscope at a magnification of ≈ 200. 202

3.6 Optical configuration. 203

3.7	Phase-Doppler calibration curve.	204
3.8	Centreline profiles of (a) mean and (b) r.m.s. axial velocity (U, u') and (c) flux normalised by the exit centreline flux, G_{om} for 200 μm beads for mass loadings of 13% and 37% compared to the single phase. Normalisation of velocities is by the single phase exit mean velocity, U_{om}.	205
3.9	Velocity and size distributions for the 200 μm beads measured by the phase-Doppler anemometer; (a) Size-velocity probability distribution, showing correlation between low velocities and small bead diameter, (b) velocity probability distribution corresponding to (a) showing bimodal distribution due to small beads.	206
3.10	Centreline profiles of (a) mean axial, U, (b) axial r.m.s., u', and (c) radial r.m.s., v', velocities for 40 μm beads for mass loadings of 13% and 80% compared to the single phase. Normalisation of velocities is by the single phase exit mean velocity, U_{om}.	207
3.11	Radial profiles of mean axial velocity (U) for 40 μm beads at x/d = 0.1, 10, 20 and 28 for mass loadings of 13% and 80% compared to the single phase. Normalisation is by the single phase centreline velocity, U_m.	208
3.12	Radial profiles of axial r.m.s. velocity (u') for 40 μm beads at x/d = 0.1, 10, 20 and 28 for mass loadings of 13% and 80% compared to the single phase. Normalisation is by the single phase centreline velocity, U_m.	209
3.13	Radial profiles of radial r.m.s. velocity (v') for 40 μm beads at x/d = 0.1, 10, 20 and 28 for mass loadings of 13% and 80% compared to the single phase. Normalisation is by the single phase centreline velocity, U_m.	210
3.14	Radial profiles of $\overline{uv}$ for 40 μm beads at x/d = 0.1, 10, 20 and 28 for mass loadings of 13% and 80% compared to the single phase. Normalisation is by the single phase centreline velocity, U_m^2.	211

3.15 Radial profiles of correlation coefficient of $\overline{uv}$ for 40 μm beads at x/d = 0.1, 10, 20 and 28 for mass loadings of 13% and 80% compared to the single phase. 212

3.16 Effect of mass loading 13% and 80% on centreline profiles of (a) 40 μm bead flux G_m, normalised by exit centreline flux, G_{om} (b) 40 μm bead concentration G_m/U_m, normalised by exit centreline concentration (c) flux half-width normalised by nozzle exit diameter and (d) concentration half-width normalised by nozzle exit diameter. 213

3.17 Effect of mass loading 13% and 80% on radial profiles of flux G of 40 μm beads at x/d = 0.1, 10, 20 and 28. Normalisation is by centreline flux G_m. R_0 is the half-width of the single phase jet. 214

3.18 Centreline profiles of (a) mean axial, U, (b) axial r.m.s., u', and (c) radial r.m.s. velocities, v', for gas phase and 80 μm beads for mass loadings of 23% and 86% compared to the single phase. Normalisation is by the single phase exit mean velocity, U_{om}. 215

3.19 Radial profiles of mean axial velocity (U) for gas phase and 80 μm beads at x/d = 0.1, 10, 20 and 28 for mass loadings of 23% and 86% compared to the single phase. Normalisation is by the single phase centreline velocity, U_m. 216

3.20 Radial profiles of axial r.m.s. velocity (u') for gas phase and 80 μm beads at x/d = 0.1, 10, 20 and 28 for mass loadings of 23% and 86% compared to the single phase. Normalisation is by the single phase centreline velocity, U_m. 217

3.21 Radial profiles of $\overline{uv}$ for 80 μm beads at x/d = 0.1, 10, 20 and 28 for mass loadings of 23% and 86% compared to the single phase. Normalisation is by the single phase centreline velocity, U_m^2. 218

3.22 Radial profiles of correlation coefficient of $\overline{uv}$ for 80 μm beads at x/d = 0.1, 10, 20 and 28 for mass loadings of 23% and 86% compared to the single phase. 219

3.23 Effect of mass loading 23% and 86% on centreline profiles of (a) 80 μm bead flux G_m, normalised by exit centreline flux, G_{om} (b) 80 μm bead concentration G_m/U_m, normalised by exit centreline concentration (c) flux half-width normalised by nozzle exit diameter and (d) concentration half-width normalised by nozzle exit diameter. 220

3.24 Effect of mass loading 23% and 86% on radial profiles of flux G of 80 μm beads at x/d = 0.1, 10, 20 and 28. Normalisation is by centreline flux G_m. R_0 is the half-width of the single phase jet. 221

3.25 Comparison of the estimated mass flowrate of the beads at four stations along the axis of the jet to the calibrated mass flowrate of the screw-feeder; (a) 40 μm beads for mass loadings of 13% and 80% and (b) 80 μm beads for mass loadings of 23% and 86%. 222

3.26 Comparison of the ratio of the estimated mass flowrate of the beads for two mass loadings at four stations along the axis of the jet to the expected ratio; (a) 40 μm beads for mass loadings of 80% and 13% (expected ratio of 80/13 = 6.1) and (b) 80 μm beads for mass loadings of 86% and 23% (expected ratio of 86/23 = 3.7). 223

3.27 Integral of momentum flux along the axis of the jet normalised by the exit momentum flux of (a) 40 μm beads and (b) 80 μm beads. 224

3.28 Radial profiles of the value of the integral of momentum flux up to radius r at x/d = 0.1, 10, 20 and 28 for 40 μm beads for mass loadings 13% and 80% compared to the single phase. 225

3.29 Radial profiles of the value of the momentum flux integral up to radius r at x/d = 0.1, 10, 20 and 28 for gas phase and 80 μm beads for mass loadings 23% and 86% compared to the single phase. 226

3.30 Comparison of the single phase results of the present experiment at x/d = 20 and 28 to these of Wygnanski and Fiedler (1969); (a) mean axial velocity and (b) axial r.m.s. velocity. Normalisation of velocities is by the local centreline value. 227

3.31 Comparison to the experiment of Shuen et al. (1985); (a) mean and (b) r.m.s. axial velocity of single phase and gas phase and 80 μm beads-mass loading 23% compared to the single phase and gas phase and 80 μm beads-mass loading 22% of Shuen et al. and (c) radial r.m.s. velocity of single phase and 80 μm beads-mass loading 23% compared to the single phase and 80 μm beads-mass loading 22% of Shuen et al. 228

3.32 Comparison to the experiment of Modarress and Tan (1984); (a) Centreline profile of mean axial velocity of single phase and 40 μm beads for mass loadings of 13% and 80% compared to the single phase and 50 μm beads for mass loading of 32% of Mod. & Tan and (b) centreline profile of mean axial velocity of single phase and gas phase and 80 μm beads-mass loading 23% compared to the single phase and gas phase and 50 μm beads-mass loading 32% of Mod. & Tan. 229

3.33	Schematic representation of "fan-spreading" phenomenon which accounts for large values of u'_b even though beads are too large to respond to turbulent frequencies in the gaseous phase. At low Stokes numbers, bead trajectories are close to being straight lines and figure shows superposition of bead trajectories at arbitrary measurement locations "I" and "II". Points "S" and "F" are the two initial positions considered at the exit of the jet: point "S" corresponds to a location which has slower U_b than does "F". The bold vectors denote velocity of bead which originates from "S" and lighter vectors are from "F". Measurement of bead turbulence at points "I" and "II" is due to superposition of fast and slow trajectories.	230
4.1	Experimental arrangement and coordinate system used.	271
4.2	Centreline profiles in sudden expansion ratio of 3.33 for 40 μm beads for mass loadings of 13%, 40% and 80% compared to the single phase; (a) mean axial velocity (U), (b) axial r.m.s. velocity (u'), (c) azimuthal r.m.s. velocity (w'). Normalisation is by the gas bulk velocity in the large tube, U_0.	272
4.3	Radial profiles of mean axial velocity (U) in sudden expansion ratio of 3.33 at z/D = 0.06, 0.3, 1.5, 2.4, 3.2, 4.4, 6 and 8 for 40 μm beads for mass loadings 13%, 40% and 80% compared to the single phase. Normalisation is by the gas bulk velocity in the large tube, U_0.	273-274
4.4	Radial profiles of axial r.m.s. velocity (u') in sudden expansion ratio of 3.33 at z/D = 0.06, 0.3, 1.5, 2.4, 3.2, 4.4, 6 and 8 for 40 μm beads for mass loadings 13%, 40% and 80% compared to the single phase. Normalisation is by the gas bulk velocity in the large tube, U_0.	275-276

4.5 Centreline profile of volume flux (G) in sudden expansion ratio of 3.33 for 40 μm beads for mass loadings 13%, 40% and 80%. Normalisation is by the centreline flux at the exit of the small pipe, G_{om}. 277

4.6 Radial profiles of volume flux (G) in sudden expansion ratio of 3.33 at z/D = 0.06, 0.3, 1.5, 2.4, 3.2, 4.4, 6 and 8 for 40 μm beads for mass loadings 13%, 40% and 80%. Normalisation is by the centreline flux, G_m. 278-279

4.7 Centreline profiles in sudden expansion ratio of 5 for 40 μm beads for mass loadings of 13%, 40% and 80% compared to the single phase; (a) mean axial velocity (U), (b) axial r.m.s. velocity (u'), (c) azimuthal r.m.s. velocity (w'). Normalisation is by the gas bulk velocity in the large tube, U_0. 280

4.8 Radial profiles of mean axial velocity (U) in sudden expansion ratio of 5 at z/D = 0.08, 0.67, 1.33, 2.67, 4 and 5.33 for 40 μm beads for mass loadings 13%, 40% and 80% compared to the single phase. Normalisation is by the gas bulk velocity in the large tube, U_0. 281-282

4.9 Radial profiles of axial r.m.s. velocity (u') in sudden expansion ratio of 5 at z/D = 0.08, 0.67, 1.33, 2.67, 4 and 5.33 for 40 μm beads for mass loadings 13%, 40% and 80% compared to the single phase. Normalisation is by the gas bulk velocity in the large tube, U_0. 283-284

4.10 Radial profiles of azimuthal r.m.s. velocity (w') in sudden expansion ratio of 5 at z/D = 0.08, 1.33, 2.67 and 5.33 for 40 μm beads for mass loadings 13%, 40% and 80% compared to the single phase. Normalisation is by the gas bulk velocity in the large tube, U_0. 285

4.11 Radial profiles of (a) mean and (b) r.m.s. radial velocity (V and v') in sudden expansion ratio of 5 at z/D = 1.33 for 40 μm beads for mass loadings 13%, 40% and 80% compared to the single phase. Normalisation is by the gas bulk velocity in the large tube, U_0. 286

4.12 Centreline profile of volume flux (G) in sudden expansion ratio of 5 for 40 μm beads for mass loadings 13%, 40% and 80%. Normalisation is by the centreline flux at the exit of the small pipe, G_{om}. 287

4.13 Radial profiles of volume flux (G) in sudden expansion ratio of 5 at z/D = 0.08, 0.67, 1.33, 2.67, 4 and 5.33 for 40 μm beads for mass loadings 13%, 40% and 80%. Normalisation is by the centreline flux, G_m. 288-289

4.14 Centreline profiles in sudden expansion ratio of 3.33 for gas phase and 80 μm beads for mass loadings of 23%, 40% and 86% compared to the single phase; (a) mean axial velocity (U), (b) axial r.m.s. velocity (u'). Normalisation is by the gas bulk velocity in the large tube, U_0. 290

4.15 Radial profiles of mean axial velocity (U) in sudden expansion ratio of 3.33 at z/D = 0.06, 0.3, 2.4, 3.2, 5 and 8 for gas phase and 80 μm beads for mass loadings 23%, 40% and 86% compared to the single phase. Normalisation is by the gas bulk velocity in the large tube, U_0. 291-292

4.16 Radial profiles of axial r.m.s. velocity (u') in sudden expansion ratio of 3.33 at z/D = 0.06, 0.3, 2.4, 3.2, 5 and 8 for gas phase and 80 μm beads for mass loadings 23%, 40% and 86% compared to the single phase. Normalisation is by the gas bulk velocity in the large tube, U_0. 293-294

4.17 (a) Centreline profile of volume flux normalised by the centreline flux at the exit of the small tube, G_{om}, (b) flux half width normalised by the diameter of the small tube, d, in sudden step expansion ratio of 3.33 for 80 μm beads for mass loadings 23%, 40% and 86%. 295

4.18 Radial profiles of volume flux (G) in sudden expansion ratio of 3.33 at z/D = 0.06, 0.3, 2.4, 3.2, 5 and 8 for 80 μm beads for mass loadings 23%, 40% and 86%. Normalisation is by the centreline flux, G_m. 296-297

4.19 Centreline profiles of (a) mean axial velocity (U), (b) axial r.m.s. velocity (u') in sudden expansion ratio of 5 for gas phase and 80 μm beads for mass loadings of 23%, 40% and 86% compared to the single phase. Normalisation is by the gas bulk velocity in the large tube, U_0. 298

4.20 Radial profiles of mean axial velocity (U) in sudden expansion ratio of 5 at z/D = 0.08, 0.67, 1.33, 2.67, 4 and 5.33 for gas phase and 80 μm beads for mass loadings 23%, 40% and 86% compared to the single phase. Normalisation is by the gas bulk velocity in the large tube, U_0. 299-300

4.21 Radial profiles of axial r.m.s. velocity (u') in sudden expansion ratio of 5 at z/D = 0.08, 0.67, 1.33, 2.67, 4 and 5.33 for gas phase and 80 μm beads for mass loadings 23%, 40% and 86% compared to the single phase. Normalisation is by the gas bulk velocity in the large tube, U_0. 301-302

4.22 Velocity probability density functions in sudden expansion ratio of 5 at z/D = 1.33 and y/D = 0.25 for (a) single phase, (b) 40 μm beads, (c) 80 μm beads. 303

4.23 Radial profiles of (a) mean and (b) r.m.s. azimuthal velocity (W and w') in sudden expansion ratio of 5 at z/D = 2.67 for 80 μm beads for mass loadings 40% and 86%. Normalisation is by the gas bulk velocity in the large tube, U_0. 304

4.24 Centreline profile of volume flux in sudden step expansion ratio of 5 for 80 μm beads for mass loadings 23%, 40% and 86%. Normalisation is by the centreline flux at the exit of the small pipe, G_{om}. 304

4.25 Radial profiles of volume flux (G) in sudden expansion ratio of 5 at z/D = 0.08, 0.67, 1.33, 2.67, 4 and 5.33 for 80 μm beads for mass loadings 23%, 40% and 86%. Normalisation is by the centreline flux, G_m. 305-306

4.26 Centreline profiles of (a) mean axial velocity (U), (b) axial r.m.s. velocity (u') in sudden expansion ratio of 3.33 for 200 μm beads for mass loadings of 19% and 58% compared to the single phase. Normalisation is by the gas bulk velocity in the large tube, U_0. 307

4.27 Radial profiles of mean axial velocity (U) in sudden expansion ratio of 3.33 at z/D = 0.06 and 8 for 200 μm beads for mass loadings 19% and 58% compared to the single phase. Normalisation is by the gas bulk velocity in the large tube, U_0. 308

4.28 Radial profiles of axial r.m.s. velocity (u') in sudden expansion ratio of 3.33 at z/D = 0.06 and 8 for 200 μm beads for mass loadings 19% and 58% compared to the single phase. Normalisation is by the gas bulk velocity in the large tube, U_0. 308

4.29 Centreline profiles of (a) mean axial velocity (U), (b) axial r.m.s. velocity (u') in sudden expansion ratio of 5 for 200 μm beads for mass loadings of 19% and 58% compared to the single phase. Normalisation is by the gas bulk velocity in the large tube, U_0. 309

4.30 Contours of zero velocity for (a) the single phase and 40 μm beads for mass loadings of 13, 40 and 80% and (b) the single phase and gas phase and 80 μm beads for mass loadings of 23, 40 and 86% and the single phase separation streamline in the expansion ratio of 3.33. 310-311

4.31 Contours of zero velocity for (a) the single phase and 40 μm beads for mass loadings of 13, 40 and 80% and (b) the single phase and gas phase and 80 μm beads for mass loadings of 23, 40 and 86% and the single phase separation streamline in the expansion ratio of 5. 312-313

4.32 Centreline profiles of (a) mean axial velocity of single phase, (b) mean slip velocity of 40 μm beads, 13% mass loading normalised by the local gas velocity and (c) mean slip velocity of 80 μm beads, 23% mass loading in the free jet and sudden expansion ratios of 5 and 3.33. 314

4.33 Centreline profiles of axial r.m.s. velocity of (a) single phase, (b) 40 μm beads, 13% mass loading and (c) 80 μm beads, 23% mass loading in the free jet and sudden expansion ratios of 5 and 3.33. Normalisation is by the centreline velocity at the exit of the small tube, U_{om}. 315

4.34 Centreline profiles of radial r.m.s. velocity of (a) single phase, (b) 40 μm beads, 13% mass loading in the free jet and sudden expansion ratios of 5 and 3.33. Normalisation is by the centreline velocity at the exit of the small tube, U_{om}. 316

4.35 Flux half width of 80 μm beads for mass loadings of 23 and 86% in the free jet and sudden expansion ratio of 3.33 Normalisation is by the diameter of the small tube, d. 316

4.36 Sketch showing the way the beads disperse into the recirculation zone. Page 260 explains the sketch. 317

GLOSSARY OF SYMBOLS

Roman characters

$A(d_i)$	effective area of the sampling volume of the anemometer for the size class "i" (equation (2.38) and (2.39))
C	particle concentration (no. m^{-3}) [C(t) = C+c']
$C(d_i)$	time average of particle number density (number of particles per m^3) of size class "i", which includes diameters between d_i and $d_i + \delta d$ (equation (2.39))
D	downstream pipe diameter of sudden expansion or divergence of the scattered light (equation (2.8))
d	jet pipe diameter or upstream pipe diameter of sudden expansion
d_p	particle diameter
$E(x,m,\theta,t)$	electric field function of the scattered light
E_0	electric field of the incident beam
E_T	electric field of the interference of the scattered light at one point in space
$E_{ij}(x,m,\theta)$	electric field of the scattered light with subscript i = 1, 2 polarisation and due to subscript j = 1, 2 one of the two beams of the laser Doppler system
E_{0ij}	electric field component of the incident beam for E_{ij}
$E_k^{(l)}$	electric field of the interference pattern of the scattered light where subscript k = 1 or 2 denoting one of the two beams and superscript (l) = (1) or (2) denoting contribution from surface reflection or refraction correspondingly
F_+, F_-	Bead flux taking into account the directional ambiguity of the flow; + for beads moving with positive velocity and - for beads moving with negative velocity
f	fringe spacing of the laser Doppler anemometer
G	particle flux (no. s^{-1} {area of measurement volume}$^{-1}$)
I_T	intensity of the interference pattern of the scattered light at one point in space
I_0	intensity of the incident beam

$I^{(ij)}$	intensity of the intensity pattern of the scattered light where superscript (ij) denotes the considered scattered light contributions to the interference pattern and i, j = 1 or 2 denoting surface reflection or refraction correspondingly while i corresponds to contributions from beam j and 1 from beam 2 (figure 2.5)
$i(x,m,\theta)$	dimensionless intensity of the scattered light
$J_1(\,.\,)$	first order Bessel function
k	wave number of the laser light ($=2\pi/\lambda$)
L_{22}	length scale of turbulence in the cross-stream direction
m	refractive index of the particle relative to the surrounding fluid
$\dot{m}_{b,f}$	mass flow rate (kg s^{-1}) of beads or air in the jet pipe
N_5	number of clock pulses measured by the counter over the duration of 5 Doppler periods
N_8	number of clock pulses measured over the duration of 8 Doppler periods
n_i	measured number of particles in the size class "i"
p	integer which determines the interface of the scattered ray with the sphere (chapter 2)
R	radius of jet pipe
Re	Reynolds number
$R_L(\tau)$	Lagrangian fluid velocity correlation, the time integral of which defines the Lagrangian fluid timescale, T_f, and the average is over all "fluid particles" that start from the point of release (equation 1.1)
r	radial coordinate of the jet experiment
$r_{1 \text{ or } 2}$	Fresnel reflection coefficients (equation 2.6)
$S_{e,m,t,tr,\omega}$	Stokes number of beads based on conditions at, respectively, the jet pipe exit, the local mean flow and local turbulent flow, the transit time through the recirculation zone and the centrifuging due to streamline curvature

$S_{1,2}$	Amplitude functions of the light scattered by a sphere located in a single beam, one polarised normal to the scattering plane and the other parallel (figure 2.2)
$S_{refr.}$	Amplitude function due to the interference from the refrected paths scattered by one sphere located in the crossing region of two beams
$S_{surf.\ refl.}$	Amplitude function due to the interference from the surface reflected paths scattered by one sphere located in the crossing region of two beams
$S_{1st\ int.\ refl.}$	Amplitude function due to the interference from the first internal reflection paths scattered by one sphere located in the crossing region of two beams
$S_{diff.}$	Amplitude function due to the interference from the diffracted light scattered by one sphere located in the crossing region of two beams
$S_{ij}(x,m,\theta)$	amplitude function of the scattered light with subscript i = 1, 2 polarisation and due to subscript j = 1, 2 one of the two beams of the laser Doppler system
t	time
t_e	large eddy timescale of a jet (equation 1.10a) or equation (4.9)
T_{dec}	timescale of deceleration of centreline velocity in single phase jet or sudden expansion centreline (equation 1.13)
T_f	Eulerian timescale of air (equation 1.7)
$T_{b,f,p}$	Lagrangian timescale of beads, air and particles, respectively (equations 1.6)
T_{tr}	transit time of the beads through the recirculation zone
T_s	total sampling time of the measurements after subtracting the dead time of the prototype counter
Tol	frequency validation tolerance; is either a function of N_8 or a constant set by the user
U_m	mean centreline velocity of single phase
U_0	bulk mean air velocity at exit of jet pipe or in the pipe downstream of the step of the sudden step expansion flow

U_{0m} mean centreline velocity of the single phase at exit of jet pipe

U_{slip} axial mean slip velocity between the fluid and the dispersed phase

U axial component of velocity [$U(t) = U + u'$]

u' r.m.s. component of U, $u' = \sqrt{\overline{u^2}}$

V radial component of velocity [$V(t) = V + v'$]

$V(d_i)$ effective volume of the intersection region of the beams of the anemometer for the size class "i" (equation (2.41))

v' r.m.s. component of V, $v' = \sqrt{\overline{v^2}}$

$\overline{v^2}$ radial variance of velocity

$\overline{v_{Lf}^2}$ Lagrangian mean square fluctuation of the fluid velocity (equation (1.1)

W tangential component of velocity [$W(t) = W + w'$]

w' r.m.s. component of W, $w' = \sqrt{\overline{w^2}}$

x Mie nondimensionless size parameter ($=\pi d_p/\lambda$) (chapter 2) or axial coordinate of the jet experiment (chapter3)

$\overline{Y^2(t)}$ mean square displacement of "fluid particles" from the point of release (equation 1.1)

y elevation angle of the observation location relative to the plane of the beams (chapter 2, figure 2.5) or radial coordinate (chapters 3 and 4)

z axial coordinate of the sudden step expansion experiment (chapter 4)

Greek characters

δ phase due to optical path length difference to the reference path passing through the centre of the scattering sphere (equation 2.12)

ε rate of dissipation of turbulent kinetic energy of air

ε_f percentage of N_8 set for the frequency validation tolerance Tol (equation 2.36)

θ	scattering angle relative to the axis of a single beam or the bisector of the intersection angle of two beams
θ'	angle between the incident ray and the ray emerging from the p interface (equation 2.9)
λ	wavelength of laser light
μ	dynamic viscosity of the air
$\nu_{eff.f,p}$	effective turbulent viscosity of air or of particle
ν	kinematic viscosity of air
ξ	rotation angle of the scattered light theory geometry (figure 2.5)
π	3.14159
$\rho_{f,p}$	density of air or particles
$(\Sigma\ t_n)_i$	the sum of residence times in the measuring volume of particles in size class "i" (equation 2.41)
σ	phase of the interference scattered fringe pattern at one point in space (equation 2.25 and 2.26)
$\sigma^{(ij)}$	phase of the interference pattern of the scattered light at one point in space where superscript (ij) denotes the considered scattered light contributions to the interference pattern and i, j = 1 or 2 denoting surface reflection or refraction correspondingly while i corresponds to contributions from beam j and l from beam 2 (figure 2.5)
τ	time (equation 1.1)
τ and τ'	angles between the surface tangent of a transparent spherical particle and the incident and refracted ray correspondingly (figure 2.3)
τ_D	Doppler signal period
τ_k	Kolmogorov timescale (equation 1.5)
τ_p	particle time constant
τ_{phase}	time of phase shift between two Doppler signals (equation 2.1)
Φ_1	phase measured between the outer detectors of the phase-Doppler system
Φ_2	phase measured between the central detector and an adjacent one of the phase-Doppler system
ϕ	intersection angle of the two beams of the phase-Doppler system

$\phi_{1,2}$	angle between the scattering plane of beam 1 or 2 and the major circle passing from the observation point in space and is normal to the plane containing the beams (figure 2.5)
χ	mass loading ratio at jet pipe exit (= $\dot{m}_b/\dot{m}_f$)
$\chi_{1,2}$	angle between the plane of the beams and the scattering plane of beam 1 or 2 (figure 2.5)
ω	angular frequency of light
ω_D	Doppler frequency

Subscripts

b	bead (dispersed phase)
s	single phase flow
f	air in the presence of the dispersed phase
Lb,f,p	Lagrangian value of bead, gas or particle
om	value on centreline at jet pipe exit
p	particle

Superscripts

---	time mean, Reynolds, average

CHAPTER 1

INTRODUCTION TO THE THESIS

1.1 The flows considered

Flows involving the simultaneous existence of two states of one material or two different materials in different states and at conditions that can be considered as carrier fluid and dispersed phase are called two phase flows. So the co-existence of liquid and solid phase or gaseous and solid phase or liquid and gaseous phase flowing together in a carrier fluid-dispersed phase combination constitute a two phase flow.

A variety of two phase flows exists in nature and in engineering applications. The wind or rivers carrying dust or sand, the snow, the rain are examples in nature and the rate at which particles spread in a turbulent flow is of interest in a number of industrial applications. Knowledge of the physics of such flows could be used to extend the life of materials which suffer from erosion caused by the dispersed phase, or to achieve efficient and stable combustion of the heterogeneous reactants of droplets of liquid fuel or pulverised coal by better control of mixing in an internal combustion engine or a power plant respectively, or to reduce emissions to the environment from power plants or internal combustion engines.

Until recently, little was known from experiments about the aerodynamics of particulate turbulent two-phase flows and of the interaction between the two phases, because of the difficulty of making the necessary measurements. Although many models have been formulated and used in the prediction of two phase flows, all suffer experimental confirmation of the assumptions of the physical processes associated with the two phase flows.

This thesis reports measurements in a particle-laden round fully turbulent jet and a round turbulent sudden step expansion using air as carrier fluid and glass beads as dispersed phase. The influences of particle size and mass loading on the dispersion of the particles as well as on the interaction between the two phases are examined and interpreted in terms of the relative timescales of the particles, due to inertia and to the mean and turbulent motion of the carrier fluid.

Reliable instrumentation for simultaneous size and velocity measurements was needed and part of this thesis examines the extension of laser Doppler anemometry for these purposes. A phase-Doppler anemometry instrument was developed for the needs of the experiments and the advantages and the limitations of this technique are examined.

1.2 Previous work

This section reviews relevant literature and provides the necessary background to establish the aims of the present contribution. The review begins by examining the effects of particle inertia, crossing trajectories and volume fraction of particles on the dispersion rate. Then, after establishing the limitation of current knowledge and further requirements, the abilities of available instrumentation to provide size-velocity correlations are considered.

a) Two phase flow : theory and experiment

(i) *Effects of particle inertia, crossing trajectories and volume fraction of particles on dispersion rate*

In two phase flows the dispersion rate of a cloud of particles released into a flow is important since it controls the concentration of the cloud as a function of time and position. Taylor (1921) assumed "fluid particles" smaller than the Kolmogorov microscale with no inertia in order to express in mathematical form the dispersion of a fluid and suggested that their statistical dispersion from any given fixed location in a stationary homogeneous turbulent flow as a function of time is described by the mean square displacement from the point of release as follows :

$$\overline{Y^2(t)} = 2\,\overline{v_{Lf}^2} \int_0^t \int_0^{t'} R_L(\tau)\, d\tau\, dt' \qquad (1.1)$$

where $\overline{v_{Lf}^2}$ is the Lagrangian mean square fluctuation of the fluid velocity, $R_L(\tau)$ is the Lagrangian fluid velocity correlation, the time

integral of which defines the Lagrangian fluid timescale, $\mathcal{T}_f$, and the average is over all "fluid particles" that start from the point of release. Lumley (1978) has suggested the use of equation (1.1) for the motion of discrete particles, which are characterised by inertia in the following form :

$$\overline{Y^2(t)} = 2\ \overline{v_{Lp}^2}\ t\,\mathcal{T}_p \qquad (1.2)$$

where $\overline{v_{Lp}^2}$ is the Lagrangian variance of the particle velocity, $\mathcal{T}_p$ is the Lagrangian timescale of the particle motion and the average is over all the particles starting from the point of release. The turbulent diffusion coefficient, or eddy diffusivity, $\nu_{eff.p}$ is the rate of dispersion (Calabrese & Middleman, 1979) given by :

$$\nu_{eff.p} = \frac{d\overline{Y^2(t)}}{dt} = 2\ \overline{v_{Lp}^2}\ \mathcal{T}_p \qquad (1.3)$$

These expressions can be extended from homogeneous turbulence to transport in uniform shear flows (Tennekes & Lumley, 1972) but there is nothing to be gained, for the purposes of this discussion, by introducing more complexity. There are two parameters of the discrete particles which differ from "fluid particle" characteristics and are practically important because they can be controlled : the inertia and the concentration of the particles.

Since the particle inertia is greater than that of a "fluid point", the particle fluctuating velocity is smaller, at least in homogeneous flows. So $\overline{v_{Lp}^2}$ is less than $\overline{v_{Lf}^2}$. The inertia is characterised by a particle time constant (Snyder & Lumley, 1971) :

$$\tau_p = \frac{d_p^2\,(1 + 2\,\frac{\rho_p}{\rho_f})}{36\nu} \qquad (1.4)$$

where the subscripts p , f mean correspondingly particle, fluid, ρ is the density and ν is the kinematic viscosity of the carrier fluid. This

time constant acts as a first order filter on the "forcing" function, which is the spectrum of frequencies of the turbulent fluid flow. The amount of low-pass filtering effected by the inertia may be evaluated by comparing τ_p with turbulent characteristic timescales of the fluid flow, such as the Kolmogorov timescale (Snyder & Lumley , 1971) :

$$\tau_k = \left(\frac{\nu}{\varepsilon}\right)^{0.5} \qquad (1.5)$$

where ν and ε are correspondingly the kinematic viscosity and the dissipation rate of the fluid flow, the Lagrangian timescale (Meek & Jones, 1973), which can be approximated (Vames & Hanratty, 1988) :

$$\mathcal{T}_f = \frac{\nu_{eff.f}}{\overline{v_f^2}} \qquad (1.6)$$

where $\nu_{eff.f}$ is the effective viscosity of the fluid and $\overline{v_f^2}$ is the Eulerian mean square fluctuation of the fluid velocity and the Eulerian fluid integral scale :

$$T_f = \int_0^\infty \frac{v_f(t-\tau)\,.v_f(t)}{v_f^2}\, d\tau \qquad (1.7)$$

The ratios between the particle inertia time constant and the different characteristic turbulent timescales of the fluid flow can be referred to as turbulent Stokes numbers which indicate the response of the particles to the turbulence of the fluid flow. Here, the Lagrangian fluid timescale, $\mathcal{T}_f$, is mainly used, which corresponds to the minimum frequency to which a particle should respond, if it is going to be influenced by fluid turbulence.

The effect of particle inertia is to cause the particle fluctuating velocity to be smaller than that of the fluid (Snyder & Lumley, 1971) and to increase the particle velocity integral timescale, $\mathcal{T}_p$ (Chao, 1964). It is obvious from equation (1.3) that the particle diffusivity is the subject of two competing trends and the net increase in the

particle turbulent diffusion coefficient as particle inertia increases is predicted to be small (Reeks, 1977, Pismen & Nir, 1978, Shih & Lumley, 1986) for small particles in the absence of external forces (e.g. gravity). This has been confirmed experimentally for homogeneous isotropic flows (Wells & Stock, 1983, Vames & Hanratty, 1987). The latter reference shows, that even when particle inertia reduces the turbulent Stokes number T_f / τ_p to about 0.5, so that $\overline{v_p^2} / \overline{v_f^2}$ is only 0.5, the turbulent Schmidt number of the particles, $\nu_{eff.f} / \nu_{eff.p}$, is still as high as 1.2. The practical importance of this result is that the dispersion rate of a particle cannot be assessed even qualitatively from the measurement of the $\overline{v_p^2} / \overline{v_f^2}$ alone.

A particle, influenced by an external force field, e.g. gravity, falls from one eddy to the other at a rate faster than the mean eddy lifetime and a mean slip velocity is established between the particles and the fluid. In contrast, a "fluid particle" remains in an eddy until the eddy decays. This effect decreases the particle Lagrangian integral timescale, T_p, and is referred as the "crossing trajectory effect" (Yudine, 1959). The decrease of the particle dispersion coefficient caused by this effect is approximately inversely related to the free fall velocity (Csanady, 1963). The coefficient $\nu_{eff.p}$ is also reduced by a small amount, because the turbulence acquired by the particle, v'_{Lp}, decreases as the time dependent frequency spectrum of the fluctuating gas velocities, as seen by the particles, increases.

The effect of "crossing trajectories" has been shown (Wells & Stock, 1983, Shih & Lumley, 1986, Snyder & Lumley, 1971) to reduce the dispersion of light particles, for which τ_k / τ_p is about 1. Wells & Stock found that if the mean slip velocity due to an external potential force field is equal to the r.m.s. fluid velocity, $U_{slip} / v'_f = 1$, the reduction in particle dispersion coefficient $\nu_{eff.p}$ is of the order of 10%. This result is valid for homogeneous flows and the "crossing trajectories effect" for heavy particles is not clear so that, for $T_f / \tau_p \lesssim 1$, implying that $\tau_k / \tau_p << 1$, as in the near field of the jets to be described below, it reduces faith in models, which assume that the particle turbulent Schmidt number is a constant.

Inspection of equations (1.2), (1.3) shows that the particle concentration does not appear in the expressions for particle dispersion, and this stems from the assumption that the particle concentration was sufficiently small, so that there was no influence of the particles on the carrier fluid, but only influence of the carrier fluid on the dispersion of the particles. If there is no mean slip between the two phases but $\tau_k / \tau_p < 1$, the modification of the fluid turbulence is due to the relative motion between the fluctuating velocities of the particles and the fluid, which constitutes an additional mechanism for turbulent energy dissipation (Pismen & Nir, 1978), the importance of which increases with the concentration of the particles. The existence of this additional mechanism does not necessarily imply that the overall dissipation will increase but rather that the mechanism for dissipation has become more efficient so that the length scale of the eddy at which dissipation takes place will be increased (Lumley, 1978). The increase in the dissipative length scale implies a decrease in τ_k, but not in T_f, and the phenomenon is probably important near a wall, where it may be responsible for the drag reduction along pipes and across cyclones carrying two-phase mixtures (Boothroyd, 1967, Soo et al, 1960) through the thickening of the viscous sublayer (Lumley, 1978). In free shear flows, particularly at the laboratory scale, it is unlikely to be significant. In contrast, Owen, 1969 suggests that there is extra dissipation, which reduces the gas turbulence and hence the effective viscosity of the suspension is also reduced :

$$\frac{\nu_{eff,f+p}}{\nu_{eff,f}} = (1 + \chi)^{-0.5} \qquad (1.8)$$

where χ is the mass loading of particles. This correlation represents the dissipation ratio and has been used by Melville & Bray (1979b) for the calculation of particle laden jets with some success. The effect of increasing concentration is to reduce particle dispersion, at least in free shear flows as a consequence of the reduction of v'_p because of a possible reduction in v'_f.

It is noted that, with the exception of Diesel sprays, the volume fraction of particles in many practical applications is much below 0.3 % and so particle-particle, as opposed to particle-fluid, interactions are negligible (Batchelor, 1971, quoted by Lumley, 1978). As an

example, the primary stream of a pulverised coal burner conveys approximately one kilogram of coal per kilogram of air, which corresponds to a volume fraction of 0.05 %, assuming that the density of pulverised coal is 2000 Kg m^{-3}.

The preceding estimates provide guidance on the expected frequency response of particles to turbulence in a variety of flows, including shear flows. Snyder & Lumley (1971) and Wells & Stock (1983), for example, have devised experiments in homogeneous turbulence to measure the velocity characteristics of isolated particles, which responded to all the turbulent frequencies up to and including the Kolmogorov timescale. To achieve this end, the scale of the confining wind tunnel must be so large, however, that it would be impractical to load these flows with sufficient particles to establish the effects of particle volume fraction on the interaction between the two phases in homogeneous turbulence. The effects of volume fraction on the turbulence of the continuous phase can be investigated only in smaller-scale flows which means, effectively, boundary free shear flows but it is difficult to arrange these so that the particles remain responsive to the Kolmogorov microscale. This is demonstrated in the following paragraph.

Appendix 3.A shows that the largest value of the ratio of the Kolmogorov to the large eddy timescale, t_e, in a fully turbulent jet is approximately

$$\frac{\tau_k}{t_e} = 0.022 \qquad (1.9)$$

and that the downstream variation of the large eddy timescale is

$$t_e = 0.05 \left(\frac{x}{d}\right)^2 \left(\frac{d}{U_o}\right) \qquad (1.10a)$$

where x is the downstream distance and U_o is the mean velocity at the exit of the nozzle of diameter d. The final bracket represents the mean exit timescale of the jet for which the largest practicable value in a laboratory would be to set d and U_o at 0.05 m and 5 m/s respectively so that

$$t_e = 5 \times 10^{-4} \left(\frac{x}{d}\right)^2 \qquad (1.10b)$$

Since the equations (1.9) and (1.10a) show that τ_k increases as the square of downstream distance, it is advantageous to measure as far downstream as possible. However, the mean velocity of the jet becomes smaller with increasing downstream distance, so that the terminal velocity of the particles becomes important, draughts in the laboratory become an increasing source of uncertainty, and the volume flow rate of the particle-laden air which must be captured increases. It is inconvenient to measure beyond 30 diameters downstream where, in the example suggested here, t_e is 500 ms and hence by equation (1.9), τ_k is 10 ms. Their timescale must be compared with the inertial timescale of the particles commonly used for laboratory scale experiments. The smallest particles that are both quasi-monodisperse and readily commercially available at reasonable cost are glass beads of approximately 40 μm diameter for which τ_p is about 10 ms. Comparison with τ_k shows that it is difficult to devise an experiment with monodisperse particles in a shear flow for which the particles are responsive to all frequencies up to the Kolmogorov scales over large distances in the flow. The particles do respond, however, to the frequencies of the turbulent spectrum which relate to the energy containing motions, characterised by the Lagrangian timescale, T_f. In appendix 3.B, it is shown that T_f is given by :

$$T_f = 3.29 \times 10^{-4} \left(\frac{x}{d}\right)^2 \left(\frac{d}{U_o}\right) \left(\frac{v'_f}{U_m}\right)^{-2} \qquad (1.11)$$

For the jet flow considered here, T_f is about 47 ms at 30 diameters from the exit of the jet and the largest glass bead diameter which remains responsive to this timescale is about 80 μm.

It would be nice to compare the conditions in laboratory-scale experiments with these in an industrial application, such as the combustion of pulverised fuel burner in a power station, for which d ≈ 0.5 m and U_o ≈ 30 m/s and hence Re is ≈ 10^6. For the purposes of this calculation the presence of the swirl-induced recirculation zone, the change of the kinematic viscosity due to the increase of the temperature of the gases and the change in the particle time constant due to devolatisation and heterogeneous combustion are ignored : the

flow from the burner is idealised to be equivalent to an isothermal jet which would issue from the burner exit. These simplifications give $\tau_k / t_e = 2.7 \times 10^{-3}$ and t_e is, at 20 diameters downstream, about 330 ms so that τ_k is about 1 ms and the corresponding value of T_f is about 35 ms. The farthest downstream station considered here is only 20 diameters downstream of the exit, rather than the value of 30 diameters taken in the laboratory-scale experiments, because this is about the limit at which the flow from a single burner can be identified as a jet before the effects of buoyancy, the opposing wall of the boiler and interference from the flow of the neighbouring burners become significant. Coal particles with equivalent diameter greater than about 80 μm will not respond to the turbulence in the flow of this burner and this represents about one-fifth of the fuel by weight. In contrast, particles smaller than about 12 μm are completely responsive to this range of frequencies but these are a small fraction of the size distribution which is typical of pulverised coal. Therefore, as for shear flow experiments in the laboratory, a large fraction of the coal particles are not responsive to the highest frequencies in the turbulence of the fluid.

ii) Particle dispersion rate in mean shear flows

The previous section was concerned with the dispersion, and the rate of dispersion, of particles due to the random motion acquired from the turbulence of the gaseous phase, without taking into account explicitly the response of the particles to the development of the mean flow of the gaseous phase. In this section experiments of particles in flows with mean shear are considered and since, with the exception of the confined mixing layer investigated by Boerner et al. (1986), all the configurations concern free jets, the possibility arises that the decay of the mean axial velocity of the continuous phase is more rapid than that to which the particles can respond. A mean slip velocity is generated from the inertia of the particles rather than their weight and it is, thus, necessary eventually to broaden the discussion and consider the possibility of the transport of particles as being due to two separate mechanisms : the mean velocity of the particles and the turbulent dispersion of the particles.

The limiting case of particles sufficiently light that there is no mean slip between the two phases, is considered first. Theoretical and experimental simplifications can be made, provided that the particle concentration is a passive scalar, similar to temperature or an inert tracer gas, and can be regarded as a continuum, and the turbulent diffusivity of the particles can be measured from the mean concentration distribution, without the need to measure velocity characteristics of particles, such as $\overline{v_{Lp}^2}$ or T_p in equations (1.2) and (1.3). It is relatively easy to measure concentration and, consequently, much of the early work in particulate flows was concerned with the dispersion of light particles. Turbulent Schmidt numbers have been reported for a variety of flows (Goldschmidt & Eskinazi, 1966, Householder & Goldschmidt, 1969, Goldschmidt, Householder, Ahmadi & Chuang, 1972, Lilly, 1973) and the measurements of Yuu et. al. (1978), for example, quantify the increase in the turbulent Schmidt number with particle inertia. The most advanced application of the limit of light particles is the solution of the modelled equation for the transport of the correlation between particle velocity and concentration fluctuations, $\overline{v_p c}$ (e.g. Shih & Lumley, 1986), by analogy to other modelled equations of the second-order correlations, such as Reynolds stress or turbulent heat flux. The solution can be extended to inhomogeneous flows with mean, constant slip between the two phases, due to the weight of the particles with consequent advantage over, say, the assumption of a constant Schmidt number in that the large reduction in the turbulent diffusion coefficient for the particle concentration due to slip can be calculated because of the phenomenon of crossing trajectories.

In the case of heavy particles, a mean slip velocity between the two phases is present due to the inertia of the particles rather than because of their weight. In this case, understanding of the development of particle concentration comes from measurements of the mean and r.m.s. velocity characteristics of the particles relative to those of the gas phase and it is important to have a quantitative estimate of the diameter of a particle, for which the mean velocity will be different from that of the gas phase. This is discussed in the following paragraphs in the context of free jets for which experiments are classified according to a dimensionless number with

responsiveness of the particles to turbulent frequencies related to the same number. It is also made clear that there have been very few measurements by laser Doppler anemometry, in which the particles disperse because of turbulent motion.

The timescale of the axial inhomogeneities of the decay of the mean fluid velocity in a jet can be estimated from an empirical expression for the centreline decay (Spalding, 1979) :

$$\frac{U_m}{U_o} = 6.57 \left(\frac{d}{x}\right) \qquad (1.12)$$

where the displacement of the virtual origin is assumed to be zero and equation (1.12) leads to the deceleration timescale

$$T_{dec} = \left(\frac{dU_m}{dx}\right)^{-1} = \left(\frac{d}{U_o}\right) \left(\frac{x}{d}\right)^2 \left(\frac{1}{6.57}\right) \qquad (1.13)$$

and T_{dec} can be normalised (Yuu et al, 1978, McComb & Salih, 1978) by the particle time constant, defining the mean Stokes number S_m, as

$$S_m = \frac{T_{dec}}{\tau_p} = S_e \left(\frac{1}{6.57}\right) \left(\frac{x}{d}\right)^2 \qquad (1.14)$$

where S_e is the Stokes number based on the mean velocity at the exit of the nozzle

$$S_e = \frac{(d/U_o)}{\tau_p} \qquad (1.15)$$

The bracketed numerator in equation (1.15) is a timescale defined by the length and velocity scales at the exit of the jet. Mean slip between the two phases is expected when $T_{dec} < \tau_p$ or, in other words, if $S_m < 1$, and table 1.1 lists some recent experiments in particle-laden jets by laser Doppler anemometry in order of decreasing particle response. The table provides the exit Stokes and Reynolds numbers as well as the range of axial distance over which measurements are reported; the latter is important because equation (1.14) shows that S_m depends on the square of the distance from the jet exit. The formulae are

optimistic estimators of the value of S_m since the virtual origin has been taken as zero. The initial concentration of the particles is expressed as a loading of the particulate phase in the gaseous phase by weight, rather than as a volume fraction, because the mass loading is informative of the proportion of the momentum flow rate carried by the particles to that carried by the gaseous phase. As a rule of thumb, modifications to the mean momentum flow rate, and hence mean velocity, of the gaseous phase can be expected only if the momentum flow rate of the particulate phase at the nozzle is greater than about one-tenth that of the gaseous phase.

The information of the preceding paragraph allows the experiments in table 1.1 to be classified into three categories. "Totally responsive" particles are those for which S_m is everywhere of the order of unity or larger, "partially responsive" particles have S_m of the order unity at the farthest downstream measurement station and "unresponsive" particles, for which S_m is less than unity everywhere. In the remainder of this subsection the effects of particles on the development of first the mean and then the turbulence of the jet is reviewed; to avoid confusion it is emphasised here that the word "responsive" is in relation to the mean and not to the turbulent motion of the particles relative to the gaseous phase.

The experiments of McComb & Salih (1977, 1978) and, nominally at least, of Popper et al (1974) are for "totally responsive" particles at negligibly small loadings, although it should be noted that some of the results were obtained in jets which may not have been fully turbulent, because the jet exit Reynolds numbers were below 10000. McComb & Salih used laser Doppler anemometry to measure concentration of light particles, rather than velocity, and validated analysis based on perturbation methods from the behaviour of infinitesimally small particles. Popper et al provide information of the mean velocity of the particles and found the existence of self-similarity of cross stream profiles of axial velocity; they stress that particle size was not accurately determined and a quoted particle diameter of 50 μm which is questionable since the magnitude and sign of the mean slip between the particles and the clean jet is larger, than the estimate of the magnitude of S_m would suggest. Since the value of τ_p depends on the particle diameter squared, a small error in the diameter propagates as a large change in the Stokes number. Both

measurement sets confirm, however, that the spread of momentum and concentration is narrower than for a single-phase jet and that the mean velocity of the particles is close to that of the single-phase jet.

"Partially" responsive particles have a mean slip velocity between the two phases, which causes momentum transfer from the particles to the gaseous phase and this transfer increases with increasing loading of particles, so that the axial velocity of the gaseous phase at a given axial location becomes larger than in the corresponding single-phase jet (Modarress et al, 1984, Shuen et al, 1985, for 79 μm particles). Because the particles are partially responsive, the rate of decay of the particle mean axial velocity also reduces, as does the spreading rate of the jet, with increasing loading. For these particles, the magnitude of the mean slip is constant with increasing loading. The measurements of Modarress et al (1982, 1984) are detailed and accurate, but th se of particle concentration are limited and this represents an important omission which shall be corrected by this work.

For the unresponsive particles (Modarress et al, 1982 for 200 μm particles, Shuen et al, 1985 for particles larger than 79 μm) the mean slip velocity is, as expected, larger than for the responsive particles and the effect of loading on the velocity of the particulate phase cannot be pronounced. There is, however, transfer of momentum to the gaseous phase which increases with mass loading and hence the slip velocity decreases with increasing loading, in contrast to "partially responsive" particles. Shuen et al (1985) measured the velocities of their 207 μm particles by laser-Doppler anemometry to be 50% lower than th se measured by double flash imaging and offered the explanation that the signal-to-noise ratio for large particles is poor due to the large pedestal component of the scattered light. An alternative explanation is offered below.

Solomon et al (1985 a, b & c) have measured non-evaporating and evaporating sprays generated by a commercial air atomiser over hundreds of diameters downstream of the nozzle exit. The velocity characteristics of the gaseous phase were measured by laser Doppler anemometry but those of the spray, together with particle size, were measured by double-flash photography. The droplets at the far field locations are "partially responsive" according to the preceding analysis, even though the exit Stokes number is small, because of the square law dependence of S_m on axial distance. Analysis of the flow in

this context is made difficult for a number of reasons including that the velocity characteristics of the droplets are determined by the way in which the liquid is atomised by the nozzle and, in this atomiser design, large drops travel fast with mean velocities greater than the air velocity; in contrast, the smaller droplets travel slower than the air. Far downstream, as expected, the mean slip is small. Another difficulty is that the sprays are inevitably polydisperse so that the interaction between the droplets is due to a superposition of responsive, partially responsive and unresponsive droplets; in addition, the droplet size distribution changes with downstream distance for the evaporating spray. These flows are qualitatively different from these considered so far in table 1.1, because the particle loading is much greater than unity and hence the momentum of the jet in the near nozzle field is due to the liquid and not to the gas phase. Also, the liquid volume fraction is greater than 0.9 % for the first 50 diameters so that there must be many collisions between droplets. The unusually broad air jet, particularly near the atomiser, is confirmation of the qualitative differences which are expected. The entrainment of the ambient air is not comparable to an equivalent air jet and the results will not therefore be considered further.

Shuen et al (1986) have investigated oil droplets with turbulence in a methane supported flame at small loadings. The interpretation of the droplet response, in terms of the mean Stokes number analysis above, is complicated by uncertainty in the particle time constant, due to the evaporation of the droplets, by the increase in the kinematic viscosity consequent on combustion, and because T_{dec} in the gas phase is modified by combustion. The results suggest that the particles are unresponsive for the first 20 diameters but the mean and r.m.s. velocities of each phase are similar after about 120 diameters. The passage of the droplets through the flame sheet at x/d $\approx$ 100 must contribute to the reduction of the particle time constant, because of the corresponding reduction in drop size, but the square law dependence of the mean Stokes number must also be significant.

Levy & Lockwood (1981) experimented with "unresponsive" particles, for which S_m is substantially smaller than unity over a large part of the measured flow field and reported results which do not accord with the trends established in the previous review. For example, they report the mean velocity of their largest particles ($\approx$1000 μm) was smaller than that of their smaller particles at 20

diameters downstream of the jet exit (≈ 200 μm) and that the corresponding gas velocity in the presence of the 1000 μm was smaller than the corresponding single phase jet. Their measurements also show that the 200 μm particle velocity at a given axial station decreases with increasing loading. However, in their experiment as well as for that of Solomon et al (1985 a, b & c) the majority of the momentum flow rate at the exit of the nozzle lies in the particulate phase and the near field structure of such jets can be reasonably expected to be different from those in which the opposite is true.

So far, the response of the mean velocity of the particles to the inhomogeneities of the mean gas velocity field in the streamwise direction has been related by means of a mean Stokes number. The concept can be extended to relate the response of the particles to the turbulent motion of the particles through a turbulent Stokes number. This dimensionless group is also dependent on S_e, as demonstrated in appendix 3.B, so the turbulent Stokes number of the particle is related to the mean Stokes number. The ratio between the two in a jet is, a constant with magnitude

$$\frac{S_m}{S_t} = \frac{T_{dec}}{T_f} = \left(\frac{v'_f}{U_m}\right)^2 \left(\frac{1}{6.57}\right) \left(\frac{1}{3.29 \times 10^{-4}}\right) \approx 29 \qquad (1.16)$$

using equation (B.8) in appendix 3.B and equation (1.14) above. It is thus easier for a given particle diameter to follow the mean rather than the turbulent motion in a jet and it would be expected that, of the experiments with monodisperse solid particles considered in the previous paragraphs, only in that of Modarress et al, 1984 would it be reasonable to expect the particles to acquire some turbulence from the fluid. Note that Popper et al (1974) and McComb & Salih (1977, 1978) do not report turbulence levels.

Modarress et al (1984) found that the presence of both the unresponsive and partially responsive particles reduce the normalised gas velocity fluctuations (in common with Solomon et al, 1985 a & b, near the atomiser) and the normalised Reynolds shear stress, as compared to the values at the same axial station of the single phase jet. This does not necessarily imply that the particle-laden jet is less turbulent than the single phase jet, since the rate of decay of the two phase jet is slower than that of the single phase jet and comparisons between normalised values at the same value of x/d serve only to

confirm the slower rate of decay. From the arguments presented in the theoretical analysis above, it is not surprising that the presence of the particles reduces the turbulence intensity in the carrier gas phase. There is, however, a second mechanism by which increasing particle concentration could modify only the turbulence in the gaseous phase, as observed in the experiments of Modarress et al (1982, 1984) which is related to the increase in the shear strain in the gas maybe due to the modification of the shape of the cross stream profile of the mean axial velocity of the gaseous phases. The increase in the shear strain, $\partial U_f / \partial r$, of the fluid will promote the rate of production of turbulence and the value of v'_f may reasonably be expected to increase causing an increase in v'_p also, if the particle is partially responsive. There are, therefore, two competing processes at work in these flows and the preceding arguments suggest that it is the suppression of turbulence due to the increase in the rate of dissipation of gas-phase turbulence which dominates in the measurements of Modarress et al (1982, 1984).

Surprisingly, all the jet experiments for which the turbulence of the particles was measured show that the particles have values of streamwise r.m.s. velocity which are large fractions of the streamwise r.m.s. velocity of the gas phase, irrespective of the turbulent Stokes number, although the particle radial r.m.s. values are generally smaller than those in the gas. This observation is not restricted to free jets, since similar results have been reported by Boerner et al (1986) in a confined plane mixing layer, for which the exit Stokes number was about 0.063 - corresponding, to unresponsive particles. The practical importance of this observation is that large values of particle turbulence are not necessarily accompanied by efficient mixing, as for example in the vicinity of the recirculation zone of the annular jet of Hardalupas et al (1986b) where large turbulent velocities did not result in any dispersion of the particles into the recirculation zone - an observation which has undesirable implications in the context of the stabilisation of pulverised coal or liquid fuel flames.

From the review of the literature, two points arise. First, there is need to measure large ($\approx$ 200 μm) particles (i.e. $S_m < 1$) in view of the unexplained results of Levy & Lockwood (1981) and in view of the difficulties, reported by Shuen et al (1985), of using a laser Doppler anemometer in this size range. Secondly, it is desirable to repeat the

difficulties, reported by Shuen et al (1985), of using a laser Doppler anemometer in this size range. Secondly, it is desirable to repeat the experiments of Modarress et al (1984) for particles which have S_m close to unity at about 30 diameters downstream of the exit so as to provide particle flux measurements. As demonstrated above, this size range corresponds to the motion of the larger fraction of particles in a boiler fired by pulverised coal and an important objective of the present work in this size range is to investigate the origin of the unexpectedly large r.m.s. streamwise velocities of the particles. Finally, the loading of the particulate phase must be as large as possible both because this condition is relevant to industrial practice and because of the interest in interaction between the particulate and the gaseous phase. Finally it is desirable to find out how the particles behave in a recirculating flow, which is very important for the combustion of pulverised coal or liquid fuel in the burners of power plants and for which there are no measurements made by laser Doppler anemometry.

b) Instrumentation for size - velocity correlation measurements

The two-phase flow equations of the earlier analysis are presented in the Lagrangian and not the Eulerian system of reference and approximations have to be made so that measurements made in the Eulerian frame can be interpreted. It is evident, therefore, that it is desirable to measure in the Lagrangian framework.

Existing methods, which could perform Lagrangian measurements are the photographic and the holographic techniques which interpret simultaneously recorded images of a number of individual particles and build up a particle size histogram. The images are produced by short light pulses (from a flash for photography and from a laser for holography), which "freeze" the particles and allow direct measurement of their size. Double flash photography or double holography provides measurement of velocity with two closely spaced light pulses used to obtain the double images. Although such technology has been used successfully (e.g. Trolinger et al., 1979), their resolution at small size ranges is poor, so that tracer particles of around 2 μm, which follow the gas motion, cannot be distinguished from larger particles; the influence of the dispersed phase on the gaseous phase cannot, therefore, be determined. Another drawback is

the images makes them unattractive for applications in dense two phase flows.

As a consequence, instrumentation performing time average measurements over the total sampling time at one point of the flow has to be used. Sampling probe methods introduce unacceptable interference and optical techniques provide a non intrusive alternative.

Optical techniques can be divided into multi-particle analysing techniques and single particle counters. The former are based on multiple scattering from or extinction of one laser beam, which passes through the flow. They provide information averaged over all the sizes in the flow and the laser diffraction technique is the most common multiscattering method for particles greater than several μm. It is based on the detection of the intensity of the diffraction pattern, scattered in the forward direction from each particle, and deconvolution schemes have been used for the reconstruction of the size distribution from the integrated scattering intensity collected in each of the rings of the photodetector used (Swithenbank et al., 1977, Hirleman et al., 1984). However, the spatial resolution of the sizing measurement is not adequate for detailed analysis of a flow field and there is no velocity information. Single particle counters are based on the detection of the scattered light from single particles crossing a small optical sample volume, which is defined at the focussing region of a light source. The interaction between the particle and the optical volume generates a signal at a detector, which has to be sufficiently large in amplitude to be descriminated from the background noise. The signal is processed to provide size and velocity information for each particle. There are two kinds of single particle counters, depending on the way that they get the velocity information.

The non-Doppler techniques use the signal produced from the interaction of a particle with a single beam or two adjacent laser beams. The time of flight of the particle through the beam can be used to estimate the velocity of the particle and the amplitude of the signal to get the sizing information. The laser Doppler anemometer can measure the velocity from the beat frequency of the signal produced from the scattered light from the particle passing through the crossing point of two laser beams. There are four characteristics of the Doppler signal, which have been used to measure the size of particles : the amplitude of the low-pass filtered signal, known as

pedestal, the amplitude of the high-pass filtered signal, the visibility and the phase.

The common strategy used for the measurement of the velocity characteristics of the gaseous flow is to introduce tracer particles, known as seeding to follow the gas motion, and to use these as scattering centres to measure the velocity. Provided a reliable means can be found to distinguish between the velocities of the continuous and discrete phases it is feasible to measure the effect of increasing the mass loading of the particulate phase on the velocity characteristics of the continuous phase. An obvious and simple way would be to introduce the discrete phase as monodisperse particles and to discriminate between the latter and seeding on the basis of the amplitude of the pedestal of the Doppler signal or the amplitude of the particle signature for the non-Doppler technique. However, there are three difficulties which may cause "cross-talk" from the velocity distribution of the large particles to that of the gas phase.

The first is that the distribution of light intensity in a laser beam is Gaussian, so that a particle at the edge of the measuring volume will give rise to a signal which has similar amplitude to that of a seeding particle passing through the centre of the measuring volume. This is referred as "trajectory ambiguity".

The second difficulty is that there are no solid particles manufactured, which can be used as the dispersed phase and are monodisperse on a number density, as opposed to a volume density basis. As a consequence, the distribution of the amplitudes will be continuous and not bimodal so that the signal level at which particles are accepted as seed is arbitrary and must depend on calibration experiments which are difficult to perform. Later, it is demonstrated that even the apparently safe procedure of reducing the sensitivity of the photomultiplier to detect only the larger particles in the flow can give errors due to the continuous distribution of particle size and this is likely to have been the cause of one documented inconsistency (Shuen et al, 1985). This difficulty also determines the need of a sizing instrument, rather than a simple velocity measuring system, even for the velocity characteristics of the solid "monodisperse" particles when used as the dispersed phase.

The third difficulty is that the intensity of the laser light incident at the measuring volume is generally not constant, because the beams pass through a "depth of field" of particles, especially when

the diameter of the particulate phase is larger than about one-quarter of the incident beam diameter. Kliafas et al (1986, 1987) proved that the depth of field introduces both systematic and random attenuation, as particles that lie outside the probe volume of the laser Doppler system pass through the beams and the random fluctuation introduces a further uncertainty in the relationship between pedestal amplitude and particle size. There is no obvious reason against the extension of the above conclusions to non-Doppler techniques, although there has been no investigation of the influence of the "depth of field" on the non-Doppler sizing instruments.

The reviews, of table 1.2 for the laser non-Doppler techniques and of table 1.3 for the laser Doppler techniques provide an indication of progress in overcoming these problems.

A number of methods have been applied to eliminate trajectory ambiguity and include observation of a selected part of the probe volume of known and constant intensity, analysis of all the measurements and later correction with deconvolution schemes and the use of the ratio of the properties of two or more signals observed at different collection angles.

For the amplitude based laser Doppler techniques, the observation of a selected part of the control volume can be achieved by introducing a pointer beam of different colour to identify the central part of the measuring volume (e.g. Hess & Espinosa, 1984, Hess, 1984, Hishida et al, 1982) or by using a second pair of beams of different colour (Modarress & Tan, 1984), a top hat intensity profile beam (Allano et al, 1984, Hishida et al., 1986), or by coincidence detectors located at forward and 90° collection angles (e.g. Ungut et al, 1978, Lightfoot & Negus, 1986). Also the ratio of the amplitudes of Doppler signals collected from separate detectors at different locations (Houser, 1980, Hess & Li, 1986) can remove trajectory ambiguity.

Of the non Doppler techniques, a deconvolution scheme, described by Holve & Self (1979a & b), can remove trajectory ambiguity and the application of a second deconvolution scheme can extract the size-velocity correlation. This approach has been applied successfully (Holve, 1986) to measure the flyash formation from pulverised coal. Hirleman (1978) suggested the use of the signals generated by a particle crossing two adjacent laser beams to measure two velocity components and the trajectory of each particle. Then

knowledge of the trajectory of the particle through the Gaussian intensity distribution removes the ambiguity from the amplitude based sizing information. The intensity ratio technique is based on the collection of signals at different scattering angles and the ratio of the amplitudes of these signals can remove the dependence of the sizing method on the incident beam intensity (Hirleman & Moon, 1982).

Although the above methods solve some of the difficulties of measurements in two phase flows, the third ambiguity of the attenuation of the intensity of the incident beams due to the particles crossing them outside the control volume, cannot be solved with any of the above techniques. Holve suggested correction of results by the average attenuation of the incident beam intensity over the total sampling time with the help of a photodetector positioned at direct forward scatter. This suggestion partly solves the problem, because the attenuation of the beam is a random effect in time, so that the correction should be applied simultaneously with each measurement. As a consequence, in the effort to measure the effect of mass loading of the discrete phase on the gas phase, the error due to the "depth of field" is increased as the mass loading is increased, and the amplitude of the pedestal becomes a less reliable mean of discrimination between the tracer particles and the discrete phase.

Although much effort has been expended in developing means of sizing particles with LDA, some experiments have been reported, which ignore the problems outlined in the preceding paragraph (Levy & Lockwood, 1981, Shuen et al, 1985), generally for particle diameters larger than 100 μm. The results of these experiments are not obviously incorrect probably because the magnitude of the error in the velocity of the gaseous phase due to cross-talk from the larger particles is also a function of the relative flux of particles and seed. The error will be small if the seeding flux is much higher than that of the particulate phase. Modarress et al (1982) claim that, for their range of mass loading of particles, it was acceptable to discriminate between 200 μm particles and the gas phase on the basis of photodetector saturation, signal overload and bandpass filtration of the velocity if the seed flux was about two orders of magnitude larger than the particle flux ($<\approx$ 400 Hz). It is not clear on what basis this assertion was made, although the comment on bandpass filtration implies that the mean slip between the two phases must have been so large that some discrimination could be made on the basis of the

velocity value alone. The condition on the relative fluxes of the two phases becomes harder to satisfy as the characteristic diameter of the particulate phase becomes smaller because the particle flux increases as the cube of the diameter of the particles for a given mass loading of the particulate phase, although this increase is partly offset by a decrease in the effective cross - section of the measurement volume of the LDA with the diameter of the scattering particle. As an example, Modarress et al (1984), found that the same method could not be used for 50 μm particles and they had to develop a more advanced approach, based on a pointer volume.

Visibility of the Doppler signal, defined as the ratio of the amplitude of the signal modulation to the amplitude of the pedestal, has a Bessel function dependence on particle size and has been suggested as a means for particle sizing by Farmer (1972), Durst (1973) and Fristrom et al (1973). This technique has been developed and applied for measurements in a variety of dilute two phase flow situations (e.g. Farmer, 1974, 1976 and 1978, Durst & Eliasson, 1974, Durst, 1978, Hong & Jones, 1976). Limitations of the forward scatter collection visibility technique to very dilute two phase flows exist due to the length of the control volume (e.g. around 20 mm, Yeoman et al, 1982) and the requirement of the LDA technique of the presence of only one particle in the probe volume; this suggested the off axis collection visibility as used by Bachalo et al (1979), Bachalo (1980) and Farmer (1980). The problem of the trajectory ambiguity for the amplitude of the signal exists in a similar way for the visibility of the signal and a pointer beam technique was used by Yeoman et al (1982) to remove it. The difficulty in the alignment of two pairs of beams of different colour to cross at the same point suggested the use of coincident detectors at forward and 90° to define the central part of the probe volume instead of the two colours for the measurements in an industrial furnace (Negus et al, 1986). Off axis collection visibility reduces trajectory ambiguity, due to the reduction of the size of the probe volume observed (Bachalo et al, 1979). The measurement of the gas phase at the presence of the particles with the visibility technique is impossible because of the "depth of field" problem (Kliafas et al, 1986, 1987), although the influence is smaller than on the amplitude of the pedestal and the low resolution at the particle sizing range up to around 15 μm, for which visibility is around unity.

A combination of the visibility and the amplitude method has been used to extend sizing range (Yeoman et al, 1982, for on axis collection, Hess, 1984b for off axis collection) and more recently Boerner et al (1986), used this approach to measure the gas phase in the presence of 110 μm glass beads. There is currently no agreement for the lower level of particle size and flux, which result to unacceptable levels of cross-talk if simple amplitude discrimination is used, although 110 μm beads are likely to be below this level.

Other techniques, which combine the velocity measurement of a LDA system and a sizing technique from another source include the white light technique of Durst & Umhauer (1975) and the variable grid technique of Wang & Tichenor (1981), but problems due to their dependence on the incident beam intensity remain.

A number of workers (Bachalo & Houser, 1984, Saffman et al, 1984, Bauckhage et al, 1984, Hardalupas, 1986) have independently developed the phase Doppler instrument originally proposed by Durst & Zaré (1975) for the sizing of spherical particles. The advantages include that the sizing information is not amplitude based but is derived from the spatial frequency of a scattered interference pattern and, as a consequence, depth of field problems are eliminated (Hardalupas et al, 1986a). There is no need to arrange two colour pointer volumes, the optical alignment is easier than for amplitude - visibility based sizing instruments and the electronics for signal processing can be constructed to handle high data rates (of the order of several kHz) in contrast to amplitude processing with transient recorders (Boerner et al, 1986, Kliafas et al, 1987, Yeoman et al, 1982) which is slow ($\approx$ 10 Hz). The ability to process high data rates is convenient and allows the measurement of particle flux. The main disadvantage of the phase-Doppler technique is its restriction to sizing spherical particles. If the latter condition is satisfied, the calibration curve can be established from calculation on the basis of either Mie theory (Saffman et al, 1986) or by assuming the mode of scattering (reflection or refraction) and using geometrical optics or without prior assumption of the type of scattering involved and using geometrical optics (Hardalupas, 1986, Al-Chalabi et al, 1987).

It should be emphasised that all off-axis collection based instruments are affected by the shape of the particle, which is not the case for on axis collection (Jones, 1987) and this is in opposition to the need for measurements in high mass loaded flows, which is

possible only for off-axis collection systems. Fortunately, the flows of interest can be simulated with spherical particles and this allows the use of the off-axis collection and a phase Doppler anemometer was developed and used for these purposes.

1.3 The present contribution

The review presented in the previous section has emphasised two main points :

a) the lack of a non-intrusive instrument which can measure reliably the size-velocity correlation of the dispersed phase and the influence of the presence of the particles on the continuous phase in dense two-phase flows.

b) few measurements in jets have been performed with particles which responded to the continuous fluid mean and turbulent motion. Conclusions drawn from these results can be misleading and the detailed process of two phase jet flows have yet to be determined.

The contributions of this thesis can be stated in relation to these two points.

The first comprises the development and evaluation of the phase Doppler technique, which can simultaneously measure size and velocity locally in two phase flows. The method is investigated theoretically and verified experimentally. The limitations of the technique are determined and design criteria for the optics and the electronics are suggested. Validation schemes, which will eliminate sizing errors are suggested based on the understanding of the light scattering phenomena involved.

The second consists of the application of the phase Doppler instrument to measure the mass flux and the velocity characteristics in two phase flows corresponding to a turbulent round jet and a turbulent axisymmetric sudden step expansion.

The turbulent particle-laden round jet was investigated over the first 29 diameters as a function of mass loading and the size of the particles. The exit Stokes numbers were 0.1, 0.020 and 0.0032, corresponding to quasi monodisperse glass beads of characteristic diameters approximately 40, 80 and 200 μm respectively. The reason for choosing these three sizes is explained as follows. The expectation for the largest diameter is that the particulate phase should be unresponsive to both mean and turbulent flow in the jet, since the

mean Stokes numbers are everywhere much smaller than unity. The experiment is intended to provide insight into the apparently paradoxical results of Levy & Lockwood (1981) and Shuen et al (1985), noted above, and explains the unexpectedly large values of the streamwise r.m.s. particle velocity which have been reported by many authors. The 80 μm beads permit, for reasons explained later, more reliable measurement of the gas phase in the presence of the beads than do the 40 μm beads. The Stokes number of the 80 μm beads should be such that, again, the mean and turbulent motion of the beads remain unresponsive to that of the surrounding air but, in contrast, the mean air velocities should be modified as the mass loading of the beads increases. For the smallest bead diameter, the effect of changing the mass loading on the motion of the beads, as well as on the gas phase flow, is pronounced because the exit Stokes number is high. The measurements of Modarress et al (1982, 1984) included neither extensive measurements of bead flux nor the bead cross-correlation coefficient. The former is as important a quantity as the velocity characteristics, particularly as a boundary condition at the exit of the nozzle. The correlation coefficient provides crucial evidence for the occurrence of a description of the dispersal of the beads which is denoted as "fan-spreading" and which applies to the motion of beads when the mean Stokes number is smaller than about unity.

The behaviour of the same particle sizes for the same mass loadings as those used for the jet experiment, is examined in a round sudden step expansion flow. Mass flux and velocity characteristics have been measured downstream of the step in the recirculation zone and in the free stream by using the phase Doppler instrument. Two expansion ratios of 3.3 and 5., defined as the ratio of the downstream tube diameter to the upstream tube diameter, were examined and the results quantify the influence of the expansion ratio, particle size and mass loading on the gas and particle flow properties.

1.4 Outline of the thesis

The remainder of the thesis is presented in four chapters.

Chapter 2 describes the phase Doppler anemometer. The theoretical analysis is based on geometrical optics and explores parameters influencing the technique. Experiments which verify the

theory and examine the performance of the method in practical two-phase flow conditions are presented. An optical and electronics design is suggested and an error estimate is attempted. Finally, a method for the measurement of particle flux and number density is reported.

Chapter 3 describes the experiments performed in the axisymmetric turbulent jet loaded with glass beads. Velocity characteristics and flux measurements are presented for the 40, 80 and 200 μm beads including value of Reynolds stress. The "fan-spreading" model for the dispersion of the particles is explained and is verified by the results. The measurements explain previous paradoxical results and the effect of the discrete phase on the gas flow characteristics is presented and explained.

Chapter 4 describes the round sudden step expansion experiment. Velocity and particle flux characteristics are presented. The way that the particles enter and leave the recirculation zone is analysed and the modification of the gas phase recirculation zone due to the presence of the beads is quantified as a function of the mass loading of the beads.

Chapter 5 presents concluding remarks and uses these to suggest further work.

TABLE 1.1

Principal characteristics of particle-laden jets measured by laser Doppler anemometry

Authors	Configuration and axial extent of measurement (jet diameters)	Suspension and density of particulate	Loading (kg part./ kg air)¶	Particle size (μm)	Particle time constant (ms)	Jet exit time constant (ms)	Exit Stokes no. S_e	Reynolds No.
McComb & Salih (1977)	Round jet $33 < X/D < 50$	TiO_2 in air	small	2.2	-	-	≈ 0.69	<15000
McComb & Salih (1978)	Round jet $15 < X/D < 30$	Tungsten in air	small	5.7	-	-	< 0.18	<11000
Popper et al (1974)	Round jet $1 < X/D < 20$	oil in air ($\rho < 1000 kgm^{-3}$)	0.001	< 50	< 7.7	3.9	≈ 0.5	10 600
		"	"	"	"	0.8	≈ 0.1	49 300
Hardalupas et al(1986c)	Annular jet X/D = 1.25••	Glass beads in air ($\rho = 2420$ kgm^{-3})	< 0.032	40	11.9	1.7•	0.14	54 000
This work	Round jet $1 < X/D < 29$	Glass beads in air ($\rho = 2420$ kgm^{-3} & 2950 kgm^{-3})	< 0.80	40	11.9	1.15	0.1	13 000
			< 0.86	80	47.6	1.15	0.020	13 000
			< 0.37	200	297.5	1.15	0.0032	13 000
Modarress et al (1984)	Round jet $0 < X/D < 30$	Glass beads in air	0.32	50	22.9	1.59	0.069	13 300
			0.85	"	"	"	"	"

Authors	Configuration and axial extent of measurement (jet diameters)	Suspension and density of particulate	Loading (kg part./ kg air)¶	Particle size (μm)	Particle time constant (ms)	Jet exit time constant (ms)	Exit Stokes no. S_e	Reynolds No.
Modarress et al (1982)	0 < X/D < 30	Round jet (ρ=2990 kgm^{-3})	< 1	200	366	"	0.0043	16 500
			< 0.64	50	22.9	"	0.069	"
Shuen et al 1985	Round jet 1 < X/D < 50	Sand in air (ρ = 2620kgm^{-3})	0.2	79	50	0.4	0.008	19 000
			0.2	119	113	0.36	0.0032	21 700
			0.66	119	113	0.43	0.0038	18 300
			0.66	207	343	0.43	0.0013	"
Solomon et al(1985a, b)	Commercial air atomiser 50 < X/D < 600	Non-evaporating Vacuumpump oil (polydisperse sprays), ‡ (ρ = 838 kgm^{-3})	1.78	30§	2.3	0.008	0.0035	30 000
			6.48	87§	19.3	0.028	0.0015	24 000
Solomon et al(1985 c)	Commercial air atomiser 50 < X/D < 500	Evaporating Freon - 11 (polydisperse sprays), ‡ (ρ =1464 kgm^{-3})	7.71	31§	4.3	0.018	0.0043	41 000
			15.78	58§	15.0	0.04	0.0027	36 000
Shuen et al 1986	Methane-fired flame† 1 < X/D < 200	Monodisperse droplets in a CH4 flame ($\rho \approx$ 790 kgm^{-3})	small	105	48	0.1	0.0021	≈11700
				180	141	0.1	0.00071	≈11700

Authors	Configuration and axial extent of measurement (jet diameters)	Suspension and density of particulate	Loading (kg part./ kg air)¶	Particle size (μm)	Particle time constant (ms)	Jet exit time constant (ms)	Exit Stokes no. S_e	Reynolds No.
Levy & Lockwood (1981)	Round jet X/D = 20	Sand in air (ρ =2620 kgm^{-3})	2.33	215	370	0.7	0.0019	≈25000
			1.14	215	"	"	"	"
			1.22	400	1280	"	0.00055	"
			2.24	540	2330	"	0.00030	"
			2.42	725	4200	"	0.00017	"
			3.5	1060	8990	0.6	0.000067	"

¶ density of air taken as 1.21 kgm^{-3}; kinematic viscosity as 15.0 x 10^{-6} m^2/s
† density of methane in non-reacting flow taken as ≈ 0.72 kgm^{-3}; kinematic viscosity as 1.4 x 10^{-5} m^2/s
§ Sauter mean diameter
• based on the bulk velocity and diameter of bluff body (28.6 mm)
•• D is outer annulus diameter (47.9 mm)
‡ Droplets' size and velocity measured by double-flash photography

TABLE 1.2

Laser non-Doppler based techniques for simultaneous particle size-velocity measurements

AUTHOR	TECHNIQUE - OPTICAL CONFIGURATION	MAIN PRINCIPLE - COMMENTS
Hirleman E.D. (1978)	Amplitude based technique. Two parallel beam system. A coaxial forward scatter detector used for collection. The beams are normal to the main flow direction.	By checking the signal signature from both beams, two velocity components can be measured and the particle trajectory can be defined. Then the particle size is defined from the amplitude of the signal. Beam attenuation will affect the size measurement. In highly turbulent flow there is no main flow direction and there are problems. Simple signal processing. Useful in low turbulent, dilute two phase flows.
Holve D., Self S.A. (1979 a & b)	Intensity of scattered light. Single beam arrangement, light being collected near forward direction.	A deconvolution scheme is used to remove the particle trajectory through the probe volume ambiguity from the measured intensity distribution and a second deconvolution to get the size-velocity correlation. Velocity is measured from the time of flight of the particle through the beam. Software intensive and limited to relatively low density flows. It can be applied to non - spherical particles.

AUTHOR	TECHNIQUE - OPTICAL CONFIGURATION	MAIN PRINCIPLE - COMMENTS
Wang J.C.F., Tichenor D.A. (1981)	Visibility of the signal generated from light collected through a variable frequency grid mask positioned in front of the detector. Light from a source is focussed at a point. Collection at 90°.	The signal is generated by imaging the particle onto a variable frequency grid and detecting the the transmitted light. When the particle size is equal to one grid spacing, the signal visibility drops to zero. Velocity can be measured from the transit time of the particle across the entire grid. Lower limit of the technique is 10 μm.
Hirleman E.D., Moon H.K. (1982)	Intensity ratio technique. The scattered light from a single beam is collected at different forward scatter angles. A ring mask is used in front of the detector.	The ratio of the scattered light intensities collected at the two forward scatter angles is a monotonic function of particle size. The method measures a particle diameter equivalent to the cross sectional area of a non-spherical particle when its aspect ratio is small. The technique is affected by the refractive index of the particle and errors occur for non-absorbing particles. The maximum limit is around 20 μm.

AUTHOR	TECHNIQUE - OPTICAL CONFIGURATION	MAIN PRINCIPLE - COMMENTS
Wang J.C.F., Hencken K.R. (1986)	Intensity of the scattered light. Single beam two colour system. A red beam is focussed in the centre of a blue beam. Collection at near forward direction for sizing and velocity measurements. 90° sidescatter collection for identification of the centre of the probe volume.	Cross-sectional area of sampling volume as a function of particle size calculation, which is used to correct the measured size distribution from the light scattered intensity at near forward direction. Time of flight of the particle through the probe volume is used for velocity measurements. Non-spherical particles in the size range of 10 - 200 μm can be identified.
Nakatani N., Kohri S., Yamada T., Sakabe T. (1987)	Visibility equivalent method used for the signal from a laser multifocus system. Five beams generated from a diffraction grating, collimated and expanded to generate light planes in equal distance from each other by a cylindrical lens. Light collected at forward scatter with a photodetector.	The similarity of the light planes to laser Doppler interference fringes in the probe volume helps to identify an equivalent visibility which has a Bessel function dependence on particle size. It can be used with non-spherical particles and has advantages over interferometric techniques.

AUTHOR	TECHNIQUE - OPTICAL CONFIGURATION	MAIN PRINCIPLE - COMMENTS
Nakatani N., Kohri S., Yamada T. (1987) Private Communication	Laser multifocus method is used in a way similar to the phase Doppler technique. Two detectors used for collection are positioned on the plane of the beams at symmetrical positions from the axis.	A particle entering a beam gives rise to a signal due to surface reflection and gives rise to a second signal as it leaves the beam. Here the first signal is observed by one detector and the second signal is observed by the other. The time delay between the five signals due to the five beams is related to particle size. The technique can be used with non-spherical particles but is limited to particles which reflect light only from their surface. More work is needed.

TABLE 1.3

Laser Doppler based techniques for simultaneous particle size-velocity measurements

AUTHOR	TECHNIQUE - OPTICAL CONFIGURATION	MAIN PRINCIPLE - COMMENTS
Farmer M.W. (1972)	Visibility. On-axis forward direction.	Bessel type variation as a function of particle size. Calculations of the visibility versus size calibration curve. The number density of a narrow size distribution can be measured as a function of the visibility of the signal in time when the fringe spacing is larger than the particle size.
Durst F. (1973)	Visibility. On-axis forward direction.	Calculations on laser Doppler anemometers. Dependence of signal quality and signal strength on particle size.
Fristrom R.M., Jones A.R., Schwar M.J.R., Weinberg F.J. (1973)	Visibility. System with non-uniform fringe spacing in the measuring volume.	The visibility of the signal from a particle traversing through a fringe system falls to zero for a certain fringe spacing. The relation between size and fringe spacing, when signal falls to zero is applied to measure particle size.

AUTHOR	TECHNIQUE - OPTICAL CONFIGURATION	MAIN PRINCIPLE - COMMENTS
Farmer M.W. (1974)	Visibility, assuming mainly diffraction part of scattered light.	Experimental investigation of the visibility variation at different collection angles by positioning known particle sizes at known positions inside the LDA probe volume. Effect of reflected-refracted scattered light on visibility.
Durst F., Zaré M. (1975)	Visibility, Amplitude of pedestal, phase shift. Different optical configurations were used to check the Doppler signal characteristics as a function of particle size.	The existence of a scattered fringe pattern from large particles in space based on the refraction or reflection of the incident rays through/on the particle. The phase Doppler technique idea is for the first time presented here. The change of the signal characteristics due to the particle trajectory through the control volume is not considered.
Durst F., Umhauer H. (1975)	White light technique. A simple LDA volume is generated inside a white light volume. Collection of the scattered white light at 90° of the white incident beam.	The amplitude of the white light signal is proportional to particle size. The LDA is used for velocity measurement. It is mainly for small particle sizes (< 20 μm).

AUTHOR	TECHNIQUE - OPTICAL CONFIGURATION	MAIN PRINCIPLE - COMMENTS
Hong N.S., Jones A.R. (1976)	Visibility. Simple LDA used with collection at small off-axis, forward scatter angles.	By changing the LDA fringe spacing the size range of the technique can be extended. Trajectory ambiguity is not considered.
Yule A.J., Chigier N.A., Atakan S., Ungut A. (1977)	Amplitude of pedestal at small forward angles.	Monotonic calibration curve for sizes between 30 and 240 μm. Oscillations on the calibration curve for smaller sizes. A method is suggested to correct the trajectory ambiguity. Depth of field is not considered.
Roberts D.W., Brasier C.W., Bomar B.W. (1978)	Visibility. Simple LDA system with forward scatter collection using a 60° mask.	Correction of the measured size distribution for the non-linear visibility calibration curve and for the change of the size of the LDA probe volume with the particle size. High electronic threshold was used to eliminate the trajectory ambiguity, but the system becomes insensitive to small particle sizes. Dense two phase flows cannot be measured by forward axis systems.

AUTHOR	TECHNIQUE - OPTICAL CONFIGURATION	MAIN PRINCIPLE - COMMENTS
Wigley G. (1978)	Simple LDA. Light is collected at forward scatter and near backscatter. A droplet larger than the beam diameter gives rise to three peak signals in forward scatter.	The side peaks of the signals are due to reflection from the particle surface as the particle enters and leaves the control volume. The central peak is due to refraction. The transit time between the two side peaks combined with the velocity information gives particle size. Limited to sizes larger than the beam diameter and moving on the plane of the beams normal to the LDA fringes.
Bachalo W.D., Hess C.F., Hartwell C.A. (1979)	Visibility. Simple LDA system with off axis collection.	The high density two phase flows can be measured by an off-axis collection system, which reduces the size of the probe volume. The visibility technique has been checked at off-axis forward scatter collection, sidescatter and backscatter. The sizing range is very wide (3 μm to 5 mm).

AUTHOR	TECHNIQUE - OPTICAL CONFIGURATION	MAIN PRINCIPLE - COMMENTS
Bachalo W.D. (1980)	Visibility, based on off-axis collection of mainly refracted or reflected part of the scattered light.	Theoretical analysis for the visibility off-axis technique is presented. The advantages are the wide sizing range and the capability of measurements in dense sprays. The existence of the scattered fringe pattern in space is mentioned, and the dependence of the visibility on particle size is determined by the phase function.
Farmer W.M. (1980)	Off-axis visibility.	Calculations of the calibration curves for visibility at 30° off-axis collection, at 90° sidescatter collection and near axis backscatter collection.
Martin W.M., Adbelmessih A.H., Liska J.J., Durst F. (1981)	Visibility, Amplitude of pedestal, Amplitude of filtered Doppler signal from large bubbles in water. Forward on axis collection.	Bubble velocity and size measurement for a range of 200 μm to 1. mm. The influence of the collection aperture diameter, the beam crossing angle, and the position in the control volume are examined. 85% similarity of the pedestal to Gaussian curve reduces particle trajectory ambiguity.

AUTHOR	TECHNIQUE - OPTICAL CONFIGURATION	MAIN PRINCIPLE - COMMENTS
Men A., Krimerman Y., Adler D. (1981)	Simple LDA with a measuring volume of almost constant intensity and crossed with two dark bands.	The velocity vector can be measured (trajectory, direction without frequency shift and Doppler frequency). Sizing information comes from the amplitude of the pedestal scattered from a top-hat control volume. Simple electronics needed.
Levy Y., Lockwood F.C. (1981)	Amplitude of the pedestal of the Doppler burst. On axis forward scatter collection.	Experiments with sand. The principle, that sand with size larger than the beam diameter is giving rise to Doppler signals with two side peaks at the pedestal, has been used for discrimination between gas phase and sand. The amplitude of the pedestal gives the size of the sand.
Yeoman M.L., Azzopardi B.J., White H.J., Bates C.J., Roberts P.J. (1982)	Visibility- up to 60-70 μm, amplitude of pedestal for larger particles. Two colour, four beams system. A larger green volume encloses a blue smaller volume. Beam cross angle less than 1°.	Frequency from both volumes is measured. Small volume to check the central trajectories. Visibility of the larger volume signal is giving size information. Non-spherical particles can be measured but at very low particle number densities, due to forward scatter collection.

AUTHOR	TECHNIQUE - OPTICAL CONFIGURATION	MAIN PRINCIPLE - COMMENTS
Mizutani Y., Kodama H., Miyasaka K. (1982)	Amplitude of pedestal. Simple LDA, collection at forward scatter and 90°.	The 90° detector limits the size of the probe volume and reduces the particle trajectory problem. The peak intensity of the pedestal at 90° is used for sizing and forward scatter signal for the velocity measurement. A method for the correction of the results after the measurement is suggested.
Hishida K., Maeda M., Imaru J., Hironaga K., Kano H. (1982)	Amplitude of the pedestal based technique. Three beam system with a larger diameter beam and two smaller diameter beams crossing at the centre of the large beam. The larger and the smaller diameter are linearly polarised with orthogonal polarisation.	The particle trajectory through the probe volume is known through the signals of the three beam system, so this ambiguity is removed from the peak amplitude of the large beam pedestal which is correlated to particle size. The velocity is measured from the frequency of the small beams Doppler burst.

AUTHOR	TECHNIQUE - OPTICAL CONFIGURATION	MAIN PRINCIPLE - COMMENTS
Modarress D., Tan H. (1983)	Amplitude of pedestal of the Doppler burst based method for discrimination between seeding and monodisperse particles. A two component LDA is used but with two different sizes measuring volumes, one lying in the center of the other.	By monitoring the pedestal of the signal of the larger probe volume the trajectory ambiguity in the small probe volume could be reduced. The amplitude of the pedestal then was used to discriminate between seed and 50 μm glass beads. The most reliable method presented here for discrimination.
Hess C.F. (1984)	Simple LDA arrangement. Makes use of the correlation between visibility and peak intensity of the pedestal. Large off-axis collection angle (30°).	For each size a minimum intensity limit is chosen which rejects signals due to particle trajectories through the edge of the control volume and the combined visibility information can measure the size. Calibration is needed before each measurement to establish the peak intensity of a certain size. The depth of field problem in dense flows will affect the technique.

AUTHOR	TECHNIQUE - OPTICAL CONFIGURATION	MAIN PRINCIPLE - COMMENTS
Hess C.F., Espinosa V.E. (1984)	Two colour or two polarisation - three beam system. Amplitude of pedestal based technique. Forward scatter collection.	Two small diameter and same colour beams are crossed in the centre of a larger beam diameter of another colour. The frequency of the Doppler signal from the small beams measures the velocity and the peak intensity of the pedestal from the large beam diameter gives the size of the particle. Simultaneous existence of both signals removes the particle trajectory through the control volume ambiguity. Calibration is needed for the amplitude of a certain size before each measurement. Depth of field problem.
Hess C.F. (1984)	Single colour-two different diameter beams crossing. Amplitude of the pedestal based technique.	The crossing of the two different diameter but same colour beams will limit the chances of erroneous size measurements due to the particle trajectory ambiguity. The frequency of the Doppler signal measures the velocity and the peak intensity of the pedestal gives the size of the particle. Increased noise from the light scattered from the large beam only. Depth of field problem.

AUTHOR	TECHNIQUE - OPTICAL CONFIGURATION	MAIN PRINCIPLE - COMMENTS
Allano D., Gouesbet G., Gréhan G., Lisiecki D. (1984)	Amplitude of pedestal. Simple LDA with a top-hat intensity probe volume. Collection at 90° to the incident axis and direction of incident electric field.	The top-hat intensity distribution removes the particle trajectory ambiguity. Sizing based on a linear relation between logarithm of peak amplitude and logarithm of particle diameter. Limited to spherical particles. Depth of field problem.
Bachalo W.D., Houser M.J. (1984)	Phase-Doppler. Simple LDA with forward off-axis collection (30°). Three photodetectors are used located in an integrated optical unit.	An instrument applying the technique is described. The three photodetectors guarantee no measurement error. The instrument is refraction based, independent of the incident beam intensity, has wide size range, simple electronics but has the restriction that can only applied to spherical particles.
Saffman M., Buchhave P., Tanger H. (1984)	Phase Doppler. Simple LDA with large off-axis collection angles (~70°). Three photodetectors are positioned separately at different collection angles.	The instrument uses surface reflection from the particles and is based on transient recorder processing which make it slow. Problem to observe the same part of the probe volume from the three separately mounted detectors.

AUTHOR	TECHNIQUE - OPTICAL CONFIGURATION	MAIN PRINCIPLE - COMMENTS
Bauckhage K., Floegel H.H. (1984)	Phase Doppler. Collection at large off-axis angles (~70°) with two photodetectors.	The collection with separately mounted detectors makes difficult the observation of the same part of the probe volume. The use of two photodetectors can result in sizing errors.
Maeda M., Hishida K., Sekine M., Watanabe N. (1986)	Amplitude of pedestal. Two colour-four beams LDA. The larger control volume is created by top-hat beams. Sidescatter collection.	Two velocity component system. Intensity used for sizing. Top-hat intensity control volume gives better resolution at large sizes and reduces the particle path ambiguity. Sidescatter collection limits the system to spherical particles but allows measurement to dense flows. Attenuation of beams affects sizing.

CHAPTER 2

DEVELOPMENT OF THE PHASE-DOPPLER TECHNIQUE

2.1 Introduction

The use of optical techniques to measure the rate at which particles disperse in turbulent flows, the velocity characteristics of each phase, size distributions, the particulate flux and the number density is becoming more widespread. The potential advantages over intrusive probes are evident and laser-based instruments can provide measurements which would be too time-consuming to attempt by analyses of photographs. The measurement of size and velocity at a point can be derived from a variety of techniques, analysed in detail in chapter 1, including single-beam instruments and laser-Doppler anemometers, using the visibility of the signal, the amplitude of the pedestal component or the phase difference between separate detectors signals. The latter method, the so called "phase-Doppler technique" suggested by Durst & Zaré (1975) and implemented by Bachalo & Houser (1984), Buchhave et al (1984), Bauckhage et al (1984) and Hardalupas et al (1986), has the unique advantage that the size information is independent of the amplitude of the signal and this suggests immunity to optical misalignment and random attenuations generated by the depth of field of the particulate flow.

Section 2.2 describes the phase-Doppler technique. The technique has not been evaluated in the past in terms of the details of experimental arrangement and the present contribution identifies and quantifies the importance of the main parameters (e.g. collection angle, beam intersection angle, particle refractive index) on the performance of the method. A theoretical description of the scattered light, upon which the method is based, is developed in section 2.3, to provide a basis for the choice of the optical arrangement. The influence of different parameters (e.g. movement of the particle in the control volume, interference of different components of the scattered light) on the technique are examined in section 2.4 by using this theory and validation procedures are suggested to reduce sizing errors. The theoretical analysis is verified experimentally in section 2.5 and practical problems arising from the application of the

technique are considered experimentally. The optical and the electronic design of the instrument is considered in section 2.6 and the main sources of error are analysed and quantified. The measurement of particle flux and particle number density is discussed separately in section 2.7 and is generally applicable to any laser Doppler based sizing technique. The chapter closes with concluding remarks and a summary of the main characteristics of the method.

2.2 The phase-Doppler anemometry technique.

The phase-Doppler technique is an extension of the laser Doppler anemometer to permit measurement of the size of spherical particles. The physical basis is the existence of a phase difference between Doppler signals observed from two different positions in space. The idea was put forward by Durst & Zaré (1975), who recognised the existence of a spatial fringe pattern scattered by a sphere located in the probe volume of an anemometer. The movement of the sphere causes a corresponding movement of this fringe pattern in front of a photodetector and its output is a conventional LDA signal. Signals from two photodetectors separated in space have the same Doppler frequency with a phase shift existing between them, because of the spatial frequency of the scattered fringe pattern. The phase shift in degrees is given by :

$$\text{phase} = \frac{\tau_{phase}}{\tau_D} 360° \qquad (2.1)$$

where τ_D is the Doppler period common to the two signals, and τ_{phase} is the time between corresponding zero crossings of the two signals (figure 2.1).

Durst and Zaré (1975) based their analysis on the so called "fringe model" of the laser Doppler anemometer in which a transparent spherical particle acts as a lens and magnifies the fringes in the LDA probe volume. A simple calculation gives the spacing of the projected fringe pattern through a transparent sphere at the position of the collection lens at an angle of 0° in the forward direction or from a reflecting sphere at 180° in the backscatter direction. Although this model explains the principle of the technique, it is not sufficient to

examine the interference of the light scattered from both beams of the laser Doppler anemometer and the physics involved and this is important in order to avoid sizing errors. Also the limitation of their analysis to direct forward or backward scattering does not allow the investigation at off-axis locations which is required for the measurement in dense two phase flows, as explained in chapter 1. This justifies a detailed analysis of the technique based on the light scattering theory of particles to evaluate the practical application of the method.

2.3 Theoretical foundation

The target is to find out more about the physics of the technique by using an expression of the phase of the interference pattern of the light scattered from both beams of the laser Doppler when a sphere is present in the probe volume. However, the analysis starts with the theory of the light scattered from a sphere located in a single beam and will be extended later for both beams. The theory gives information about the amplitude and the phase of the scattered light in space, which is used to establish the relation between particle size and frequency of the spatial interference fringe pattern.

a) Light scattered by a sphere located in a single beam.

Generally, the electric field of the scattered light wave is described by :

$$E(x,m,\theta,t) = E_0 \; S(x,m,\theta) \; \frac{-i}{kr} \exp(i(\omega t - kr)) \qquad (2.2)$$

where E_0 is the incident beam's electric field amplitude, $k = 2\pi/\lambda$ is the wave number, ω is the angular frequency of light, r is the spatial coordinate along the beam and $S(x,m,\theta)$ is the amplitude function which characterises the amplitude and the phase of the light, where x is a dimensionless particle size parameter, m is the refractive index of the sphere relative to the surrounding fluid and θ is the angle of the scattering direction. The dimensionless intensity of the scattered light is then :

$$i(x,m,\theta) = |S(x,m,\theta)|^2 \qquad (2.3)$$

The main concern in the above equations is the calculation of $S(x,m,\theta)$ and two approaches have been used; "Mie theory" and "geometrical optics".

Electromagnetic theory describes the propagation of electromagnetic waves through Maxwell's equations and have been solved by Lorentz and Mie independently, for the case of a homogeneous sphere of arbitrary size and refractive index illuminated by a uniform field of light. The commonly called "Mie theory", which is a solution in terms of an infinite series with the dimensionless particle size Mie parameter $x = \pi d_p/\lambda$ as argument, where d_p is the sphere diameter and λ the wavelength of light, has been used for calculations related to optical techniques of particle sizing (e.g. Hong & Jones, 1976, Grehan et al, 1981, Pendleton, 1982, Negus & Drain, 1982). Related calculations of the series must be obtained numerically and are expensive of computer time, especially as the particle diameter increases. The restriction to uniform illumination of the sphere is undesirable for reasons discussed later.

For spheres larger than the wavelength of light and with a refractive index different from the surroundings geometrical optics provide a good approximation to the Mie theory for values of the Mie parameter x greater than 10; for the wavelengths of laser light used, this implies sphere diameters larger than approximately 3 μm. Geometrical optics is a more attractive option than Mie theory because it is cheap in computer time and can separate the scattered light in its components and provide physical insight in the contribution of each part. The geometrical optics approximation (Van de Hulst, 1981) suggests that the scattered light can be separated into diffraction, refraction, surface reflection and a series of internal reflections. With his notation, the scattered light can be described by two "amplitude" functions, $S_1(x,m,\theta)$ for the amplitude and phase of light with polarisation perpendicular to the scattering plane and $S_2(x,m,\theta)$ for light with polarisation parallel to the scattering plane. Both are perpendicular to the scattering direction, θ, as shown on figure 2.2. Refraction and surface and internal reflections are described in terms of ray optics and the Fresnel reflection coefficients, as follows.

The general form of the amplitude function with polarisation perpendicular to the scattering plane, $S_1(x,m,\theta)$, is :

$$S_1(x,m,\theta) = x\ |\varepsilon_1|\ D^{1/2} \exp(i\,\sigma_1) \qquad (2.4)$$

and the same formulation is valid for the amplitude function with parallel polarisation to the scattering plane, $S_2(x,m,\theta)$, but the relevant equations are presented here only for $S_1(x,m,\theta)$ and can easily be extended for $S_2(x,m,\theta)$.

The terms of equation (2.4) for the refracted and reflected rays are explained and quantified in the following section. The term $|\varepsilon_1|$ determines the part of the incident light contained in the ray which emerges from different interfaces which are determined by the integer p, which is p=0 for the surface reflection, p=1 for the refracted ray, p=2 for the ray emerging after the first internal reflection and so on. The value of ε_1 is determined by the Fresnel coefficients :

$$\begin{aligned} \varepsilon_1 &= r_1 && \text{for } p = 0 \\ \varepsilon_1 &= (1 - r_1^2)\,(-r_1)^{p-1} && \text{for } p = 1, 2, 3, \ldots \end{aligned} \qquad (2.5)$$

where the Fresnel reflection coefficients for both polarisations of light are :

$$r_1 = \frac{\sin\tau - m\sin\tau'}{\sin\tau + m\sin\tau'}$$

$$r_2 = \frac{m\sin\tau - \sin\tau'}{m\sin\tau + \sin\tau'} \qquad (2.6)$$

and τ, τ' are the angles between the surface tangent and the incident and refracted ray correspondingly, shown on figure 2.3. Snell's law relates these angles by :

$$\cos\tau = m\cos\tau' \qquad (2.7)$$

where m is the refractive index of the medium.

The term D of equation (2.4) is sometimes called divergence or gain and accounts for the influence of the particle shape on the angular dispersion of the scattered light and is given by :

$$D = \frac{\sin\tau \cos\tau}{\sin\theta \left| \frac{d\theta'}{d\tau} \right|} \qquad (2.8)$$

where θ' is the angle between the incident ray and the ray emerging from the p interface given by :

$$\theta' = 2\tau - 2p\tau' \qquad (2.9)$$

and $$\frac{d\theta'}{d\tau} = 2 - 2p\frac{\tan\tau}{\tan\tau'} \qquad (2.10)$$

and p is again the integer which determines the interface from where the ray emerges.

The term $\exp(i\sigma_1)$ of equation (2.4) is the phase term of the scattered light and σ_1 is given by :

$$\sigma_1 = \frac{\pi}{2} + (\text{ phase of } \varepsilon_1) + \delta + \frac{\pi}{2}(p - 2k + \frac{1}{2}s - \frac{1}{2}q) \qquad (2.11)$$

where the individual terms are :

- δ : phase due to optical path length difference to the reference path, which is passing through the centre of the sphere (figure 2.3)

$$\delta = 2x (\sin\tau - p\, m \sin\tau') \qquad (2.12)$$

- phase shifts due to focal lines :

k : integer and q = +1 or -1 defined from :

$$\theta' = k\, 2\pi + q\theta \qquad (2.13)$$

so that the scattering angle θ is in the interval $(0,\pi)$

and

s = +1 or -1 equal to the sign of $\frac{d\theta'}{d\tau}$

It should be noted that geometrical optics approximation cannot be applied for the Brewster's angle and for the rainbow angles. Brewster's angle is defined as the incident angle, τ, for which surface reflection occurs only with perpendicular polarisation to the scattering plane and is estimated by :

$$\tan\tau = \frac{1}{m} \qquad (2.14)$$

The rainbow angles for each internal reflection are defined by the incident angle, τ, for which the considered internal reflection contribution to the scattered light ceases and this occurs when the angle θ' of equation (2.9) takes its maximum value :

$$\sin^2\tau = \frac{m^2-1}{p^2-1} \qquad (2.15)$$

Since both angles are dependent on the refractive index of the sphere, limitations on the application of the geometrical optics approximation change with refractive index.

The above equations determine the amplitude functions for the refracted and reflected part of scattered light and not for the diffracted part. The contribution of diffraction to the scattered light to both polarisations is given by :

$$S_{diff}(x,\theta) = x^2 \frac{J_1(x\sin\theta)}{x\sin\theta} \qquad (2.16)$$

where $J_1(\ .\ )$ is the first order Bessel function.

The total amplitude functions then are the sum of the partial amplitude functions for the different contributions to the scattered light :

$$S(x,m,\theta) = S_{diff}(x,\theta) + S_{refr.}(x,m,\theta) + S_{surf.\ refl.}(x,m,\theta) + S_{1st\ int.\ refl.}(x,m,\theta) + ... \qquad (2.17)$$

Equation (2.17) is quite complicated but it can be simplified when applied in certain regions of scattering angles, θ. The combination of paths that light can follow to reach a given scattering

angle can be seen on the diagram of figure 2.4a, taken from Van de Hulst (1981) which shows the surface reflection, refraction and first and second internal reflection distribution over the scattering angle interval $0° < \theta < 180°$ and is valid for a water droplet ($m = 1.33$). So the space around a scattering transparent sphere can be divided into seven areas, as shown on figure 2.4b, as a function of the mean scatter angle θ measured from the axis of the beam, where contributions to the total scattered light from certain paths are much larger relative to the rest (Van de Hulst, 1981, Glantschnig & Chen, 1982) and equation (2.17) can be simplified when applied there by approximating the total scattered light by considering only the main contributions. So the total scattered light in each zone is mainly due to the following :

- Zone I : $0° < \theta < \approx 25°$. Diffraction, refraction and surface reflection are the main contributions to the scattered light. Diffraction dominates the pattern for small angles.
- Zone II : $\approx 25° < \theta < \approx 80°$. Diffraction, refraction and surface reflection are again the main contributions but refraction is the dominant term in equation (2.17) while diffraction becomes negligibly small as the scattering angle increases.
- Zone III : $\approx 80° < \theta < \approx 110°$. Surface reflection dominates the scattered light, while refraction does not exist.
- Zone IV : $\approx 110° < \theta < \approx 130°$. The main contributions are due to surface reflection and second internal reflection but surface reflection dominates again.
- Zone V : $\approx 130° < \theta < \approx 140°$. The region between the first and second rainbow angle, where again surface reflection is the main contribution.
- Zone VI : $\approx 140° < \theta < \approx 170°$. First internal reflection and surface reflection are considered and first internal reflection dominates the pattern.
- Zone VII: $\approx 170° < \theta < 180°$. Edge rays (several internal reflections) and diffraction.

Glantschnig & Chen (1982) obtained the analytical expressions for the amplitude functions of the light scattered by a sphere present in a single beam in the forward direction using only diffraction, refraction and surface reflection as a function of the scattering angle θ and found good agreement with Mie theory. These expressions can be found in appendix 2.A.

The followings can be observed from the above mentioned expressions. The angular variation of the scattered light depends on particle size only through the phase term (equ. (2.11) and (2.12)). The scattered intensity is related to the particle diameter squared, as concluded from equations (2.3) and (2.4). The refractive index, m, affects both the phase and the amplitude term of the refracted light. However the phase term (equation (2.11)) of the surface reflection contribution is independent of refractive index.

b) Light scattered by a sphere located at the crossing section of a laser Doppler anemometer.

The theory will now be extended to describe mathematically the intensity variation in space of the light scattered by a sphere present in the crossing area of two laser beams, as used in a conventional laser Doppler anemometer. The scattering angle θ, defined here relative to the bisector of the intersection angle of the beams, the beam intersection angle ϕ, the refractive index of the sphere m and the particle size parameter x influence the scattered interference pattern in space and its phase is of particular interest, because according to the phase-Doppler technique the phase difference between two locations in space is linearly related to particle size. The geometry used for the analysis of light scattered by a particle with two incident beams is shown on figure 2.5. The expressions are obtained for the case of incident beams linearly polarised normal to the plane of the beams. The relationships between the angles characterising the geometry are given in appendix 2.B. The scattered wave perpendicular to the scattering plane along the direction OP (figure 2.5) has an electric field given by :

$$E_{ij}(x,m,\theta,t)=E_{0ij}\ S_{ij}(x,m,\theta)\ \cos\chi_j\ \frac{-i}{kr}\ \exp(i(\omega_j t-kr)) \quad (2.18)$$

where subscript i = 1, 2 denotes polarisation of the scattered light, subscript j = 1, 2 represents one of the two beams of the laser Doppler system, E_{0ij} is the electric field component of the incident beam, χ_j is an angle defined in figure 2.5 and $S_{ij}(x,m,\theta)$ is the amplitude function of the scattered light. Again, as for the single beam, the main concern in equation (2.18) is to estimate the amplitude function. Thus for the

interaction of the scattered light from two beams there are four components of the scattered wave at each point P in space defined from the two states of polarisation of the scattered light for each beam, as shown in figure 2.5c. Each of these four components is given by equation (2.17) and is a summation of combinations of light scattered by following different paths through the sphere. The electric field of the scattered wave is now resolved into a plane containing the scattering direction and perpendicular to the plane of the beams and into a plane parallel to the plane of the beams. If the particle is in motion with a velocity V normal to the bisector of the two beams (which cross with a half angle of $\phi/2$), then the angular frequency ω of each beam as perceived by the particle is different and it can be shown that the movement can be simulated by adding a frequency of +n into one beam and -n into the other beam where

$$n = \left(\frac{2\pi V}{\lambda}\right) \sin\left(\frac{\phi}{2}\right) \qquad (2.19)$$

The total scattered wave from a particle moving with velocity V through the probe volume of a laser Doppler system, at a point in space is given by :

$$E_T = E_0 \left(C_1 e^{int} + C_2 e^{-int}\right) \frac{-i}{kr} \exp(i(\omega t - kr)) \qquad (2.20)$$

where C_1 and C_2 for direction Y, perpendicular to the plane of the beams :

$$C_1 = S_{11} \cos\chi_1 \sin\phi_1 + S_{21} \sin\chi_1 \cos\phi_1$$
$$C_2 = S_{12} \cos\chi_2 \sin\phi_2 + S_{22} \sin\chi_2 \cos\phi_2 \qquad (2.21a)$$

and for direction X, parallel to the plane of the beams (figure 2.5c) are :

$$C_1 = S_{11} \cos\chi_1 \cos\phi_1 + S_{21} \sin\chi_1 \sin\phi_1$$
$$C_2 = S_{12} \cos\chi_2 \cos\phi_2 + S_{22} \sin\chi_2 \sin\phi_2 \qquad (2.21b)$$

The intensity of the total scattered light at this position in space is :

$$I_T = E_T \, E_T^* \tag{2.22}$$

(where * denotes the conjugate function), which becomes :

$$I_T = \frac{I_0}{k^2 r^2} (C_1 e^{int} + C_2 e^{-int}) (C_1 e^{int} + C_2 e^{-int})^*$$

and with $$A = \frac{I_0}{k^2 r^2} (C_1 C_1^* + C_2 C_2^*) \tag{2.23}$$

and $$K+iT = 2 \frac{I_0}{k^2 r^2} C_1^* C_2 e^{2int} \tag{2.24}$$

So equation (2.21) may be written :

$$I_T = A + N \cos(2nt - \sigma) \tag{2.25}$$

where $N = \sqrt{K^2 + T^2}$, $\sigma = \tan^{-1}(\frac{T}{K})$ (2.26)

There were no simplifications involved in the derivation so far and equation (2.25) which is generally valid describes the temporal and spatial variation of the intensity of light scattered by a sphere moving through the crossing area of two laser beams, which is observed by a photodetector. The second term of the right hand side of the equation is that measured by a Doppler signal processor. The Doppler frequency ω_D is equal to $2n/2\pi$ and is independent of the spatial location of the photodetector and of the particle size, but the phase σ is a function of both the location of the detector and the particle size. Figure 2.6 explains the meaning of the terms A and N of equation (2.25) and A is the amplitude of the pedestal and the ratio N/A is the visibility of the Doppler signal. The calibration curve of the phase-Doppler technique can be established by estimating the phase of the Doppler signals at two positions in space using equation (2.25) and then subtracting them to evaluate the phase difference as a function of particle diameter.

The scattered light in the forward direction using geometrical optics approximation will be examined in an effort to get physical insight in the information that equation (2.25) is giving about the technique. Zone II as defined in the previous chapter, $25° < \theta < 80°$ where scattering angle θ here is measured relative to the bisector of the beams, is chosen to check the information of equation (2.25). For this zone, it can be assumed that diffraction is negligible and that refraction and surface reflection are the main contributions to the scattered light, which may interfere in six possible ways : refraction from different beams, reflection from different beams, refraction-reflection from different beams (two terms) and refraction-reflection from the same beam (two terms). The terms C_1 and C_2 in equation (2.21) contain two terms each, which are due to surface reflection and refraction from each beam. Then the cross term $C_1^* C_2$ of equation (2.24), which is the only time variable term and describes the interference fringe pattern, is the result of the four time variable terms : refraction from different beams, surface reflection from different beams, refraction-surface reflection from different beams (two terms). The other two remaining terms resulting from the interference due to refraction-surface reflection from the same beam are the result of $C_1 C_1^*$ and $C_2 C_2^*$ in equation (2.23) and as was found are time independent terms and do not contribute to the Doppler signal, but give rise only to a pattern, which is not changing with time and they are referred to as resonances on the scattering intensity distribution. However, the phase σ in equation (2.25) is defined by the cross term $C_1^* C_2$ only so is a result of the interference of the four time variable terms and is that observed by a single photodetector. The intensity of the four time variable terms examined each separately are as follows :

- interference due to surface reflection from each beam (11) :

$$I^{(11)}(x,m,\theta,t) = |E_1^{(1)}|^2 + |E_2^{(1)}|^2 + 2|E_1^{(1)}||E_2^{(1)}| \cos(\omega_D t - \sigma^{(11)})$$

- interference due to refraction from each beam (22) :

$$I^{(22)}(x,m,\theta,t) = |E_1^{(2)}|^2 + |E_2^{(2)}|^2 + 2|E_1^{(2)}||E_2^{(2)}| \cos(\omega_D t - \sigma^{(22)})$$

- interference due to refraction-surface reflection from different beams (12) or (21) :

$$I^{(12)}(x,m,\theta,t) = |E_1^{(1)}|^2 + |E_2^{(2)}|^2 + 2|E_1^{(1)}||E_2^{(2)}| \cos(\omega_D t - \sigma^{(12)})$$
$$I^{(21)}(x,m,\theta,t) = |E_1^{(2)}|^2 + |E_2^{(1)}|^2 + 2|E_1^{(2)}||E_2^{(1)}| \cos(\omega_D t - \sigma^{(21)})$$

where $I^{(ij)}$ is the intensity of the scattered light where superscript (ij) denotes the considered scattered light contributions to the interference pattern and i, j = 1 or 2 denoting surface reflection or refraction correspondingly while i corresponds to contributions from beam 1 and j from beam 2 (figure 2.5), $E_k^{(l)}$ is the electric field with subscript k = 1 or 2 denoting one of the two beams and superscript (l) = (1) or (2) denoting contribution from surface reflection or refraction correspondingly and $\sigma^{(ij)}$ is the phase of the light scattered interference pattern from the (ij) contributions at one point in space. The phase term can be expressed by using equations (2.11), (2.12) and (2.13) for each beam as follows :

$$\begin{aligned}
\sigma^{(11)} &= 2x\,((\sin\tau_1 - \sin\tau_2) \\
\sigma^{(22)} &= 2x\,((\sin\tau_1 - \sin\tau_2) - m\,(\sin\tau_1' - \sin\tau_2')) \\
\sigma^{(12)} &= 2x\,((\sin\tau_1 - \sin\tau_2) - m\,(-\sin\tau_2')) \\
\sigma^{(21)} &= 2x\,((\sin\tau_1 - \sin\tau_2) - m\,(\sin\tau_1'))
\end{aligned} \qquad (2.27)$$

Each of the terms in equation (2.27) is the path length difference between the light scattered by a sphere located in each beam through the considered paths at one point in space and each one is linearly related to the size parameter x and hence also to particle diameter. However, the resulting phase of the interference of all four terms is no longer linearly related to particle diameter and can be determined only by numerical calculation. It is desirable then to collect light at positions where the scattered light is dominated by one path (e.g. either surface reflection or refraction) so that the chances of the existence of monotonic relation between phase and particle diameter are higher. However, there are reasons (e.g. the Gaussian intensity distribution of the incident beam), examined later in the

chapter, which make the investigation of the interference of all the terms necessary even where one path of the scattered light is dominant. This is the reason why the relationships of the phase difference between two Doppler signals observed from two photodetectors and particle diameter given by Saffman et al (1984) and Bauckhage et al (1984) considering only the interference from either surface reflection or refraction from both beams are not enough to examine the performance of the method and eliminate sizing errors that might occur. Also the application of these relationships is limited to optical configurations where the photodetectors are located at symmetrical positions around the scattering plane which contains the bisector of the intersection angle of the beams and is normal to the plane of the beams and this limitation is corrected by the above analysis.

2.4 Parametric evaluation of the phase-Doppler method

This section examines theoretically the influence of different parameters on the phase-Doppler method. Scattering angle regions are identified where a monotonic relationship of phase difference between two Doppler signals and particle size can be established, which coincides with that of the dominant part of the scattered light there. Then the influence of parameters, such as the collection angle, the beam intersection angle, the finite size of the collection aperture, the Gaussian intensity distribution of the incident beams, the particle refractive index, the angular spacing between the photodectors, the polarisation of the incident beams and the flow turbidity on this relationship is examined and sizing errors which may occur are identified. For these purposes a computer program was developed to solve equations (2.25) and (2.26) and calculate the total intensity pattern I_T and the phase shift σ at different positions in space and can provide information on the total as well as the separate components of scattered light interference patterns.

a) Collection angle.

In section 2.3(a) the space around a scattering transparent sphere from a single beam was divided in seven areas, as shown on

figure 2.4b, as a function of the mean scattering angle θ. The same classification can be applied to a two beam laser Doppler anemometer system with the scattering angle θ measured from the plane of symmetry of the anemometer (figure 2.4b), when the intersection angle of the beams is small (e.g. ≈ 10°). In the following section each zone will be examined and the calibration curve of the phase-Doppler method will be established where this can be done. The calculations assume that the beam diameter is much larger than the particle diameter, so that the Gaussian intensity distribution of the incident laser beams is not considered. The influence of this assumption on the results will be discussed later. The results presented here are for a beam intersection angle of 10° and for a laser light wavelength, λ, 0.6328 μm, which is needed to estimate from the dimensionless size parameter x (= $\pi d_p/\lambda$) the particle diameter d_p. The results are generally presented at a single point in space. However, the photodetectors observe light through a finite size aperture and results are presented after integration on a rectangular collection aperture located around a point. The shape of the used aperture is explained later in this section and its size is important for the sizing of particles smaller than around 10 μm.

Forward scatter direction (Zone I (0° < θ < ≈25°) and II (≈25° < θ < ≈80°))

In this zone diffraction, refraction and surface reflection mainly exist and it will be shown that diffraction dominates the scattered light in zone I, while refraction dominates in zone II. Figure 2.7 shows the intensity variation of the light scattered by a glass bead (m = 1.5) of 40 μm diameter in planes parallel to that containing the incident beams and at elevation angles of 0° and 30°. The continuous lines on figures 2.7a and c show the spatial intensity variation for the total (diffraction, surface reflection and refraction) pattern and the dashed lines show the refraction intensity variation in planes defined by elevation angles of 0° and 30° respectively. Figures 2.7b and d show the intensity variation due to interference between surface reflection and refraction. Comparison between the total and the refraction-surface reflection pattern shows that diffracted light is a large component of the scattered light up to a scattering angle θ ≈ 20° and

that there is no influence due to diffraction at the elevation angle 30°. The comparison between the refraction and the refraction-surface reflection interference pattern shows that the influence of surface reflection is small for the 30° elevation angle, close to the symmetry plane of the anemometer (0° rotation angle) and increases with the scattering angle. So diffraction dominates at small collection angles (<≈25°) and surface reflection dominates at large angles (close to ≈80°). At intermediate angles, refraction is the main part of the scattered light but reflection is still present and is responsible for the oscillations of the spatial intensity variation (figure 2.7) around a mean which is the refraction pattern. Zone I where diffraction is the dominant mechanism of light scattering should be avoided to make sure that no refraction-diffraction interference occurs. Zone II, where refraction dominates the scattered light, can be useful for sizing if problems due to surface reflection can be avoided.

The relative amplitudes of refraction and surface reflection for forward scatter are responsible for the oscillations on the interference pattern as can be seen in figure 2.8. The intensity variations of refraction only (continuous line) and surface reflection only (dashed line) interference from both beams with particle size for elevation and rotational angles of 30° and 5.3° are shown in figure 2.8a. It is obvious that for diameters between 30 and 40 μm the relative amplitudes of refraction and surface reflection are similar and this cannot be avoided and can give rise to sizing errors as will be explained later, although the Gaussian distribution of the incident light reduces this effect when the particle crosses through the centre of the probe volume. Figure 2.8b confirms that the high frequency oscillations of the refraction-surface reflection interference intensity pattern have larger amplitude when their relative amplitudes are similar and similar is the effect on the phase of the scattered interference pattern at a point in space.

Figure 2.9 shows the refraction intensity pattern at different elevation angle planes parallel to the plane of the beams for a 40 μm glass bead. The fringes are apparent by inspection and have the appearance of hyperbolic lines which are normal to the plane containing the incident beams. Close to the plane of symmetry of the anemometer they are nearly straight lines vertical to the plane of the beams with their curvature increasing with rotation angle ξ. The collection of the scattered light in a LDA system is succeeded through

apertures. The shape of the fringes suggests the use of rectangular apertures, long in height and narrow in width, parallel to the direction of the fringes so that a large part of the fringes is observed. Also, the fringe pattern suggests that the best position to collect light is close to the symmetry plane, where the fringes are nearly straight lines and fringe curvature will not influence the integration across the collection apertures.

The phase difference between two fixed points in space versus droplet diameter with refractive index of 1.5 is shown in figure 2.10a. The two detectors are located at an elevation angle of $y = 30°$ and angle of rotation relative to the plane of symmetry of the anemometer, of $\xi = 5.3°$ and $1.0°$. The dashed line shows the results assuming only interference due to refraction from both beams. The continuous line shows the phase difference between two Doppler signals observed at photodetectors collecting light through point apertures due to the interference of refraction, surface reflection and diffraction and direction of polarisation of the incident beams normal to the plane which contains the two beams. The refraction calibration curve exhibits a linear relationship between phase shift and size as expected from the analysis of the previous section. The full geometrical optics curve exhibits high frequency oscillations around a mean value, which is the refraction phase difference.

The calibration curve of figure 2.10a may be calculated by integration of the scattered fringe pattern over finite size collection apertures and figure 2.10b show the result of integration over rectangular apertures with dimensions $\delta\xi = 0.95°$ and $\delta y = 9.5°$, which corresponds to 50 mm to 5 mm slits placed at 300 mm from the probe volume of the anemometer. The fluctuations of the curve have been reduced greatly. The continuous line is the Mie theory calculation after integration over the finite apertures, described by Al Chalabi et al, (1987) and the dashed line is the solution from geometrical optics. The agreement between the two curves is good and it may be concluded that the "integration" of the apertures of the collection lens over the intensity pattern establishes a linear calibration curve with conversion constant identical with that predicted from the simplified theory of Saffman et al (1984). Also, since the Mie theory solution agrees well with the geometrical optics approximation in the forward scatter region examined here,

contributions to the scattered light in this interval from paths undergoing more than one internal reflection can be neglected. The implications for the phase-Doppler technique are that oscillations in the calibration curve are due to interference between two or more paths and that similar qualitative results can be expected over most of this scattering interval.

Sidescatter direction (Zone III and IV)

Zone III ($\approx 80° < \theta < \approx 110°$)

The scattered light in this interval is due to surface reflection only, since it was decided not to include in the calculations light scattered by two internal reflections, which according to Van de Hulst (1981) is less than 5% of the incident energy scattered by a water droplet in this interval. It is expected to see small oscillations in the Mie theory calculated calibration curve, because there is mainly one contribution to the scattered light (surface reflection) present. Figure 2.11 allows comparison of the phase of the scattered light by a water droplet (m=1.33) determined by Mie theory and geometrical optics for one observer located at a mean scatter angle between the two beams of 100°, corresponding to $\xi = 178°$ and $y = 80°$. The phase difference for two observers has not been calculated because of the relatively large cost of evaluating the Mie solution and since no vital information is lost in doing so. For the same reasons integration over apertures was not performed, although as was demonstrated earlier reduction in the amplitude of the oscillations can be anticipated by comparison with the prediction from a single path, but this needs further work to be proved.

The discontinuous straight line of figure 2.11 is due to surface reflection only and the solid line is the Mie solution. The amplitude of the oscillations, as expected, is small and may be further reduced by integration over the detector aperture. In this interval, the change in phase with particle size is slow so it is suitable for the sizing of large particles (e.g. around 1 mm). If high size resolution is necessary, it can be achieved by separating the detectors by relatively large angles which precludes mounting the detectors in a single, integrated unit.

Zone IV ($\approx 110° < \theta < \approx 130°$)

The components of the scattered light for zone IV are, in principle, the same as for zone III. However figure 2.4a shows that the ray which undergoes two internal reflections gives rise to a second rainbow (Van de Hulst, 1981) and, since rainbows contain appreciable energy and large interference effects, it is expected that the calibration curve will be qualitatively different. This is confirmed by figure 2.12 for a mean scatter angle of 120°; the geometrical optics solution remains a straight line with a small gradient but the Mie solution shows large amplitude oscillations around this line. Further work is needed to establish the influence of aperture integration on the phase oscillations as effectively as in figure 2.10b.

Backscatter direction (Zone V, Zone VI, Zone VII)

Zone V ($\approx 130° < \theta < \approx 140°$)

Geometrical rays in this region arise from surface reflection or from those which undergo three, or more, internal reflections. Generally, the larger the number of internal reflections, the weaker the emerging ray and it would be reasonable to expect that the calibration curve should be dominated by the effects of the reflected on the surface of the sphere rays alone. Figure 2.13 shows the surprising result that, for a mean scatter angle of 133°, the amplitude of the phase oscillations of a water droplet is violent, although the mean trend resembles the solution predicted from geometrical optics. The explanation is that this interval is narrow ($\approx 10°$) and, as a consequence, the scatter angle from each beam is close to either the main or the second rainbow angles. As demonstrated already, the rainbow angles generate large oscillations in the calibration curves due to the associated interference patterns.

It should be noted here that the rainbow angles are functions of the refractive index, m, of the particle. The angles of the main and the second rainbows for water (m = 1.33), the case examined here, are 138° and 128.7° respectively. For glass beads (m = 1.5) the corresponding angles are 157.2° and 97.4°. The interval between the rainbows is much larger for the latter case and it is possible that the calibration curve for glass is smoother than that for water shown in

figure 2.13. The influence of the refractive index on the technique is discussed later.

Zone VI ($\approx 140° < \theta < \approx 170°$)

This region is occupied by the main rainbow and covers a range of angles, which is potentially useful for measurements near backscatter. The paths which contribute to light scattered in this direction are surface reflection and two separate branches from one internal reflection (figure 2.14). Figure 2.15a shows that both geometrical optics and the Mie solution predict high frequency oscillations and large amplitude excursions over two separate size ranges of water droplets, between 4 and 8 μm and between 20 and 30 μm at a scattering angle of 150°. It is not apparent why the sign of the phase for the first range is different for the two solutions, but this is of lower importance than the amplitude of the oscillations. It should be noted that the phase results are presented in the interval (-180°,+180°), so phase values larger than +180° are presented as negative phase values (e.g. for the size range between 20 and 30 μm-figure 2.15a).

The effect of the surface reflection on the calibration curve is shown by comparing in figure 2.15b, solutions from the geometrical optics approximation for the phase due to light undergoing one internal reflection only (dashed line) and that due to the interference between surface reflection and first internal reflection (solid line) : the high frequency oscillations are now absent from the phase due to light undergoing one internal reflection but it is not a straight line as probably someone would expect. The excursions between 4 and 8 μm and between 20 and 30 μm remain prominent, however, and must be due to interference between the two branches of the internally reflected light existing before and after the rainbow (figure 2.4a). The calibration curve based only on the first internal reflection path is multi-valued and qualitatively different from the surface reflection only or the refraction only calibration curve. There is no reason why integration over an aperture will remove this effect, so the tentative conclusion is drawn that a useful calibration curve cannot be established in this scattering angle interval. However, Bachalo et al (1988) recently performed aperture integration calculations in the backscatter direction and found that a useful calibration curve can be

established at a scattering angle of 150°, but the explanation for that is still unknown.

Zone VII (≈170° < θ < 180°)

It is known that the approximation used in geometrical optics is no longer valid in this interval due to the existence of the so called "edge rays" and no attempt was made to produce calibration curves based on the geometrical optics approximation. Mie theory solution obtained in this zone (Al Chalabi et al, 1987) without aperture integration show large phase oscillations suggesting that no useful calibration is obtainable in this interval.

The effects of collection angle may be summarised as follows :

i) Forward scatter collection (≈25° < θ < ≈80°) can be used for size measurements of transparent spheres based on refracted light. Collection angles around 30° are appropriate for this purpose for the following reasons: surface reflection has small influence on the results and diffraction is negligible; the intensity of the scattered light decreases with increase in scattering angle resulting in poorer signal-to-noise ratio.

ii) For sidescatter collection (≈80° < θ < ≈110°) the surface reflection part of the scattered light establishes a calibration curve useful for applications involving large particle sizes.

iii) For backscatter collection (≈140° < θ < ≈170°) maybe is possible to establish a useful calibration curve, but more work is needed.

b) Beam intersection angle.

There is a linear relationship between phase difference/diameter ratio and beam intersection angle for LDA intersection angles up to 30° and can be seen on figure 2.16, for locations at an elevation angle y=30° and rotation angles ξ_1=5.3° and ξ_2=1° and for refractive index m=1.5. It can be seen that the size resolution at one light collection optical arrangement increases with beam intersection angle, but the possible size range decreases.

The intersection angle of the laser Doppler anemometer beams, ϕ, defines the fringe spacing, f, of the anemometer, which changes linearly with angle :

$$f = \frac{\lambda}{2 \sin\frac{\phi}{2}} \qquad (2.28)$$

According to the simple theory of Durst and Zaré (1975) the fringe spacing f projected through a transparent sphere, which acts as a lens, determines the frequency of the scattered fringe pattern. So the change of the beam intersection changes accordingly the frequency of the spatial fringe pattern and this means that the fringe spacing can be used as a parameter to normalise the particle diameter and obtain a unique calibration curve of the instrument (phase - d_p/f) for different intersection angles.

c) Finite collection aperture.

The effect of the collection aperture on the calibration curve was mentioned in the previous section and it is obvious from figure 2.10b that integration of the intensity interference pattern over the rectangular aperture dampens the amplitude of the phase difference oscillations. Although this occurs for all particle sizes, it is more effective for larger sizes. Figure 2.17 shows the phase lag between two Doppler signals for sizes up to 10 μm through ractangular apertures centred at two points with elevation angle 30° and rotation angles of 8° and 1° to the optical axis of a laser Doppler anemometer for a particle refractive index 1.5, where the polarisation is normal to the plane of the incident beams and intersection angle is 10°. The height and width of the apertures are 9.5° and 1.1° respectively which correspond closely to a rectangle with sides 50 mm by 6 mm for a collection lens placed 300 mm away from the measurement volume of the LDA. These dimensions can be realised in a practical arrangement. The continuous line represents the phase lag after integration over the apertures and the dashed line the phase lag due to refraction only. It can be seen that the calibration curve is multivalued for the small particle sizes (<~10 μm) even after integration. This occurs because the spacing of the spatial fringe

pattern increases with decreasing particle diameter and the integration efficiency of a practical aperture decreases. These oscillations limit the ability of the technique for small sizes as further discussed by Saffman (1986) and Hardalupas & Taylor (1988). Different aperture sizes have been examined by Saffman (1986) who demonstrated that the oscillations become negligible only if light is collected through apertures (6.8 f-number) which are too large to incorporate in receiving optics in which the same lens is used by all photodetectors. However, for practical aperture dimensions, Hardalupas & Taylor (1988) have shown that oscillations exist for small particle sizes and for collection angles in the range of 30° and 70°.

Using the sizing feature of the instrument, the velocity of particles as large as 2 μm could be measured and considered as the continuous phase characteristics. This is not that straightforward because of the oscillations left on the calibration curve, and results in low data rates due to rejection of particles with aerodynamic diameter less than 2 μm, but which have an optical diameter larger than 2 μm (Hardalupas & Taylor, 1988). The sizing ability of the instrument is limited to particles larger than around 10 μm for the case examined here, which corresponds to particle sizes with ratio $\frac{d_p}{f} \sim 2.5$, where f is the fringe spacing and d_p is the particle diameter. This means, that by increasing the angle of the beams, the minimum diameter that the technique can size decreases. So for optical arrangements with small possible size range (e.g. up to around 20 μm), particles larger than around 5 μm may be sized, but when the possible sizing range has to be large (at least of the order of 80 μm), as for the case of Hardalupas & Taylor (1988) then the lower sizing limit increases.

d) Gaussian intensity distribution.

All of the above calculations assumed uniform illumination of the sphere, due to the small particle diameter relative to the beam waist diameter. However, the incident intensity distribution of the laser light is Gaussian and a particle comparable to the beam waist provides, for example, stronger surface reflection amplitude relative to that of the refraction when it crosses the probe volume close to the edge than through the centre (figure 2.18). The possibility of the occurrence of

the problem shown in figure 2.18 increases with collection angle because the observed area of the probe volume decreases, and provides an additional reason for choosing 30° for light collection in forward scatter rather than a larger angle.

The practical implication is that, for example, refraction through a transparent sphere may not be dominant over surface reflection in the forward direction and then errors can occur and special care is needed in the form of software validation as follows.

The fringe pattern due to refraction alone has a temporal variation that makes the "refraction" fringes appear to move in the direction of the particle motion. Fringes due to the interference of the surface reflection from the two beams appear to move in the opposite direction and this may assist in the discrimination between the phase difference due to refraction or surface reflection. If the phase due to refraction is measured and define it to be positive then the phase due to surface reflection will be negative at the same position. So the phase variation due to refraction increases linearly with size is linearly increasing from 0° to 360°, whereas that due to surface reflection decreases linearly from 360° to 0°. Figure 2.19a shows the phase difference between two positions with elevation angle $y = 30°$ and rotation angles $\xi_1 = 5.3°$ and $\xi_2 = 1.0°$ as a function of particle size: the solid line is due to refraction and the solid thich line is due to surface reflection. Large phase shifts can be due to refraction and large particles, or due to surface reflection and small particles. Also small phase shifts can appear from larger particles reflecting light from their surface or small particles refracting through them. Thus size measurements assuming refraction can be contaminated from surface reflection due to the Gaussian distribution of the incident light. One solution to the above problem is to use three photodetectors so that there are two phase difference calibration curves (figure 2.19b). The ratio between the two phase values of the steeper calibration curve to the shallower can be used to discriminate surface reflection from refraction signals with small uncertainties, as figure 2.19c shows, which can also be eliminated by choosing an optical arrangement which gives symmetry between the phase shift due to refraction and surface reflection.

This arrangement of the receiving optics helps also to provide a "vernier" arrangement whereby the steeper of the two calibration

curves is used to provide increased measurement accuracy over the size range of the shallower calibration curve (Bachalo, 1984, Saffman et al, 1986).

e) Particle refractive index.

The sizing principle is independent of the particle refractive index when surface reflection is the only scattered light (e.g. steel beads with polished shiny surface) or when surface reflection dominates (e.g. air bubbles in water). The refractive index is generally a complex number, where the imaginary part describes the absorption occurring as light is transmitted through the particle material.

When there is no absorption by the particle, so that the refractive index is a real number, refraction dominates in the forward direction ($30° < \theta < 80°$). The phase shift due to refraction depends on the refractive index and figure 2.20a shows calibration curves for different refractive indices and figure 2.20b the variation of the slope of the calibration curve, defined in degrees/μm, as a function of the particle refractive index for an anemometer with beam intersection angle 10°, laser light wavelength 0.6328 μm and photodetectors located at elevation angle y = 30° and rotation angles ξ_1 = 5.3° and ξ_2 = 1.0°. It can be seen that the sensitivity of the calibration curve to particle size decreases with decreasing refractive index. The decrease is linear for refractive indices up to 1.4 and less than linear as the refractive index increases. Thus when the exact refractive index is not known *a priori* or there is a refractive index change during the measurement (e.g. due to fuel droplets in a region of combustion where the refractive index of the fuel droplets changes with temperature), there can be an uncertainty of 10% in particle diameter for spheres of nominal refractive index 1.4 and a refractive index change of 7%.

When absorption from the particle is significant, the intensity of the surface reflection may become of the same order, or larger than, the refraction part of the scattered light. Then errors can occur because the calibration curve changes. For such cases, the relative amplitude of surface reflection to refraction or internal reflection has to be examined before deciding if the technique can be used. Further

work is required on this subject to quantify the magnitude of absorption, as represented by an imaginary refractive index.

f) Detector angular spacing.

Figure 2.21 shows the effect of the change of the angular spacing between the detectors of the scattered light. The characteristics of the optical arrangement are : beam intersection angle=10°, elevation angle y=30°, rotation angle for one detector ξ_2=1.0° and ξ_1 varies to give different angular spacings between the detectors, but always close to the symmetry plane of the anemometer. Increasing the angular spacing results in increased sensitivity to size and a decreased possible size range. The size sensitivity is presented by the ratio of phase/diameter in figure 2.21.

g) Polarisation of the incident beams.

The effect of polarisation of the beams is to decrease the amplitude of the oscillations on the phase calibration curve, when the polarisation is normal to the plane defined by the beams and the collection position is out of the plane of the beams and close to the symmetry plane of the anemometer. The opposite is true when the collection position lies on the plane of the beams.

The scattered light is generally polarised elliptically at a point in space, even when the incident beams are polarised linearly. This means that the components of the amplitude functions in both Y and X directions (figure 2.5c) may be important. For incident beams polarised vertically relative to the plane of the beams, detection of the scattered light in the forward direction and off axis from the plane of the beams, in the Y direction, can be assumed to preserve the vertical polarisation of the scattered light, so there is no need for a polarising filter to be used. However, the polarisation of the incident beams can be used, as Saffman (1986) demonstrated, to eliminate surface reflection contribution to the scattered light by using light collection through a linear polariser at a certain direction.

h) Flow turbidity.

Flow turbidity is a measure of the interaction of the two-phase flow with the incident laser beams and the scattered light. In dispersed two phase flows both the incident beams and the scattered light in the direction of the collection optics can be interrupted by particles, which do not pass through the probe volume. Kliafas et al (1986, 1987) examined the "depth of field" effect on amplitude and visibility techniques, which could be disastrous for both techniques. The theory will be examined here to find out what the effect of "depth of field" is on the phase-Doppler technique.

One effect of the depth of field is to make the intensities of the incident beams unequal. Thus equation (2.20) becomes :

$$E_T = (E_{01}\, C_1\, e^{int} + E_{02}\, C_2\, e^{-int})\, (\frac{-i}{kr})\, \exp(i(\omega t - kr)) \qquad (2.29)$$

and the total intensity, $I_T = E_T\, E_T^*$ is given by :

$$I_T = \frac{1}{k^2 r^2} (I_{01}\, C_1\, C_1^* + I_{02}\, C_2\, C_2^* + (I_{01}\, I_{02})^{1/2}\, C_1\, C_2^*\, e^{i2nt} + (I_{01}\, I_{02})^{1/2}\, C_1^*\, C_2\, e^{i2nt}) \qquad (2.30)$$

Finally the coefficients of equation (2.24), $I_T = A + N\cos\sigma$, are :

$$A = \frac{I_{01}}{k^2 r^2}\, C_1\, C_1^* + \frac{I_{02}}{k^2 r^2}\, C_2\, C_2^* \qquad (2.31)$$

$$K + iT = 2\, (I_{01}\, I_{02})^{1/2}\, C_1^*\, C_2\, e^{i2nt} \qquad (2.32)$$

$$\text{where} \quad N = (K^2 + T^2)^{1/2}\,, \quad \sigma = \tan^{-1}(\frac{T}{K}) \qquad (2.33)$$

Equation (2.33) shows that the phase shift σ of the scattered fringe pattern at one position in space is given as the ratio of the imaginary to the real part of $C_1^*\, C_2$ and, as a consequence, it is independent of any inequality of the two beams. This means that any random, unsteady variation of beam intensity has no effect on the difference in the relative phase between Doppler signals at any two locations in space and so does not affect the accuracy of the particle

diameter. Another implication of depth of field concerns the accuracy of measurements of particle flux in the presence of flow turbidity, but this is examined separately in section 2.7.

2.5 Experimental verification

Experiments were carried out to verify the theory and to quantify the influence of the optical arrangement and the signal quality on the results.

a) Calibration curve

The optical arrangement of figure 2.22 was used initially to verify the analysis with a laser Doppler anemometer based on a 5 mW He-Ne laser. The scattered light was observed through a photodetector system, which could be rotated around the probe volume formed by the incident beams at different collection angles. A 200 mm plano-convex focal length collection lens was used with two slits placed at symmetrical positions from the collection optical axis and the light passing through them was directed to two photodetectors by mirrors. The beam intersection angle was 11.3° and the fringe spacing was 3.21 μm.

Single particles were mounted on a rotating optical flat and the particle diameter was defined with an error of ±1 fringe spacing by projecting, with a magnifying lens, the image of the glass bead inside the laser crossing point onto a screen. Rotation of the optical flat made the particle move across the probe volume. Care was taken to keep the optical flat clean so as to ensure the presence of only one particle. The glass beads had diameters between 30 and 150 μm. The Doppler signals generated from each particle were amplified, high pass filtered and transfered to a two-channel transient recorder (DATALAB model DL912) with a 20 MHz clock for each channel. The measurements were transfered, via an 488 interface, from the transient recorder to a PDP 11/03 computer.

The maximum amplitude positions of the Doppler bursts were located and the frequency was calculated by autocorrelation and the phase shift between the Doppler signals by crosscorrelation of the ±4 cycles around the maximum position. More information about the

technique used to extract frequency and phase shift of the Doppler bursts can be found in Hardalupas (1986).

The theoretical calibration curve and experimental results are shown in figure 2.23 as a function of the glass bead diameter (m=1.5). The detectors were positioned at elevation angle of 30° and rotation angles ξ_1=3.5° and ξ_2=1.9°, the beam intersection angle was 11.3° and the aperture dimensions were 50 mm by 5 mm. Good agreement is shown between the theoretical curve (continuous line) and the experimental results (black circles). The small differences from the theoretical results are due to imperfections in the sphericity of the glass beads and in their surface quality.

b) Flow turbidity

Experimental investigations were carried out for different depths of field in the transmission or the collection path with glass beads of different sizes (Hardalupas et al, 1986) to verify that turbidity does not affect the measured size. A repetitive Doppler signal was generated by rotation of a 100 μm glass sphere at constant angular velocity through the probe volume of a laser Doppler anemometer. This sphere was mounted on an optical flat which was placed on the shaft of an electric motor; special care was taken to keep the disc free of particles other than that of interest. Figure 2.24 shows the optical arrangement used to check the influence of the interruption of the beams on particle sizing with phase-Doppler and the principal characteristics are summarised in table 2.1. The beam from a 5 mW He-Ne laser was divided into two equal-intensity beams, with polarisation lying in the plane of the beams, which were focused to define the probe volume of the anemometer. The scattered light was observed by two photodetectors, which were positioned at an elevation angle, relative to the plane containing the two beams, of 30° and near the plane of symmetry at rotation angles ξ_1=3.5° and ξ_2=1.9°. The 300 mm focal length collection lens and the collection apertures were positioned on the lens and had dimensions 5 mm wide and 50 mm long. The random interruption of the laser beams between the transmission optics and the probe volume was simulated by a transparent, plane sided tank of water which contained a known mass of particles (see table 2.2) set in motion by a paddle stirrer. Similarly,

the random interruption of the scattered light was introduced by placing a tank of water between the control volume and the collection lens. Two tanks were used to provide depths of field corresponding to 5 cm and 14 cm. The distances from the control volume to the tanks were 35 mm and 70 mm for the transmission and reception paths respectively.

After narrow bandpass filtering between 100 and 500 kHz, the Doppler frequency and the phase shift between the two Doppler bursts were measured by a prototype zero-crossing counter processor, incorporating a 250 MHz clock. The error (due to the ±1 clock count error) of the measured frequency and phase was 0.08% and 3% respectively for the frequency of 0.21 MHz and phase 85° of the repetitive signal.

Figure 2.25 shows that the measured phase has a broadening which is a function of the void fraction. The measurements of figure 2.25a correspond to interruption of the transmission path over a depth of field of 14 cm and figure 2.25b to interruption of the collection path over a depth of field of 5 cm by 40-75 μm particles. The ordinate has been normalised by the mean phase of the 100 μm bead with no interrupting particles; the symbols represent the mean value of the phase at any given void fraction and the attached vertical error bars show the range between maximum and minimum measured values. It is clear that changes in the mean values are smaller than 5% and the r.m.s. error was always smaller than 5% with the error increasing with void fraction and the diameter of the interrupting particles. The errors are rather due to the lower signal-to-noise ratio than due to the principle of the method which was proved theoretically that is not affected by random attenuation of the beams and the scattered light.

These results, when compared to those of Kliafas et al (1986, 1987), show that the influence of depth of field on the systematic and random errors of measurement of particle diameter are much smaller for the phase-Doppler method than for either the pedestal amplitude or the visibility techniques. Table 2.3 summarises typical r.m.s. errors for 3 particle size ranges at similar void fractions for measurements made from phase-Doppler and visibility; pedestal amplitude has similar r.m.s. errors but is not considered because of the large systematic component which is associated with increasing void

fraction and which is smaller for visibility and virtually absent for the phase-Doppler technique. It should be reminded that, because of the smaller dimensions of the probe volume in the results of this experiment, the phase-Doppler measurements have been made under more demanding conditions than those of Kliafas et al (1986) since the ratio of the beam diameter to the interrupting bead diameter is smaller.

c) Signal-to-noise ratio of signals.

The experiment described in the previous section allowed the influence of the signal-to-noise ratio to be examined. The increase of the r.m.s. error of the phase shift with the increase of the void fraction is due to the decrease in the signal-to-noise ratio of the signals. The signal-to-noise ratio is also affected by the width of the bandpass filtering. Figure 2.26 shows the increase in the r.m.s. error of the phase shift, over a depth of field of 14 cm in the transmission part with 14-40 μm interrupting glass beads at a void fraction of 0.05%, as the low pass filter setting was increased to 2 and 10 MHz. It should be noted that the frequency was unchanged between the two filter settings, proving that the measurement of phase is more easily affected by low signal-to-noise ratio than is the frequency.

d) Aerodynamic sizing - Phase-Doppler comparison

In order to evaluate a phase-Doppler instrument in a two-phase flow and not with single particles as was done in section (a), independent information of particle size is required. Wilson & Liu (1980) have shown how to relate the aerodynamic diameter of a particle to the measurement of its velocity at the exit plane of a rapidly converging nozzle and Haghgooie et al (1986) have recently used the principle to measure seed particle diameters. The concept has been adapted here to assess the correlation between the phase generated by a glass bead and its aerodynamic diameter, through the simultaneous measurement of phase and velocity by the phase-Doppler anemometer.

The principal characteristics of the phase-Doppler anemometer used for this experiment can be found in table 2.4. Figure 2.27a shows the calibration curve of the system which involves the use of three

photodetectors. There are two pairs of photodetectors which give independent information about the size and with two sensitivity levels. Signals were processed by a zero-crossing counter described later in section 2.6. The line designated as "Φ_2" in figure 2.27a corresponds to the phase measured between the central detector and an adjacent one and has lower sensitivity and "Φ_1" corresponds to phase measured between the outer detectors. A tolerance at the measurement of the phase for each curve is assigned, which for this experiment was ±15% of the expected phase value (figure 2.27b). A signal is accepted as valid when the ratio of the two phase measurements is within a certain tolerance defined as :

$$\text{ratio} = \frac{\Phi_1 \pm \varepsilon \Phi_1}{\Phi_2 \pm \varepsilon \Phi_2} = \frac{\Phi_1 (1 \pm \varepsilon)}{\Phi_2 (1 \pm \varepsilon)} \qquad (2.34)$$

where ε is the tolerance of the phase measurement. The nominal value of the ratio for this optical arrangement is 2.0 and by using equation (2.34) with $\varepsilon = 0.15$, the tolerance of the ratio is 2.0 ± 0.6. For small phase shifts, the error is comparable to the phase measurement itself and ratios of 2.0 become progressively rarer so the ratio is relaxed to 1.0 for phase measurements which correspond to sizes smaller than 5 μm. This procedure is specific to the present electronic arrangement which is described in the next section, but does not affect the conclusions drawn below. It should be emphasised that the expected phase ratio is for refraction and, as already mentioned in the previous section, phase ratio due to surface reflection varies with particle sizes. Figure 2.28 shows the sets of calibration curves used for this experiment due to either refraction or surface reflection and the phase ratios as a function of particle size. It can seen that for 40 μm glass beads the phase ratio expected due to surface reflection is around 0.5, while due to refraction is 2.

Figure 2.29 shows the essential details of the nozzle. Air was introduced and passed through drinking straws which straightened the flow before flowing through the nozzle, with a 72 : 1 area contraction. The shop-air supply, was metered by a rotameter at approximately 40 lt/min to give an area-averaged exit velocity of about 7.7 m/s and seeded with kaolin by a reverse cyclone arrangement (Glass & Kennedy, 1977). The turbulence intensity, measured by the

phase-Doppler anemometer at the exit of the nozzle and in the absence of the beads, was 2%.

The large particles, in this case 40 μm glass beads, were added through a 5 mm diameter pipe, at the smallest attainable flowrate from a screw feeder arrangement, described in the following chapter, to ensure that the velocity of the air in the nozzle was not affected. The mean velocity and turbulence intensity of the 40 μm beads at the pipe exit, measured by the phase-Doppler anemometer in the absence of the accelerating nozzle, were 0.24 m/s and 56% for a phase window of 130° - 170°, which corresponds to approximately 35 - 45 μm for the optical arrangement used here. This velocity is larger than the expected terminal velocity of a single 40 μm glass bead of nominal density 2,420 kg/m^3 (≈0.11 m/s, calculated according to Fuchs, 1964), probably due to the "shielding" effect of the surrounding cloud of glass beads which permits the attainment of velocities larger than the terminal velocity. The count distribution of the 40 μm glass beads used in this experiment (nominally in the range 37 - 44 μm on a volume basis) shows that the number of "fines" below 37 μm is not negligible (figure 3.2b).

The velocity of the glass beads at the exit of the nozzle and on the centreline was measured by the phase-Doppler anemometer as a function of the phase of the signal and the probability distributions of the velocity of the beads and of the seeding particles are shown in figure 2.30, each normalised separately. The acceleration through the nozzle generates a slip velocity between the air and the beads, which increases with the aerodynamic diameter of the bead. Since the velocities of the gas and of the largest beads can be measured, "velocity windows" can be assigned which always correspond to the seeding particles and to beads which have aerodynamic diameter close to 40 μm. The concept of these "windows" will be used to find out how accurately 40 μm glass beads can be discriminated from seeding using the phase-Doppler technique. The details of the other aerodynamic diameters between, say, 35 μm and 5 μm have not been investigated and it is for this reason that the experiment is referred as "semi-quantitative". Two are the purposes of this experiment : a) to prove validation of the sizing measurements, b) to find out the sizing accuracy of the measurement of 40 μm glass beads and c) to find out the behaviour of the phase-Doppler instrument with powders used for

seeding air flows and the degree of discrimination between optically sized seed particles and 40 μm glass beads. Although the experiment is referring to 40 μm glass beads, there is no reason why the results of this experiment cannot be applied to other glass beads sizes.

Sizing measurements

Figure 2.31a shows that the number-frequency distribution of the ratio of the two pairs of phase measurements with laser power of 300 mW exhibits two peaks : at around 0.5 and 2.0. This is expected and proves that measurement due to surface reflection only can give rise to the ratio peak value of around 0.5. The ratio validation is important to eliminate measurements caused by surface reflection and this makes the use of three photodetectors a necessary feature of the instrument rather than a way to extend the size accuracy possible for one optical arrangement. Figure 2.31b shows the ratio distribution after rejecting the measurements with phase "Φ_2" greater than 180°. The size range possible up to phase shift "Φ_2" of 180° is around 100 μm and there are no particles larger than 45 μm in the glass beads. So the ratio distribution of figure 2.31b proves that this validation rejects most of the measurements with ratio around 0.5 which are due to surface reflection. There are also phase ratio values between 1. and 5. and, although part of this broadening is due to a 10° r.m.s. error in the phase measurement a large part must be due to aspherical particles. Eventually rejecting results with phase ratios due to reflection, there are phase ratios which can only be due to non-spherical particles. But it is shown that the ratio validation of 2.±0.6 is going to reject measurements from non-spherical particles.

Finally the effect of the laser power can be seen in figure 2.32, which shows the ratio distribution before any validation for a laser power of 60 mW. Comparison between figures 2.31a and 2.32 shows that two peaks remain on the ratio distribution, but the relative number of measurements at the peak around ratio values 0.5 is smaller for lower laser power. The Gaussian distribution of the light in the incident beams is responsible for signals due to surface reflection only, which are associated with particle trajectories through the edge of the control volume. Signals from the edge of the probe volume processed by the zero crossing counter reduce with decreasing laser power,

because the probability of having signals from the edge of the control volume with enough number of zero crossings for the counter to process decreases with laser power, so the relative number of surface reflection measurements is also reduced.

Sizing 40 μm glass beads

Figure 2.33 shows the phase distribution on channel "Φ_1" of figure 2.28a of the 40 μm glass beads measured by the prototype counter with a ratio validation of 2±0.60, for a laser power of 300 mW. The phase distribution has a modal value at about 150° which theoretically corresponds to approximately 40 μm. This is an encouraging result, given the uncertainties in the sphericity of the glass beads. If the beads were totally amorphous then the phase and the ratio distributions of figures 2.33 and 2.31a would be uniform over all values. The smallest phase measured is about 10° which corresponds to 3 μm. Note that the shapes of the number density in figures 2.33 and 3.2a are not expected to be quantitatively similar because the probability of measurement by a phase-Doppler anemometer is proportional to cross-sectional area of the measurement volume and this is a strongly non-linear function of particle size, because of the Gaussian distribution of light intensity in the incident beams (see, e.g. Roberts et al, 1979). On-line correction can be made for this effect (Saffman, 1987).

Figure 2.34 shows simultaneous measurements of velocity and associated phase at the exit of the nozzle, after phase ratio (2±0.60) validation. It is clear that the maximum number frequency of beads is again at around 150° and the associated velocity confirms that these are equivalent to about 40 μm. A number of beads have low velocity correlated to phase smaller than 130°, or optically determined diameter smaller than 35 μm. This result can only be due to particles which have an aerodynamic diameter near 40 μm but which are insufficiently spherical to produce the expected phase. This figure was used to quantify the cross talk into the 35-45 μm window from beads outside the window and the cross-talk from this window into size ranges outside this window and in particular into the phase difference window assigned to the seed particles.

It is convenient to define the following terms explained in figure 2.35 :

* the "40 μm beads phase-window" is defined as lying between 130° and 170°, which corresponds to optically-measured diameters of spherical scatter of between 35 μm and 45 μm. This is area "A" in figure 2.35;

* the "40 μm beads velocity window" is defined as lying between $U_b \pm u'_b$, where U_b and u'_b are, respectively, the measured mean and r.m.s. of the beads at the exit of the nozzle, measured at low (60 mW) laser power. This is area "B" in figure 2.35. The window defines the velocity of beads with aerodynamic diameters of between about 35 to 45 μm;

* the width of the "seeding particles phase-window" is defined as 40° which corresponds to optically-measured diameters of spherical scatterers up to about 10 μm;

* the minimum gas velocity, $V_{gas,min}$ is the measured minimum velocity of seed particles at the exit of the nozzle.

The cross talk into the 40 μm phase window, area "A", from beads with aerodynamic diameters outside the 35-45 μm range can be estimated from figure 2.36, which shows the velocity probability distribution of all signals (10000) within the 40 μm phase-window measured at 300 mW laser power - which corresponds to the power used to measure the seeding particles. About 80% of the distribution, area "C", lies within the 40 μm velocity window. The width of the latter was defined as twice the r.m.s. of the measured velocity of the beads and thus the figure demonstrates that cross-talk from aspherical beads outside this range is negligibly small.

The cross-talk from beads with aerodynamic diameters in the 35-45 μm window into optically determined size ranges outside this window is shown in figure 2.37. The figure shows the probability distribution of phase for all signals (19000) within the 40 μm velocity window, area "B", after imposing a phase ratio validation of 2 ± 0.60. The distribution is bell shaped and 42% of the signals fall within the 40 μm phase-window, designated area "C" : this percentage means that there is a large cross-talk from the 40 μm beads into other size ranges. One of the implications of this result is that, in a size distribution which is dominated by nominally 40 μm beads, there is no justification in using phase to examine the velocity characteristics of a

smaller size range, say 20 ± 5 μm. It should be mentioned here that the results of this paragraph are independent of a five fold decrease in the laser power from 300 mW.

Seeding measurement - cross-talk from glass beads

The sizing of seeding particles (e.g. powder or mineral oil) introduced in the flow to determine the characteristics of the gas phase is discussed in this section. One of the main purposes of this work is to measure the gas phase at the presence of the dispersed phase. For this reason signals from seeding particles should be discriminated from these generated from the dispersed phase. This is not always successful when glass beads are used as the dispersed phase and the following section quantifies experimentally the amount of particles with large aerodynamic diameter which could be considered as seeding particles when their diameter is optically determined.

Mineral oil droplets smaller than 3 μm, atomised by a Norgren "micro fog" lubricator and tested with an aerodynamic particle sizer (A.P.S. 33, T.S.I. Inc.), were used to check the calibration curve as well as that of a commercial instrument (Aerometrics Inc.). The results from the two instruments, figures 2.38a and b, show that the phase-Doppler technique can identify spherical seeding particles to a tolerance which is adequate for many engineering applications, but not to size them.

The optically-measured diameter corresponding to kaolin (society of Leather Trades Chemists' specification; BDH Chemicals Ltd.), dispersed by a reverse cyclone generator and measured by the Aerometrics system, is shown in figure 2.39a. The kaolin is specified to have a diameter smaller than 2 μm, and tests with the aerodynamic particle sizer for similar generators confirms this, but here the phase-Doppler measures up to 70 μm. The zero-crossing counter gives similar results, figure 2.39b, and it is concluded that the micrometer-sized solid seeding particles can result in measurements of inappropriately large diameters. The focus of attention is the measurement of the velocity of the gas phase and, in a system which used atomised mineral oil for seeding, this would be done by retaining signals with a phase which corresponded to diameters smaller than,

say, 2 μm. The same procedure could be used for the solid seed but, as shown below, it is necessary to maintain the data rate from the seeding particles as high as possible to minimise the error generated by cross-talk from the beads. The restriction of the seed measurements to particles smaller than 2 μm would be wasteful of the seed signals if there are no beads below, about 5-10 μm, which is close to the truth in the flow examined here (figure 3.2). Signals are accepted as gas phase over a 40° window which still results in rejection of about 76% of all seeding particles. This percentage which is undesirably high, is dependent on the type of solid particles used as the seeding phase : figure 2.39c shows that when titanium dioxide powder (Kronos R1053; Kronos Titan - GmbH) is generated by a reverse cyclone then the phase distributions measured by the zero-crossings counter are substantially narrower. For this powder, 68% of all seeding particles are rejected by the validation procedure of the instrument. On the basis of the number of discarded seed signals, there is advantage in using the titanium dioxide powder rather than kaolin. It should be noted, however, that the amplitude of the signals from the titanium dioxide is smaller than that from the kaolin and it depends on the sensitivity of the receiving optics as to whether the reduced rejection ratio is translated into higher flux of accepted seed signals, which is the object of this procedure. This paragraph concludes with two warnings. First, preliminary tests suggest that kaolin and titanium dioxide from different manufacturers give different results, so the conclusions are specific to the products examined. Secondly, extensive tests on different types of solid seeding particles have not been performed. There may be other solid powders, or methods of generation, which result in smaller numbers of rejected signals than the titanium dioxide reported here.

The cross-talk into the seed phase-window from the particles with aerodynamic diameter larger than about 10 μm was determined by the following experiment. The laser power was set at 300 mW and the number of signals which were within the seed phase-window with velocity smaller than $V_{gas,min}$ were counted (673) during the time it took to collect 10000 signals within the 40 μm phase-window : the resulting probability distribution is shown in figure 2.40a. The important conclusion is that the number of cross-talk signals is approximately 7% of the number of the measurements collected in the

40 μm phase window. This conclusion is going to be used in chapter 3, in a suggested procedure for reducing the effect of cross-talk in the gas phase measurements. The phase ratio validation in the seed phase-window was, as mentioned earlier, reduced to 1 ± 0.30. The lower velocity limit, $V_{gas,min}$, was imposed to exclude any true seeding particles which might pass through the probe volume. The cross-talk is expressed as a percentage of the signals within the 40 μm phase-window for reasons explained in the following section. The number of cross-talk signals reduces to 3.73% when the laser power is reduced to 60 mW, figure 2.40b, because fewer beads with diameter smaller than, say, 35 μm can contribute to the cross-talk at the lower laser power.

It is useful to close this section by considering the sensitivity of the phase-Doppler technique to surface anomalies, because the explanation has implications for other techniques based on the reflection or refraction of scattered light, such as the amplitude or visibility of the signal. Figure 2.41 shows a ray diagram of light reflected from one of the incident beams to the aperture of the photodetector. Although the phase shift is due to refracted light, the argument is more easily proved for reflected light. The figure shows that the fan of the light received at the aperture of the photomultiplier is of the order of its angular width which is of the order of one degree. As a consequence, the segment of the sphere which is observed is half this angular size. Even though the height of the aperture is typically 10 times the width, each photodetector thus is sensitive to a relatively small part of the bead and surface irregularities need extend over only a few degrees to generate departures from the expected calibration curve. These arguments can be equally applied to refraction. An additional potential source of departure of the measured phase from the calibration curve for a spherical scatterer is that the air bubbles contained by some glass beads.

If the cross-talk occurs for the above reasons, the determination of the size from amplitude or visibility will be similarly sensitive. It is unlikely that the wider apertures which are, in principle, possible for use when measuring the Doppler signal-amplitude will give any material advantages.

2.6 Design of a phase-Doppler instrument.

The experience obtained from the theoretical analysis and the experimental investigation of the phase-Doppler technique was used to design of the optical and electronic components of an instrument based on the phase-Doppler principle.

a) Optical Design

The transmission optics is identical to that of a common laser Doppler anemometer so that the beam from a laser may be focused on a rotating grating and two equal intensity beams (±1 order) are selected. Rotation of the grating provides frequency shift and the two beams are collimated and finally focused to cross and generate the probe volume of the anemometer.

The collection optics involves the use of three photodetectors instead of one, as for a one component laser anemometer. Early experimentation with two photomultipliers with separate collection optics confirmed the problem of arranging them to observe the same part of the probe volume, especially in dense dispersed two phase flows where the possibility of each detector observing different particles is increased. This becomes even more difficult when three photodetectors are required and the need for a single common spatial filter (pinhole). A similar solution is adopted in some commercial designs of two channel LDAs.

Figure 2.42 shows a scale drawing of the collection optics used for these experiments. The first lens (L1) collected the scattered light through three rectangular apertures and collimated it. The second lens (L2) focussed the light onto a common spatial filter of 100 μm width and 1 mm length. The light transmitted through the spatial filter was collimated by a third lens (L3) with smaller focal length than the focussing lens (L2), so that the size of the three aperture images was reduced by a factor of 3. Then the light from each aperture is directed though a system of prisms to the photosensitive surface of the detectors without any other spatial filter. There are masks between the detectors to make sure that there is no optical cross-talk between them. The optical components are sealed from daylight in a

aluminium cover and an eyepiece is provided on the outside surface of the optics to observe the spatial filter and facilitate alignment.

Spherical aberration can be avoided by the use of achromat lenses with a combination of triplets especially for the front lens (L1) but the cost is high. Good quality lenses are in addition diffraction limited so that their blur spot size (Melles Griot, Optics Guide) is kept small and measurements of particle flux and number density may be obtained more accurately, as explained in the following section. The present arrangement might also be improved by positioning the apertures after the last lens (L3) although this will make change of the apertures' spacing more difficult and the dimensional tolerance more critical, because the image is smaller by a factor of 3 there. Finally, the spatial filter was chosen to have a slit shape to limit the length of the anemometer probe volume observed by the collection optics is limited (figure 2.43) with a slit being used rather than a pinhole for ease of alignment. The observed length of the probe volume, which is limited by the width of the spatial filter has implications for the measurement of the particle flux and number density for which the knowledge of the size of the probe volume is necessary and allows measurement in dense two phase flows where the requirement of the existence of only one particle at a time in the probe volume is critically satisfied.

b) Signal processing

The scattered light was directed at front window photodetectors, and the signals from them were high passed from passive phase-matched filters. Amplifiers were not used to avoid the introduction of phase shift between the three signals. The signals then were fed to the electronic processor, which was developed as a consequence of experience gained through the experimental program.

The initial experiments were based on signal processing by a transient recorder, which digitised two Doppler bursts and used software, based on autocorrelation and crosscorrelation techniques, to measure the frequency and phase shift. This system had the disadvantage that it was slow and, even if the computer code had been optimised, with extensive use of assemply language, could not have extended a data rate of the order of ten measurements per second.

Data rates of this order almost preclude the measurement of particle flux or number density. The same disadvantage also apply to sizing systems using transient recorders to measure the amplitude of the pedestal and the visibility of the Doppler burst.

After confirmation of the theoretical analysis of the technique through experiments, the Doppler frequency and phase shift between two channels were measured by a zero-crossing counter, incorporating a 250 MHz clock. The counter circuit was based on the design of Heitor et al, 1984 and could measure (Hardalupas et al, 1986) fast enough but involved only two channels, which were insufficient to ensure error free size measurement. In addition, the resolution of the phase measurement (especially for small phase shifts), was undesirably small due to the 250 MHz clock.

The zero-crossing counter was therefore redesigned and rebuilt to incorporate three channels and a 500 MHz clock to give a 2 ns time resolution. The counter measured the time corresponding to five Doppler periods, the time corresponding to eight Doppler periods, the Doppler frequency, the time corresponding to the phases between channels 1 and 2 and between channels 1 and 3, the residence time of the particle in the probe volume, defined above, and the elapsed time between measurements. This information was translated in seven 16-bit words and transfered to a PDP11/03 computer by Direct Memory Access (DMA). The electronic circuit incorporates validation checks in the amplitude and the time domain so that noisy signals which would lead to erronious frequency and phase measurement were rejected.

The amplitude validation was based on a three amplitude level check. The crossing of the central threshold gave rise to a square wave (figure 2.44), which was used to measure the frequency of the Doppler signal. However, the counting circuit was not activated before both the central and the two outer, higher amplitude threshold levels had been crossed in the correct sequence. The amplitude validation check was performed on all three signals independently and the magnitude of the outer thresholds on all three channels was variable. The beginning of a Doppler burst was detected by the first correctly sequenced crossing of the outer threshold and the end was deemed to have occured at the first absence of outer threshold crossing.

The time-domain validation is adopted only on one of the three Doppler bursts. This signal, in crossing the lower threshold, activates a Schmitt trigger and the period of the resulting wave is used to gate the counting of clock pulses from the 500 MHz crystal. As shown in the timing diagram, the crystal clock pulses are gated to two high-speed counters. The first counter counts the number of 500 MHz clock pulses occuring between the first positive threshold crossing and the sixth crossing, which corresponds to 5 periods of the square wave (figure 2.44), and the second counts the time of 8 Doppler periods which have satisfied the amplitude validation. These two Doppler frequencies, corresponding to these time measurements, must be within a variable tolerance, as described below in equations (2.35) and (2.36). If the signals satisfy the validation requirement, the Doppler period for a valid signal is calculated by dividing the measured time of 8 Doppler periods by 8.

The phase shift was measured relative to the reference channel of the counter, which was the one validated in the time domain. Figure 2.45 shows the timing diagram for the measurement of the phase shift between channel 1 and 2 of the counter and a similar circuit existed for the phase shift between channel 1 and 3. The low threshold produced a square wave, which had successfully satisfied the amplitude validation and was used for the time validation and the frequency measurement was divided by two to give four square wave pulses for each channel which were equal to the Doppler period. Then the phase pulse sequence was produced (figure 2.45) and a counter determined the number of the 500 MHz clock pulses during the period that the pulse was set. This count included four times the phase shift between channel 1 and 2 and four Doppler periods and the phase shift was calculated in software. The division of the initial square wave pulses from the low threshold by two was needed to avoid electronic ambiguity for signals with phase shifts around 180°. The same information was delivered from the counter for the phase shift between channel 1 and 3.

The counter measured the elapsed time between each burst successfully satisfied the amplitude validation, using a 100 kHz clock. The time between measurements was used to find the particle flux, expressed as valid measurements per second per unit area. Finally, the counter also measured the time over which the amplitude

validation was satisfied during a burst, which is approximately the residence time of a particle in the probe volume of the anemometer, assuming bursts with good signal-to-noise ratio. The residence time of the particle in the probe volume was used to measure the particle number density, as explained in section 2.7.

The counter's dead time associated with each measurement was approximately 50 μs, of which around 30 μs was required for a now-redundant Doppler-frequency calculation in hardware. Although this dead time, between succesive measurements, ensured that the counter did not measure twice in the same burst, the data rate was currently limited to 20,000 measurements per second, which had been proved sufficient for the requirements of the flows measured. In some cases a data rate of 20 KHz would correspond to more than one particle in the probe volume of the anemometer and hence is satisfactory for many applications.

The upper frequency limit of the counter was around 15 MHz. This was set by the amplitude validation circuit, which cannot operate at higher frequencies and amplifiers of the input module of the counter, which had cut-off frequency of around 20 MHz. The accuracy of the measurement of frequency and phase is examined now below.

Frequency measurement

The time domain validation criterion of Heitor et al, 1984 is :

$$| 2 N_5 - (N_8 + \frac{N_8}{4}) | \leq Tol \qquad (2.35)$$

where N_5 is the number of clock pulses measured by the counter over the duration of 5 Doppler periods, N_8 is the number of clock pulses measured over the duration of 8 Doppler periods and Tol is either a function of N_8 or a constant set by the user. Usually (e.g. Heitor et al, 1984) Tol is defined as :

$$Tol = \varepsilon_f \; N_8 \qquad (2.36)$$

where ε_f is a constant defined by the user (usually 0.015). The accuracy of the measurement of the counter cannot be more than ± 1 clock pulse. Equation (2.35) can be modified :

$$\left| \frac{N_5}{5} - \frac{N_8}{8} \right| \leq \frac{Tol}{10} \qquad (2.37)$$

which shows that the difference between the number of clock pulses corresponding to the Doppler period calculated from the N_5 and N_8 is limited by a certain tolerance which obviously cannot be less than 1 clock pulse. So if Tol is set equal to 1 clock pulse of a 500 MHz clock and ε_f equal to 0.015, equation (2.36) estimates the upper frequency which can be measured by the counter as 6 MHz after which the counter will ultimately fail to measure even in the absence of noise. This limitation was overcome in Heitor et al (1984), where the time domain validation was performed in hardware, by using a comparison between the measured time of 10 and 16 Doppler periods, which increases the maximum frequency limit of the counter due to the above condition to around 12 MHz. However, the number of zero-crossings available in a Doppler burst, especially for systems applied to dispersed two-phase flows, is frequently less than 16 and the requirement of at least 16 zero-crossings in each validated Doppler bursts by the counter would lead to rejections of a lot of otherwise valid signals. To avoid this condition here, the time domain validation was performed in software and after a certain frequency the tolerance $(\frac{Tol}{10})$ of equation (2.37) was kept constant and equal to at least 1 clock pulse. This resulted to a larger uncertainty in the higher frequencies (>6 MHz) and figure 2.46 shows the variation of ε_f as a function of the Doppler frequency where the tolerance has to be increased at higher frequencies in order to make sure that the time domain validation is not failing due to the counting error (± 1 clock pulse) of the counter. However, for the measurements presented in the next chapters the maximum frequency measured was lower than 7 MHz, limiting the error of the measured Doppler frequency to less than 1%.

Phase measurement

The phase measurement is more sensitive than the frequency to signal-to-noise ratio and the amplitude of the signal as shown by Hardalupas et al (1986). The accuracy of the measurement of Doppler frequency also influences the accuracy of phase measurement, Doppler frequency can be measured more accurately at lower than at higher frequencies. Also, large phase shifts will be measured more accurately than small, because the ±1 pulse of a 500 MHz clock error, which exists also for the phase measurement becomes relatively larger when the phase shift decreases. As an example here the error of a phase shift between two Doppler signals of 10° when the Doppler frequency is 2.5 MHz is estimated. The period of a 2.5 MHz signal is 400 ns, so 200 clock pulses of a 500 MHz clock, and 10° phase shift at this case is around 6 clock pulses. This implies that the uncertainty of ± 1 clock pulses on the phase measurement is translated to a phase error of around 15%.

Figure 2.47 shows constant percentage of phase shift error as a function of phase shift and Doppler frequency due to the ±1 pulse of a 500 MHz clock uncertainty of the counter. The line corresponds to 12.5% error on the phase measurement. The area above the line corresponds to phase measurements with less percentage error. This uncertainty is one of the reasons of using phase shifts up to around 40° for the measurements of seeding particles and ratio validation relaxed to 1. ± 0.3 in this region. The Doppler frequencies including frequency shift, measured during the experiments described later, were always smaller than 7 MHz, so for phase shifts larger than around 40°, the error of the phase measurement was always smaller than 10%.

Although the phase difference between signals is independent of amplitude, the circuits which measured the phase difference had a small sensitivity to inequalities in signal amplitude. This effect is explained and quantified in Appendix 2.C, and can lead to wider phase distributions, especially for seeding particles which give small amplitude Doppler signals. This error source can be reduced by the use of logarithmic amplifiers, although this is not straightforward since phase matching is required and would involve some development effort which was not available here.

The dynamic range of the photomultipliers is a matter of concern and photomultiplier saturation may be a problem. However, the visibility of signals at off-axis positions and for practical apertures is close to unity over a wide size range and this delays the occurence of saturation of the photodetectors to higher size ranges. Photodetectors' specifications indicate a possible dynamic range in amplitude of 1000 : 1, which, assuming that the amplitude of the pedestal of the Doppler signal increases with the particle diameter squared, is translated to a size dynamic range of 35 : 1.

2.7 Particle flux and number density measurement

The measurement of particle flux and particle number density locally in a flow is important for two phase flows and is examined here. The method to be described here is not specific for the phase-Doppler technique and can be used with any sizing technique based on a laser Doppler system.

Flux is defined as the number of Doppler signals per second per unit area and number density is defined as the number of Doppler signals per m^3 and the primary quantities required, namely the time between measurements and the number of mesurements, are easily measured. Finally the size of the control volume can be calculated, so particle flux and number density can be measured. However, there are two effects in practice which complicate the above approach. The first is the Gaussian distribution of the light in the incident beams and the second is the depth of field due to particles randomly attenuating the incident beams and the scattered light.

The calculated dimensions of the control volume of the anemometer are at e^{-2} intensity level. However, the effective size of the probe volume is determined by the electronic threshold level and the amplitude of the Doppler signal which is proportional to the particle diameter squared. The Gaussian distribution of the light in the incident beams in combination with the electronic threshold level and the larger amplitude signals from large particles makes the effective size of the probe volume to increase with particle size.

Another implication of depth of field considered here concerns the accuracy of measurements of particle flux and number density in the presence of flow turbidity. It is a matter of observation that the

time taken to collect a *given* number of Doppler signals increases with increasing turbidity. In other words, the estimate of particle flux measured by a laser Doppler anemometer is closer to the truth at small than at large depth of field.

There is a number of ways to correct the results for the above effects. One strategy is to compensate for the variable attenuation of the signal by increasing the electronic amplification so that the signal strength *of a given particle size* is constant across a profile. This can be accomplished, for example, by measuring the particle size using the phase-Doppler technique and monitoring signal strength of the selected diameter on a transient recorder. This implies the use of the transient recorder, which makes the measurements time consuming and more complicated because the system has to be calibrated for each measurement (Saffman et al, 1984, Hardalupas et al, 1986).

Another strategy is to measure on-line the effective size of the probe volume of the anemometer for each size class. This method was suggested by Saffman (1987), Bachalo et al (1988), and extended to include the effect of frequency shift by Hardalupas and Taylor (1989). It can be achieved by using the interference fringes to provide an absolute length scale in the probe volume (figure 2.48), from which the size of the probe volume can be measured as a function of particle size. Hence a processor which can count the number of cycles in each Doppler burst and relate it to particle size gives the desired information. The analysis for this calculation can be found in Appendix 2.D and the theoretical curve showing the change of the cross sectional area of the probe volume as a function of particle size can be seen in figure 2.49.

This analysis depends on the particle trajectories being normal to the scattering fringes and, since this is not true generally, errors are inevitable with a one component measuring system. The advantage of the on-line measurement of the size of the probe volume is that corrects the measurements even for the effect of depth of field, so absolute measurements of flux and number density are possible for the phase-Doppler instrument, which can also size particles independently of the depth of field.

a) Particle flux

The instrument at the end of each measurement produces a size distribution, which is influenced by the change of the size of the probe volume. However, the laser Doppler measures the area of the probe volume normal to the direction of the velocity for each size class and the size distribution can be corrected by dividing the number of particles in each size class with the corresponding area of the control volume. So the particle flux is :

$$\text{Flux} = \frac{\pi}{6} \frac{1}{T_s} \Sigma \frac{n_i d_i^3}{A(d_i)} \qquad (2.38)$$

where T_s is the total sampling time after subtracting the dead time, mentioned above, n_i is the measured number of particles in the size class "i" with diameters between d_i and $d_i + \delta d$ and $A(d_i)$ is the effective area of the sampling volume of the anemometer for the size class "i" (equation (D.4)). In equation (2.38) the diameter of each size class is cubed, so the particle flux is strongly dependent on the larger particles of the size distribution, so even a small overestimation of the number of larger particles can result in large errors of the flux.

b) Particle number density

Let $C(d_i)$ represent the time average of particle number density (number of particles per m^3) of size class "i", which includes diameters between d_i and $d_i + \delta d$. If the instrument measures n_i particles in this class over a sampling time, T_s, then Saffman (1987) and Bachalo et al (1986) propose that, for one-dimensional flow normal to the fringes :

$$C(d_i) = \frac{n_i}{|U_i| \, A(d_i) \, T_s} \qquad (2.39)$$

where $|U_i|$ is the magnitude of the time-mean velocity of particles in size class "i" and $A(d_i)$ is the effective cross-sectional area (m^2) of the probe volume of the anemometer normal to the flow for the size class "i". Equation (2.39) entails neglection of <c'u'>, the time-averaged

cross-correlation between the fluctuating components of velocity and particle concentration and may be a justifiable approximation in some flows (Shih and Lumley, 1986). The time-mean velocity can be found from either the arithmetic mean of the sample in the class or by using the correction for "velocity biassing" proposed by McLaughlin & Tiederman (1973)

$$U_i = \frac{n_i}{[\Sigma \mid U_n \mid^{-1}]_i} \qquad (2.40)$$

The major qualitative disadvantage of the definition of $C(d_i)$ in equation (2.39) is that as $|U_i| \rightarrow 0$, $C(d_i) \rightarrow \infty$. There is no reason why $C(d_i)$ should become indefinitely large near, say, the stagnation point of a recirculation zone and this suggests that equation (2.39), though plausible, has restricted application.

An alternative definition of particle number density (Capp, 1983; Buchhave et al, 1979, who suggest it for measurement of seeding concentration) is based on the measurement of $\frac{(\Sigma\, t_n)_i}{T_s}$, the sum of residence times of particles in size class "i", $(\Sigma\, t_n)_i$, expressed as a proportion of the sampling time, T_s. This definition is similar to the phase indicator function used by Aliod and Dopazo (1987) in the modelling of two-phase flows. By definition of a single particle counting instrument, this quotient is less than unity. The expression for particle number density is

$$C(d_i) = \left[\frac{(\Sigma\, t_n)_i}{T_s} \right] \frac{1}{V(d_i)} \qquad (2.41)$$

where $V(d_i)$ is the effective volume of the intersection region of the beams of the anemometer, as defined in equation (E.5) of Appendix 2.E. $V(d_i)$ is closely related to $A(d_i)$ and is known either from analysis or the "on-line" measurement discussed in appendix 2.D. Equation (2.41) has a qualitatively different basis from equation (2.39) and states that the particle number density is the percentage of time that particle class "i" exists inside the effective volume of the instrument. The advantage of $C(d_i)$ as defined by equation (2.41) is that it remains a positive definite quantity even when $U_i = 0$, in contrast to equation

(2.39). A subsidiary advantage is that it is not necessary to measure the particle velocity vector to measure $C(d_i)$, although it may be advantageous to have a multi-component anemometer to find an accurate measurement of $A(d_i)$ (Saffman, 1987). Instrumentation to measure $(t_n)_i$ must be included in the anemometer and already exists in some commercial Doppler zero-crossing counters. The number density depends on the smaller particles, which have large population. It is difficult to identify the smaller particles, which are often involved in multiple particle occurences in the probe volume of dense two phase flows and can lead in measurement errors.

2.8 Conclusions

The theory of the phase-Doppler anemometer was verified experimentally by mounting glass beads on an optical flat and it has been established that the technique can be used for sizing spherical particles larger than 10 μm while a special optical arrangement is needed to size particles smaller than 10 μm, when sizing of larger particles is not required at the same time. The main parameters influencing the size range of the technique for one optical setting are : the beam intersection angle, the collection angle, the angular spacing between the different photodetectors used and, in some cases, the refractive index. All the above parameters have been examined and their influences established.

The influence of depth of field has been examined experimentally and found to be unimportant, in contrast to results for amplitude- and visibility- based instruments. The technique is applicable to liquid sprays, because droplets are spherical and have no surface imperfections. Its application to solid particles, and especially spherical glass beads, has been examined experimentally and its accuracy quantified.

A method for the "on-line" measurement of the effective size of the cross-sectional area of the control volume has been described and, as a result, a new method for the measurement of particle number density has been suggested.

Finally, an optical and electronic design of an instrument based on the phase-Doppler principle was suggested and certain validation

procedures to ensure correct measurement of velocity and size were described.

The main characteristics of the technique may be summarised as follows:

* Simultaneous size, velocity, flux and number density measurements of spherical particles are possible.
* The sizing calibration curve is linear with uniform sensitivity for particles with diameter larger than around 10 μm.
* High spatial resolution (sampling volume much less than 1 mm^3).
* Measurements at high number density flows (up to 10^{12} particles/m^3) can be performed with off-axis collection of scattered light, which limits the size of the probe volume.
* Beam attenuation, due for example to depth of field interaction, does not affect the measurements.
* A wide size range (of the order of hundreds of μm) can easily be achieved from suitable optical arrangements.
* The technique is an extension of the laser Doppler anemometry and can be added to an existing laser Doppler anemometer.
* Depending on the part of the scattered light used for the sizing information, measurements independent of the refractive index can be performed. The influence of the refractive index change is small (10% sizing error for 7% change of refractive index) for non-absorbing particles.
* The measurements of the phase-Doppler anemometer can be used to distinguish between gas (seeding) and particle velocity characteristics; however, careful checks should be performed before using the technique for such applications. It was found here a 7% cross talk from monodispersed glass beads on the velocity characteristics of seeding particles.
* It can be used with large off-axis forward-scatter collection angles, with sidescatter collection when large possible size range is required and the backscatter application although it seems possible needs more research.
* An integrated collection optical unit can be used, which makes the alignment of the system easy.
* A zero-crossing counter can be used for signal processing, with large data rate which make flux measurement possible.

* Three photodetectors and appropriate validation checks are needed to ensure that no sizing error can occur.

TABLE 2.1

Principal characteristics of the phase-Doppler anemometer used for the depth of field experiment

5 mW He-Ne laser wavelength	632.8 nm
Focal length of the lenses	
imaging lens	300 mm
light-collecting lens	300 mm
Beam diameter, at e^{-2} intensity, of laser	0.65 mm
Measured half-angle of intersection	5.9 degr.
Fringe spacing	3.08 μm
Calculated dimensions of measuring volume:	
minor axis to e^{-2} intensity	0.10 mm
major axis to e^{-2} intensity	0.91 mm
Calculated number of fringes within e^{-2} intensity level	31
Collection aperture	50 X 5 mm
Pinhole diameter	0.48 mm

TABLE 2.2

Principal characteristics of scattering particles used for the depth of field experiment.

size range	particle material	density	refractive index
(μm)		(kg/m^3)	
14-40	lead glass	2950	1.6
40-75	perspex	1190	1.49
90-105	perspex	1190	1.49
150-212	perspex	1190	1.49
300-425	perspex	1190	1.49
600-800	perspex	1190	1.49

TABLE 2.3

Comparison of random errors due to depth of field in sizing using phase-Doppler and visibility

Interrupting particle size	Void fraction	Phase Doppler	Visibility
(μm)	(%)	(%)	(%)
300-425	0.14	3.1	31
90-105	0.040	2.4	7
14-40	0.015	1.4	5

TABLE 2.4

Principal characteristics of the phase-Doppler instrument used for the accelerating nozzle experiment

Laser power (nominal)	0.7	W
wavelength	514.5	nm
Beam crossing half-angle	5.7	degr.
Frequency shift	1.93	MHz
Receiving optics axis	30°	relative to forward scatter
Distance of receiving lens from mesurement volume	600	mm
f-number of lens	6.3	
Magnification of lens	2	
Separation of pmt apertures	25	mm
Aperture dimensions	50 X 5	mm

APPENDIX 2.A

Expressions for the amplitude functions of the scattered light from a sphere illuminated from a single beam

Glantschnig & Chen (1982) obtained the following expressions for the amplitude functions of the scattered light from a sphere illuminated from a single beam. The amplitude functions describing the rays reflected from the external surface of the sphere are :

$$S_1^{(1)}(x,m,\theta) = x\,\frac{\sin\frac{\theta}{2}-\sqrt{m^2-\cos^2\frac{\theta}{2}}}{\sin\frac{\theta}{2}+\sqrt{m^2-\cos^2\frac{\theta}{2}}}\,\frac{1}{2}\,\exp\left(i\left(\frac{\pi}{2}+2x\sin\frac{\theta}{2}\right)\right) \qquad (A.1)$$

$$S_2^{(1)}(x,m,\theta) = x\,\frac{m^2\sin\frac{\theta}{2}-\sqrt{m^2-\cos^2\frac{\theta}{2}}}{m^2\sin\frac{\theta}{2}+\sqrt{m^2-\cos^2\frac{\theta}{2}}}\,\frac{1}{2}\,\exp\left(i\left(\frac{\pi}{2}+2x\sin\frac{\theta}{2}\right)\right) \qquad (A.2)$$

where superscript 1 denotes the interface p=0 surface reflection and subscripts 1 and 2 represent the perpendicular and the parallel polarisations respectively. The amplitude functions for the rays emerging after refraction through the sphere are :

$$S_1^{(2)}(x,m,\theta) = x\left(1-\left(\frac{1+m^2-2m\cos\frac{\theta}{2}}{1-m^2}\right)^2\right)$$

$$\sqrt{\frac{m^2\sin\frac{\theta}{2}\left(m\cos\frac{\theta}{2}-1\right)\left(m-\cos\frac{\theta}{2}\right)}{2\sin\theta\left(1+m^2-2m\cos\frac{\theta}{2}\right)^2}}\,\exp\left(i\left(\frac{3\pi}{2}-2x\sqrt{1+m^2-2m\cos\frac{\theta}{2}}\right)\right) \qquad (A.3)$$

$$S_1^{(2)}(x,m,\theta) = x\left(1-\left(\frac{(1+m^2)\cos\frac{\theta}{2}-2m}{(m^2-1)\cos\frac{\theta}{2}}\right)^2\right)$$

$$\sqrt{\frac{m^2 \sin\frac{\theta}{2}(m\cos\frac{\theta}{2}-1)(m-\cos\frac{\theta}{2})}{2\sin\theta(1+m^2-2m\cos\frac{\theta}{2})^2}}\ \exp\left(i\left(\frac{3\pi}{2} - 2x\sqrt{1+m^2-2m\cos\frac{\theta}{2}}\right)\right) \qquad \text{(A.4)}$$

where superscript 2 implies the p=1 refraction and subscripts 1 and 2 imply the polarisation direction.

APPENDIX 2.B

Expressions for the geometrical parameters of the scattered light theory

The relationships for the geometrical parameters of figure 2.3 are given below. The equations were derived using spherical trigonometry. In all the equations subscript j = 1, 2 and refers to the beam examined.

$$\cos\theta_j = \cos\xi_j \cos y_j \tag{B.1}$$

$$\cos\chi_j = \frac{\sin y_j}{\sin\theta_j} \tag{B.2}$$

$$\sin\phi_j = \frac{\sin\xi_j}{\sin\theta_j} \tag{B.3}$$

The calculations are performed using as a reference polar coordinate system, located on the bisector of the two beams and our reference angles are defined for this coordinate system as y, ξ. The angles for each beam are given by :

$$\xi_1 = \xi + \frac{\phi}{2} \qquad \xi_2 = \xi - \frac{\phi}{2} \tag{B.4}$$

$$y_1 = y_2 = y \tag{B.5}$$

APPENDIX 2.C

Influence of Doppler signal amplitude on the phase measurement in a zero crossing counter with finite threshold levels

We assume that at two different channels of the counter we have signals with amplitude A and B, as is shown at the figure below. Both signals are drawn on the same reference system and, for simplification, only one period T is shown. The low threshold of the counter which is used for the zero-crossing detection is not exactly at the zero volt level, but at a level V_T. The threshold identifies a zero crossing at signal A at time t_A and at signal B at time t_B. The difference between t_A and t_B, δt, is going to be expressed as a function of the amplitudes of each signal and the Doppler period T.

Both signals can be expressed as sinusoidal waves :

$$V_1 = A \sin\omega t \quad \text{and} \quad V_2 = B \sin\omega t \tag{C.1}$$

where ω is the angular frequency of the Doppler signal and $\omega = 2\pi/T$. Then we can express the derivatives of equations (C.1) as :

$$\frac{dV_1}{dt} = A\,\omega\cos\omega t \quad \text{and} \quad \frac{dV_2}{dt} = B\,\omega\cos\omega t \tag{C.2}$$

At the beginning of the signal we can assume that :

$$\frac{dV}{dt} = \frac{\delta V}{\delta t} \tag{C.3}$$

so $\delta t = t_B - t_A = (\frac{dV}{dt} / \delta V)^{-1} = (\frac{B\,\omega\cos\omega t}{V_T})^{-1} - (\frac{A\,\omega\cos\omega t}{V_T})^{-1}$ and hence :

$$\delta t = (\frac{\omega\cos\omega t}{V_T})^{-1} \quad \frac{A - B}{AB} \tag{C.4}$$

At t = 0, equation (C.4) becomes after substituting ω with $2\pi/T$:

$$\frac{\delta t}{T} = \frac{V_T}{2\pi} \frac{A - B}{AB} \qquad (C.5)$$

Typically, the level of the threshold, V_T, is $\approx A/20$. Using this assumption equation (C.5) becomes :

$$\frac{\delta t}{T} = \frac{1}{2\pi\, 20} \left(\frac{A}{B} - 1\right) \qquad (C.6)$$

For the extreme case that the ratio of the amplitudes of the two signals, $\frac{A}{B}$, is 5, equation (C.6) shows that a false phase shift is introduced between the two signals, due to finite threshold of the zero-crossing counter, of approximately 11° and is independent of the Doppler frequency.

APPENDIX 2.D

On-line calculation of effective size of measuring volume of a laser Doppler anemometer with frequency shift

The effective area of the measuring volume, $A(d_i)$, for one - dimensional flow normal to the fringes, is

$$A(d_i) = 2 \cdot z_p \cdot y(d_i)_{max} \qquad (D.1)$$

where z_p is the known length of the image of the spatial filter (slit) incorporated in the receiving optics and $y(d_i)_{max}$ is the, as yet unknown, maximum cross-stream displacement from the centre of the measurement volume of the anemometer for which a measurable signal can be obtained. Saffman (1987) shows that $y(d_i)_{max}$ can be related to the number of zero-crossings existing in a Doppler burst measured by a laser- Doppler anemometer and presents an analysis for an anemometer, but in the absence of frequency shifting. Saffman's analysis is therefore here extended to establish whether the effect of frequency shifting on the magnitude of $y(d_i)_{max}$, and hence $A(d_i)$, is large.

The object of the analysis is to replace the unknown in equation (D.1), $y(d_i)_{max}$, by a function based on the length of the intersection volume in the streamwise direction, $x(d_i)$. This length is chosen because it is a function of the size class, d_i, and is easily measured by a zero-crossing counter from the total number of fringes detected in a burst above the trigger level voltage, V_T. The starting point of the analysis is to note that $y(d_i)_{max}$ is defined partly by the existence of a trigger level voltage and partly by the minimum number, N_0, of zero crossings required by the counter to validate a Doppler burst. These constraints on $y(d_i)_{max}$ can be expressed as the following replacement of equation (Saffman. 4),

$$y(d_i)_{max} = \frac{1}{\sqrt{2}}\ b_y \left\{\ln\left[\frac{V_m\,(d_i)}{V_T}\right] - 2\ \frac{x(d_i)_{min}}{N_f f}\right\}^{1/2} \qquad (D.2)$$

which now takes account of frequency shifting. Here b_y is the Gaussian waist diameter at the intersection region, $V_m\ (d_i)$ is the

maximum amplitude at the centre of the Doppler burst, N_f is the number of fringes inside the Gaussian waist and $x(d_i)_{min}$ is the distance (μm) over which the particle is detected in the x (flow) direction, corresponding to the maximum trajectory displacement, $y(d_i)_{max}$ (figure 2.47). $x(d_i)_{min}$ is smaller than it would have been in the absence of frequency shifting and is given, in terms of known or measurable quantities, by

$$x(d_i)_{min} = \frac{N_0 \; f}{2} \left[\frac{| U_i(t) |}{U_{shift} + U_i(t)}\right] \qquad (D.3)$$

where f is the fringe spacing (μm), U_{shift} is the linear velocity of the moving fringes and $U_i(t)$ is the instantaneous flow velocity. Equation (D.2) is inconvenient because neither $V_m(d_i)$ nor V_T is measured by a counter but the quotient $\frac{V_m(d_i)}{V_T}$ can be expressed in terms of the average of the square of all burst lengths, $< x_i^2 >$, which is a directly measurable quantity. Equation (D.1) is thus rewritten as

$$A(d_i) = (\frac{3}{2})^{1/2} z_p \, b_y \{\cos^2 \frac{\theta}{2} \frac{< x_i^2 >}{b_y^2} - (\frac{N_0}{N_f})^2 [\sum \frac{1}{n_i} \frac{| U_i(t) |}{U_{shift} + U_i(t)}]\}^{1/2} \qquad (D.4)$$

replacing equation (Saffman. 9). Here θ is the beam intersection angle.

If $N_f >> N_0$ then the term which accounts for frequency shifting in equation (D.4) is negligible. Generally any sizing instrument based on a laser-Doppler anemometer has a small beam intersection angle, θ, in order to identify a wide sizing range and small beam waist diameter at the measuring volume, b_y, to increase spatial resolution. Hence the extreme condition that N_f is just slightly larger than N_0 is not as rare as it is in conventional laser-Doppler anemometry.

The implications of equation (D.4) are shown in figure 2.48 which plots $A(d_i)$ as a function of particle diameter with S = \f(| U_i | , $U_{shift} + U_i$) as the "shifting" parameter, where U_i is the arithmetic mean velocity of the d_i size class. This term replaces $\sum$ \f(1 , n_i) \f(| $U_i(t)$ | , $U_{shift} + U_i(t)$) for convenience and, in accordance with

the arguments of the preceding paragraph, N_0 / N_f is set at 8/10. $A(d_i)$ is calculated from equations (D.2) and (D.3), rather than (D.4), for computational ease and it has been assumed that V_m = const d_i^2. The abscissa in figure 2.48 is normalised by d_0, the size class for which $V_m = V_T$, to facilitate comparison with Saffman (1987) and for which $A(d_0)$ is zero. The area is a strong function of the particle diameter, because of the square-law dependence of the signal amplitude and hence, at a normalised diameter of 100, the cross-sectional area for a slow moving particle, for which S = 0.032, is only 5% larger than for a fast moving particle, for which S =0.75. At the smallest diameters, however, the correction to the cross-sectional area for the slow moving particle is about 25% larger than that of the fast particle.

The correction to the cross-sectional area of the instrument, due to frequency shifting, is large at small diameters if N_0 / $N_f \approx 1$. Qualitatively, the same will be true in two-dimensional flows and must be added to the considerations, described by Saffman (1987), for these flows. As a final comment, it is noted that the slit width, z_p, in equation (D.1) is assumed to be both known and independent of particle size. Dodge et al. (1987) have suggested that both of these statements are open to question and the resulting tolerance on $A(d_i)$ and $V(d_i)$ should form the subject of future research.

APPENDIX 2.E

Comparison between two methods suggested for particle number density measurement

For completeness, it is demonstrated that there is a relationship between equations (2.38) and (2.40), which are the two definitions of particle number density, as follows. If the time-mean velocity of size class "i" is evaluated as (e.g. Buchhave, George & Lumley, 1979)

$$|U_i| = \frac{\{ \Sigma\, t_n\, |U_n| \}_i}{\{ \Sigma\, t_n \}_i} \qquad (E.1)$$

substituting equation (E.1) in (2.38) gives

$$C(d_i) = \frac{n_i \{ \Sigma\, t_n \}_i}{\{ \Sigma\, t_n\, |U_n| \}_i\, A(d_i)\, T_s} \qquad (E.2)$$

The average length of the measuring volume normal to the fringes can be written as

$$\langle x_i \rangle = \frac{\{ \Sigma\, t_n\, |U_n| \}_i}{n_i} \qquad (E.3)$$

where the term in parenthesis in (E.3) is the total number of fringes crossed by particles of class "i" during time T_s. Substitution of equation (E.3) in (E.2) gives

$$C(d_i) = \frac{\{ \Sigma\, t_n \}_i}{\langle x_i \rangle\, A(d_i)\, T_s} \qquad (E.4)$$

and if

$$V(d_i) = A(d_i)\, \langle x_i \rangle \qquad (E.5)$$

equation (2.40) is recovered.

Equation (E.5) is important, because it is the basis of the calculation of the volume of the crossing region of the anemometer beams.

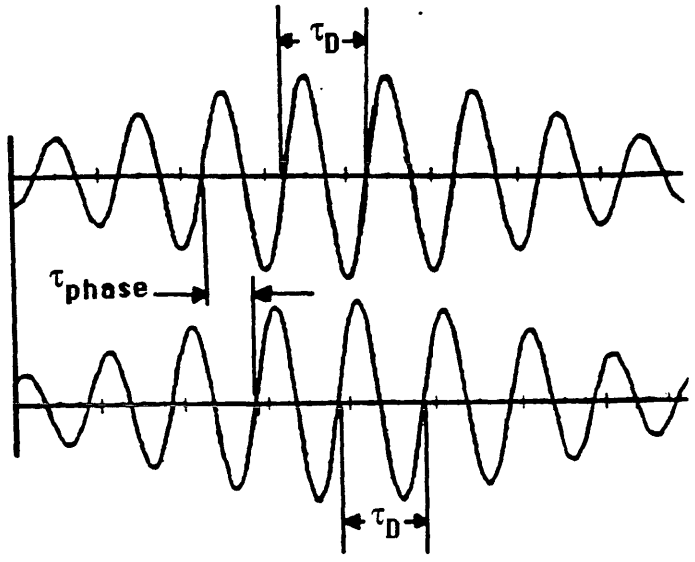


FIGURE 2.1 Phase shifted Doppler signals showing the phase shift τ_{phase} and the Doppler period τ_D

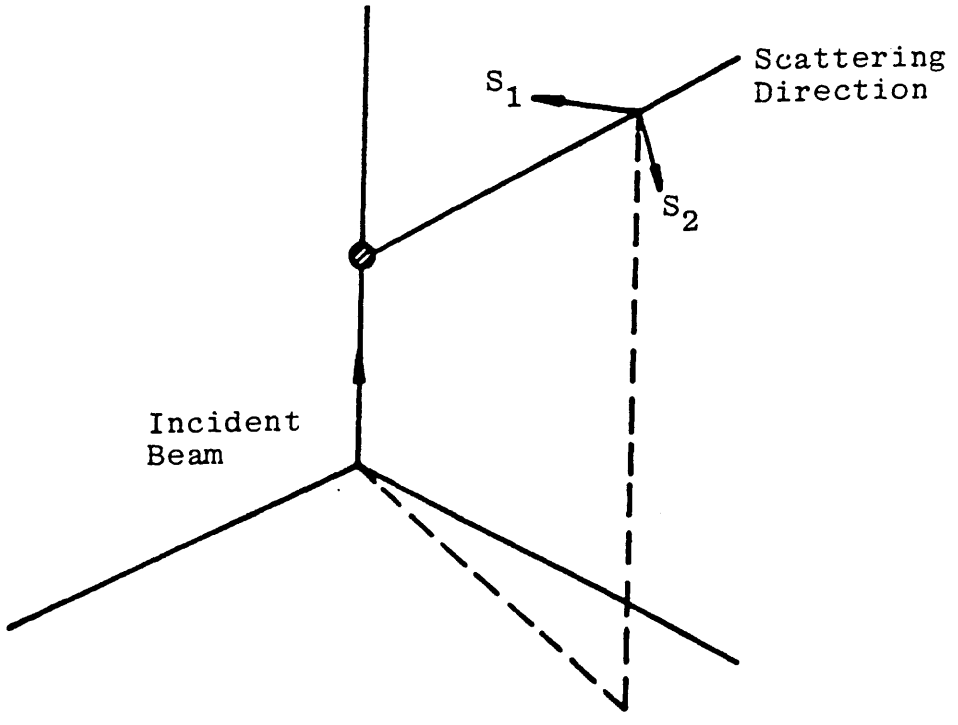


FIGURE 2.2 The amplitude functions S_1 and S_2 of the light scattered by a sphere located in one beam according to the notation of Van de Hulst (1981); S_1 is normal and S_2 parallel to the scattering plane defined by the incident beam and the scattering direction.

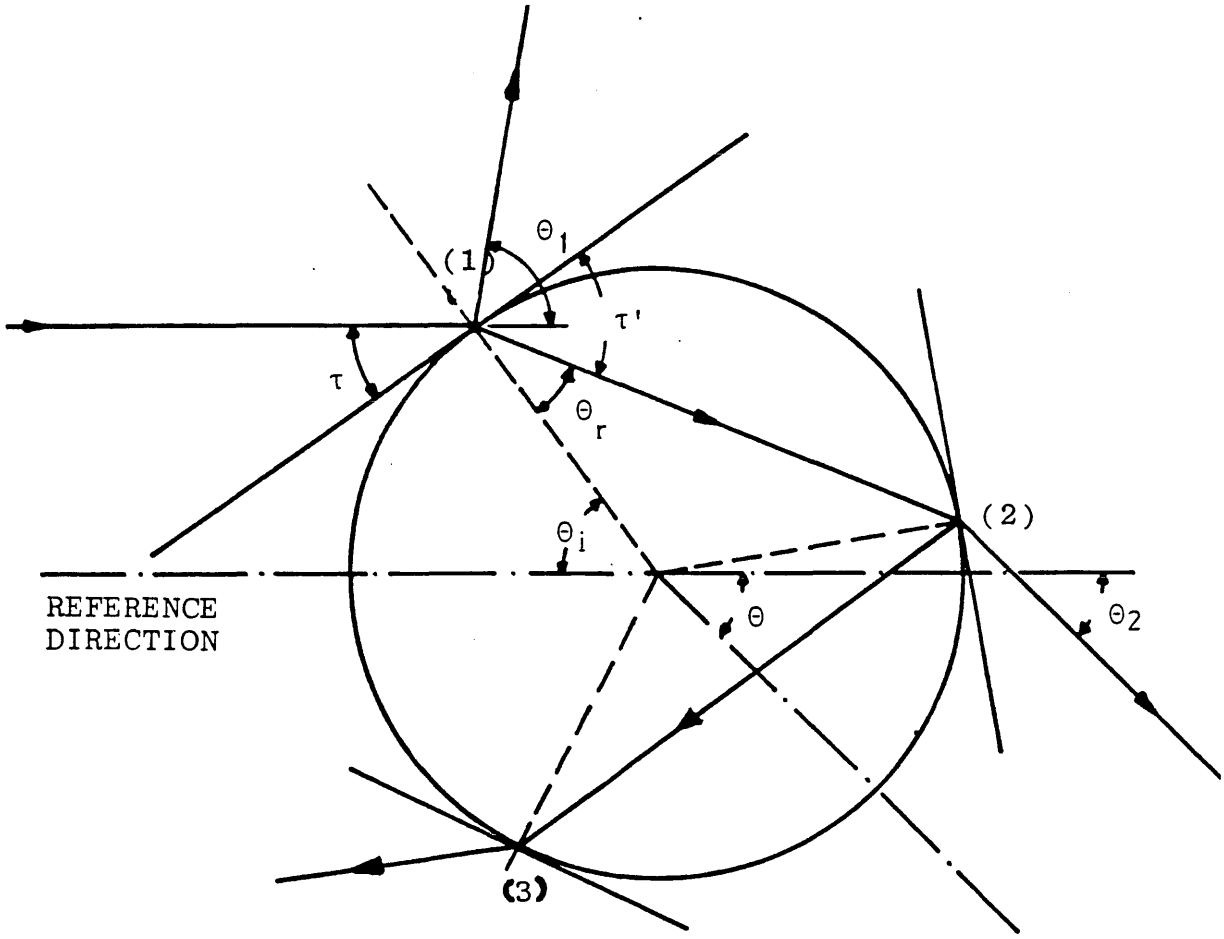


FIGURE 2.3 Ray optics of a transparent sphere showing paths due to surface reflection, refraction and first internal reflection.

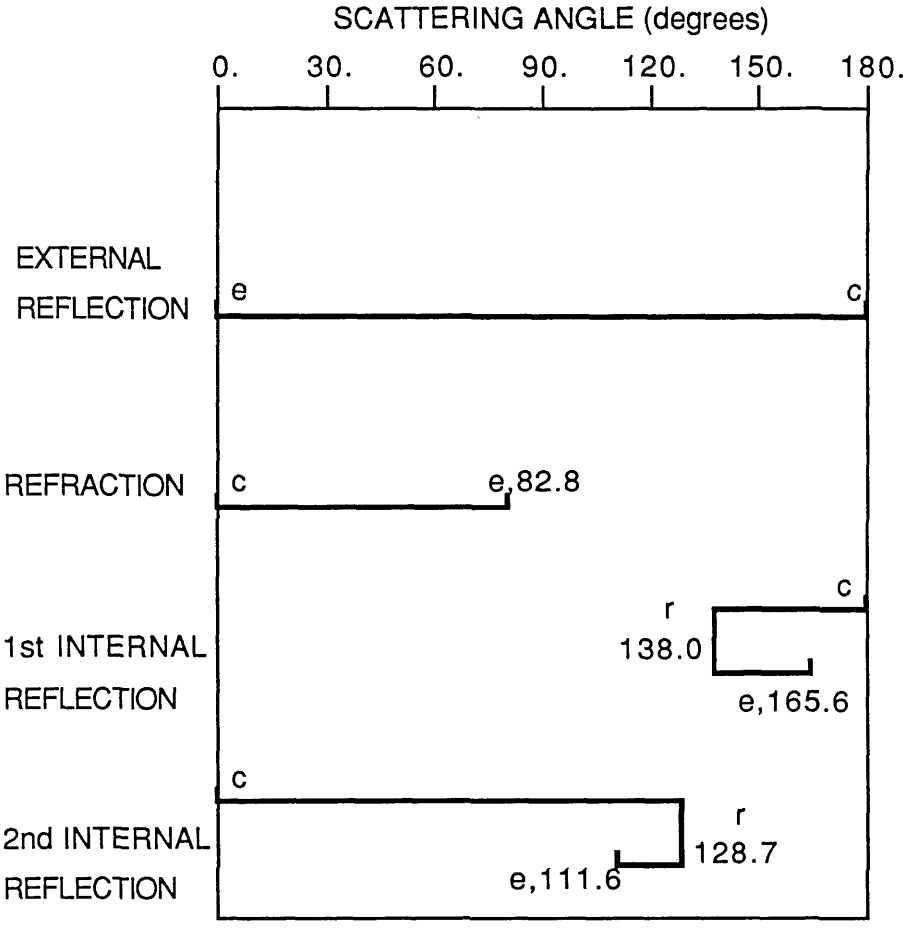


FIGURE 2.4(a) Diagram is after Van de Hulst (1981) showing the scattering angle regions where paths due to surface reflection, refraction and first internal reflection across a water droplet are present.

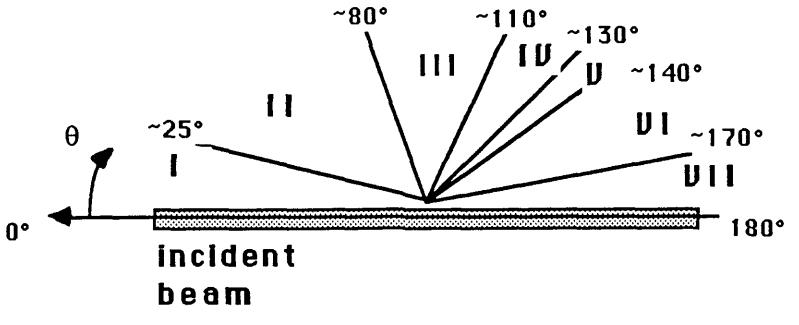


FIGURE 2.4(b) Classification of scattering angle into seven intervals according to the combination of ray paths across a water droplet.

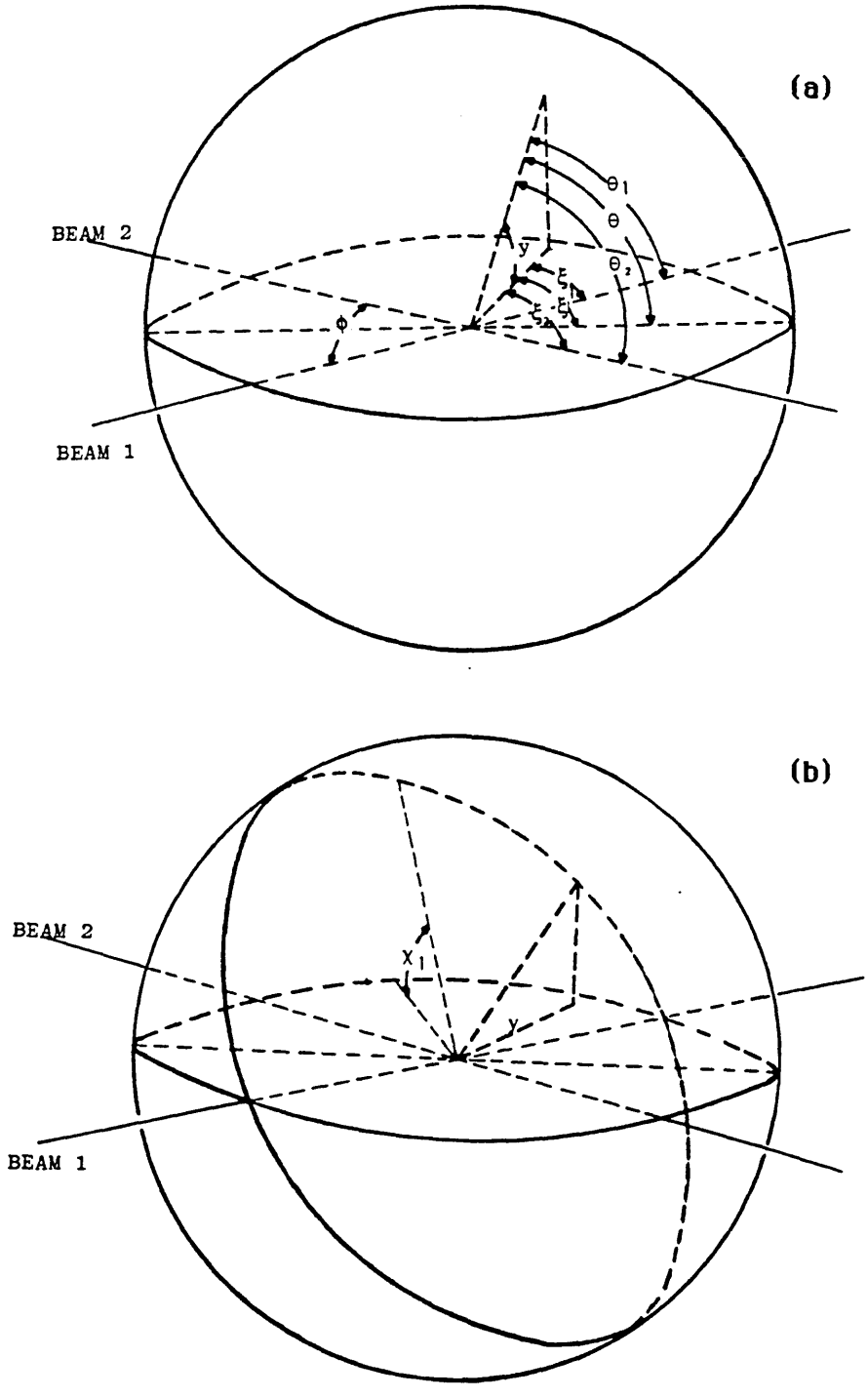


FIGURE 2.5 Definitions of angles used in the theoretical analysis of the light scattered by a sphere located in the crossing region of two laser beams.

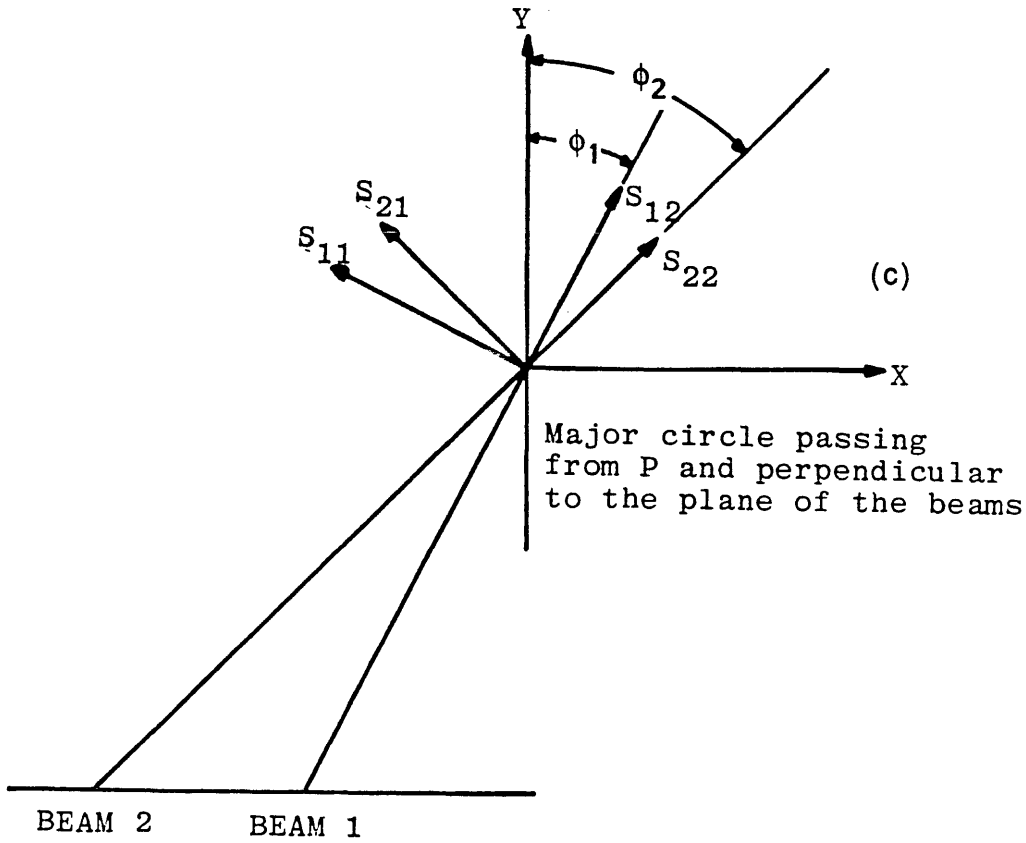
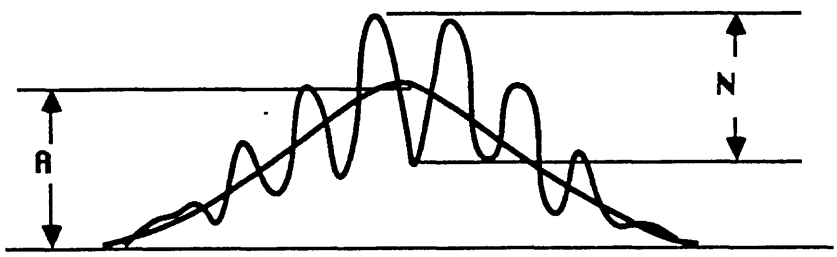


FIGURE 2.5(c) Definitions of angles used in the theoretical analysis of the light scattered by a sphere located in the crossing region of two laser beams.



$$\text{Visibility} = \frac{N}{A} \qquad A : \text{amplitude of pedestal}$$

FIGURE 2.6 The physical meaning of the terms A and N of equation (2.25) for a Doppler signal; A is the amplitude of the pedestal and N is the modulation depth.

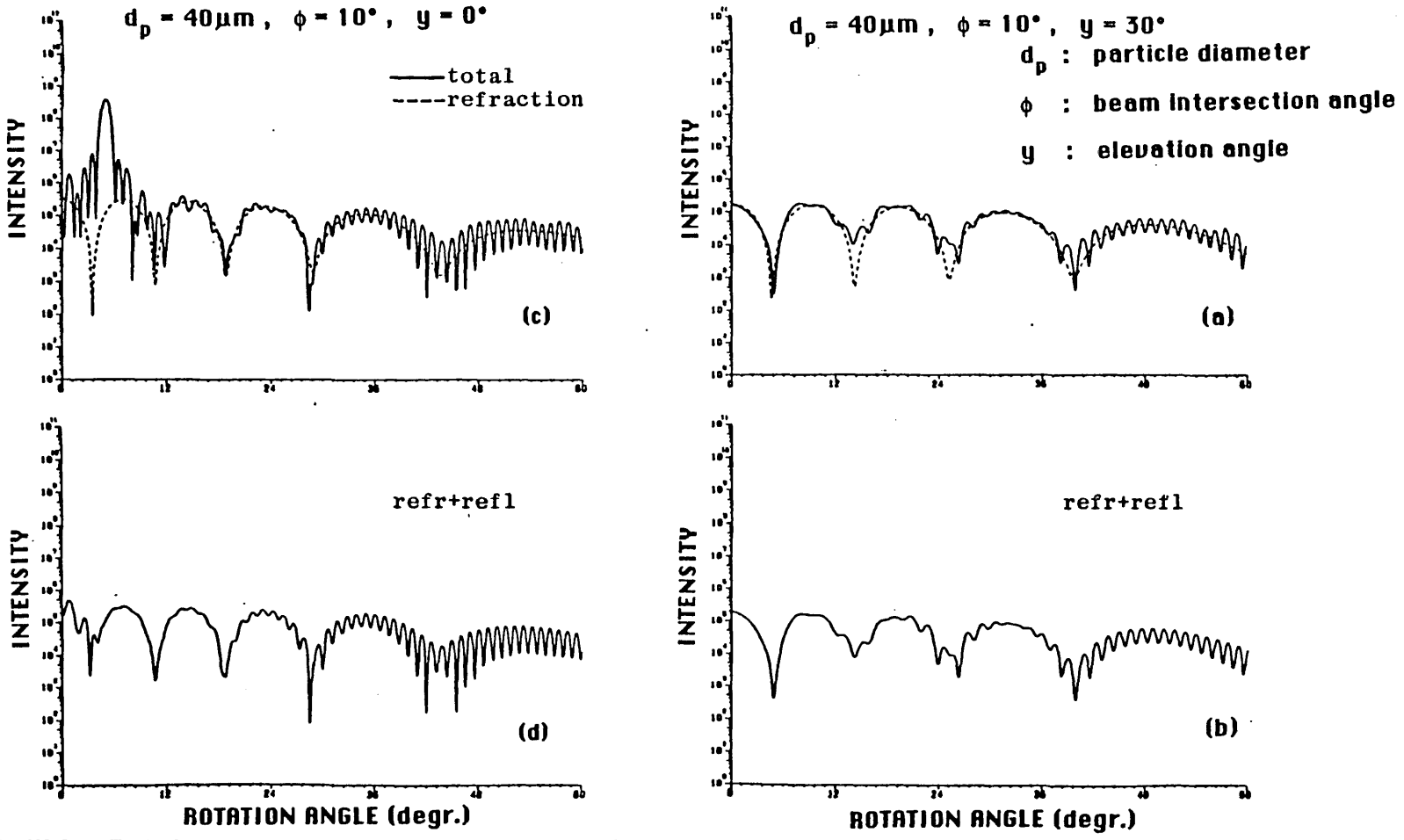


FIGURE 2.7 Intensity interference pattern of the light scattered by a 40 µm glass bead located in the crossing region of two laser beams as a function of the rotation angle; (a) pattern due to interference of surface reflection, refraction and diffraction (solid line) and due to refraction only (dashed line) and (b) pattern due to surface reflection and refraction only, at the plane parallel to that of the beams at an elevation angle y=30°, (c) and (d) the same as above but for the plane of the beams (y=0°).

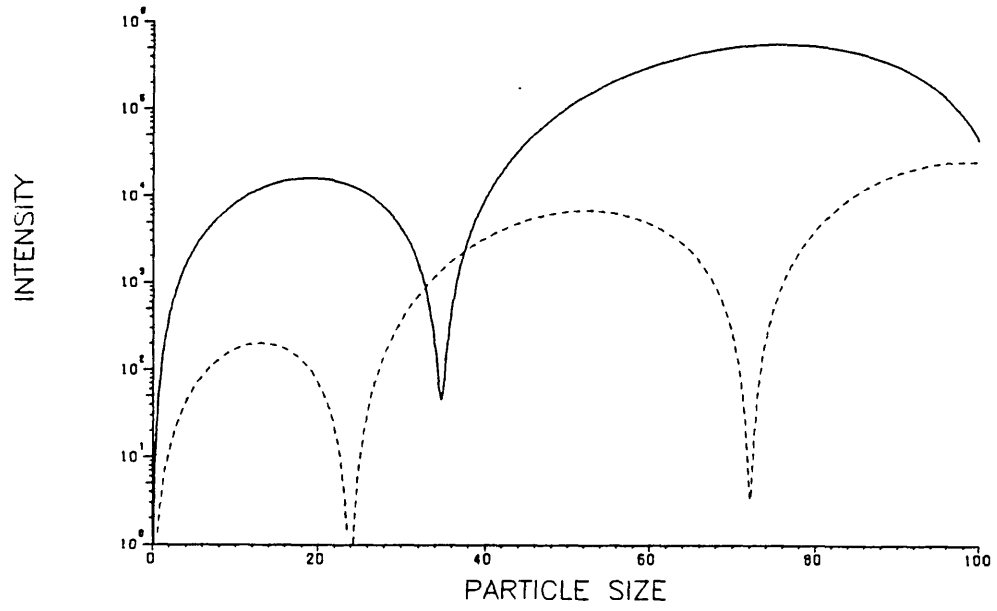


FIGURE 2.8(a) Intensity of the scattered fringe pattern due to refraction only (solid line) and due to surface reflection (dashed line) showing the relative amplitude of the two patterns as a function of particle diameter. Observation at a position with elevation angle of 30° and rotation angle of 5.3°.

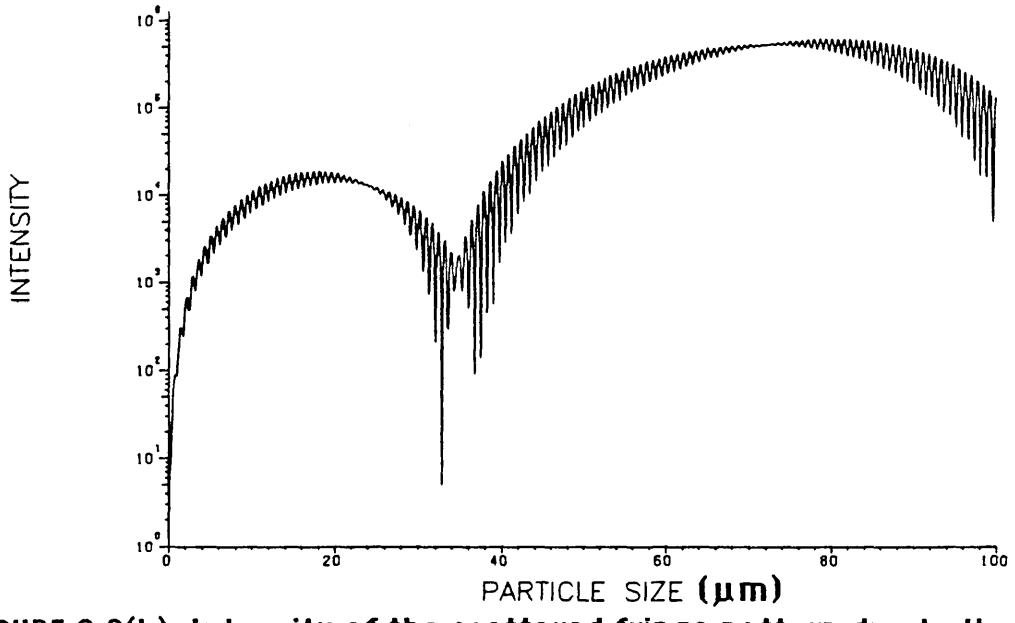


FIGURE 2.8(b) Intensity of the scattered fringe pattern due to the interference from refraction and surface reflection showing increased oscillations around the mean value due to the refraction only pattern when their relative amplitudes are similar.

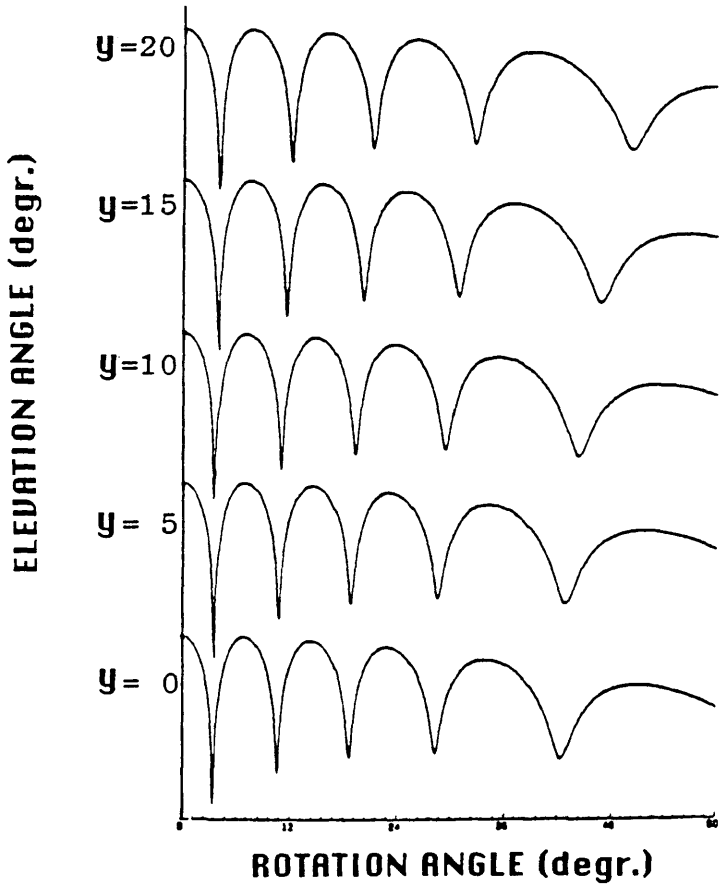


FIGURE 2.9 Refraction only interference fringe pattern scattered by a 40 μm glass bead located in the probe volume of a LDA system with beam intersection angle 10°.

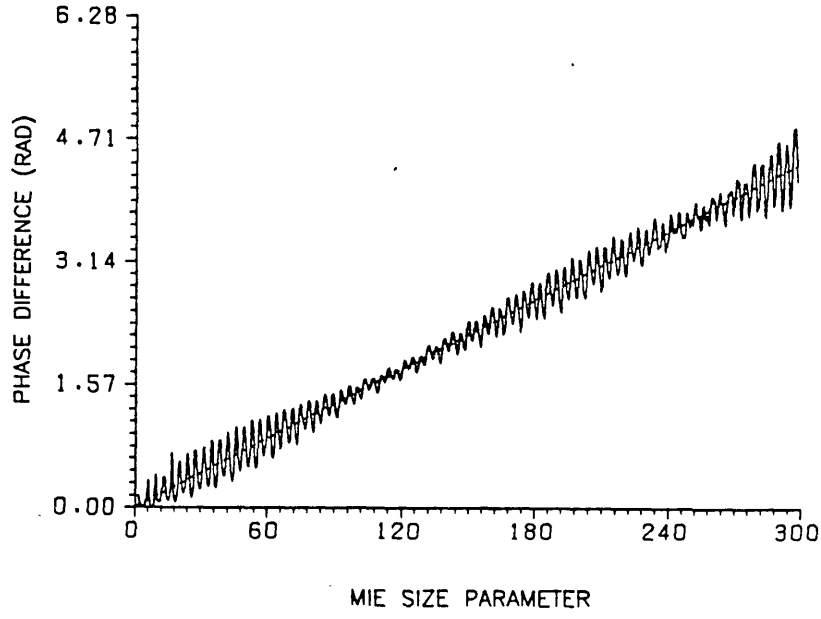


FIGURE 2.10(a) Oscillations in the calibration curve due to use of point apertures for a mean scatter angle of 30°. Solid line is full geometrical optics approximation and straight dashed line is the calibration curve due to refracted light only. Abscissa is Mie size parameter and ordinate is phase difference in radians.

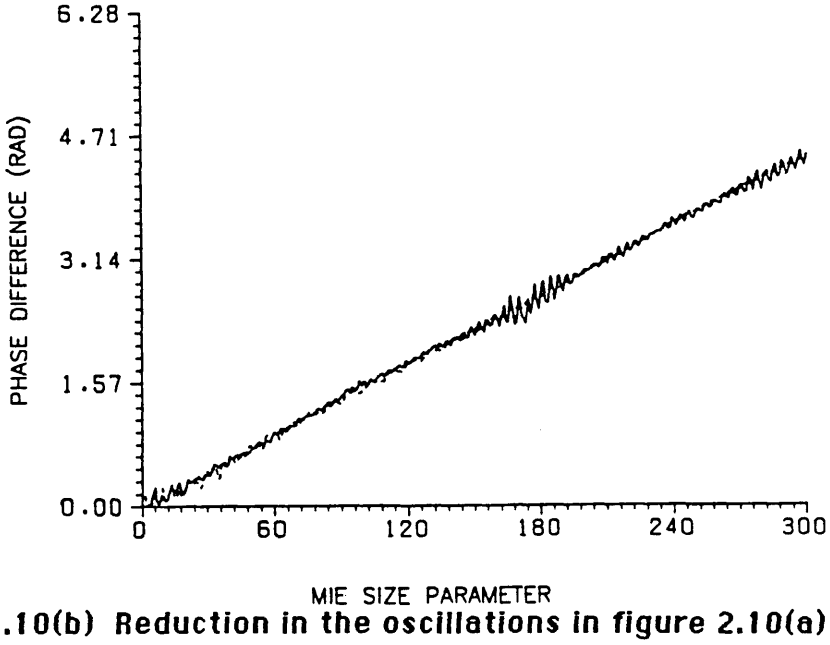


FIGURE 2.10(b) Reduction in the oscillations in figure 2.10(a) owing to inclusion of finite aperture size, 0.95° x 9.5°, in the calculations. Mie's solution is the solid curve and full geometrical optics approximation is the dashed line.

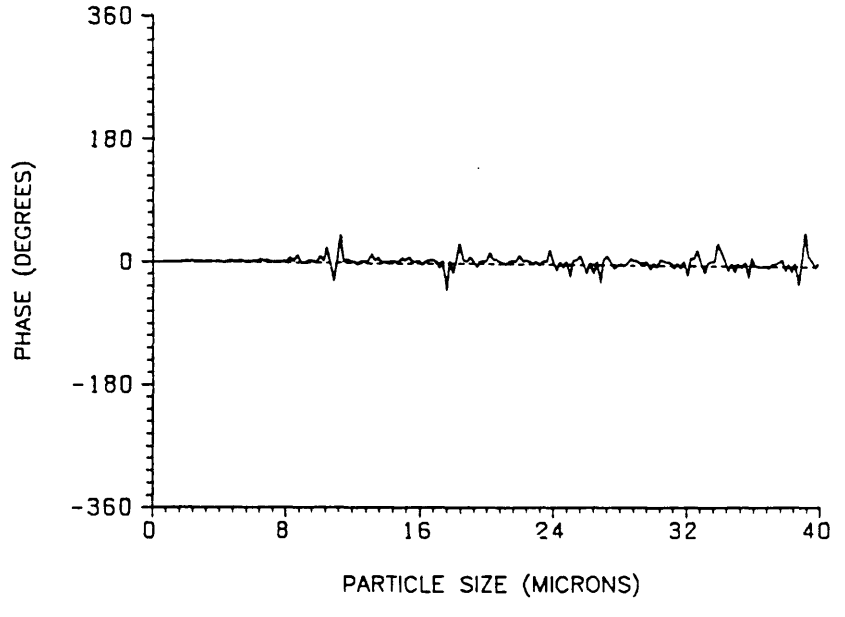


FIGURE 2.11 Variation of phase (degrees) with water droplet diameter (μm) at a mean scatter angle of 100° showing comparison between Mie's solution (solid line) and approximation based on surface reflected light only (dashed line).

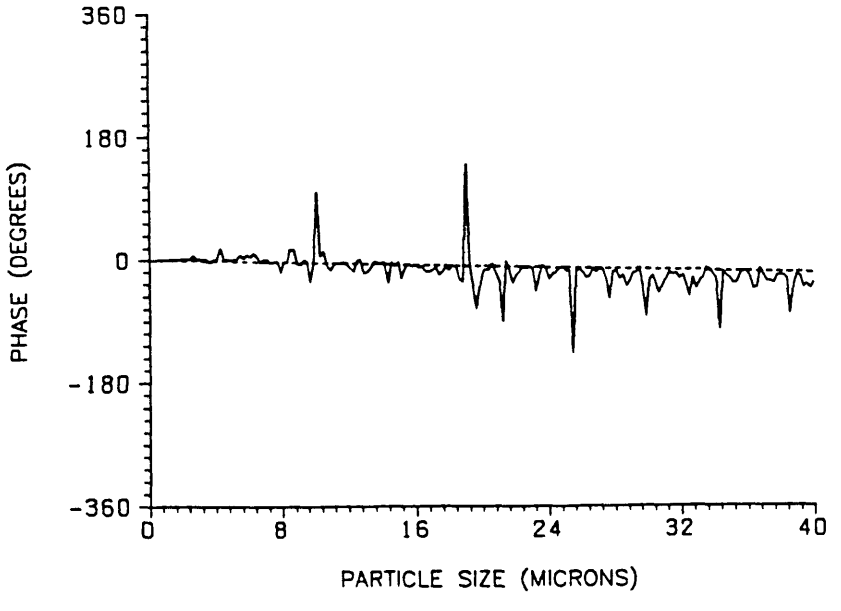


FIGURE 2.12 Variation of phase (degrees) with water droplet diameter (μm) in the second rainbow, mean scatter angle of 120°, showing comparison between Mie's solution (solid line) and approximation based on surface reflected light only (dashed line).

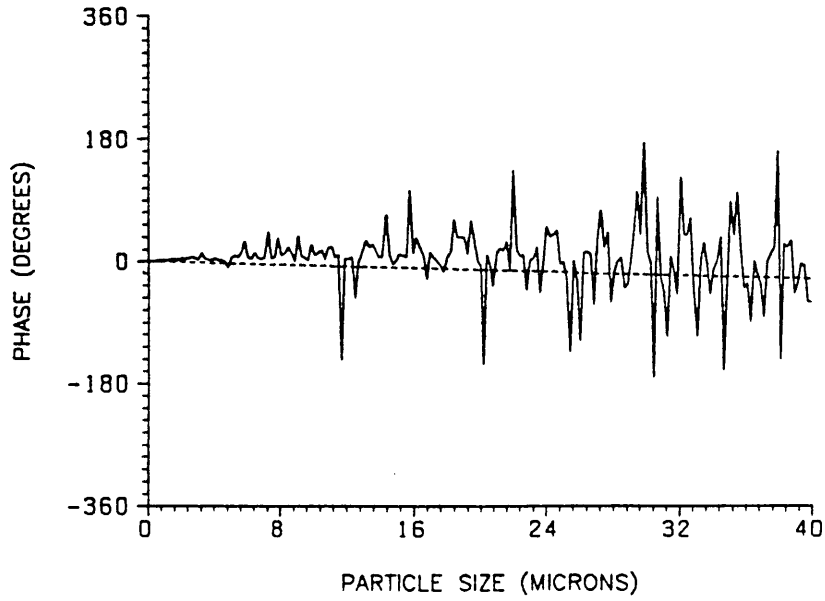


FIGURE 2.13 Variation of phase (degrees) with water droplet diameter (μm) between the second and the main rainbow angles, mean scatter angle of 133°, showing comparison between Mie's solution (solid line) and approximation based on surface reflected light only (dashed line).

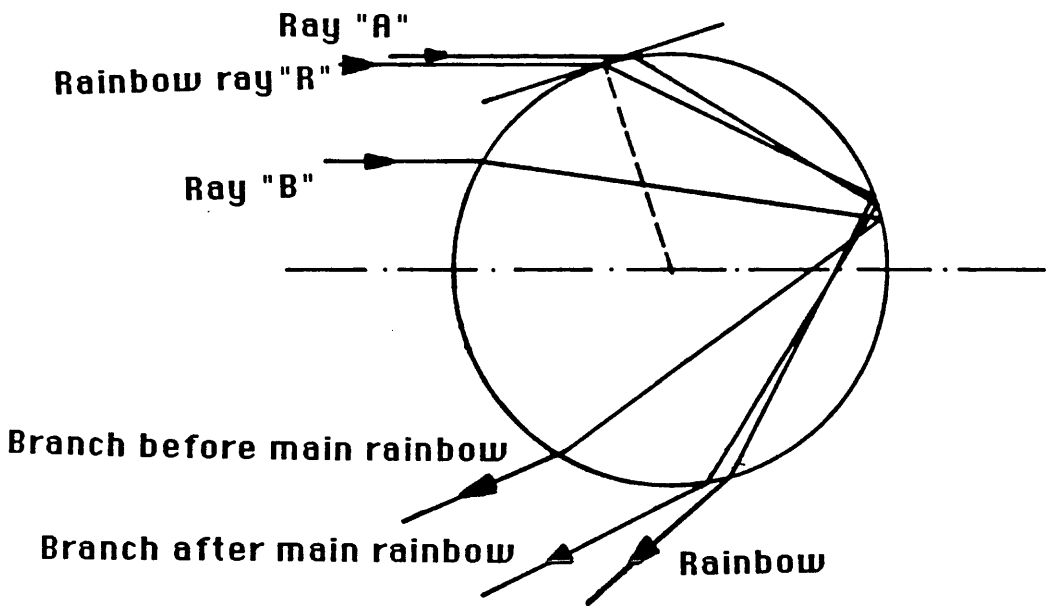


FIGURE 2.14 Ray optics of a transparent sphere showing the two branches of the first internal reflection. Ray 'R' is the rainbow ray, rays "A" after the ray 'R' give rise to the branch of first internal reflection after the rainbow and rays "B" before ray R give rise to the branch of first internal reflection before the main rainbow

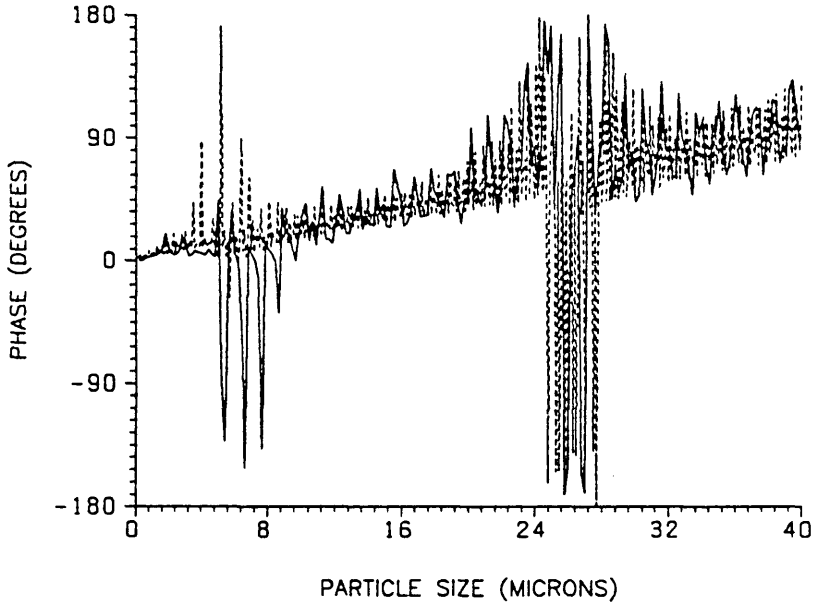


FIGURE 2.15(a) Variation of phase (degrees) with water droplet diameter (μm) within the main rainbow, mean scatter angle of 150°, showing comparison between Mie's solution (solid line) and geometrical optics approximation (dashed line).

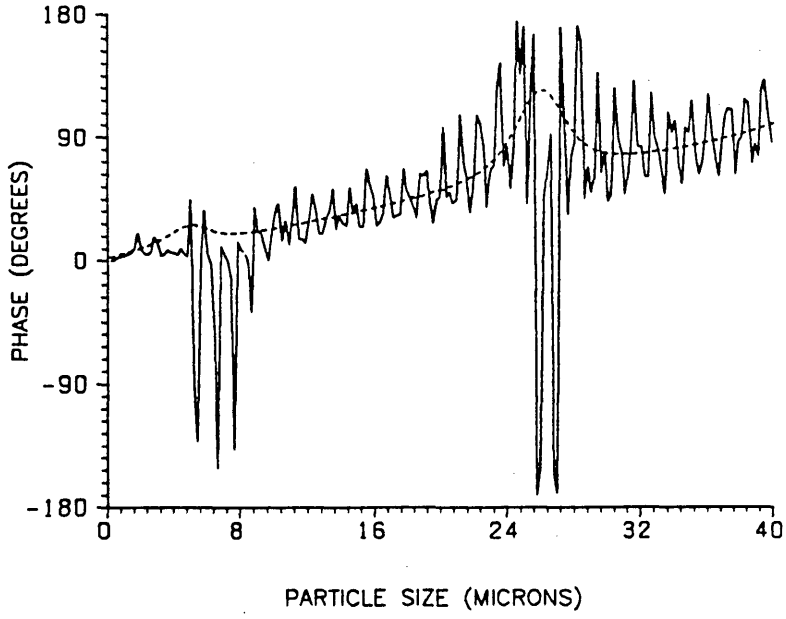


FIGURE 2.15(b) Comparison of Mie's solution (solid line) of figure 2.15(a) with approximation based on internally reflected light (dashed line).

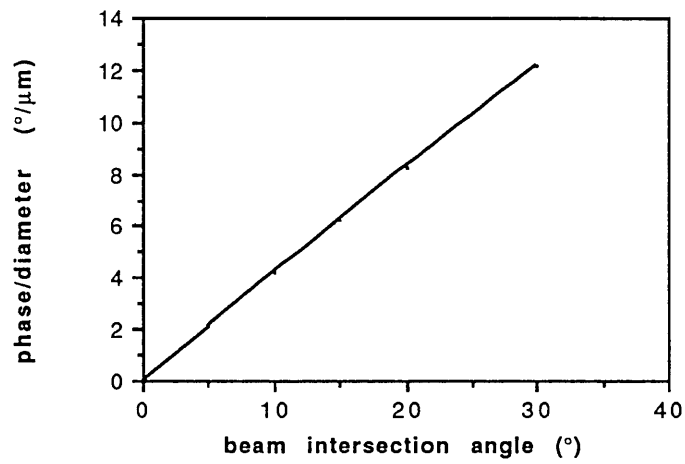


FIGURE 2.16 Effect of beam intersection angle on the size resolution of the phase-Doppler, expressed as the ratio of phase/particle diameter. The figure shows a linear dependence between size resolution and beam intersection angle up to 30 °; the detectors' locations were at elevation angle of 30° and rotation angles of 5.3° and 1°.

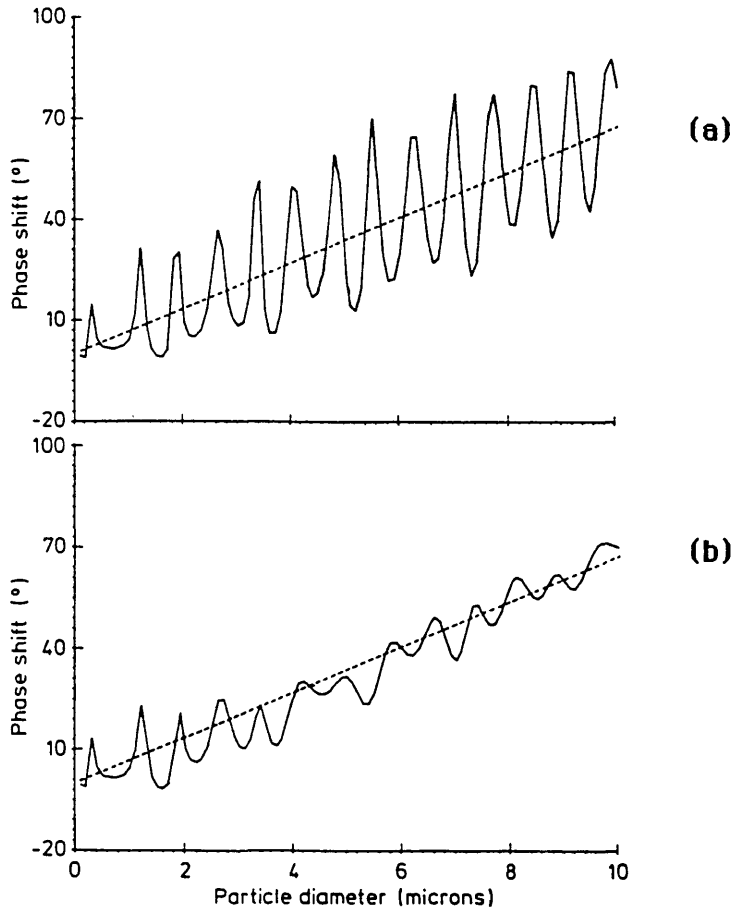


FIGURE 2.17 Calibration curve for variation of phase difference between Doppler signals observed at two points which are at an elevation angle of 30° and rotation angles of 8° and 1° with the diameter of spherical particles smaller than 10 μm with refractive index 1.5 for incident beams intersection angle 10°; (a) results for point aperture, (b) results for finite apertures with height of 9.5° and width 1.1°. Solid line is full geometrical optics approximation and dashed line is refraction only calculation.

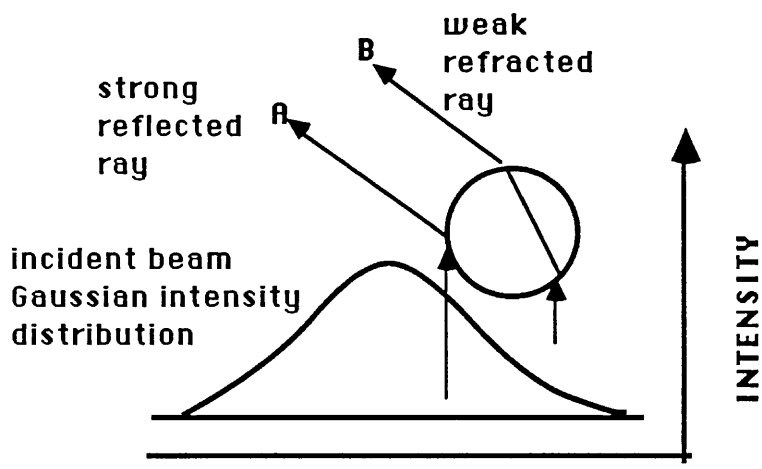


FIGURE 2.18 Sketch showing the effect of the Gaussian intensity distribution of the incident beams on the relative amplitude of the refracted and surface-reflected rays scattered by a sphere crossing at the edge of the LDA probe volume. Ray "A" due to surface reflection has larger amplitude than ray "B" due to refraction.

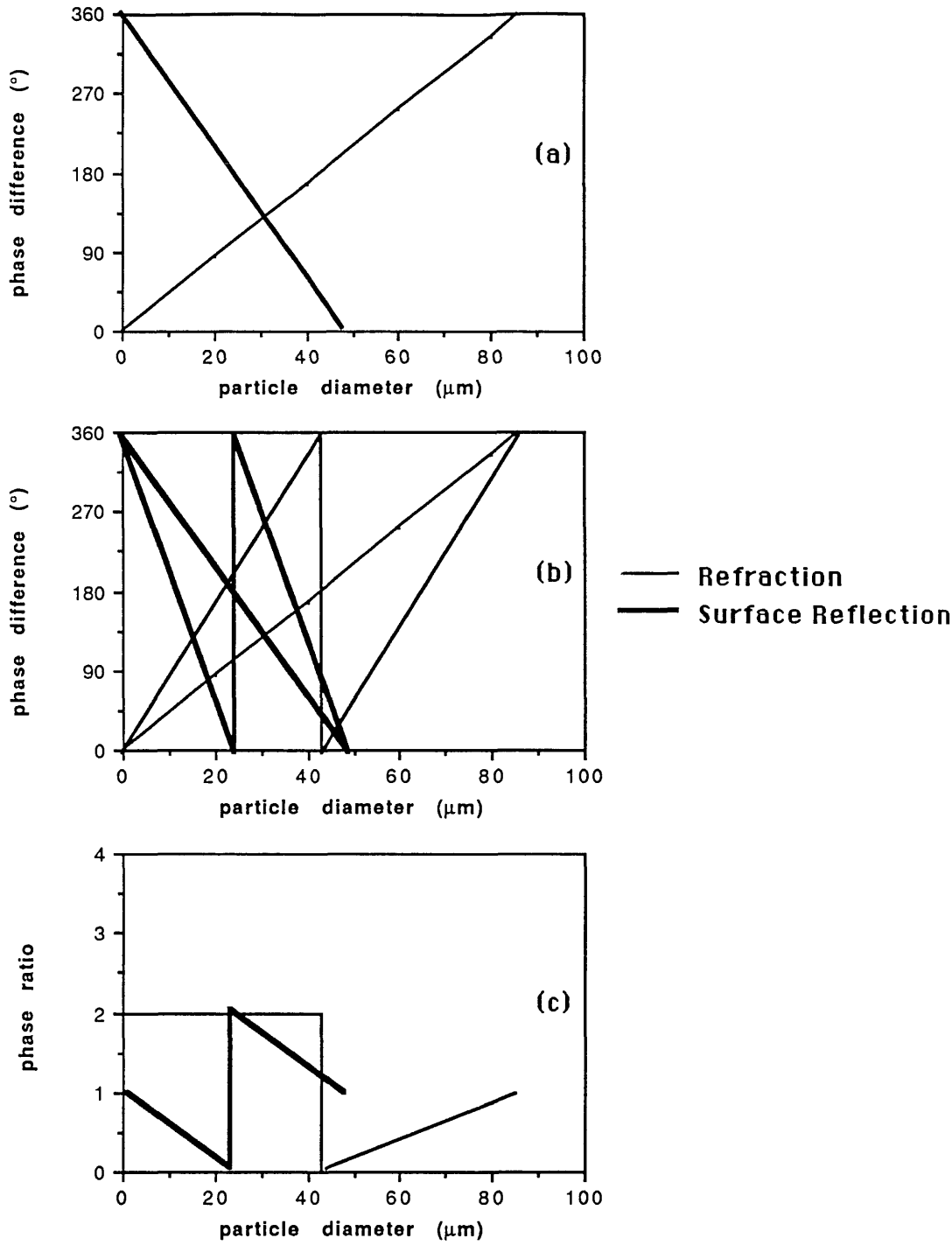


FIGURE 2.19 (a) Phase shift calibration curves due to refraction only and surface reflection only; (b) Two calibration curves with different size resolution by using three photodetectors; (c) Phase ratio, defined in equ. (2.34) as the phase of the steeper calibration curve to that of the shallower curve, from refrection only and surface reflection shows that the refraction phase ratio can be successfully discriminated from the surface reflection phase ratio.

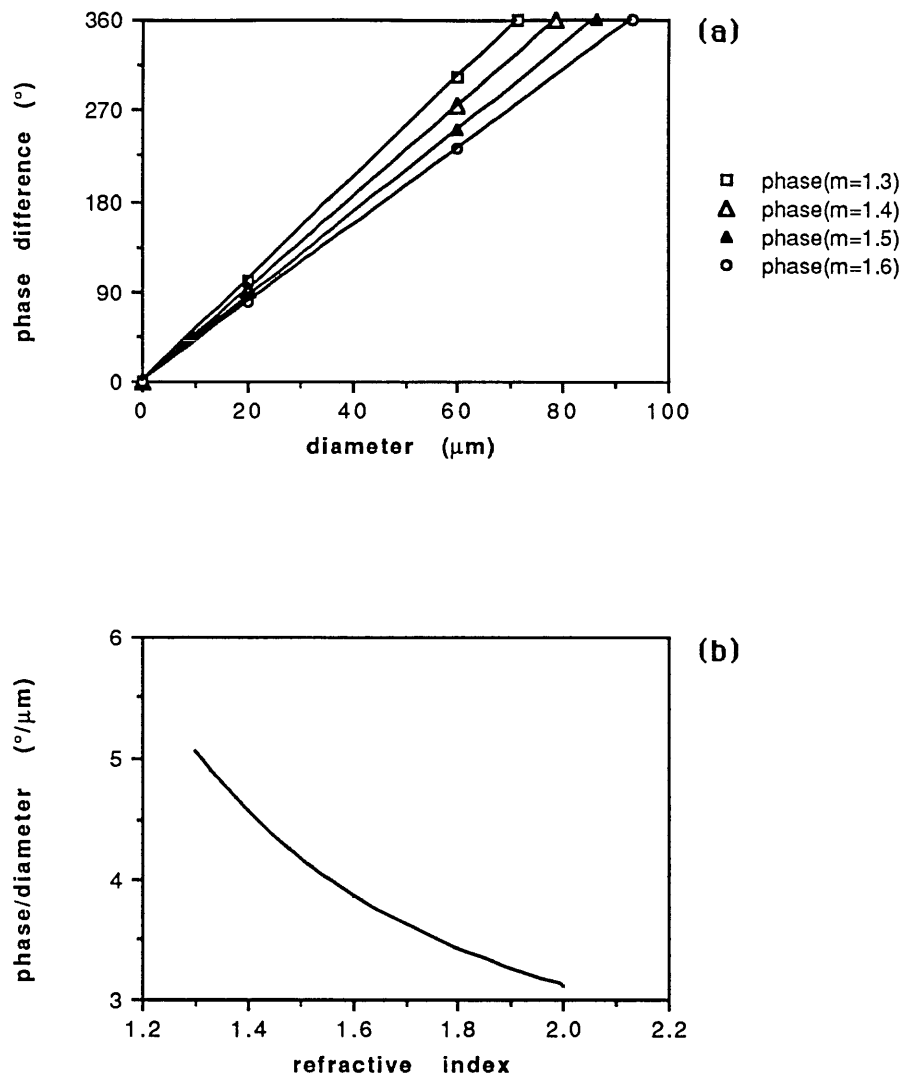


Figure 2.20 Effect of refractive index of non-absorbing spheres on the phase-Doppler calibration curve; (a) calibration curves for refractive indices 1.3 - 1.6, (b) variation of the phase-Doppler size resolution as a function of refractive index showing that decreases with refractive index increase. Size resolution is expressed as the ratio of phase/particle diameter. The beam intersection angle was 10°, the laser light wavelength 0.6328 μm and the detectors were located at elevation angle of 30° and rotation angles of 5.3° and 1°.

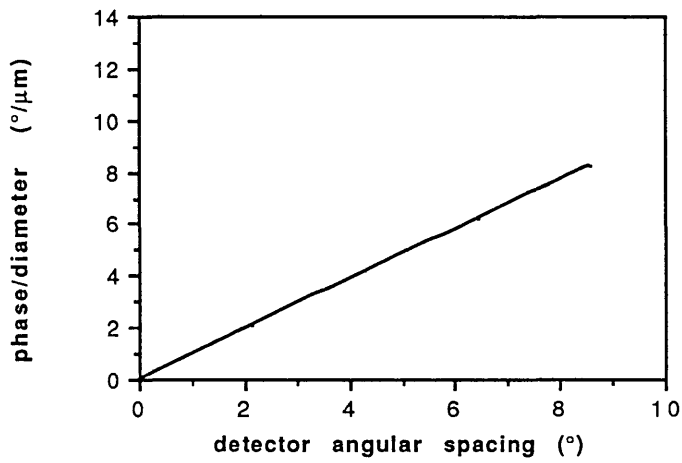


FIGURE 2.21 Effect of angular spacing of the detectors on the size resolution of the phase-Doppler, showing that increases linearly with angular spacing increase. Size resolution is expressed as the ratio of phase/particle diameter.

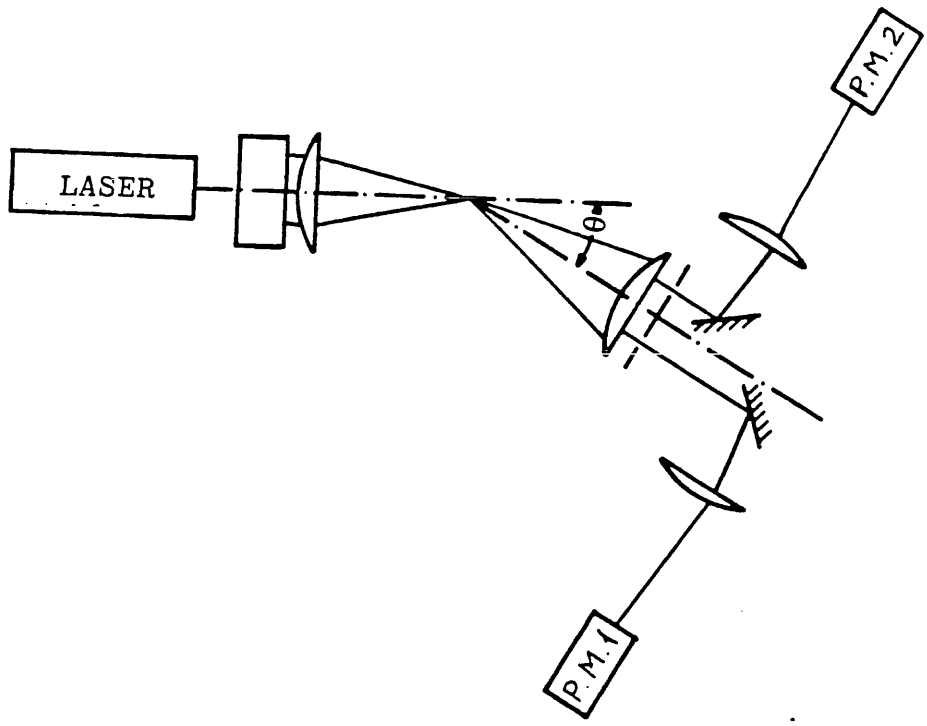


FIGURE 2.22 Experimental arrangement used for the verification of the theoretical calibration curve.

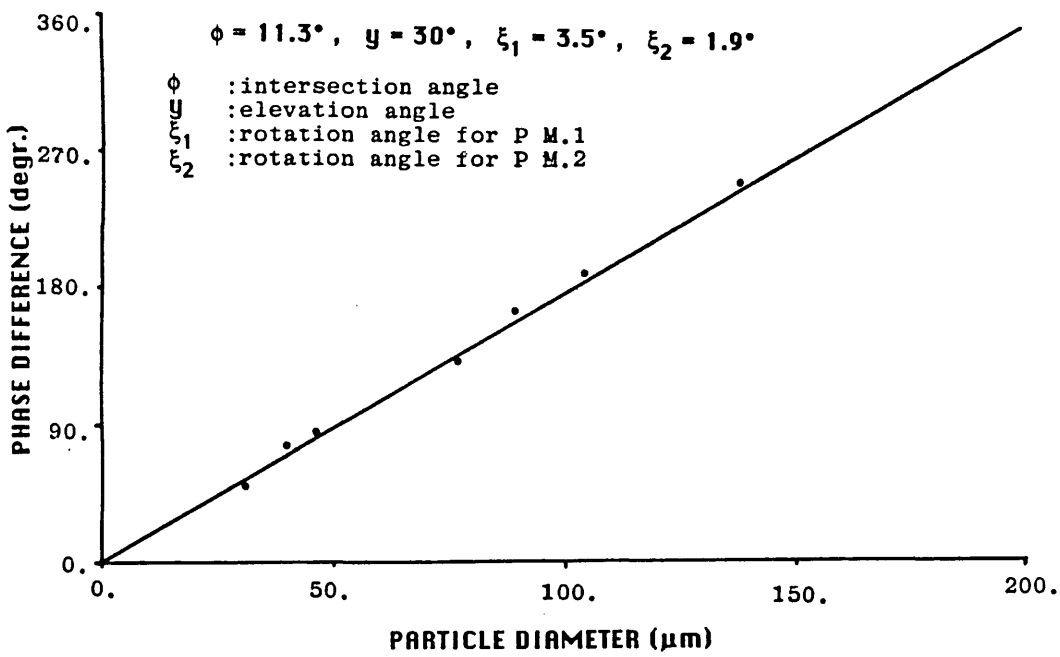


FIGURE 2.23 Comparison between experimental and theoretical results for beam intersection angle of 11.3° and observation locations of the detectors at elevation angle of 30° and rotation angles of 3.5° and 1.9°.

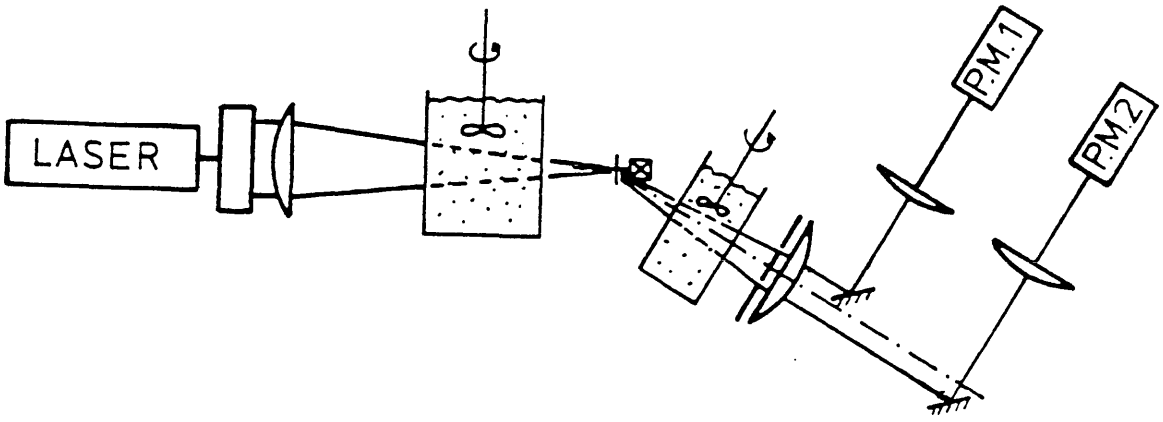


FIGURE 2.24 Experimental arrangement used for the depth of field experiment.

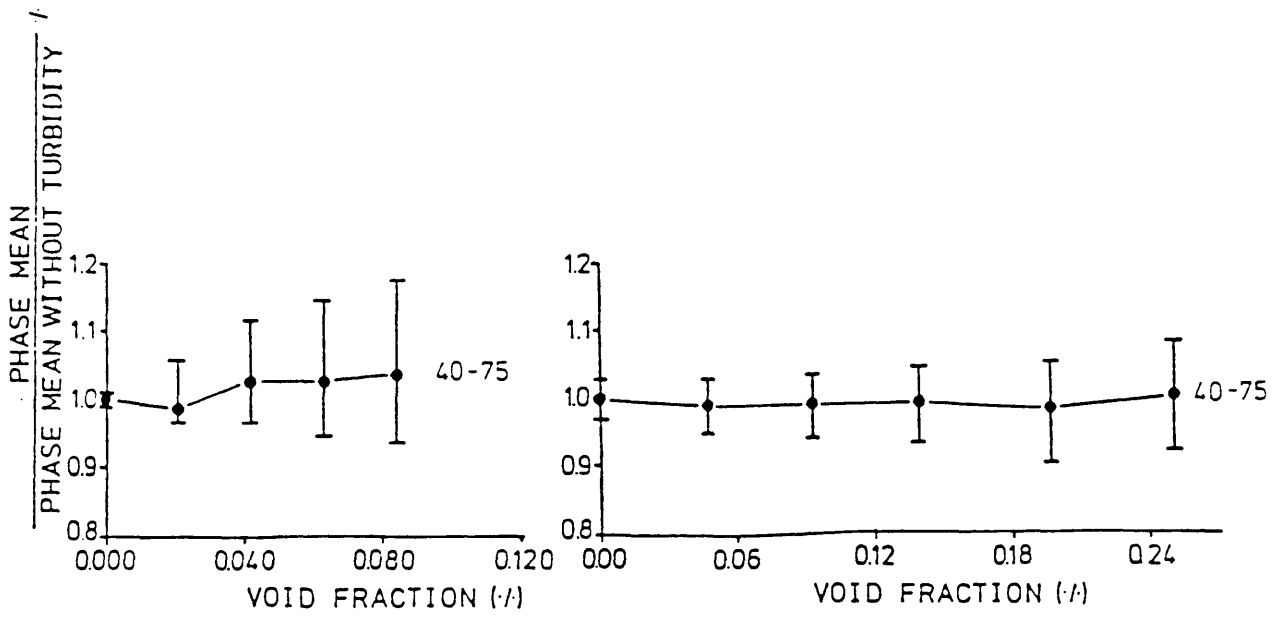


FIGURE 2.25(a) Phase as a function of void fraction. Interruption in (i) transmission, 14 cm depth of field, and (ii) reception, 5 cm depth of field, paths by 40-75 μm particles.

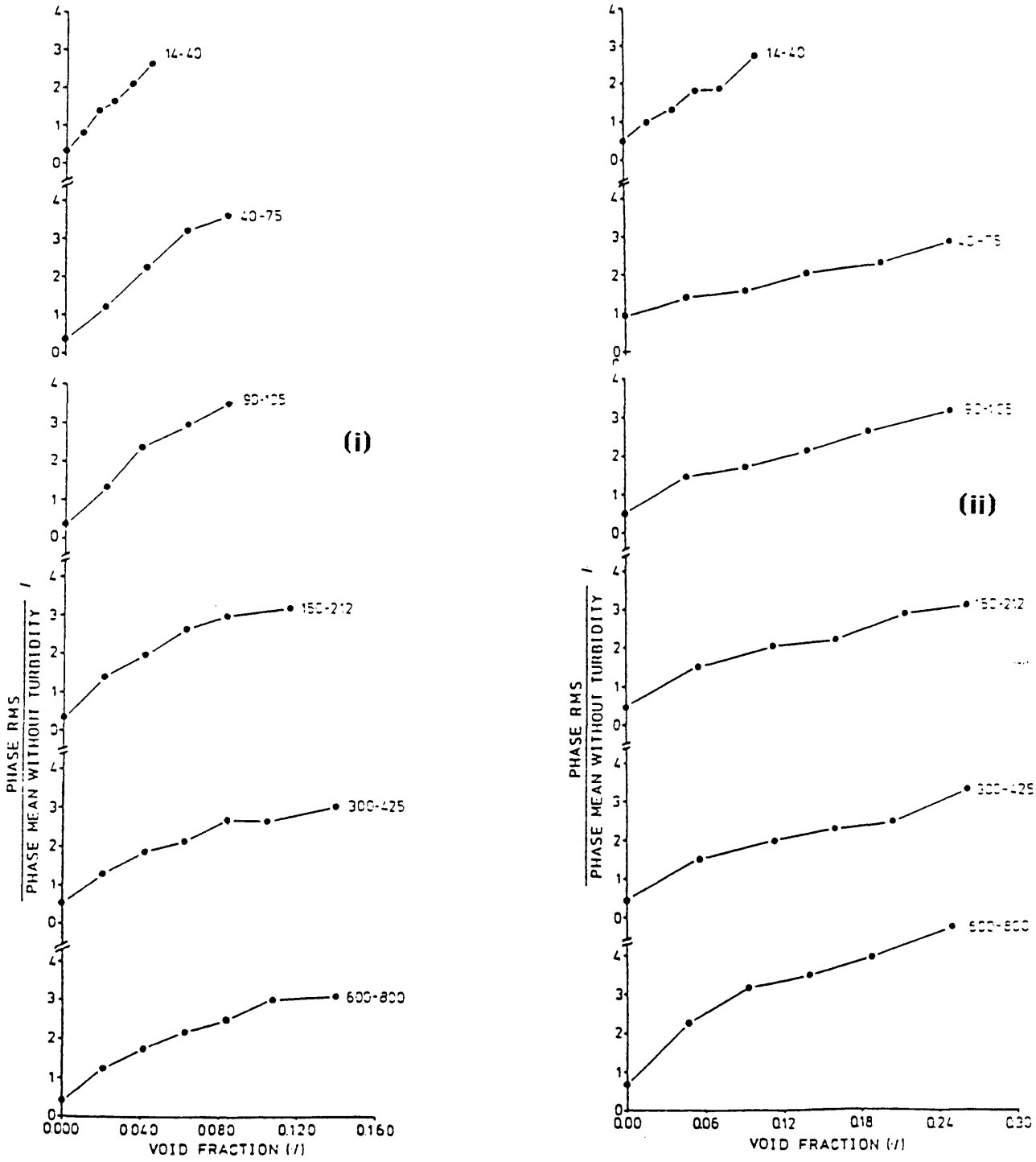


FIGURE 2.25(b) R.m.s. error as a function of void fraction. Interruption in (i) transmission, 14 cm depth of field, and (ii) reception, 5 cm depth of field, paths with interrupting particle diameter (μm) as parameter.

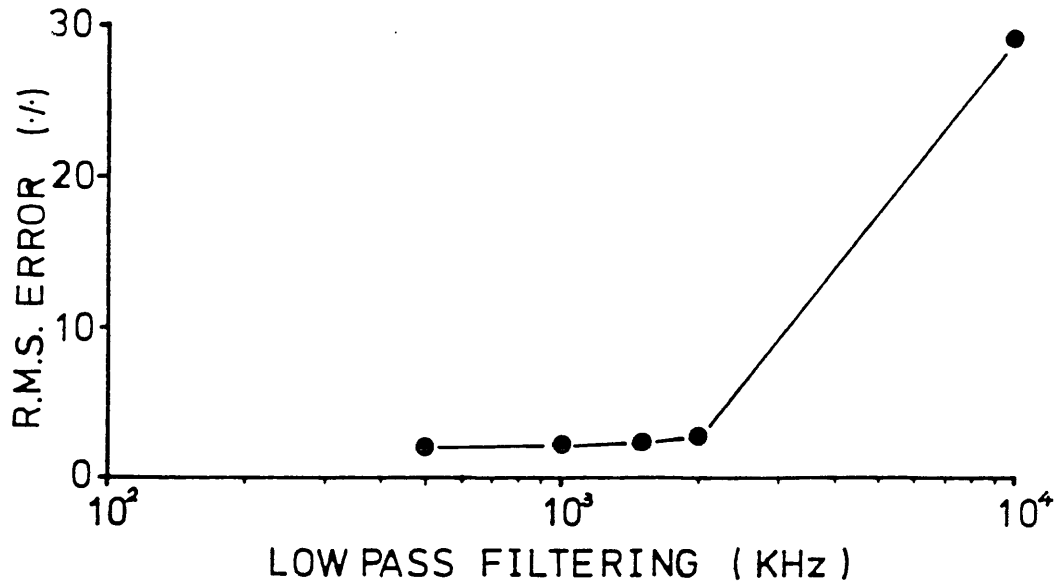


FIGURE 2.26 R.m.s. error as a function of filter settings, showing the effect of noise in the signal on the phase measurement. Interruption in transmission path (14 cm depth of field) by 14-40 μm particles at 0.05% void fraction.

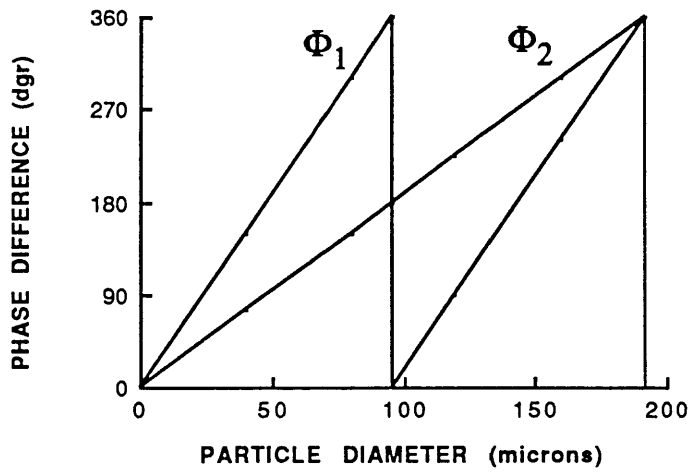


FIGURE 2.27(a) Calibration curve of phase-Doppler for droplets with refractive index of 1.5 used for the accelerating nozzle experiment. Φ_2 is curve for phase between central and an outer detector and Φ_1 is curve for the phase between outer detectors.

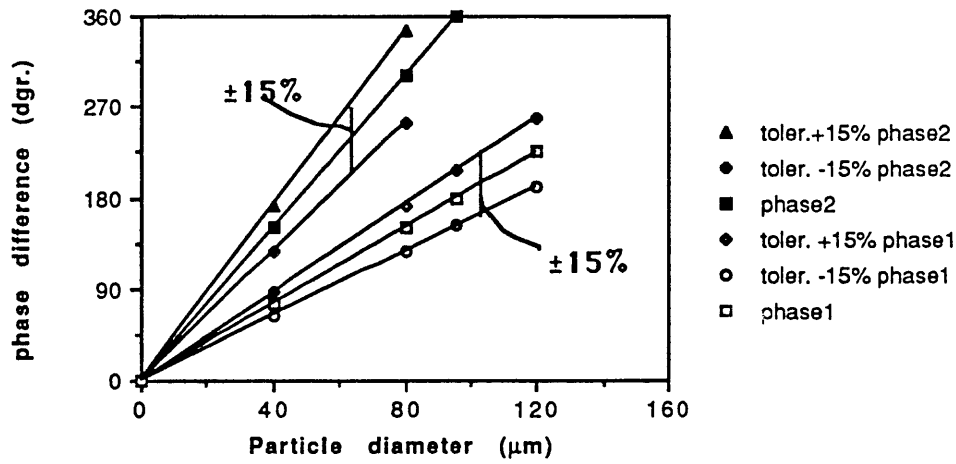


FIGURE 2.27(b) Tolerance of ±15% of the phase shift value applied on the calibration curve of the system.

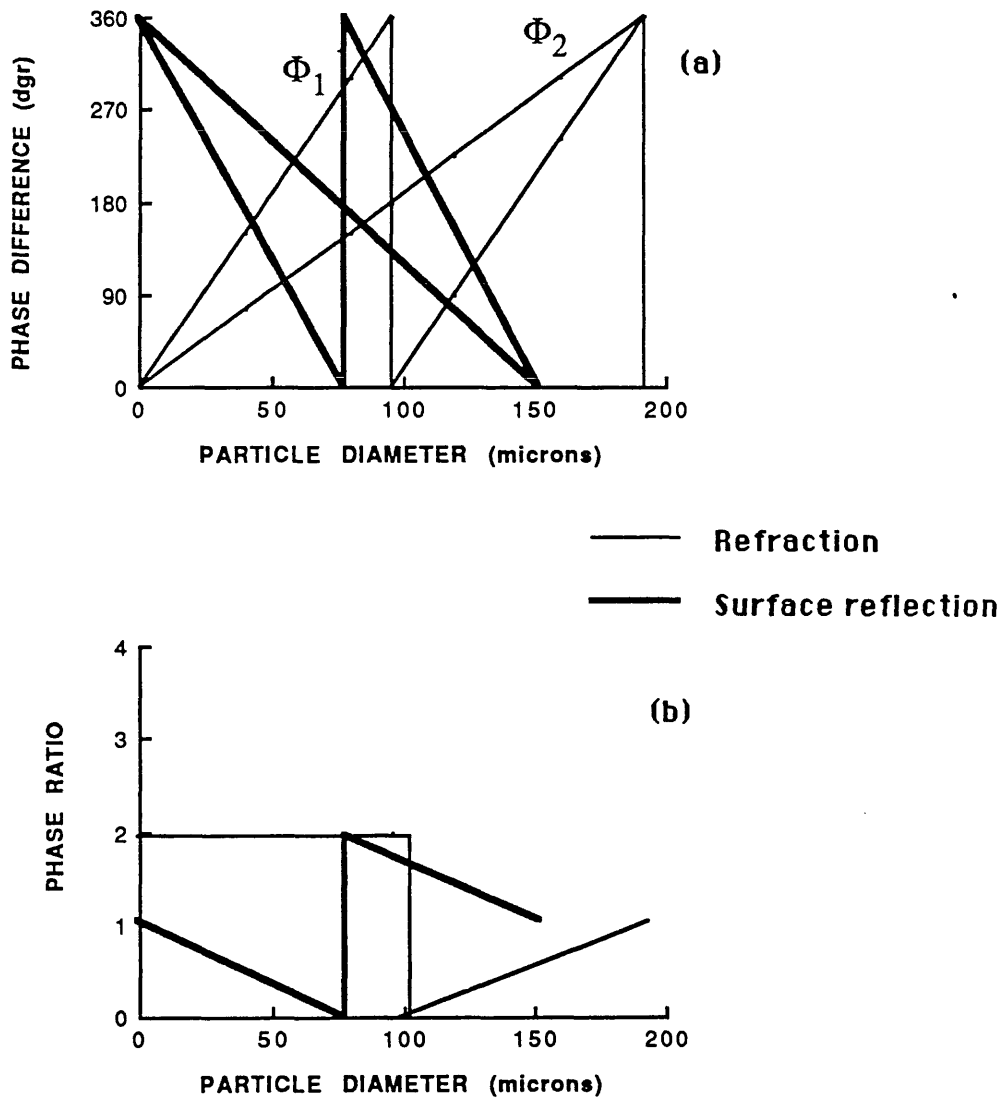


FIGURE 2.28 (a) Refraction only and surface reflection only calibration curves for accelerating nozzle experiment with two size resolution levels. (b) Phase ratio for refraction and surface reflection curves as a function of particle diameter showing that the expected ratio due to surface reflection for a 40 μm bead is around 0.5 and due to refraction is 2.

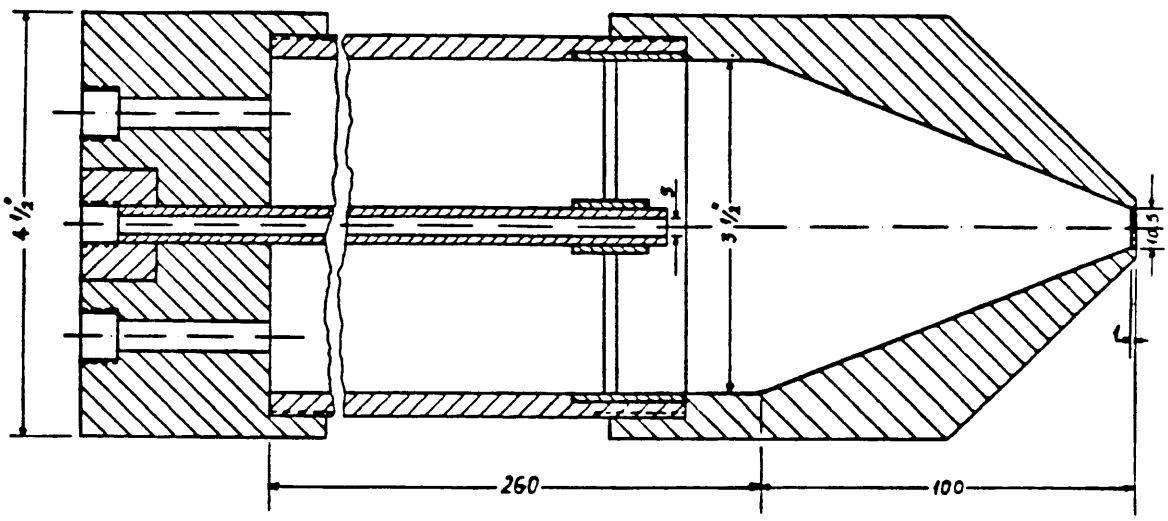


FIGURE 2.29 Cross-section of converging nozzle used to produce acceleration of beads as a function of aerodynamic diameter.

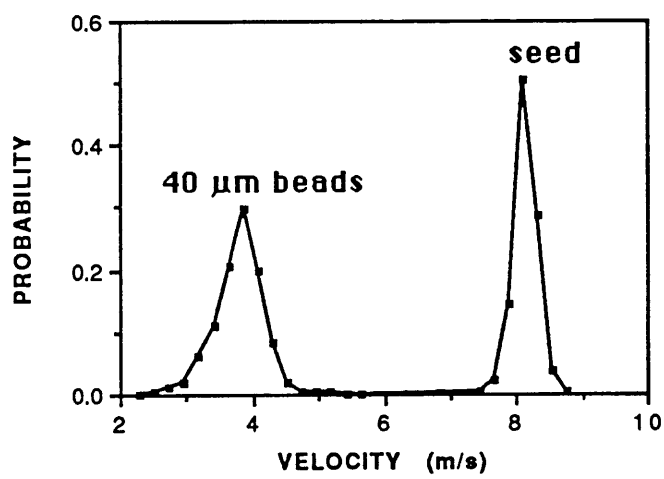


FIGURE 2.30 Velocity probability distributions of gas phase and of nominally 40 µm diameter beads at the exit of the accelerating nozzle, showing separation due to acceleration.

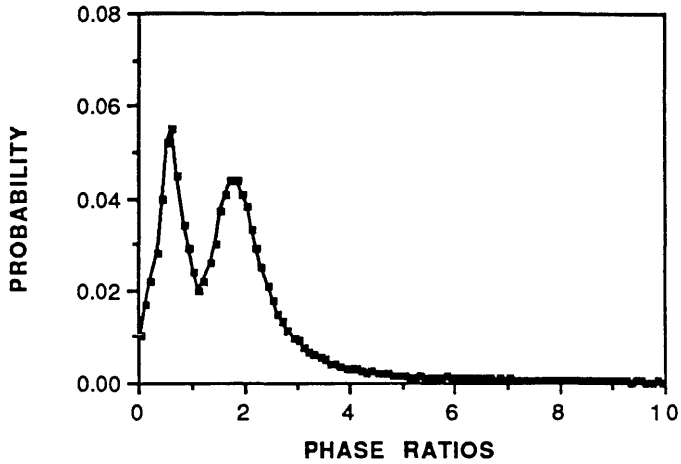


FIGURE 2.31(a) Probability distribution of ratio of phases measured on channels Φ_1 and Φ_2 (figure 2.27) for laser power of 300 mW showing two peaks one at 0.5 which is due to surface reflection measurements and one at 2. which is the expected value due to refraction phase shift.

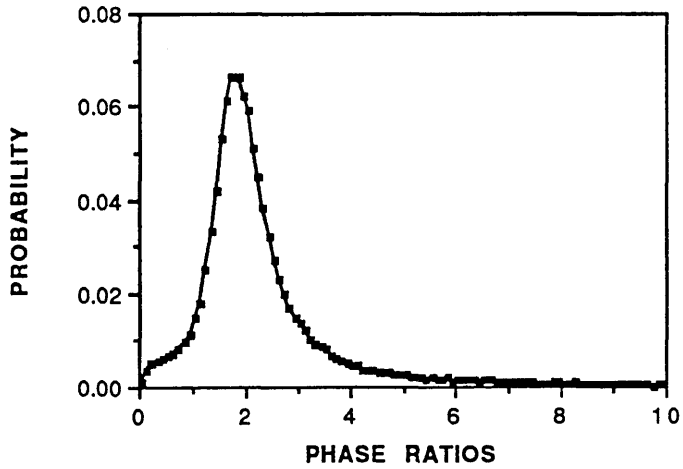


FIGURE 2.31(b) Probability distribution of ratio of phases of figure 2.31(a) after phase validation showing only one peak near the expected value of 2.

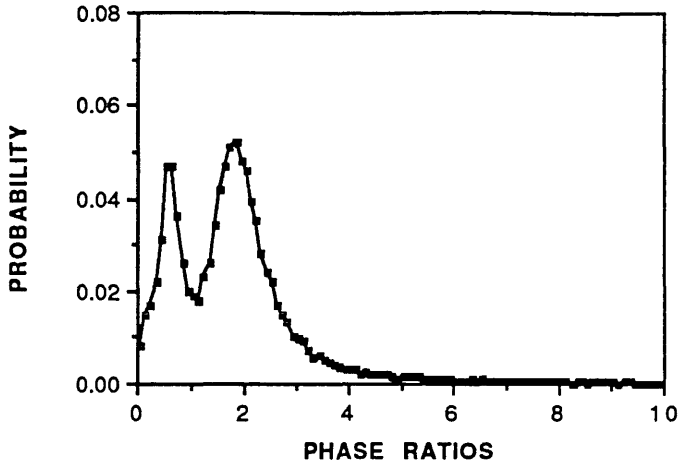


FIGURE 2.32 Probability distribution of ratio of phases measured on channels Φ_1 and Φ_2 (figure 2.27) before phase validation for laser power of 60 mW showing smaller peak at 0.5 than in figure 2.31(a).

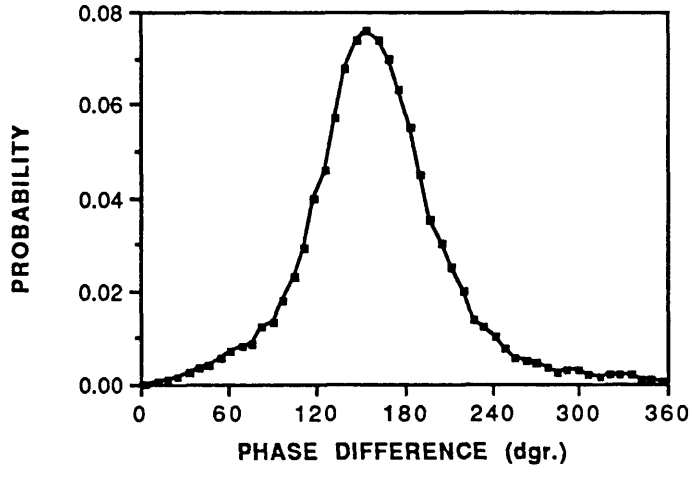


FIGURE 2.33 Phase distribution of nominally 40 μm diameter bead measured on channel Φ_1 (figure 2.27) by the prototype counter 150° ± 10 μm.

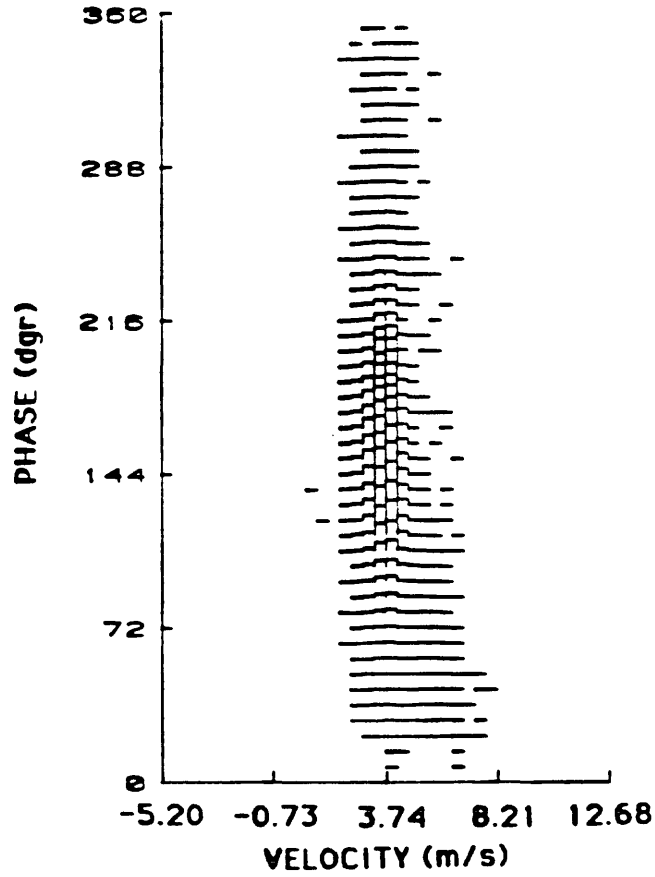


FIGURE 2.34 Simultaneous measurements of phase and velocity of nominally 40 µm diameter beads at the exit of the converging nozzle.

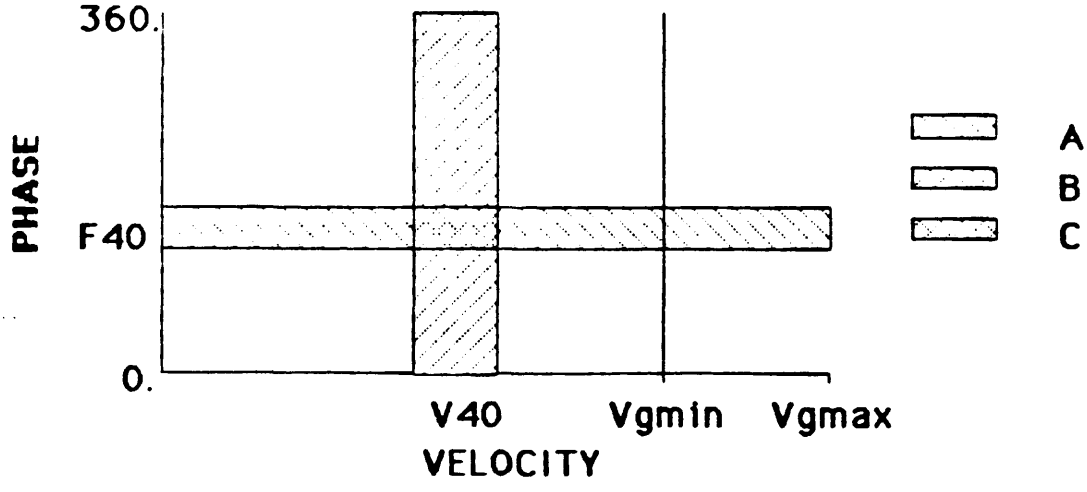


FIGURE 2.35 Graphical definitions of terms: area "A" 40 µm phase window; area "B" 40 µm velocity-window; F40 signifies the phase corresponding to 40 µm; V40 is the velocity-window corresponding to 40 µm, taken from figure 2.30; and Vgmin and Vgmax are the minimum and maximum velocities of the gaseous phase, also taken from figure 2.30.

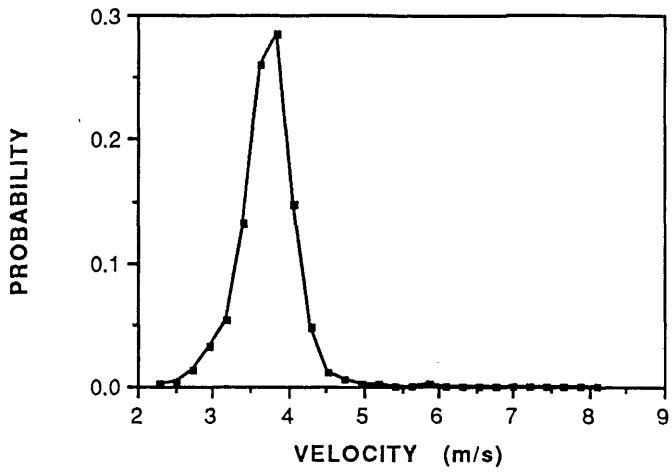


FIGURE 2.36 Velocity probability distribution of signals in 40 μm velocity window, area "A" of figure 2.35, showing small cross-talk from other diameters.

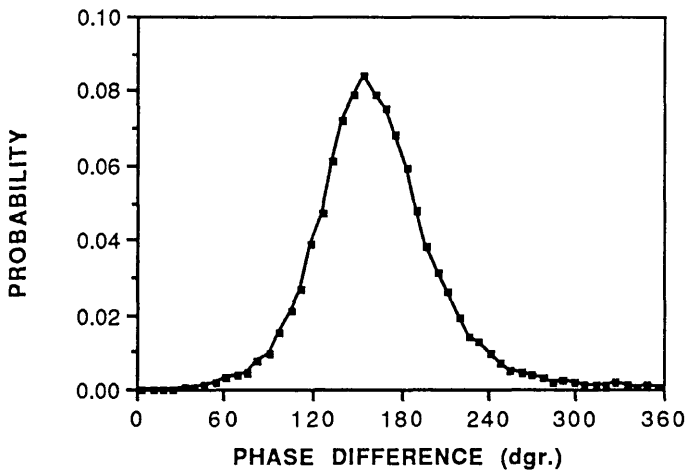


FIGURE 2.37 Phase probability distribution of signals in the 40 μm velocity window, area "B" of figure 2.35, showing optical cross-talk into size ranges outside the 130° - 170° phase-window.

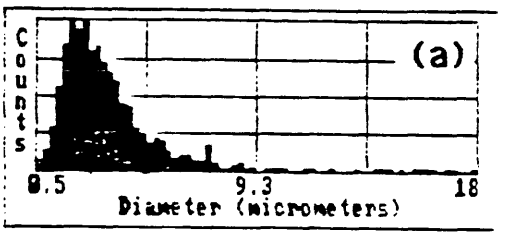


FIGURE 2.38(a) Size distributions of atomised mineral oil seed measured by Aerometrics instrument.

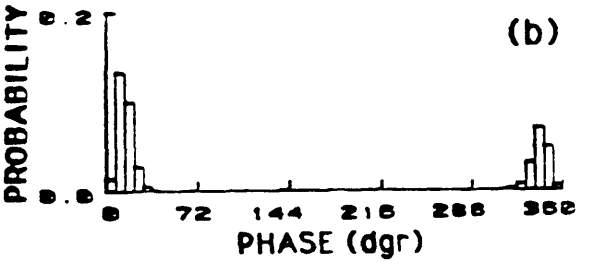


FIGURE 2.38(b) Phase distributions of atomised mineral oil seed measured by the prototype counter : 40° ≈ 10 µm.

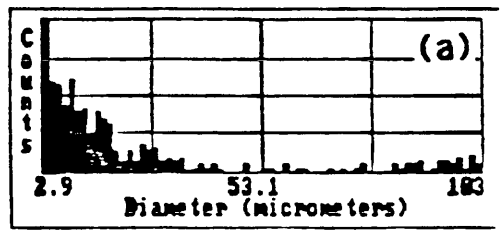


FIGURE 2.39(a) Size distributions of kaolin powder seed measured by Aerometrics instrument.

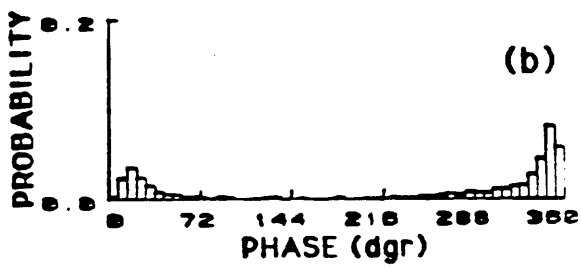


FIGURE 2.39(b) Phase distributions of kaolin powder seed measured by the prototype counter : 40° ≈ 10 µm.

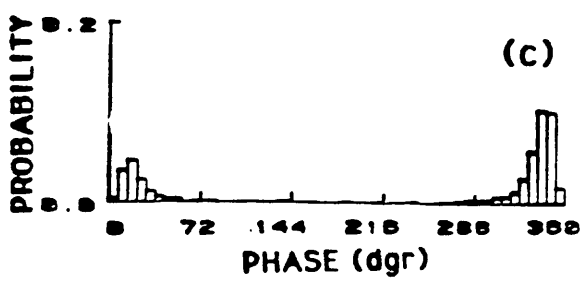


FIGURE 2.39(c) Phase distributions of titanium dioxide powder seed measured by the prototype counter : 40° ≈ 10 µm.

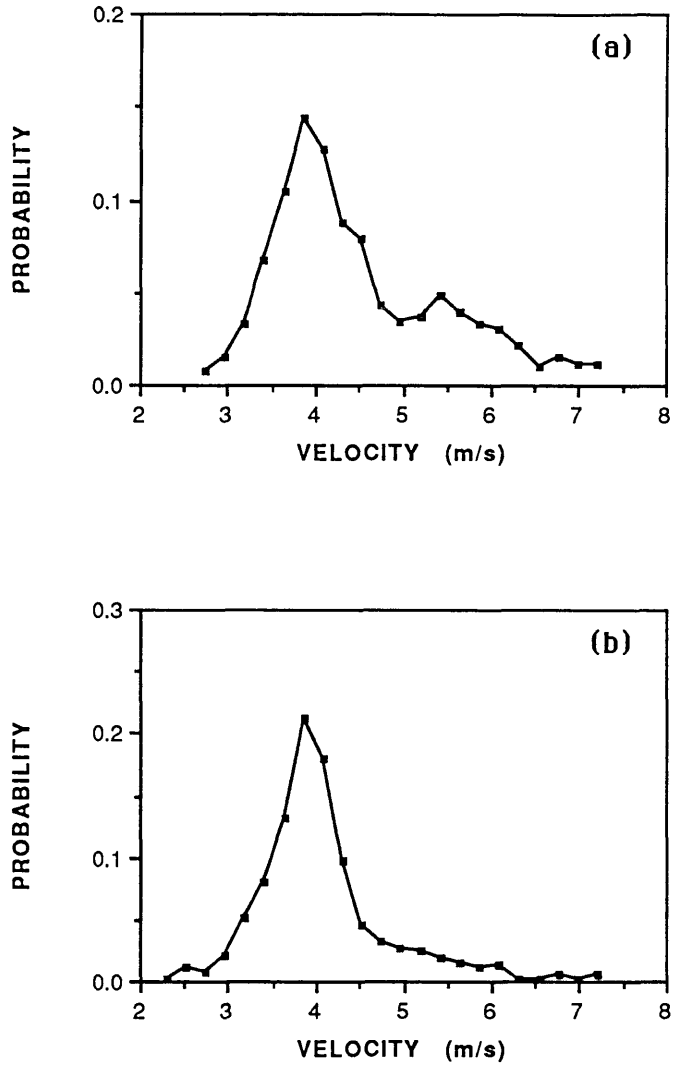


FIGURE 2.40 Velocity probability distribution of signals with both phase in the seed window and velocity less than Vgmin, showing cross-talk from beads; (a) the laser power was 300 mW and in (b) it was 60 mW.

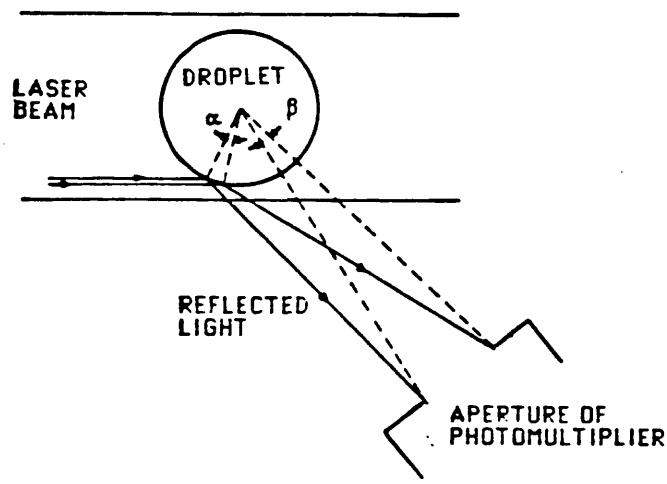


FIGURE 2.41 Schematic of a droplet in a laser beam showing the angular width of droplet α which reflects light into the aperture of a photomultiplier of angular width β. Scales have been exaggerated for clarity.

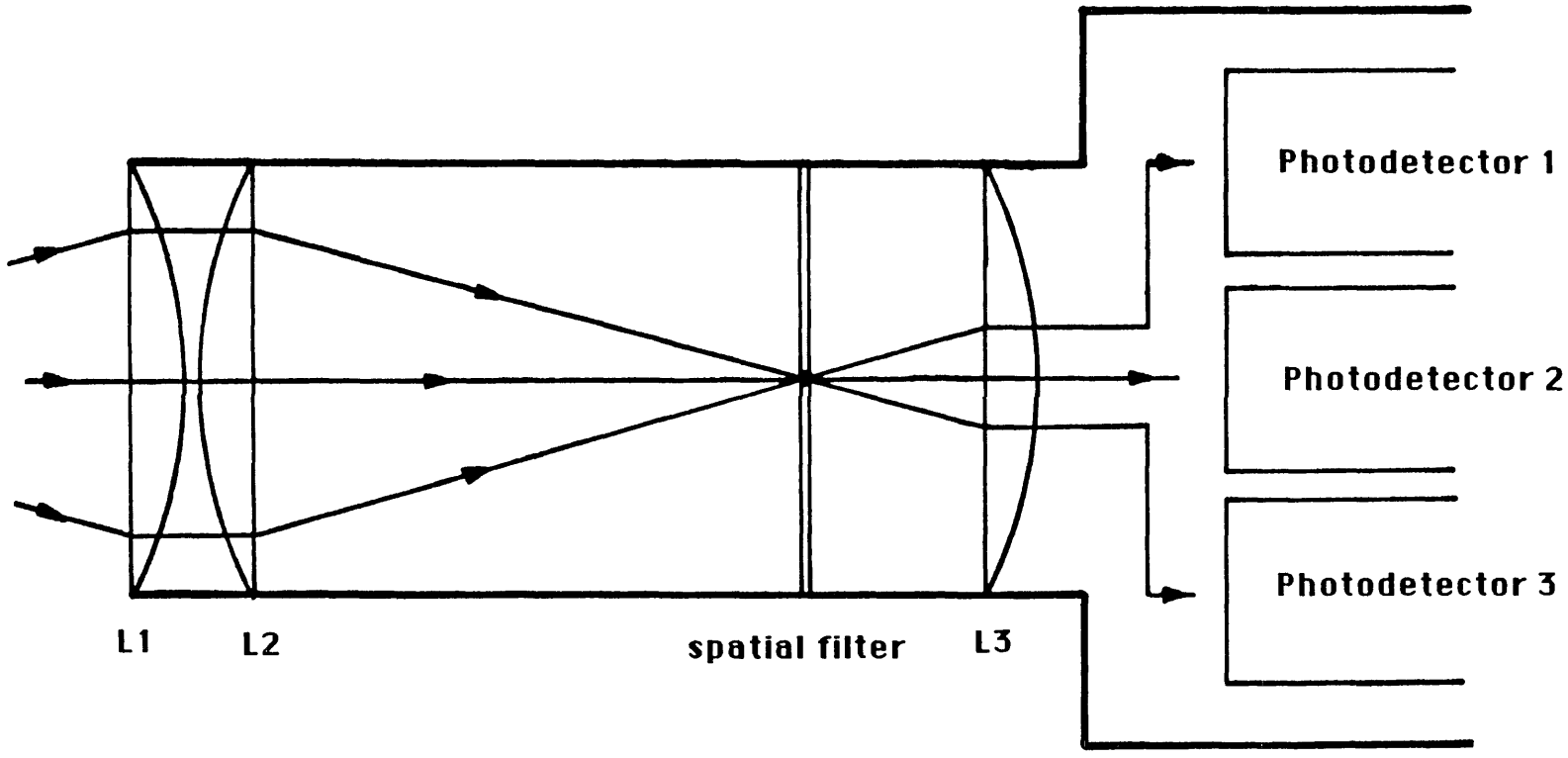


FIGURE 2.42 Sketch showing the geometry of the receiving optics

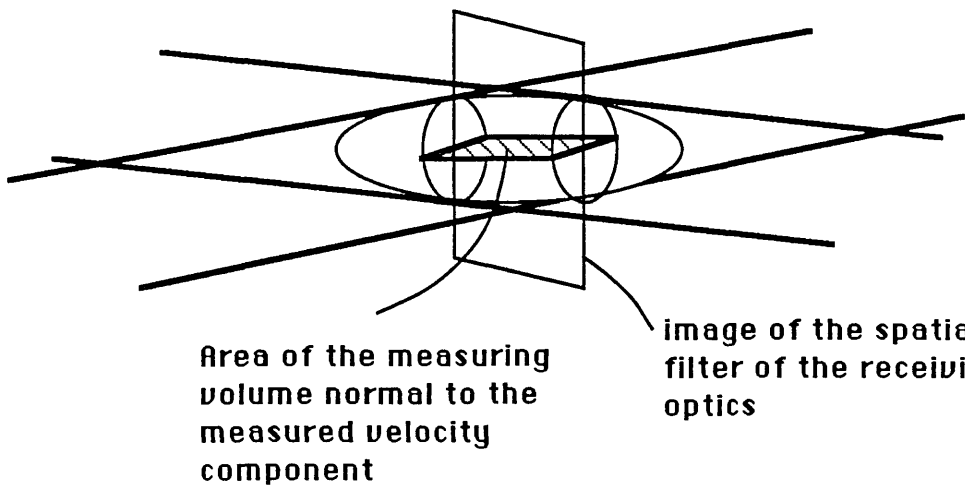


FIGURE 2.43 Sketch of the probe volume of the phase-Doppler showing the image of the spatial filter of the receiving optics; its width limits the length of the probe volume and determines the area of the measuring volume.

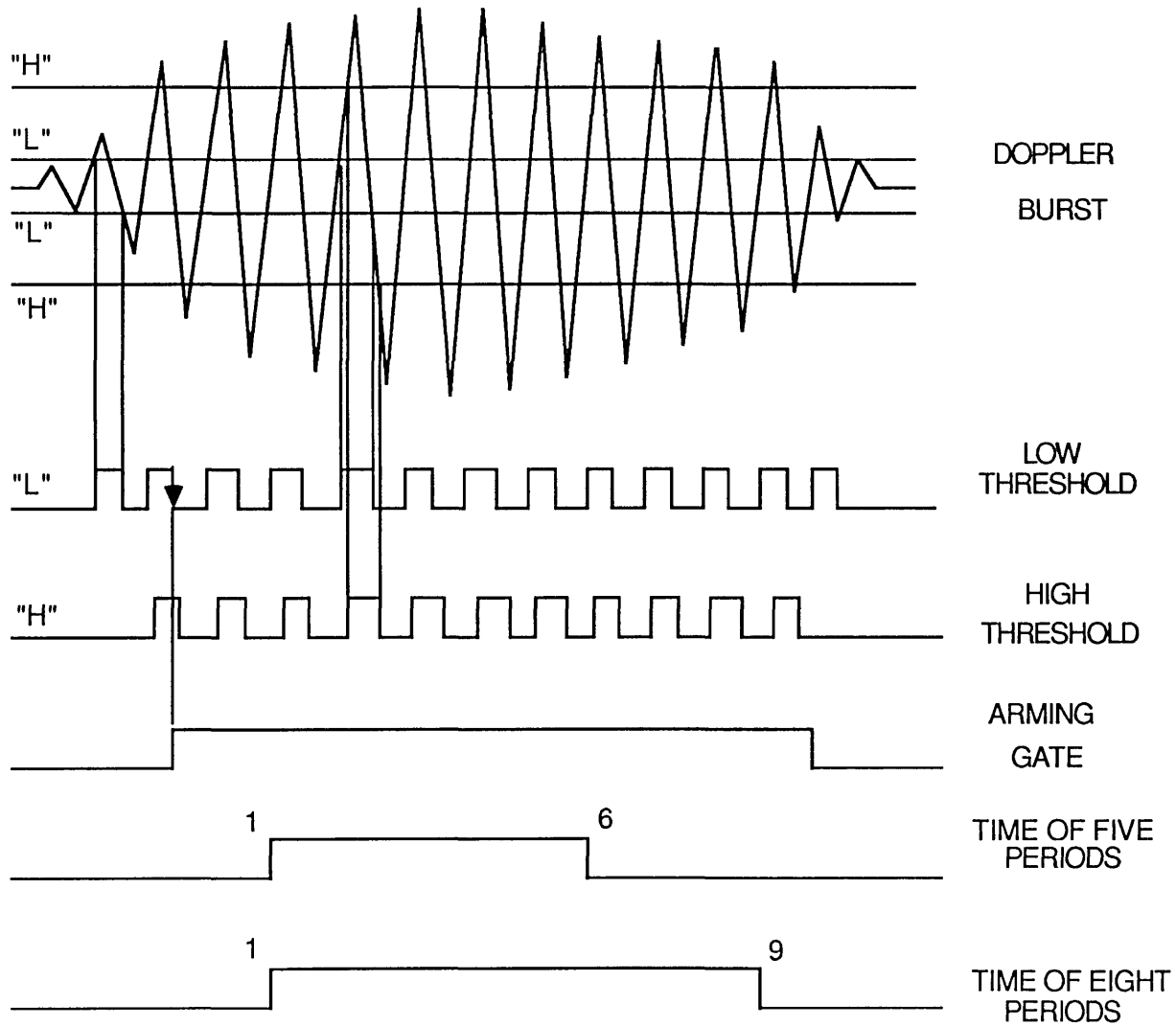


FIGURE 2.44 Amplitude and frequency validation timing diagram.

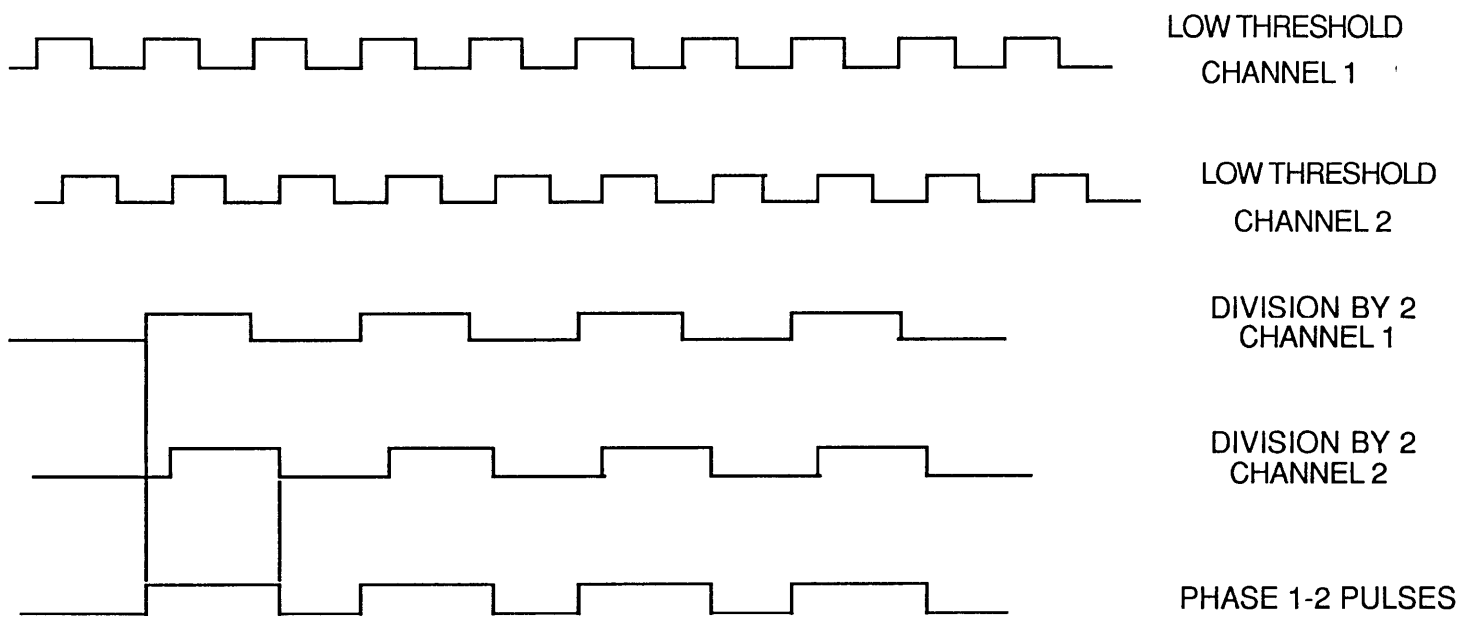


FIGURE 2.45 Phase measurement 1-2 timing diagram. The low threshold pulses of the channels are generated only if the sequence between the high and low threshold of the amplitude validation of figure 2.44 is correct.

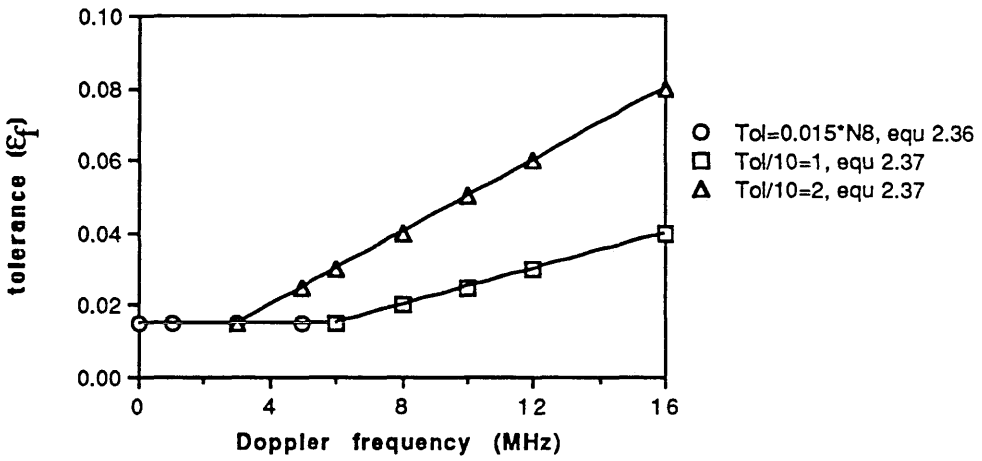


FIGURE 2.46 Percentage of number of 500 MHz clock pulses of 8 Doppler periods tolerance ε_f used for the frequency validation as a function of the Doppler frequency. Constant (0.015) tolerance (circles) and variable tolerance such that the difference between the number of clock pulses of the Doppler period based on the measurement of eight periods and that of five periods is 1 (square) or 2 (triangle).

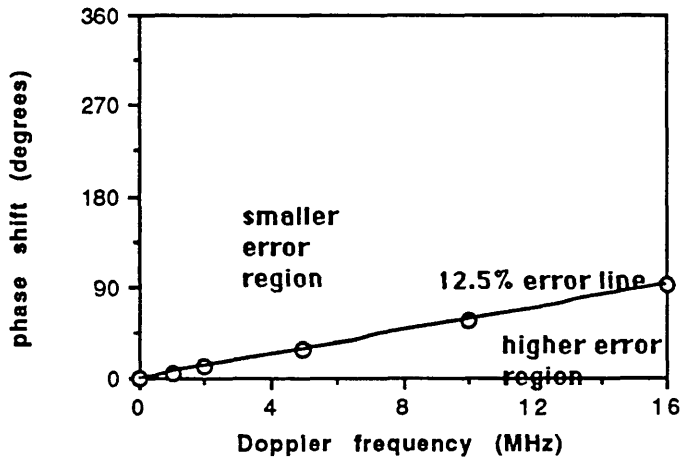


FIGURE 2.47 Phase error due to the uncertainty of 1 pulse of a 500 MHz clock as a function of the phase and the Doppler frequency. Figure shows the 12.5% of the real phase shift error line. At the region above this line the error is lower.

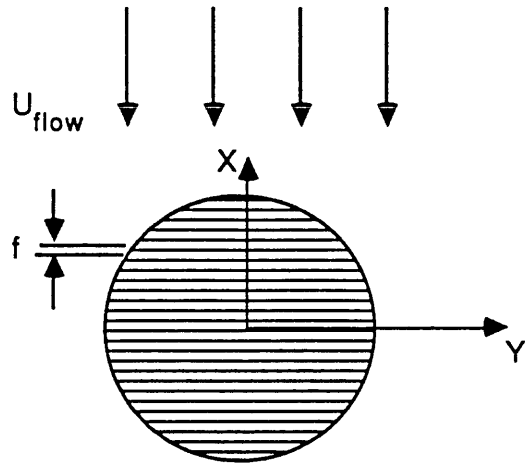


FIGURE 2.48 Cross section of the probe volume of the phase-Doppler anemometer showing the fringes, which can be used to provide a length scale in the probe volume which can be used to measure on-line its size as the fringe spacing f is known.

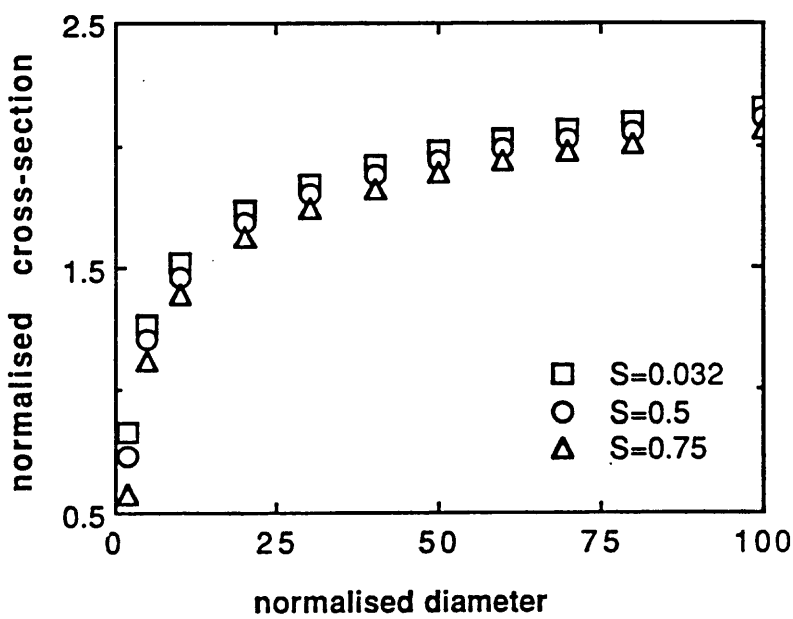


FIGURE 2.49 Dependence of cross section of measuring volume of phase-Doppler intersection region as a function of particle size with the frequency shifting parameter, $S = [\ |U_i|/(U_{shift}+U_i)\ ]$(appendix 2.D). $N_0/N_f = 8/10$.

CHAPTER 3

AXISYMMETRIC TURBULENT PARTICLE-LADEN JET

3.1 Introduction

The work presented in this chapter describes experiments with isothermal particle-laden jets. The phase Doppler instrument described in the previous chapter was used to obtain measurements in two-phase flow jets. Solid glass beads were used for the dispersed phase and the behaviour of different sizes, 40, 80 and 200 μm, is examined. The exit mean Stokes number for these cases is less than unity. For the 200 μm beads, the mean Stokes number remains less than 0.1 along the centreline of the jet, suggesting unresponsive particles; for the 80 μm beads, it remains less than 1 along the centreline over the distance considered by the experiments; and for the 40 μm beads, the mean Stokes number is approximately unity at a distance x/d = 28 from the jet nozzle, which suggests response of the particles to the large scale motion as they move downstream. The influence of the mass loading on the particle flow characteristics is examined and the effect on the fluid flow field due the 80 μm particles is measured and suggests a "two way" interaction between the particles and the fluid as the mass loading increases.

The following section describes the flow arrangement, the characteristics of the particles and the optical arrangement of the phase Doppler instrument. In addition, an estimate of the errors involved in the sizing and the velocity measurements is given. Section 3.3 presents the experimental results in four sub-sections. The first three sub-sections report the results in the following order; velocity and flux characteristics of the 200 μm particles, velocity and flux characteristics of the 40 μm beads and gas measurements in the presence of the 80 μm beads as well as the characteristics of the 80 μm particles. In all cases the single phase jet is reported. The fourth sub-section provides balances of the mass and momentum fluxes of the two phase flow jet. Section 3.4 compares the present results with those of previous experiments. The results are discussed in section 3.5 and a "fan spreading model" is suggested to explain the dispersion of the beads. Finally, section 3.6 summarises the main conclusions.

In the following text, the terms "beads" and "particles" are reserved for the glass beads (subscript b) and "seed" or "seeding" for the seeding material. The term "single phase" refers to the jet flow without any beads added (subscript s) and "gas" or "fluid" flow to the motion of the air in the presence of the beads (subscript f). It is expected that the velocities measured in the single phase jet to be a good approximation to the gas flow at low volume fractions of the beads and therefore frequently use the single phase as a reference. "Mass loading" is defined as the ratio of the mass flow rate of particles to the mass flow rate of gas within the jet nozzle.

3.2 Materials and methods

a) Jet flow, bead feed and recovery

Figure 3.1 shows the jet configuration together with the arrangements for metering the air flow rate to the jet and for supplying and recovering the beads. The jet exhausted vertically downwards towards a collection hopper placed 50 jet diameters from the jet exit; it had an exit Reynolds number of 13 000, corresponding to a bulk velocity of 13.2 m s^{-1}. The air to the jet came from a central compressor and a pressure regulator kept this flow constant and independent of fluctuations in the supply pressure. The air was divided and metered by rotameters to provide pneumatic transport for the glass beads and for the seeding tracer for the phase-Doppler anemometer. The two streams were recombined upstream of a smooth contraction with 11.1 : 1 area contraction and subsequently developed in a 15 mm diameter precision bore stainless steel tube for 100 diameters before exhausting into ambient air. The rotameters operated at a gauge pressure between 0.1 and 0.3 atmospheres and the flow rates were corrected to N.T.P. from calibration charts provided by the manufacturer.

The glass beads were metered by a screw feeder which was driven by a variable speed motor through a reduction gearbox : the stock of beads was drawn from a hopper and this was vibrated at 50 Hz to prevent the bridging of particles at the entrance to the barrel of the screw. The vibrator also evened out the particle flow rate since the screw rotated at speeds between 0.33 and 10 Hz and gave rise to

fluctuations in the delivery. As noted by Stårner and Bilger (1981), this unsteadiness does not influence the particle velocity characteristics because they are uncorrelated with the fluctuations in particle feed rate. The flow rate of the beads as a function of the motor speed was found by weighting the output over a fixed time interval. The motor, screw feeder and hopper resided within a box maintained at the same pressure as the duct upstream of the contraction (see figure 3.1). As a consequence the screw feeder calibration, which had been obtained at atmospheric pressure, remained valid because there were no differential pressures across any part of the screw feeder. Note that, to minimise any disturbance of the operating conditions, the air flow rate through this box (1 $dm^3 s^{-1}$) was maintained even when no beads were added to the jet.

The flow was seeded with a variety of refractory powders (e.g. kaolin, titanium dioxide), all of which were nominally micron-sized before agglomeration. The refractory powders were dispensed initially from a modified form of a spark-discharge generator (Altgeld et al., 1980) but this was replaced by a reverse cyclone feeder (Glass & Kennedy, 1977). The former method had the disadvantages that a relatively small fraction of the air flow could be seeded and that the electrodes had to be wiped clean at regular intervals. The reverse-cyclone arrangement permitted a greater fraction of the air passing through the nozzle exit to be seeded, at a higher concentration and without deterioration of performance. The flow rate through the reverse-cyclone was maintained at around 1.4 $dm^3 s^{-1}$, even when seeding powder was not introduced in the flow, by using a second reverse-cyclone which had no seed inside it. This was done in order to keep the pressure drop through the system constant, when the beads flow characteristics were measured and seeding was not introduced in the flow. The seeded air flow was directed against the falling beads to promote the radial dispersion of the beads, as shown in figure 3.1, before arriving at the contraction.

The beads and seeded air were discharged into the laboratory with the discharge protected from draughts by curtains. The flow was captured by a collection hopper that was placed on the inlet of a large fan to provide a suction flow. The particles were recovered by passing this induced flow through a cyclone and collecting them in a bin at the

base of the cyclone. This bin was periodically emptied and the particles were returned to the hopper of the screwfeeder.

b) Glass beads

The beads had the properties quoted in table 3.1. The bead size ranges of 37-44, 60-95 and 165-255 μm will be refered to in the rest of the text as 40, 80 and 200 μm for convenience. The nominally 40 μm range represents the smallest narrow-sized range which could be found at acceptable cost; it provided an exit mean Stokes number which allowed the particles to follow the development of the mean motion of the jet with some fidelity. In this size range the particles are strongly hygroscopic and the factory-optional coating of a molecular film of silicone material is vital to prevent agglomeration due to atmospheric humidity. The size ranges quoted by the manufacturers are based on the cumulative volume of beads, however, and it is more relevant to examine the size range in terms of the number-frequency distribution since the phase-Doppler anemometer records a particle flux based on the latter. The distributions of the beads were measured by a Coulter Counter (model ZM; Coulter Electronics) and figure 3.2 shows the volume and number distribution of the 40 μm glass beads. The size distribution is continuous down to at least 6 μm and thus the size distribution seen by the phase-Doppler anemometer is continuous from between about 1 μm and 44 μm.

Figures 3.3 and 3.4 (a) and (b) show the volume and the number distributions of the 80 and 200 μm beads used in the experiment, where the number distributions reveal the existence of a large number of particles smaller than the nominal diameter, especially for the 200 μm beads. For example, figure 3.4(b) shows that the number of beads with mean diameter around 200 μm is much smaller than the number of smaller sizes existing in the batch. Figure 3.3(c) shows the effect of half year use on the number distribution of the 80 μm glass beads. The number of the smaller particles has been increased, partly because of the mixing of the particles with the seeding powder and partly because some of them break as they pass through the collection cyclone. However, there are still in the distribution a lot of large particles, which proves that most of them do not break in the cyclone. Similar effects of long use were found with other bead sizes. As it is

shown below, the continuous distribution here has implications for the interpretation of the results for the solid particles.

The sphericity of the glass beads was examined by light- and scanning electron- microscopy. Figure 3.5 is a photograph, at a magnification of about 200, of glass beads (nominal diameter 40 μm) which have been in continuous use for about one year. Some of the particles are spherical, but there are many irregular objects. Also, observation with a scanning electron microscope at larger magnification of single particles with 40 μm nominal diameter showed that the surface of the otherwise spherical glass bead is scratched and pitted. The number count and the asphericity of the particles has been quantified by an image analysis system attached to a light microscope (Leitz "Autoscope P",; E. Leitz Wetzlar GmbH), where asphericity is quantified through a shape factor defined as

$$4\pi^*(\text{particle projected surface area})/(\text{perimeter})^2$$

where unity corresponds to a circle. In a given batch of nominally 40 μm glass beads, there were about 60% more particles which had a shape factor of between 0.8 to 0.9 than there were "spherical" particles, defined as having shape factor between 0.9 and 1.0; and there were 43% more with an elongation factor of between 5 and 50. These results show that there are more aspherical than spherical particles and it is unlikely that the large number of aspherical particles is peculiar to this size range. Similar analysis of nominally 200 μm glass beads (Jencons (Scientific) Ltd.) showed that there were 3.56 times as many particles with amorphous shape (factor between 0. and 0.2) as there were "spherical" beads. Similar observations were made by Mostafa et al (1987) for the glass beads used for their experiment. As described in the experiments of the previous chapter, and shown below, the asphericity and the surface roughness of the glass beads has implications for the measurement of the gas phase in the presence of the glass beads.

c) Phase-Doppler anemometer

Optical arrangement

The characteristics of the transmitting optics are given in the top portion of table 3.2 : a high power laser was used to give adequate signal-to-noise ratio for the seeding powder and frequency shifting was provided by the rotation of a radial diffraction grating. Measurements of the radial mean and r.m.s. velocities, and of the cross-correlation $\overline{uv}$, were made by taking readings of the mean and variance of the Doppler frequency at 0° and ± 45° to the jet axis, using the approach outlined by Melling and Whitelaw (1975).

The modular receiving optical unit, shown schematically in figure 3.6, was mounted on an optical bench with the transmitting optics and radial and vertical profiles of velocity and flux were measured by moving the optical bench on a three-axis translation stage. The receiving optics were placed at 30° to the forward scatter direction both to reduce the contribution of the diffracted light to the total scattered light to negligible levels (Hardalupas, 1986) and to reduce the effective size of the measurement volume (Bachalo, 1980). The latter consideration is important because the phase-Doppler instrument is a "single particle" counter and, at the highest volume fractions of the 40 μm beads, the probability of observing more than one particle in the volume formed by the intersection of the two laser beams becomes unacceptably large. This is so both because of the many particles smaller than 37 μm which are present in the size distribution and because the effective volume over which a measurable signal from an approximately 40 μm bead is visible is much larger than for a 1 μm seed.

The principal characteristics of the receiving optics are given in lower portion of table 3.2, together with the effective length (200 μm) of the measuring volume as seen by the collection optics. The reduction from the length of the beam intersection volume of 1.13 mm, quoted earlier in the table, is due to observation of the intersection of the laser beams at 30° from the forward scatter direction with a 100 μm slit.

Electronic arrangement

The outputs of the photomultipliers were high-pass filtered by three phase-matched passive filters at 1 MHz. The filtered signals were passed to the zero-crossing counter, based on a 500 MHz clock, described in chapter 2. No amplifiers were used in order to avoid phase shifts introduced between the channels due to the electronics.

The particle size was related to the measured phase difference by the calibration curve of figure 3.7, which was calculated on the basis of the theory described in chapter 2. The required quantities are the laser light wavelength, the beam intersection angle, the refractive index of the beads, the receiving optics angle and the aperture separation on the receiving optics module (table 3.2). As explained in chapter 2, signals with phase shifts in the interval 0° - 40° were accepted as being generated mainly from the seeding powder.

d) Uncertainties in the measurement of the gas in the presence of the dispersed phase.

Table 3.3 provides estimates of the uncertainties in positioning the anemometer, in the measurement of the air and bead flow rates by rotameters and screw feeder respectively and of the velocity characteristics of each phase. There was no uncertainty involved in discriminating between the velocity characteristics of the beads and those from the gas phase, even though about 25 % of the beads fell below the nominal size range on a number-count basis, because signals from the under-size beads can be successfully discarded by a combination of reducing the sensitivity of the receiving optics and accepting phase·measurements corresponding to the nominal size range (Hardalupas et al., 1988). Thus the estimation of the tolerance on the measurement of the velocity characteristics of both the beads - and of the single phase jet - is straightforward and is based on the specification of the anemometer, of the electronics for processing the signal (e. g. resolution of the crystal frequency in the counter) and on the size of the sample used to estimate the moments of the distributions. The largest contributor to the random error was due to the population size of the data. Typically, estimates of the axial mean and r.m.s. of velocity of the beads were based on about 3000 total

measurements, which result in (Yanta & Smith, 1978) errors of 1 % and 3 % respectively.

The major source of error in the measurement of gas phase velocities in the presence of solid, nominally spherical beads is that, as shown in chapter 2, some larger bead sizes will be erroneously identified as seeding because of the presence of non-spherical beads in any batch. It is argued in chapter 2 that any measurement of bead size which is based on the observation of light reflected or refracted by the bead is subject to this error, irrespective of whether the measurement is of the amplitude, visibility or phase of the Doppler signal. The proportion of beads having an aerodynamic diameter larger than 5 μm, but an optically measured diameter below 5 μm, was found to be about 7 % of all the beads with an aerodynamic diameter between 35 and 45 μm beads and this figure is taken as representative of the three bead sizes considered in this experiment. The following paragraph examines the relative fluxes of the beads and of the seed to establish the importance of this "cross-talk" between the phases and describes the strategy used to reduce the effect of cross-talk in the gas phase measurements.

In these experiments, the phase-difference range for the seeding was of the order of 40° between the channels and entailed a rejection of about 50% of the total signals from the seeding powder, because the remainder lie outside this range. The high rejection ratio of signals from seeding is inevitable because of the use of aspherical seed. The ratio of the flux of seed to that of the beads is small for two additional reasons. The first is that the low-amplitude seed signal had to satisfy the "amplitude validation" level simultaneously on three separate input channels on the counter; when the same counter is operated on only one channel for straigthforward laser-Doppler anemometry, the data rate was almost an order of magnitude greater. A contributory factor to the low data rate when the counter is used for phase-Doppler measurements may also be the comparatively small number of fringes within the $1/e^2$ levels of the measurement volume (table 3.2). The second is that the effective cross-sectional area of the measuring volume is larger for the beads than for the seed. The implication of the preceding statements is that the moments of the probability distribution of velocity of signals in the 40° phase difference range may be biassed towards those of the beads and the

error cannot be readily identified as having occurred since it modifies the mean gas velocity, qualitatively at least, in the same manner as the expected effect of increasing the mass loading of the beads.

The velocity characteristics of the gas phase were recovered by using a correction procedure which involves subtracting the measured probability distribution of bead velocity from the "contaminated" distribution in the 40° phase-shift range assigned for seeding and is described below :

i) measure the velocity probability distribution, $p(U_{large})$, of the beads within a phase-shift range $\Phi_{large} \pm \delta\Phi_{large}$, which corresponds to the size of dispersed phase of interest and at a sensitivity of the receiving optics which permits only the beads to contribute to the velocity distribution.

ii) measure the probability distribution, $p(U_{small})$, of the seeding powder within a phase-shift interval, $\Phi_{small} \pm \delta\Phi_{small}$, corresponding to small particles and seed, say less than 10 μm. Simultaneously, measure the flux, G_{large} , of the large beads in the phase-shift range $\Phi_{large} \pm \delta\Phi_{large}$. Hence, estimate the cross-talk flux, G_{ct}, in the phase-shift range $\Phi_{small} \pm \delta\Phi_{small}$, using $G_{ct} = 0.07\ G_{large}$ as described in chapter 2.

iii) correct $p(U_{small})$ by subtracting $p(U_{large}) * \frac{G_{ct}}{G_{large}}$ to give $p(U_{gas})$, the estimate of the velocity probability distribution of the gas phase.

Typically, at a mass loading of 86 %, 3000 signals from 80 μm beads were measured during the time taken to collect 1000 signals in the phase shift range assigned to seeding. If there is 7 % cross-talk (as suggested in chapter 2) this implies that about 210 signals of the 1000 were not due to seeding and must be removed by a correction procedure.

The error in the corrected gas phase velocity distribution is smaller when 80 μm, rather than 40 μm, beads are used for two reasons. The first is that the flux of the 80 μm beads is smaller by a factor of $(80/40)^3$ for a given mass loading of beads and hence the relative importance of cross-talk into the seed phase-shift range is smaller by almost one order of magnitude. Secondly, as shown by the measurements in section 3.3, the mean velocity of the 80 μm beads is larger than that of the 40 μm beads, because the inertia of the 80 μm

beads is greater than that of the 40 μm beads by $(80/40)^2$. The probability distributions of velocity of the gas and beads within the 40° seeding phase interval are, therefore, at least partly distinguishable by inspection and thus subtraction of the bead velocity distribution can be supplemented by inspection and "on-line" filtering of the corrected velocity probability distributions of the gas phase. It is worth noting that the velocity difference between the two phases cannot be used to separate the phases successfully without the phase of the signals because the flux of the beads would swamp that of the gas phase. It is estimated that the uncertainties in U_f and u'_f, from the likely uncertainty in G_{ct} are about 3 - 4 % and 5 - 10 % of the quoted values respectively.

The accuracy of the measurement of the gas phase in the presence of the beads increases with the diameter of the beads. The choice of 80 μm beads, rather than larger size, is a compromise between ease of measurement, having good sizing resolution and the desire to keep the exit Stokes number as high as possible, so that the beads are responsive to the motion of the gas phase. Another factor is that a maximum bead diameter of around 95 μm can be unambiguously recognized by the phase-Doppler velocimetry without changing the characteristics of table 3.2. Therefore the velocity of the gas phase in the presence of 80 μm beads is presented, rather than in the presence of 40 μm beads, in section 3.3.

3.3 Results

The results are divided into four sub-sections, relating to the data for the 200, 80 and 40 μm. In sub-sections (a) and (b) the velocity and flux characteristics of the 200 μm and 40 μm beads, respectively, are described and the velocity characteristics of the 80 μm glass beads and of the gas phase in the presence of the beads are examined in sub-section (c). Sub-section (d) examines the balances of mass and momentum flux for the 40 and 80 μm beads as well as for the single phase and the gas flow. The 200 μm beads are"unresponsive" by virtue of the small value of S_e (see table 1.1) and the 40 μm beads are "partially responsive" since S_e is less than order unity, although S_m rapidly becomes of order unity farther downstream. The velocities of the gas phase were measured in the presence of 80

μm beads, which are on the border between being unresponsive and partially responsive, together with the mass flux of the beads.

a) Measurements of velocity characteristics of "unresponsive" beads

Figure 3.8(a) shows the decay of centreline mean velocity of the single phase jet and the 200 μm beads, the latter for mass loadings of 13 and 37%; the influence of mass loading on the bead velocity are within the experimental error of the measurements. Bead-to-bead interactions are not expected at this volume fraction (≈ 0.04 %) which is well below that (≈ 0.3 %) at which such interactions are expected. The 200 μm beads leave the nozzle with a velocity substantially (≈ 50%) less than that of the single phase since the time of flight along the delivery pipe is of the order of 100 ms and is short compared to the bead time constant (≈ 300 ms). The particle velocity at the pipe exit is therefore not "fully- developed". Similar results at the exit of nozzles have been found by others who have measured at the jet exit (Modarress et al., 1982; Shuen et al., 1985) and, as expected, the magnitude of the slip velocity at the jet exit varies with the length of the upstream pipe and with the size of the bead. The apparently anomalous results of Levy & Lockwood (1981), obtained at 20 diameters downstream of their pipe exit, which show that larger particles (1 mm) move slower than smaller sizes (200 μm), are because the bead velocities, for diameters larger than about 40 μm, are not fully developed at the exit of their pipe, which was about 40 diameters long. The bead Reynolds number here, based on diameter and mean slip velocity, is about 80 at the farthest downstream station and thus the flow about the 200 μm beads is not Stokesian so that the use of equation (1.4) for the particle time constant is an approximation. The modification to the formula for τ_p will still result in a small value for S_m which corresponds to unresponsive flow and, for convenience, the use of equation (1.4) is retained.

Figure 3.8(b) shows the centreline development of the r.m.s. of the fluctuations of the axial velocity of the beads as a function of the mass loading and compares this with that of the single phase. The effect of increasing the mass loading is small and is to decrease the bead r.m.s. fluctuations. Surprisingly, given the large inertia of the beads ($S_t << 1$), u'_b at x/d = 0.1 is greater than that of the single

phase, although the subsequent development of the gas turbulence reverses this observation within a few diameters of the exit. The velocities of both phases in figure 3.8 have been normalised by a single constant velocity, the centreline exit mean velocity U_{om} of the single phase, rather than by the local mean velocity which is the customary way of presenting such data in single phase experiments. This permits the turbulence measurements to represent the proportion of the gas phase fluctuations acquired by the particles. That u'_b is greater than u'_s (and u'_s is likely to be an adequate approximation to u'_f, at least for the lower mass loading) appears to be physically impossible, since it is not clear how the turbulence in the particulate phase can become larger than that of the carrying gaseous phase. Although the wake of each bead is likely to be unsteady, because the mean slip Reynolds number is greater than 44, the beads are too large to respond to these gas-phase fluctuations in their own wake. This paradox is resolved in section 3.5. Taken together, figures 3.8(a) and (b) demonstrate that neither the mean nor the turbulent motion of the bead phase is a function of the downstream distance over the first 28 nozzle diameters and this is expected from the small values of S_e and S_m($\approx$ 0.5) at x/d = 28. It is doubtful whether the beads in this flow are spread by their turbulent motion, although their presence does change the velocity characteristics of the gas phase (Modarress et al., 1982; see section 3.4 for more information).

Figure 3.8(c) shows the decay of the bead flux, defined as the number of validated Doppler signals per second, normalised by the value at the exit and on the centreline, G_{om}. The bead flux is not the same as bead concentration, since the flux depends on the mean velocity of the bead in a way that concentration does not. However, figure 3.8(a) shows that the mean velocity of the beads is almost constant over the first 30 diameters from the exit of the nozzle so that the decrease in the flux seems to be due to the radial spread of the beads.

The desire to have simultaneous size and velocity information when the beads are, as in the present case, poly- rather than mono-disperse is illustrated by the results of figure 3.9. Figure 3.9(a) is the velocity probability function of the 200 μm glass beads on the jet centreline at a location where $U_b > U_s$ as would be measured by a system without any sizing information and it can be seen that the

probability function is bimodal. This bimodality can be explained from figure 3.9(b), which is the cross-correlation between the velocity and the bead size, measured by the phase-Doppler anemometer. Figure 3.9(b) shows that there is a strong correlation between bead size and velocity, with small beads move slower than do larger ones. So the minor peak on the left hand side of the velocity probability function, figure 3.9(a), is due to contributions from beads with diameters smaller than 200 μm. Carlson & Peskin (1975) have suggested that the variance of particle size can be a major factor in determining particle statistics and figure 3.9 is experimental evidence in favour of their statement.

A conclusion from the discussion in the preceeding paragraph is that, in general, it may be unsatisfactory to measure the "large" bead sizes in a polydisperse distribution by arbitrarily reducing the sensitivity of the detection system, since the amount by which reduction is required to see only 200 μm beads, and not for example 100 μm, is unknown. This effect gives rise to errors in other experiments in the literature, as discussed in section 3.4.

b) Measurements of velocity and flux characteristics of "partially responsive" beads

The results for the 40 μm beads are presented under the following four headings: centreline development, radial profiles of mean, turbulent velocities and bead flux. The gas phase characteristics in the presence of the 40 μm glass beads were not measured, due to the difficulties in the discrimination between signals due to seeding and glass beads, but a qualitative conclusion of the modification of the gas phase characteristics can be drawn from the measurements presented later for the 80 μm beads. The 40 μm beads are "partially responsive" at the exit of the pipe, but S_m is of the order of 10 at x/d = 28, the farthest downstream station, and are likely to be responsive there. The 40 μm beads have been measured in detail because this size is likely to be small enough to acquire some turbulence from the gaseous phase.

Centreline development of bead velocity

Figure 3.10(a) shows that the effect of increasing the mass loading from 13 to 80% is to decrease, relative to the single phase, the rate of centreline decay of the mean velocity of the beads. It is likely that the decay of U_f, which has not measured for this bead size, is also smaller as the mass loading of beads increases. The interaction between the mean velocity of the two phases is thus "two way", since both the gas and the bead velocity increase as a function of loading at a given point. The lag between the mean velocity of the beads and the velocity of the single phase is small at the exit of the nozzle, in contrast to figure 3.8(a), because the lighter beads are accelerated faster from rest at the beginning of the long pipe by the conveying fluid than were the 200 μm beads. The bead Reynolds number, based on the mean slip velocity, is at most of the order of unity and justifies the use of the formula for the particle time constant in equation (1.4) which is based on Stokes flow around the particle.

The effect of increasing the mass loading of the beads on the axial development of the centreline turbulence, u'_b and v'_b, is depicted in figures 3.10(b) and (c). The values are, again, normalised by the centreline mean exit velocity of the single phase, U_{om}, and show that the random error in v'_b is greater than for u'_b, a trend that has been found throughout the measurements and is probably because measurements of v'_b are based on two readings at ± 45° to the jet axis. [Normalisation of the single phase turbulence by the local mean axial velocity confirms the familiar result for the single phase jet that the axial turbulence intensity is about 25 % at 28 diameters from the exit.] Three notable features of the development are as follows. First, there is large anisotropy in the turbulence of the beads, largely because v'_b is small and does not change with downstream distance whereas u'_b, qualitatively at least, follows the development of u'_s. The development of u'_b is discussed further below. Secondly, although v'_b is always smaller than v'_s, as might be expected, u'_b is larger than u'_s at the exit of the nozzle and beyond $x/d \approx 15$; here the assumption is made that u'_s is a good approximation to u'_f, which is reasonable for the lower mass loading at least. The behaviour far downstream may be explained by postulating that the rate of decay of turbulence in the single phase jet is larger than that of the beads because, as noted by Snyder &

Lumley (1971), T_f is smaller than T_b. The explanation begs the question of how u'_b increases between the nozzle exit and $x/d \approx 15$. It is highly unlikely that it is due to transfer from u'_f, despite the apparently similar development in the two phases, because straightforward arguments developed in the discussion suggest that the inertia of the beads is so great that the response to the turbulence of the gas phase can only be partial in this region (i.e. $x/d < 15$) and the behaviour of v'_b supports this. The difference between the axial r.m.s. velocities of the two phases at the exit of the nozzle is also a surprising result, because it is not clear how u'_b can rise above the turbulent component of the host gas. Thirdly, the effect of increasing the mass loading results in increasing u'_b downstream of $x/d \approx 15$ and in the displacement of the location of the maximum value of u'_b. In contrast the effect of mass loading on v'_b is small and seems to decrease its already small magnitude. A hypothesis is put forward in the discussion which accounts for all three of these features.

Radial profiles of mean velocities

All radial profiles of the velocity characteristics and flux were obtained by traversing the probe volume in the direction normal to the plane containing the beams so as to minimise mean velocity gradient broadening (Durst, Melling & Whitelaw, 1981). The figures show that the quality of the symmetry is excellent.

Figure 3.11(a) shows the profiles of axial velocity at $x/d = 0.1$ and thus almost within the pipe. As the mass loading increases, the bead profiles are flatter and at the same time the slip velocity relative to the single phase, which is included as a reference profile throughout this series of graphs, is greater. The origin of the change in the shape of the profile of U_b is not clear but it cannot be associated with a reduction in the magnitude of the profile of U_f, comparable or proportional to that measured in U_b, because this would violate the requirement of mass continuity in the gaseous phase. Another possibility which should be excluded is that of particle-particle interaction, since the volume fraction of the beads is, even at its highest value, far below that at which this phenomenon is expected to occur. A possibility which deserves further analysis is that the shape of the profile of U_f is modified by the presence of a favourable pressure

gradient in the pipe. The pressure gradient arises to finance the acceleration of the beads from rest, at the beginning of the pipe, to the velocity which these attain at the exit of the pipe. The magnitude of the pressure difference across the pipe has not been measured , but by conservation of momentum it must be of the order of $\Delta P = \frac{\dot{m}_b \ 0.9 \ U_{om}}{\pi D^2/4} \approx 0.72 \ \rho \ U_{om}^2$ for the highest mass loading, since $\dot{m}_b \approx 0.8 \ \dot{m}_f$ and $U_b \approx 0.9 \ U_{om}$ at the exit of the pipe. The magnitude of ΔP is comparable to the dynamic head of the gas flow and is therefore sufficient to modify the shape of the gas profile.

The subsequent development of U_b is shown for x/d = 10, 20 and 28 (figures 3.11 (b), (c) and (d)): the flatter shape of the profiles which was evident for the higher loadings is lost downstream but the coincidence of the profiles at x/d = 10 is fortuitous and not indicative of, for example, self-similar behaviour of U_b. The beads move faster than the single phase except at the edges and it is likely this is because U_f is also larger than U_s. The flux of axial momentum in the jet is constant, but the increase in U_f implies an increase in the momentum flux in the gas phase: the source of the "extra" gas phase momentum, relative to the single phase, is the corresponding loss of bead momentum flux (see balances in section (d)). The width of the profile of U_b and, by implication, of U_f is also narrower than that of U_s, which is consistent with larger values of U_f near the axis of symmetry, because the entrainment velocity of the gas at the edge of jet must, by continuity, be higher than that in the single phase jet. The higher entrainment velocity, in turn, reduces the growth of the bead-laden jet as the bead mass loading increases.

The magnitude of the corresponding profiles of V_b is small and of the order of 3% of the axial centreline velocity of the single phase flow.

Radial profiles of r.m.s. bead velocity

The radial profiles of u'_b, figures 3.12(a) - (d), and of v'_b, figures 3.13(a) - (d), confirm that the observations made on the centreline measurements above are also consistent in the radial direction. The radial profiles of u'_b bear some resemblance to those of u'_s, in contrast

to the small values of v'_b relative to v'_s. The values of v'_b exhibit noticeable random scatter which is absent from u'_b and v'_s.

Figures 3.14 and 3.15 show the radial profiles of $\overline{u_b v_b}$ and $\overline{u_s v_s}$, together with the correlation coefficient $\frac{\overline{u_b v_b}}{u'_b v'_b}$, at the axial locations of x/d = 0.1, 10, 20 and 28. At the exit, the correlation (figure 3.14(a)) is similar to that of the single phase and this is surprising given the disparity between u'_b and v'_b and u'_s and v'_s: the profile is also remarkable for its smoothness, given the scatter in v'_b. For x/d = 10, the cross-correlation in the beads is smaller than for the single phase (figures 3.14(b) and 3.14(c)) but by the farthest downstream station $\overline{u_b v_b} > \overline{u_s v_s}$ and the cross-correlation is higher for the larger mass loading.

The axial development of the correlation coefficient, figures 3.15(a) - (d), is more instructive than is that of the cross-correlation. The maximum value of the coefficient in gas is about |0.5|, as expected for boundary layer gas flow, but the coefficient for the beads is systematically larger, although the scatter, which is presumably related to that in v'_b, does not allow any trend with increasing mass loading to emerge. For a few radial locations, the random error in the three separate measurements which are required to measure the cross-correlation accumulated to yield a value greater than unity. The coefficient is bounded at unity by definition and, where larger values were found, we have set them to unity in the figures. At some radial positions, the coefficient is substantially larger than |0.5| and this shows that the values of u'_b and v'_b are less stochastic than is the host turbulent field and the implications of this statement are explored in the discussion.

Bead flux and concentration

The amount of the discrete phase at a given point in space is frequently the quantity of primary interest. For example, in a fuel spray or stream of pulverised solid fuel the amount of fuel is directly analogous to the concentration of the gaseous fuel and is required to predict the local air-fuel ratio, the local temperature and the concentration of products of combustion. The quantity measured by

the anemometer is the bead flux, from which bead number density can be deduced.

The rate of decay of the centreline flux, defined as valid Doppler signals in the size range 35 - 45 μm per second per effective area of the measurement volume normal to the flow of beads, and normalised by the nozzle-exit centreline value, G_{om}, is shown in figure 3.16(a). The effective area of the measurement volume from which a detectable signal can be generated is, in general, decreased by the reduction of the intensity of laser incident beams and light detected by the receiving optics. For this reason all values of the flux, for a given value of x/d, were obtained with the same alignment of the receiving optics as well as the same laser power. The effective area, A, of the measurement volume as discussed in chapter 2 changes with particle size. Here, this dependence is omitted because the instrumentation to measure the effective area of the probe volume was not available in the electronics at the time of the experiment. So it is assumed constant everywhere in the flow and for every particle size and is approximated by

$$A \approx s \times b = 200 \times 55\ \mu m^2 \qquad (3.1)$$

where s is the image of the slit in the receiving optics (see table 3.2) and b is the dimension of the minor axis of the measurement volume (see table 3.2). The ordinate is the square root of the flux, because this is the similarity variable (Melville & Bray, 1979a) and, as for the velocity, the reciprocal of the dependent variable has been plotted. The measurements do not extend far enough downstream to establish whether the decay is indeed proportional to X^{-1}, as similarity arguments suggest but they show that the rate of decay of the flux is quicker for the lower mass loading. This observation is similar to results obtained for different density fluids expanding from a nozzle in the same environment. Laats and Frishman (1970) have proposed that the effect of increasing the mass loading on the decay of G results in self-similar profiles when the axial distance is weighted by exp(-0.69 χ_o), where χ_o is the mass loading of the jet at the nozzle exit. Our results do not fall into this pattern.

The absolute values of G_{om} are tabulated in table 3.4 for reference and, particularly for the 40 μm beads, these do not increase

in proportion to the mass loading. Since the centreline bead axial velocity at the nozzle exit is a function of mass loading, there is no a *priori* reason that the centreline value of flux should be linearly proportional to mass loading. However, this result is rather due to the performance of the instrument than due to the development of the flow and is going to be discussed in sub-section (d).

The bead flux (no. of beads $m^{-2} s^{-1}$), G, is not equivalent to concentration C (number of beads m^{-3}) and the distinction is important because concentration is the variable used in many "Eulerian" (e.g. Shih & Lumley, 1986), as opposed to Lagrangian (e.g. Gosman & Ioannides, 1983), models of particulate two-phase flow. The conversion from concentration to flux is not straightforward, because concentration is a continuum concept and, since a phase-Doppler anemometer can function correctly only with one bead in the measuring volume at a time, the anemometer by definition makes a non-continuum measurement. An approximation to the value of the mean concentration was obtained from the measurements of the anemometer by dividing the local mass flux, G, by the local mean velocity, U_b. The approximation arises because the anemometer measures

$$G(t) = C(t)\, U_b\,(t) = C\, U_b + \overline{c'\, u'_b} \qquad (3.1)$$

and to equate C to $\frac{G}{U_b}$ is to assume $\overline{c'\, u'}_b = 0$, which may be an inadequate approximation far from the centreline, because it is near to the "intermittent" edge of the "concentration" profile (Shih & Lumley, 1986). It should also be noted that C is undefined when $U_b = 0$ (say at the free stagnation point of a recirculation bubble; see chapter 2), which is physically incorrect and shows that the definition of C has shortcomings other than those related to the approximation mentioned above. Also, equation (3.1) requires the doubtful assumption that these bead-laden jets satisfy the concept (Lumley, 1978) of a continuum with scales as large as the energy-containing turbulence, an issue which is independent of the problems of measuring concentration presented by the phase-Doppler anemometer.

With these provisos, figure 3.16(b) shows that the axial decay of bead concentration is faster for the lower of the two mass loadings measured. Thus the radial dispersion of the beads is greater at the lower mass loading and this observation is consistent with the measured decay of the centreline velocity, while surprisingly is not reflected in the profiles of v'_b.

The radial profiles of normalised flux, G, at the exit of the nozzle (x/d = 0.1, figure 3.17(a)) are non-uniform across the exit of the nozzle and noticeably asymmetric. The corresponding radial profiles of concentration (not shown) are also non-uniform across the exit. Farther downstream, at x/d = 10 and 20 (figures 3.17(b) and (c)), the flux profiles become bell-shaped and there is no effect of the mass loading on the normalised shape of the profile. By the farthest downstream station, x/d = 28 (figure 3.17(d)), the apparently self-similar behaviour is no longer evident and the half-width of the flux profile is greater at the lower mass loading.

We have assumed symmetry and plotted from these radial profiles the flux and concentration half-widths on figures 3.16(c) and (d) as a function of axial distance, respectively. The notable feature of the rate of spread is that what little there is occurs after 20 diameters downstream of the exit of the jet and that the effect of increasing mass loading is to decrease the rate of spread of the flux and concentration half-widths.

c) Measurements of gas velocities and rate of spread at the presence of 80 μm beads.

Figure 3.18(a) shows that although the centreline decay of U_b is virtually the same for both mass loadings measured, the rate of decay of the centreline velocity of U_f becomes slower as the mass loading of the beads increases: consequently, U_f is larger than U_s at any given axial location. The interaction between the phases is essentially "one-way", from the beads to the gas. In contrast to the 40 μm beads, the source of the additional momentum flux for the gas phase at the higher loading, relative to the single phase, comes from the loss of momentum flux by the beads. Since the decay in U_b is about the same for the two loadings (figure 3.18(a)), it follows that the total momentum flux lost by the beads is nearly proportional to the mass

loading itself, and hence the momentum transfered to the gas increases with mass loading (see below sub-section (d)). The maximum value of the slip Reynolds number is about 15, at x/d = 28 and for the 23 % mass loading. As for the 200 μm beads, the flow past the 80 μm beads is not Stokesian so that the use of equation (1.4) for the particle time constant is an approximation which it is convenient to retain.

The centreline values of u'_b decrease as the mass loading of the beads increases, figure 3.18(b), because of the shape of the profile of U_b at the exit of the nozzle, which is flatter for higher mass loading, rather than through interaction with the turbulence of the gas phase. The r.m.s. fluctuation u'_f for the gas phase is virtually indistinguishable from u'_s at the smaller mass loading and, since this result is physically plausible because the change in the centreline decay of U_f is relatively small, the result lends confidence to our ability to measure the gas phase correctly in the presence of the beads. At the higher mass loading, with the exception of the farther downstream position x/d=28, u'_f is smaller than u'_s and is direct evidence of the effect of the presence of the beads on the turbulence of the gaseous phase. The latter observation is in agreement with Owen's arguments (1969) and suggests that the presence of the beads gives rise to more than just a reduction in the length scale at which dissipation takes place (Lumley, 1978). Finally, v'_b is smaller (figure 3.18(c)) than u'_b and, as for the 40 μm beads, there is no systematic effect of increasing the mass loading on the magnitude of v'_b.

Figures 3.19(a) - (d) show the radial profiles of U_b at four axial stations and on the first and last stations the profiles of U_f are also presented. At the nozzle exit, the U_b profile is flatter for the higher mass loading, in accordance with the measurements of the 40 μm beads. The profile of U_f at the lower mass loading is indistinguishable from U_s as might be expected. At the higher loading, U_f is lower than U_s at every measured point by about 7 %. This result also violates the requirement of mass continuity of the air because the air flow rate to the test section was unchanged on the introduction of the beads. U_f has been probably lowered by the increase in cross-talk between the two phases due to the larger mass loading of the beads and despite the procedure of Hardalupas et al. (1988). This hypothesis is not totally convincing because it is hard to conceive of cross-talk which is large

enough to change U_f and yet leave u'_f similar to u'_s, as discussed below. An alternative explanation is that U_f is indeed as measured, lower than U_s, but that U_f is larger than U_s in the regions closer to the walls of the nozzle than those at which measurement was possible. The amount by which the gas phase would have to be larger to account for mass continuity is small because of the increased contribution to the mass flow rate of flow near the walls relative to flow near the centreline. The justification for believing that the behaviour of U_f near the walls is different from that near the centreline is that the measurements below show that the mass flux, or concentration, of beads is smaller near the walls.

The development of U_b at x/d = 10 and 20, figures 3.19(b) and (c), confirms that the rate of spread of the 80 μm beads is smaller than that of the 40 μm beads and that the separation between U_b and U_s, and by implication U_f, increases with downstream distance. At x/d = 28, figure 3.19(d), U_f is greater than U_s, although the acceleration of the gas phase is confined to the region where the beads and the gas co-exist : the measurements just outside the jet of beads suggest that U_f is smaller than U_s. In accordance with expectation, the slip velocity between the two phases is greater for the larger mass loading of beads.

The turbulence of the gas phase, figure 3.20(a), at the exit of the nozzle is unchanged from u'_s by the presence of a mass loading of 23 % of 80 μm beads. At the higher loading, u'_f is smaller than u'_s by about a factor of 2, which casts doubt on the suggestion that there is cross-talk from the beads. The turbulence of the beads at x/d = 10 and 20, figures 3.20(b) and (c), is smaller than and not even qualitatively related to u'_s. At x/d = 28, figure 3.20(d), u'_f is larger for the higher mass loading of beads and, in both cases, u'_f is greater than u'_s. It is likely that the increase in u'_f is due to the generation of $\overline{u_f^2}$ by $[\overline{u_f v_f}\,\frac{\partial U_f}{\partial r}]$ which is larger due to the increase in the value of mean rate of strain, $\partial U_f / \partial r$, and will be discussed in section 3.5. The r.m.s. radial velocity of the beads was measured, as for the 40 μm beads, but is not presented here since the profiles do not show any new features.

Figures 3.21 and 3.22 show measurements of the radial profiles of $\overline{u_b v_b}$ and the associated correlation coefficient. The cross

correlation is smaller than that for the 40 μm beads at x/d = 0.1, 10, 20 and 28 and although the corresponding correlation coefficient is higher than that of the single phase for the last two stations, its value is noticeably smaller than that of the 40 μm beads. There is no difference between the results for the two mass loadings.

The rates of decay of centreline flux and concentration are shown in figures 3.23(a) and (b) in the same form as figure 3.16 for the 40 μm beads, and the relevant normalising quantities are given in table 3.4. The values of G_{om} for the 80 μm beads increase more closely in proportion with the loading than do the results for the 40 μm beads and this observation is discussed in sub-section (d). The effect of mass loading is smaller than with the 40 μm beads, in common with the centreline velocity, but the trend is opposite to that in figure 3.16, namely an increase in loading increases the centreline decay. This observation is consistent with measured increase in both the flux- and concentration- half width with increasing loading, demonstrated in figures 3.23(c) and (d).

The radial profiles of bead flux are shown in figure 3.24 and that at the exit of the jet, figure 3.24(a), is the only asymmetric profile measured. If the flux really were asymmetric at the exit of the pipe, as the measurements suggests, the comparatively slow axial development of the 80 μm beads would ensure that the asymmetry would be present for a long way downstream but this is not observed in the subsequent profile of flux at x/d = 10, figure 3.24(b). The likeliest explanation for the asymmetry remains that it is an artefact of the measurement technique, but the origin is not clear.

(d) Mass flowrate and momentum flux.

The measurements presented in this work are intended for use in evaluation of calculation methods and it is important to know the quantitative reliability of the experimental results. As suggested by Rodi (1975), consistency checks of the experiments are required, which provide an independent evaluation of the accuracy. The quantities providing these checks for all jet experiments are the mass flowrate and the conservation of momentum flux, estimated here for the single phase flow and the beads and compared to the expected value.

The mass flowrate of the single phase flow at the exit of the nozzle, obtained by integration of the velocity profile, was ≈15% lower than the flowrate measured to the rotameter and the discrepancy is due to the absence of data points very close to the pipe wall. Downstream of the nozzle the mass flowrate increases as expected and follows the results of Ricou and Spalding (1961), suggesting that the jet entrains air from the stagnant environment equal to the initial flowrate every 6 nozzle diameters. At the farthest downstream location, differences up to 20% exist which are due to the uncertainty in the definition of the edge of the jet. The results for the momentum flux, which is the conserved quantity for the jet, show similar differences at the downstream locations.

The calculation of the mass flowrate and momentum flux for the solid phase cannot be obtained by integration of the velocity profiles alone, since the particles are not a continuous medium. The mass flux of the beads was obtained by integration of the profiles of the particle flux G for an effective area of the laser Doppler probe volume A = 200 x 55 μm^2 (section 3.3 c). The mass flowrate of the beads is a conserved quantity. The supplied flowrate of the beads to the flow for every mass loading was known and used here to normalise the estimated flowrate of the beads for each case and the results are presented at figures 3.25(a) and (b) for the 40 μm and 80 μm beads. The estimated mass flowrate of the beads is larger than the supplied flowrate for all cases. For the 80 μm beads, it is larger by a systematic factor of 3.5 times, which is approximately independent of measuring location and mass loading and suggests that the effective area of the probe volume, A, is larger than the approximate value used for the calculation by around 3.5 times. The estimated flowrate for the 40 μm beads is initially less overestimated than for the 80 μm beads but eventually also rises to around 3.5 times larger for the lower mass loading. It is likely that the difference is due to larger turbidity of the 40 μm flow, since the number of 40 μm beads present in the flow is $(80/40)^3$ times larger than the 80 μm for the same mass loading. Also an increased proportion of measurements may fail to satisfy the amplitude and the frequency validation criterion because of the reduced signal-to-noise ratio at higher loadings. The comparison of the ratio of the estimated bead flowrates for the two mass loadings with the expected ratio (e.g. 80/13 ≈ 6 for the 40 μm), shown in

figures 3.26(a) and (b) supports the above explanation for the results obtained for the 40 μm and explains why the values of the flowrates for the 80 μm beads increase more closely in proportion with the initial loading.

The beads are continuously loosing momentum to the gas flow. The integral of the momentum flux of the beads along the developing region of the jet, normalised by the momentum flux at the exit for each case, is shown in figure 3.27. The momentum flux integral of the beads was corrected for the error of the estimated mass flowrate (figure 3.25) by multiplying with the ratio of the supplied to the estimated mass flowrates. Although the initial momentum flux of the beads for both mass loadings is approximately the same for the 40 and 80 μm beads, the rate of momentum loss is lower for the 80 μm beads and at x/d = 28 the 80 μm beads have twice the momentum flux of the 40 μm beads. In Appendix 3.C the drag coefficient of the beads in the jet flow at x/d = 28 is calculated under certain assumptions and is found to be nearly two times larger for the 40 μm beads than for the 80 μm, which supports the observations of the momentum flux balances. A side issue from this calculation is that the drag coefficient is affected by the presence of a large amount of beads and does not follow the drag law for single spheres. The amount of momentum flux transfered from the 40 μm beads to the gas phase accelerates the gas and decreases the slip velocity between the two phases, so the rate of momentum flux loss decreases after x/d = 20, which does not happen for the 80 μm up to x/d = 28. This explains also the difference of the rate of momentum loss between the two mass loadings for the same size, which is lower for the higher loadings.

Figures 3.28(a) - (d) and 3.29(a) - (d) show the variation of the momentum flux integral as a function of the radius at axial locations x/d = 0.1, 10, 20, 28 for the 40 and 80 μm beads respectively. The momentum flux of the beads is concentrated over the central region of the jet (r/d < 1) and for the lower mass loadings is smaller than that of the single phase flow by at least 50 %, so the influence on the mean gas phase flow must be small. For the higher mass loadings it is larger or equal to the momentum flux of the single phase flow and can affect the air as shown by the estimation of the momentum flux of the gas phase in the presence of the 80 μm beads (figure 3.29(d)). This suggests that the ratio of the momentum flux of the single phase jet to

the momentum flux of the beads at the exit is an indication of the influence that the presence of the beads can have on the mean gas flow. The estimated values of momentum flux, and the ratio of the momentum flux of the single phase flow to that of the beads, at the exit of the nozzle are given at table 3.6 and show that the momentum flux of the beads relative to the single phase is approximately proportional to their mass loading. The small momentum flux of the particles at the outer region suggests that the beads loose most of their momentum in getting there.

The integration of the profiles of the gas flow shows that the momentum flux of the gas increases relative to that of the single phase flow by 20% at x/d = 28 for the higher bead mass loading, which is less than the momentum lost by the beads by 50 %. This suggests that the measurements of the gas phase are not affected by cross talk with the beads because this would result in the acquisition of much higher momentum flux by the gas.

3.4 Comparison with previous experimental results.

Before comparison with other two-phase flow experiments can be made, it is necessary to establish that the present single phase jet measurements are in good agreement with previous results. The radial profiles of the axial mean and r.m.s. velocity at x/d = 20 and 28 normalised by the mean centreline velocity at each station are plotted as a function of the radial distance from the centreline r, which is normalised by the distance from the nozzle exit, x, and are compared to the results of Wygnanski and Fiedler (1969) in figure 3.30. The turbulence intensity results at x/d =20 agree very well with these of Wygnanski and Fiedler at the same station and, as expected, are smaller by 25% to these of the self-preserving jet (x/d > 50). At x/d = 28 the turbulence intensity increases approaching that of the self preserving jet. The mean axial velocity results agree perfectly. The observed trends establish confidence in the single phase jet results of the present experiment.

It is necessary to establish a single set of scales which will be used for normalisation during the comparison with the other two phase experiments. Mean centreline velocity was normalised by that at the exit of the nozzle and the radial profiles were normalised by the

local mean centreline axial velocity of the single phase, which is usual in the jet experiments (e.g. Wygnanski & Fiedler, 1969). However, in contrast to practice for single phase jet experiments (e.g Wygnanski & Fiedler, 1969, who used the local mean centreline velocity) or for two phase jets (e.g. Shuen at al, 1985 and Modarress et al, 1982 used the centreline velocity of each phase) the turbulence r.m.s. centreline velocities for both phases were normalised by a single constant velocity, the centreline exit mean velocity of the single phase, U_{om}. This allows direct comparison of the proportion of the gas phase fluctuations that is acquired by the particles; normalisation by the local mean velocity of each phase would obscure this comparison.

Two experiments with two-phase jets were chosen for comparison, due to the similarity of the experimental conditions, and are examined separately in two sections. The experiments of Shuen et al (1985) will be presented first and the experiments of Modarress & Tan (1982, 1984) will follow.

a) Comparison with the experiment of Shuen et al (1985).

Shuen et al (1985) measured gas and particle velocity in jet flows for 79 μm, 119 μm and 207 μm diameter sand. The conditions of their experiments suggest that the particles are not responsive to the mean gas flow (table 1.1, chapter 1) and their results here are normalised by the exit mean centreline velocity of the single phase. The following conclusions can be drawn from the comparison:

i) the single phase characteristics for both experiments are the same;

ii) the mean centreline development of the 79 μm sand is similar to the development of the 80 μm beads;

iii) the axial r.m.s. centreline fluctuating velocities of the 79 μm particles have a maximum at approximately x/d = 20 and then decrease in a similar way as the single phase (figure 3.31(b)). This is not observed in the results presented here, where the r.m.s. axial velocity decreases continuously downstream of the nozzle. This conflict is not justified by any difference between the flow conditions and is rather due to the inability of their instrumentation to size the particles and the measured velocity distribution is modified due to cross talk from smaller sizes. Similar observations are true of the 119

μm particles results, although to a smaller extent. Additionally, the shortcomings of the instrumentation are the reason for the discrepancies of 40 - 60 % which they observed between the mean velocity of the 207 μm particles measured by L.D.A. (low bead mean velocity) and double-flash photography (high bead mean velocity). Their explanation, based on the large Doppler pedestal components, is less plausible;

iv) the radial r.m.s. fluctuating velocities of the particles are much smaller than the axial, as observed in our results. However the radial r.m.s. of the 79 μm particles is larger than measured here for the 80 μm beads (figure 3.31(c)), which should again be due to cross talk from smaller sizes;

v) the gas phase mean velocity at the presence of the 79 μm particles is smaller than that of the single phase after x/d=30 (figure 3.31(a)). There is no physical ground for this as the momentum transfer from the particles to the gas accelerates the gas flow. Again the measurement seems to be in error;

vi) the gas phase axial turbulence in the presence of 79 μm particles is reduced relative to the single phase close to the nozzle of the jet and is larger far downstream. Similar results has been obtained for the gas at the presence of 80 μm beads but for larger mass loadings.

b) Comparison with the experiment of Modarress and Tan (1982, 1984).

The instrumentation that they used is more advanced than that of Shuen et al. They measured gas and particle velocities for 200 μm and 50 μm diameter glass beads and the conditions of their experiment are also found in table 1.1. Using the mean exit centreline axial velocity to normalise their results the following conclusions can be drawn:

i) the single phase results for both experiments are very similar;

ii) the mean axial centreline velocity development of the 200 μm is the same for both experiments and is not affected by bead mass loading. They do not present results for the r.m.s. velocity of the 200 μm beads;

iii) the change of mass loading affects only the 50 μm beads and they find that the particle velocity decreases along the centreline with decreasing mass loading. Similar observations were made for the 40 μm beads. Also for the same mass loading, the rate of centreline velocity decrease is inversely proportional to particle size (figure 3.32);

iv) the mean gas phase velocity has been increased in the presence of the 50 μm beads in a similar way to our results for the 80 μm beads. This effect is larger for the 50 μm rather than for the 80 μm due to the difference in their relaxation time (figure 3.32(b));

v) their radial profiles of axial r.m.s. velocity at x/d = 20 for the 50 μm beads for 32% and 85% mass loadings show that the axial r.m.s. fluctuations of the beads and the gas in the presence of the particles are larger than that of the single phase jet and this is true for both mass loadings. This result is similar to our observation for the 80 μm beads at x/d = 28 (figure 3.20(d)), where the velocity fluctuations of the gas in the presence of the particles are larger than these of the single phase flow;

vi) they also find large anisotropy between axial and radial r.m.s. fluctuating velocity of the 50 μm particles.

Finally, it should be emphasised that both the above experiments do not present any measurements of the bead cross-correlation coefficient and the bead flux and these shortcomings are corrected by this work.

3.5 Discussion

There are two questions which need to be answered. Do the particles disperse due to turbulence acquired from the gas phase ? What is the effect of the particles on the mean and turbulent gas phase characteristics ?

The discussion begins with an assessment of the magnitude of the contribution of the turbulent motion of the beads to their spread and this leads to an explanation of the high anisotropy and correlation coefficient of the bead turbulence relative to that of the single phase jet. It is useful to be able to arrive at some a *priori* estimate as to whether the turbulent velocity component of the beads in these experiments is important to dispersion. This can be important to

mathematical models of particulate dispersion, for example the Lagrangian particle-tracking approach of Gosman & Ioannides (1983), which assumes that a bead is subjected to aerodynamic drag forces, related to the difference in instantaneous velocities between beads and air.

Vames and Hanratty (1988) have noted that the trajectories of the beads cannot be "random walks" if the turbulent Stokes number is less than 0.1 since the inertia of the beads filters out most of the frequency spectrum of the gas phase turbulence, leaving the beads to travel in straight lines. The turbulent Stokes number at the nozzle exit is about 0.1 for the 40 μm beads (Appendix 3.B) and lower for the larger diameters so that, at least within the pipe, the beads will move in straight lines. As these emerge from the pipe, the characteristic turbulent frequencies of the air decrease so that the turbulent Stokes number, S_t, is an increasing function of the downstream distance and is tabulated in table 3.5, calculated in Appendix 3.B, for the 40, 80 and 200 μm beads. The magnitudes suggest that only the 40 μm beads are sufficiently small to acquire turbulent motion from the gas phase, and only after twenty nozzle diameters downstream.

The finite values of v'_b measured at the nozzle exit for all three bead diameters show that the bead trajectories are straight lines which are inclined at an angle to the jet axis. The r.m.s. angle of trajectories at the exit of the nozzle is ±3° to the jet axis for the 40 μm beads. The inclined particle trajectories give rise to radial profiles of bead flux which extend farther than the location of R_0, the radial location of the streamline in the jet which contains all the mass flow rate from the nozzle of the jet. The radial r.m.s. velocity component at the exit of the jet thus contributes to bead spread and figures 3.17(b) and (c) quantify the amount by which the beads lie outside R_0 for the 40 μm beads. Within the pipe leading to the nozzle exit, this angle suggests that some of the beads must hit the wall of the pipe as they move along the pipe tube. After impact, they return to the flow, having lost some of their momentum, at distances from the wall which are proportional to their inertia. So larger beads return closer to the centre of the tube after hitting the wall. This can be the reason for the shape of the mean velocity profiles at the nozzle exit and their difference between the 40 and 80 μm beads, the non-uniform

concentration profiles and the increased u'_b and v'_b at the region of the gas boundary layer.

The magnitude of the S_t suggests that the motion of the 40 μm beads within 20 diameters of the nozzle should be relatively unresponsive to the frequencies of the energy-containing velocity fluctuations of the gas and this is supported by the measurements of v'_b since, even as far as 28 diameters downstream, $v'_s \approx 2\, v'_b$ (figure 3.10(c)). It is therefore surprising that $u'_b \approx u'_s$ everywhere on the centreline (figure 3.10(b)) since the magnitude of u'_s is similar to v'_s and it is known (Gibson, 1963) that there is little difference between the wave numbers corresponding to the energy-containing scales of the axial and the radial velocity.

The explanation of the phenomenon is based on two features of this jet. First, the trajectories of the beads on exit from the nozzle are virtually straight lines. Secondly, the beads near the nozzle wall travel markedly slower than do those near the centreline of the jet. A bead will maintain its trajectory over the Lagrangian integral timescale, $\mathcal{T}_b$, which has magnitude (Meek & Jones, 1973; Pismen & Nir, 1978, 1979)

$$\mathcal{T}_b \approx \tau_p \qquad \text{when } S_t < 1 \ \{ \Rightarrow \mathcal{T}_f < \tau_p \} \tag{3.7}$$

$$\mathcal{T}_b \approx \mathcal{T}_f \qquad \text{when } S_t > 1 \ \{ \Rightarrow \mathcal{T}_f > \tau_p \} \tag{3.8}$$

Close to the nozzle, say for $x/d \lesssim 20$, the first condition is appropriate (table 3.5) and hence a bead travels in a given direction for time $\mathcal{T}_b$ of order τ_p : in this time the bead travels over axial and radial distances given by

$$\Delta x_b \approx U_{Lb}\, \mathcal{T}_b \tag{3.9}$$

$$\Delta r_b \approx \pm v'_{Lb}\, \mathcal{T}_b \tag{3.10}$$

Assuming that the Lagrangian quantity is of the same order as the Eulerian, typical values for U_{Lb} and v'_{Lb} are 10 and 1 m/s, respectively and, with $\tau_p \approx 10$ ms for the 40 μm beads,

$\Delta x_b \approx 10$ cm = 6 exit diameters
$\Delta r_b \approx \pm 1$ cm = $\pm$ 0.7 exit diameters

with larger distances for the 80 and 200 μm beads. Thus the beads travel over large fractions of the width of the jet without modification of the velocity magnitude or direction because the radial distance, Δr_b, which is the "mixing length" of the beads (Owen, 1969), is comparable to that of the half-width. This behaviour is analogous to a Knudsen flow, where the mean-free-path of the molecules is of the order of the diameter of the duct in which the flow occurs (Vames & Hanratty, 1988). After $x/d \approx 20$, there is a transition region for the 40 μm beads which begin to acquire some turbulence from the gas as they approach at $x/d = 30$ where the S_t is of the order of 1. However, the acquired turbulence cannot be large because v'_b is of the order of 5% and much smaller than that of the single phase.

The importance of the magnitude of the radial gradient in the profile of the bead mean axial velocity, at the exit of the nozzle, to the generation of bead anisotropy is explained by reference to figure 3.33. The mean bead velocity at point "S" which lies close to the wall of the nozzle is slower than that at position "F" which is close to the fast stream of beads around the centreline (see, e.g., figure 3.11(a)) and the beads spread in "fan-like" paths from every point at the exit of the nozzle with the r.m.s. angle of the "fan" given locally by $\pm\arctan[\frac{v'_b(r)}{U_b(r)}]$, which is approximately ±3° near the axis at the nozzle exit. An Eulerian measurement of axial velocity at either I or II is therefore "broadened" by contributions from beads originating at "S" and "F" and since the magnitude of u'_b is not due to turbulence interaction between the gaseous and the particulate phase, results such as those obtained at the exit of the jet pipe, e.g. figure 3.10(b) and 3.12(c), where $u'_b > u'_s$ are not physically impossible. In contrast there is no comparable mechanism for the generation of v'_b and the difference in the way in which u'_b and v'_b are produced explains the large observed anisotropy in the r.m.s. bead velocities.

The mass flux profile, G, of the beads at the exit of the nozzle is also important as a boundary condition for any calculation of the particle-laden jet. The relative number of trajectories arriving at any point in the jet from, for example, near the wall of the nozzle to those

from the axis of the jet is related to the distribution of mass flux at the exit and this information cannot be deduced from the particle velocity profile. It is for this reason that the measurement of G at the exit of the nozzle was one of the objectives of this work.

Fan-spreading also accounts for the high measured value of the shear stress correlation coefficient for the beads. Consider a point near the half-width of the profile of bead flux for, say, $x/d <\approx 20$. If the instantaneous value of u'_b is positive, which implies that the instantaneous velocity is faster than the local mean, then from the geometry of the fan, this implies that the bead originated near the centreline, where bead mean axial velocities are high, and must be associated with positive v'_b. Similar arguments when u'_b is negative imply that the bead originated near the nozzle wall and hence that v'_b is also negative. The straight line trajectories implied by the fan-spreading model suggest that there is a strong correlation between the magnitude of u'_b and v'_b and this leads to the large value of the correlation coefficient. The correlation coefficient of $\overline{u'_b v'_b}$ for the 80 μm beads is smaller than for the 40 μm beads because the profile of U_b is flatter for the larger diameter at the exit of the nozzle. As the beads travel further downstream, the trajectories become less unidirectional and hence the shear stress correlation coefficient of the beads is no longer found to be close to unity. Peak values of the correlation coefficient near unity are thus experimental evidence for fan-spreading.

The preceding paragraphs have two important, related implications for the evaluation of calculations of particulate two-phase flow, and particularly for Lagrangian stochastic simulations. The first is that, at least over the first 20 diameters or so and for beads of diameter greater than 30 μm, the magnitude of u'_b can have little to do with the transfer of turbulence to the particulate flow from the gas. Here it should be noted that the agreement reported between calculations and experimentally measured values of u'_b in a similar jet flow (e.g. Shuen et al., 1985) must be essentially the result of incorporation of measured initial conditions for U_b and v'_b at the exit of the nozzle into the calculation and not because of the good performance of the mathematical model for "turbulent" particulate flow. It is emphasized that this result depends on the value of S_t being smaller than about 0.1. Experiments performed with, for example,

atomised liquids are more likely to result in droplets which acquire turbulence from the continuous phase since liquids possess smaller densities relative to solids and because of the small size classes generated by atomisation.

The second implication is that all of the measurements of the particulate flows suspended in fully turbulent (i.e. Re > 12 000) jets, quoted in table 1.1, relate to fan-spreading of the beads. Fan-spreading ceases when S_t is of order 1 and the axial station where this occurs can be found from equation (B.8) in appendix 3.B by setting $\frac{v'_f}{U_m}$ $\approx$ 0.25 appropriate for the self-similar region. With these values,

$$S_t = 3.29 \ 10^{-4} \ (\frac{x}{d})^2 \ S_e \ (0.25)^{-2} \qquad (3.11)$$

hence $S_t \approx 1$ when

$$(\frac{x}{d})^2 \approx \frac{190}{S_e} \qquad (3.12)$$

It is experimentally desirable to achieve this condition at small values of x/d, which implies large values of S_e : however, the largest practicable values of S_e, which at the same time result in fully-turbulent jets, are of order 0.1 (e.g. this work and Modarress et al., 1982) and hence

$S_t \approx 1$ at $x \approx 40 - 50$ d

Most of the remaining references of table 1.1 have $S_e <\approx 0.01$ and only Solomon et al. (1985a, b & c) have measured sufficiently far downstream for S_t to equal 1, but their flow was generated by an atomising nozzle which produced polydisperse liquid droplets. This implies that new measurements are required which relate to "random walk" motion of the dispersed phase in a particle-laden jet.

The effect of the particles on the characteristics of the gas phase has only been measured in the presence of the 80 μm beads, which do not respond to the fluid turbulence ($S_t < 1$). The centreline axial r.m.s. fluctuation (figure 3.18(b)) of the single phase, u'_s, increases to a maximum value at x/d = 8. Similarly the maximum value

of the gas phase r.m.s. fluctuation u'_f is lower and displaced farther downstream from the nozzle, so u'_f appears to be reduced relative to the single phase close to the nozzle and larger downstream. Thus the presence of the beads not only delays the mean development of the jet, but also changes the turbulence characteristics of the gas.

There are three candidate mechanisms for the observed effects. The first is that the addition of the particles results in increased dissipation. Pismen & Nir (1978) examined the dissipation rate of isotropic turbulence at the presence of particles with no slip velocity by using a parameter, λ, the ratio of a characteristic time of the fluctuations corresponding to the maximum of the turbulence spectrum to the particle relaxation time. They showed that the maximum dissipation rate per unit particle mass is achieved for particles with relaxation time of the same order of magnitude as the characteristic turbulence time ($\lambda \approx 1$) and the increase of the relative dissipation rate with wavenumber of the spectrum k is most drastic at intermediate wavelengths for values of $\lambda = 0(1)$. The parameter λ is equivalent to the turbulent Stokes number, S_t, which was used in the above analysis. So close to the jet nozzle where the slip velocity between particles and gas is very small and $0.1 < S_t < 1$ (Table 3.5), it is expected to have higher dissipation rate per unit particle mass than for the single phase flow.

The second is due to Al Taweel and Landau (1977), who examined the turbulence energy dissipation in dispersed two phase jets and found that the presence of the particles alters the turbulence structure of the jets by attenuating the high frequency fluctuations while the energy containing low frequency eddies are not affected. The turbulence intensity of the gas phase thus reduces with increasing mass loading and decreasing particle diameter. Their conclusions agree well with the present experimental results. However, the model they used assumes that the particles are always confined to the same fluid eddy (no mean slip velocity), so they cannot predict the effect observed at x/d = 28, figure 3.20(d), where u'_f is greater than u'_s.

The third suggestion which accounts for an increase in the turbulence of the gas, is that it is due to the wakes "shed" from the beads due to the mean slip velocity between the two phases. It is doubtful whether this is possible because the slip Reynolds number is about 20 and hence well below the value 44, at which the wake behind

a sphere becomes unsteady. Furthermore, the scale of the wake will be of the order of the diameter of the beads and hence close to the Kolmogorov microscale, rather than near the energy-containing scales as would be necessary for the increase of the gas turbulence. It is more likely that the increase in u'_f is due to the generation of $\overline{u_f^2}$ by $[\overline{u_f v_f} \frac{\partial U_f}{\partial r}]$ which is larger due to the increase in the value of mean rate of strain, $\partial U_f / \partial r$ as the fluid is accelerated by the momentum transfer from the particles.

3.6 Conclusions

i) This work describes the velocity and mass flux characteristics in the non self-similar region ($x/d < 30$) of round turbulent bead-laden jets for bead diameters of 200, 80 and 40 μm, at two mass loadings. The corresponding volume fractions were always sufficiently small that bead-to-bead interaction is negligible.

ii) The mean and r.m.s. motion of the beads is governed by their inertia which is conveniently characterised by the mean Stokes number (S_m) and the turbulent Stokes number (S_t), which increase as the product of the square of the axial distance and mean exit Stokes number (S_e).

iii) The mean velocity of the 200 μm beads is virtually constant and there is little influence of mass loading on their mean motion, because the mean Stokes number is small. The interaction between the phases is thus "one-way", from the beads to the gas.

iv) The centreline velocity of the 80 μm beads decays independently of mass loading for the values examined here. The mean velocity of the beads at the jet exit is slower than that of the fluid and becomes slower still with increasing mass loading. The flux and concentration of the beads is larger near the axis than at the walls of the nozzle.

v) The presence of the 80 μm beads influences the fluid flow. The centreline decay of the mean velocity of the gas phase is slower in the presence of the beads and the gas phase turbulence is lower close to the nozzle of the jet and higher further downstream. It is likely that the increase in turbulence is related to the increase in the mean rate of strain, $\partial U_f / \partial r$. Close to the nozzle the mean rate of strain has

not been changed by the presence of the beads. The turbulence is reduced by the increased gas phase dissipation rate per unit particle mass in the presence of the beads with relaxation time of the order of the characteristic turbulence time.

vi) For the 40 μm beads, the rate of decay of the centreline bead velocity decreases with increasing mass loading. The axial r.m.s. velocity of the beads is larger than that of the single phase jet for $x/d \gtrapprox 15$ and is always larger than the radial r.m.s. velocity of the beads. The downstream location of the maximum value of the centreline r.m.s. velocity of the beads increases with increasing loading.

vii) The "fan-spreading" model for the motion of the beads refers to quasi-unidirectional trajectories of the beads from the exit of the jet up to about 20 diameters downstream for the 40 μm beads, and farther for the larger beads. This model accounts for the observed high anisotropy in the r.m.s. velocities of the beads, u'_b being greater than u'_f at some locations, and the high cross-correlation coefficient of the beads relative to that of the turbulence in the single phase jet. It also resolves the apparently paradoxical result that the beads spread due to turbulent motion even though theoretical arguments suggest that the beads cannot acquire turbulence from the gaseous phase. An important implication for the evaluation of mathematical models of particulate two phase flow is that the observed value of u'_b, here and in the majority of experiments published in the literature, can have little to do with transfer of turbulence from the gas to the beads.

TABLE 3.1

Nominal properties of glass beads

	40 μm[a]	80 μm[b]	200 μm[b]
Nominal diameter range(μm)	37 - 44[c]	60 - 95[d]	165 - 255[e]
Density (kg m^{-3})	2420.	2950.	2950.
Stokesian time constant (ms)	11.9	47.6	298.
Terminal velocity (cm s^{-1}) †	11.1	44.8	154.
Time constant based on terminal velocity (ms)	11.1	45.7	157.
Refractive index	1.51	1.6	1.6

[a] Ferro Corporation, Jackson, Mississippi 39205, U. S. A.

[b] Jencons (Scientific) Ltd., Leighton Buzzard, Beds., LU7 8UA, England

[c] "Class V, close sized uni-spheres". 90% within size range; 90% true spheres; < 2% irregularly shaped beads.

[d] "Grade 15". 20% normally outside 42 - 102 μm

[e] "Grade 11". 80% within size range; remaining 20% normally between 124 - 318 μm

† based on table 5 in Fuchs (1964, p. 32)

TABLE 3.2

Principal characteristics of the phase-Doppler anemometer

1 Watt (nominal) Ar^+ laser wavelength	514.5	nm
Beam diameter, at e^{-2} intensity, of laser	1.25	mm
Focal length of lenses:		
imaging lens from laser to grating	80	mm
collimating lens after grating	300	mm
imaging lens to form measuring volume	300	mm
Number of lines on radial diffraction grating	8192	-
Shift frequency (nominal) due		
to rotation of grating	3	MHz
Short-term stability of shift frequency (r.m.s.)	0.3	%
Beam separation	27.7	mm
Measured half-angle of intersection	2.64	degrees
Calculated dimensions of beam intersection		
volume at e^{-2} intensity	1.13	mm
	0.052	mm
	0.052	mm
Fringe spacing	5.58	μm
Calculated number of fringes		
within e^{-2} intensity	8	-
Frequency to velocity conversion factor	0.18	MHz/(ms^{-1})
Location of collection optics from		
forward scatter	30	degrees
Focal length of collimating lens in		
receiving optics module	600	mm
Apertures at collimating lens:		
dimension of rectangular apertures	45 x 6	mm
separation between apertures 1 and 2	25	mm
separation between apertures 1 and 3	50	mm
Focal length of imaging lens in receiving		
optics module	300	mm
Width of spatial filter before the		
photodetectors	100	μm
Magnification of receiving optics	2	-
hence effective length of measuring volume	200	μm
Phase angle-to-diameter conversion factor		
for channel 1 and 3	0.263	μm/degree

TABLE 3.3

Estimates of systematic and random errors in quantities measured

QUANTITY	SYSTEMATIC ERROR	RANDOM ERROR
position	1. mm	± 1. mm
Mass loading of beads	-	5. %
Bulk gas velocity	-	3. %
Gas phase in presence of beads:		
mean velocity	3. to 4 % (towards U_b)	-
r. m. s. velocity	+5. to +10 %	-
Beads and "clean jet":		
mean velocity	+ 3. %	1. %
axial r. m. s. velocity	- 3. %	3. %
radial r. m. s. velocity	- 5. %	5. %
cross-correlation	- 4. %	4. %
cross-correlation coefficient	7. %	6. %
flux of beads		3. %

TABLE 3.4

Values of centerline velocity and flux used to normalise quantities

For clean jet:

U_{om} 14.7 ms^{-1}

For 40 μm beads:

13% loading:

G_{om} 1225 # s^{-1} {area of measurement volume}$^{-1}$

U_{om} 13.1 ms^{-1}

80% loading:

G_{om} 3461 # s^{-1} {area of measurement volume}$^{-1}$

U_{om} 12.2 ms^{-1}

For 80 μm beads:

23% loading:

G_{om} 299 # s^{-1} {area of measurement volume}$^{-1}$

U_{om} 12.4 ms^{-1}

86% loading:

G_{om} 844 # s^{-1} {area of measurement volume}$^{-1}$

U_{om} 11.4 ms^{-1}

TABLE 3.5

Turbulent Stokes number as a function of axial distance along a jet for three bead diameters

X/D	v_s/U_m	τ_f	S_t		
(-)	(-)	(ms)	40 μm	80 μm	200 μm
10	0.10	3	0.25	0.06	0.01
20	0.20	3	0.25	0.06	0.01
30	0.22	7	0.59	0.15	0.02
40	0.25	13	1.10	0.27	0.04

TABLE 3.6

MOMENTUM FLUX OF 40 AND 80 μm BEADS

Clean flow exit momentum flux : 0.242×10^{-1}

Case	40μm-13%	40μm-80%	80μm-23%	80μm-86%
Calculated momentum flux ($x10^{-1}$)				
- X/D = 0.1	0.041	0.238	0.076	0.265
Ratio of momentum fluxes of beads to the single phase jet				
- X/D = 0.1	0.17	0.98	0.31	1.09

APPENDIX 3.A

Derivation of expressions for the axial variation of the timescales of the "energy containing motion" & Kolmogorov scales in a jet

The following analysis establishes the axial variation in the timescales of the energy-containing, or large-eddy, motions and of the Kolmogorov scales in a turbulent round jet; these scales are compared, in the introduction, with the inertial timescale of typical beads. The ratio of the Kolmogorov timescale, τ_k, to the large eddy timescale, t_e, is given by (Tennekes & Lumley, 1972)

$$\frac{\tau_k}{t_e} = \left(\frac{v'_f \, \ell}{\nu_f} \right)^{-0.5} \qquad (A.1)$$

where ℓ is the lengthscale associated with the large eddies. If ℓ is identified as the jet half-width and v'_f is taken to be $\approx 0.25 \, U_m$, where U_m is the local centreline velocity, then using equations (B.6) and (B.7) in Appendix 3.B equation (A.1) becomes

$$\frac{\tau_k}{t_e} = (0.139 \, Re)^{-0.5} \qquad (A.2)$$

where Re is the Reynolds number of the jet based on the mean velocity at the exit of the nozzle. For fully turbulent flow in a jet, Re must be of the order of 10000 so that the smallest value for the ratio is

$$\frac{\tau_k}{t_e} = 0.022 \qquad (A.3)$$

If

$$t_e = \frac{\ell}{v'_f} \qquad (A.4)$$

then

$$t_e = 0.05 \left(\frac{x}{d} \right)^2 \left(\frac{d}{U_o} \right) \qquad (A.5)$$

For completeness, we mention that T_f, the Lagrangian scale used in Appendix 3.B, is about one-tenth of t_e, as quoted in Tennekes & Lumley (1972).

APPENDIX 3.B

Estimation of bead turbulent Stokes number in a turbulent, round jet

(i) Turbulent Stokes number at jet exit

The Lagrangian integral scale of the gas, T_f, can be estimated from (Vames & Hanratty, 1988, Tennekes & Lumley, 1972)

$$T_f = \frac{\nu_{eff.f}}{\overline{\overline{v_f^2}}} \qquad (B.1)$$

and where we will use estimates of the values of $\nu_{eff.f}$ and $\overline{\overline{v_f^2}}$ from a clean jet for convenience and since there is little error involved in doing so. Now a correlation for $\nu_{eff.f}$ which is appropriate to the Reynolds number of this flow is (Vames & Hanratty, 1988)

$$\frac{\nu_{eff.f}}{u^* 2 R} = 0.037 \qquad (B.2)$$

where R is the pipe radius and u* can be found from a Nikuradse-Moody diagram since

$$f = 8 \frac{u^{*2}}{U_m^{\ 2}} \qquad (B.3)$$

and f = 0.027 at this Reynolds number for a hydraulically smooth pipe. Hence $\nu_{eff.f} = 3 \times 10^{-4}$ m^2/s and, from our measurements that v'_f is approximately 0.05 U_m or 0.65 m/s, v_f^2 is 0.4 m^2 / s^2. Substituting these values into equation (B.1) gives T_f = 0.75 ms. This gives S_t of about 0.06, 0.016 and 0.003 for glass beads of diameter of 40, 80 and 200 μm respectively and it is hence likely that even the 40 μm beads move in unidirectional motion, at least within the pipe.

(ii) Turbulent Stokes number as a function of axial distance in jet

In the jet we revise our estimate of $\nu_{eff.f}$ as follows (Spalding, 1979)

$$\nu_{eff.f} = 0.0256\ U_m\ r_{1/2} \qquad (B.4)$$

and hence from equation (B.2) and rearranging

$$\mathcal{T}_f = (0.0256\ \frac{r_{1/2}}{U_m})\ (\frac{v_f^2}{U_m^2})^{-1} \qquad (B.5)$$

where (Spalding, 1979)

$$r_{1/2} = 0.0845\ x \qquad (B.6)$$

$$U_m = 6.57\ (\frac{d}{x})\ U_o \qquad (B.7)$$

Hence

$$\mathcal{T}_f = 3.29 \times 10^{-4}\ (\frac{x}{d})^2\ (\frac{d}{U_o})\ (\frac{v'_f}{U_m})^{-2}$$

and thus

$$S_t = 3.29 \times 10^{-4}\ (\frac{x}{d})^2\ (S_e)\ (\frac{v'_f}{U_m})^{-2} \qquad (B.8)$$

where S_e is the exit-mean-Stokes number defined in equation (1.15). In table 3.5, we summarise the values of S_t as a function of downstream distance for 200, 80 and 40 μm beads and for convenience we have approximated v'_f by v'_s. The value of $\mathcal{T}_f$ is the same at x/d = 10 and 20 because the increase in x/d is matched by the change in (v'_f / U_m). The magnitudes of S_t suggest that by 30 diameters downstream of the exit, only the 40 μm beads may be responsive to the turbulent motion of the gas and that even by 40 diameters it is unlikely that the 80 μm beads are responsive.

APPENDIX 3.C

Estimation of the drag coefficient of the beads in the jet

Assuming that gravitational forces are negligible, that the gas density is small relative to the particle density, that the relative velocity between the particle and the gas flow remains constant at the observation region and that the particle is spherical, the inertia force balances the drag force acting on it, without taking into account the Basset, the added mass and the pressure term forces :

$$m_b \frac{dV_b}{dt} = \frac{1}{2} \rho_f V_r^2 C_D \frac{\pi d_b^2}{4} \qquad (C.1)$$

where $m_b = \rho_b \frac{\pi d_b^3}{6}$ is the mass of the spherical bead, ρ_b is the density of the bead, ρ_f is the fluid density, V_r is the relative velocity between the two phases, V_b is the bead velocity, d_b is the bead diameter and C_D is the drag coefficient of the bead in the jet flow.

If m_b is substituted to equation (C.1) the following expression for the drag coefficient of the spherical particle is derived:

$$C_D = \frac{4}{3} \left(\frac{\rho_b}{\rho_f} \right) \left(\frac{d_b \, dV_b/dt}{V_r^2} \right) \qquad (C.2)$$

The deceleration, dV_b / dt, of the bead can be calculated from the axial bead velocity gradient in the jet. If we assume that the particle moves with the local measured mean velocity V_0 at x/d = 20 and decelerates over a distance x up to x/d = 28 with a constant rate to reach the mean velocity V at x/d = 28 then the rate of bead deceleration can be calculated

$$\frac{dV_b}{dt} = \frac{V_0^2 - V^2}{2x} \qquad (C.3)$$

The relative velocity for the 80 μm beads at x/d = 28 can be estimated because the gas velocity at the presence of the particles has been measured for both mass loadings. For the 40 μm beads the

relative velocity can be estimated only for the lower (13%) mass loading, assuming that the gas phase has not been affected from the presence of the beads.

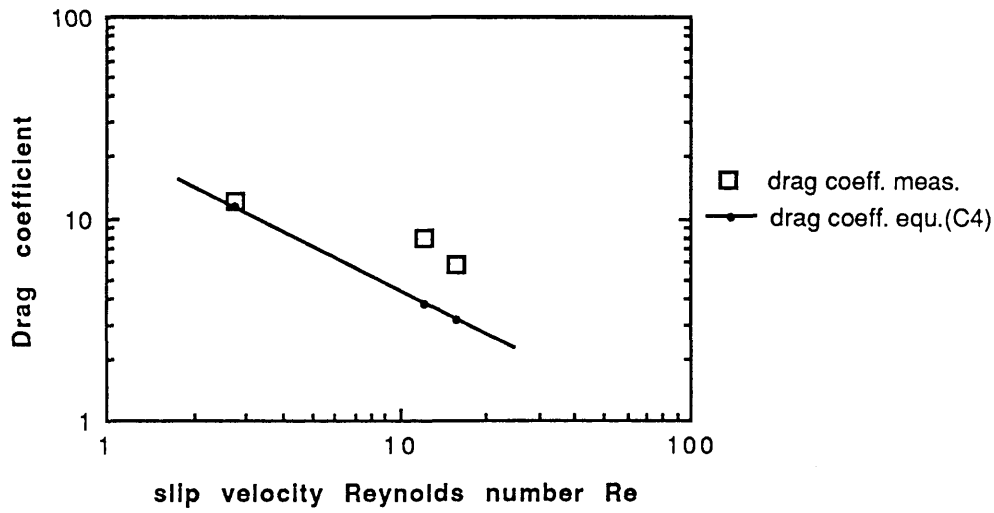
The results from the equation (C.2) as a function of the bead Reynolds number are given at the following table.

Beads	C_D meas.	Re_b	C_D correl.
40 μm-13%	12.19	2.72	11.40
80 μm-23%	5.92	15.72	3.15
80 μm-86%	7.92	12.21	3.72

The values of C_D correl. are from the following correlation between drag coefficient and bead Reynolds number, Re_b, mentioned by Clift et al, 1978 :

$$C_D \text{ correl.} = \frac{24}{Re_b} \left(1 + 0.1315\, Re_b^{(0.82-0.05w)} \right) \qquad (C.4)$$

where $w = \log_{10} Re_b$ and is valid for $0 < Re_b < 20$, where $Re_b = \frac{V_r D_b}{\nu_f}$.



It can be seen at the above figure that the drag coefficient of 40 μm beads-13% mass loading is close to that expected from the correlation for a single sphere. However, the 80 μm beads do not follow the relation (C.4), and this suggests that the drag coefficient of particles with a certain mass loading in a flow is different from that of a single sphere. More work is needed to establish this result.

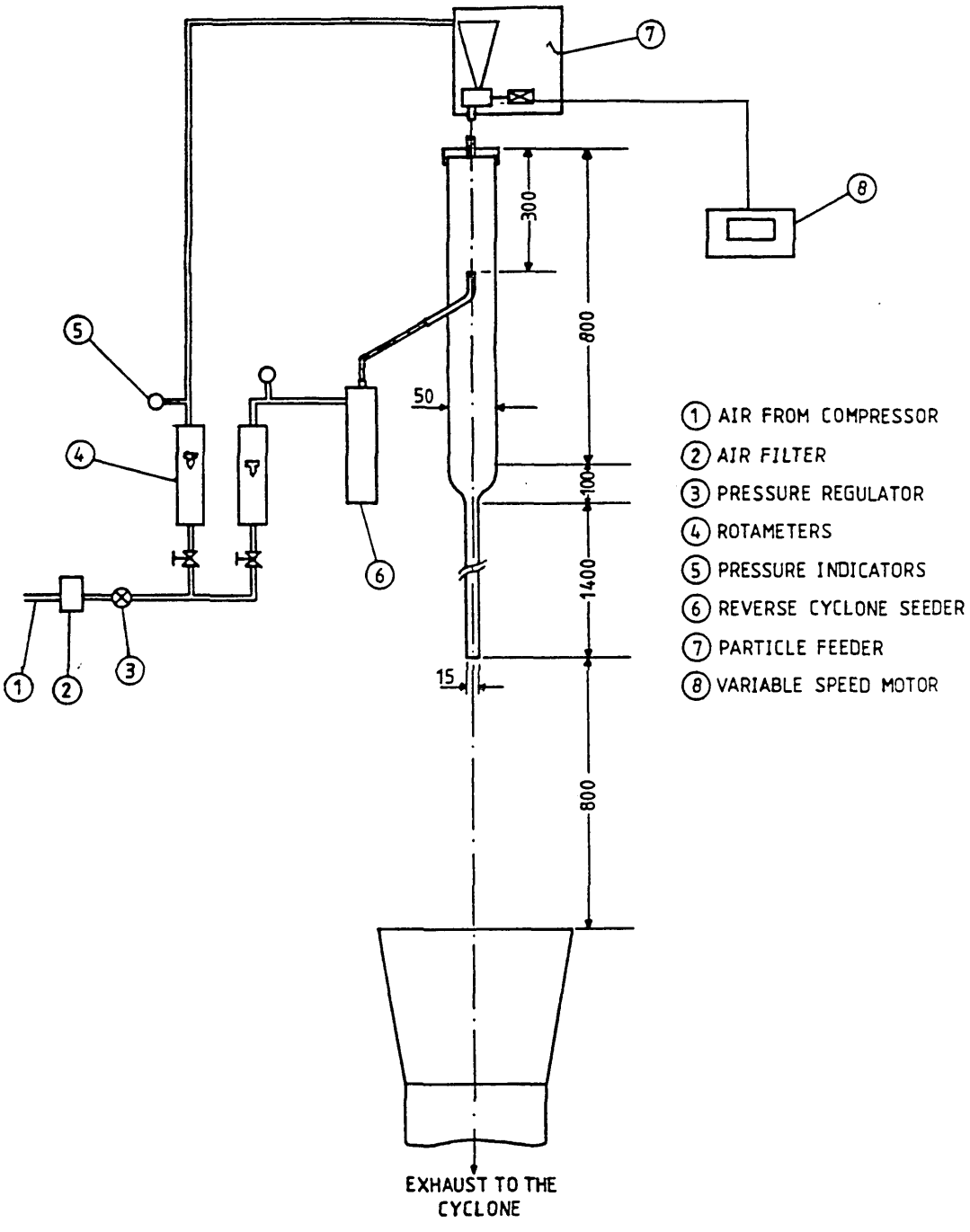


FIGURE 3.1 Experimental arrangement.

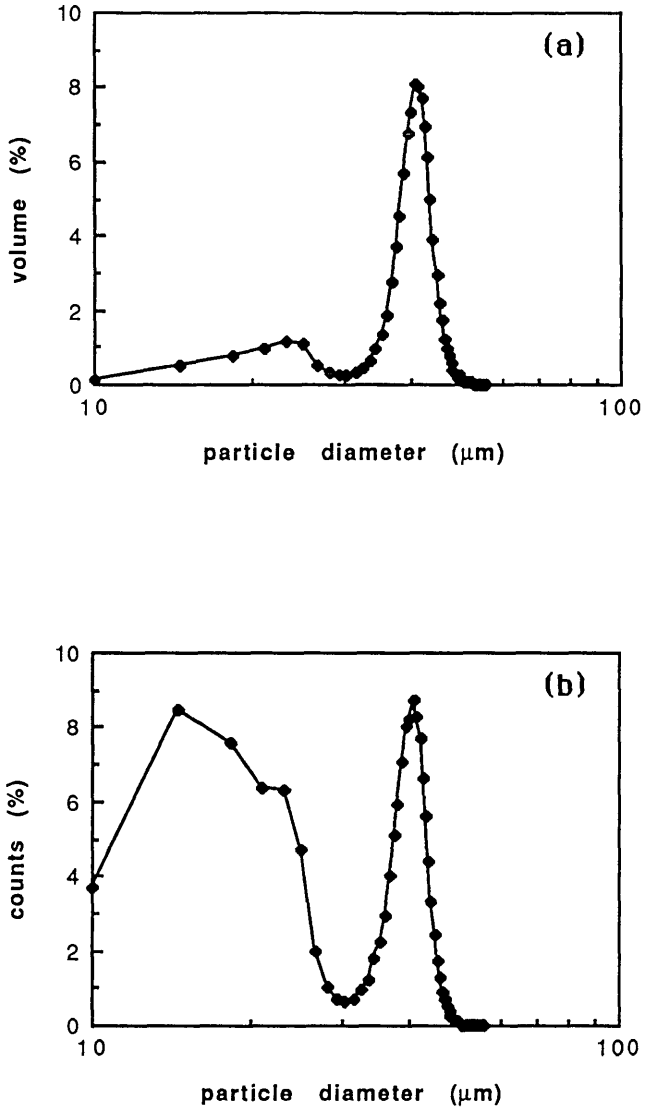


FIGURE 3.2 Size distributions of 40 μm beads used in the experiment; (a) volume (%), (b) number of counts (%).

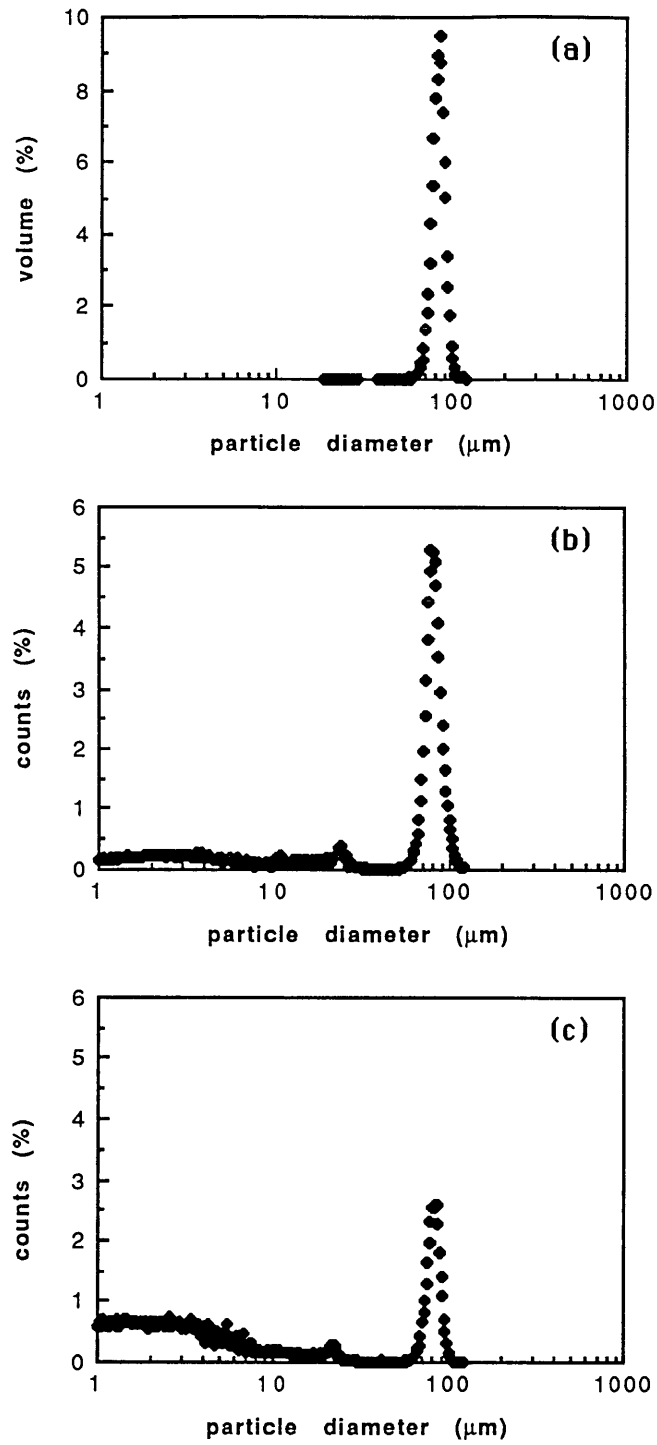


FIGURE 3.3 Size distributions of the 80 μm beads used in the experiment; (a) volume (%) of new beads, (b) counts (%) of new beads, (c) counts (%) of beads after half year use.

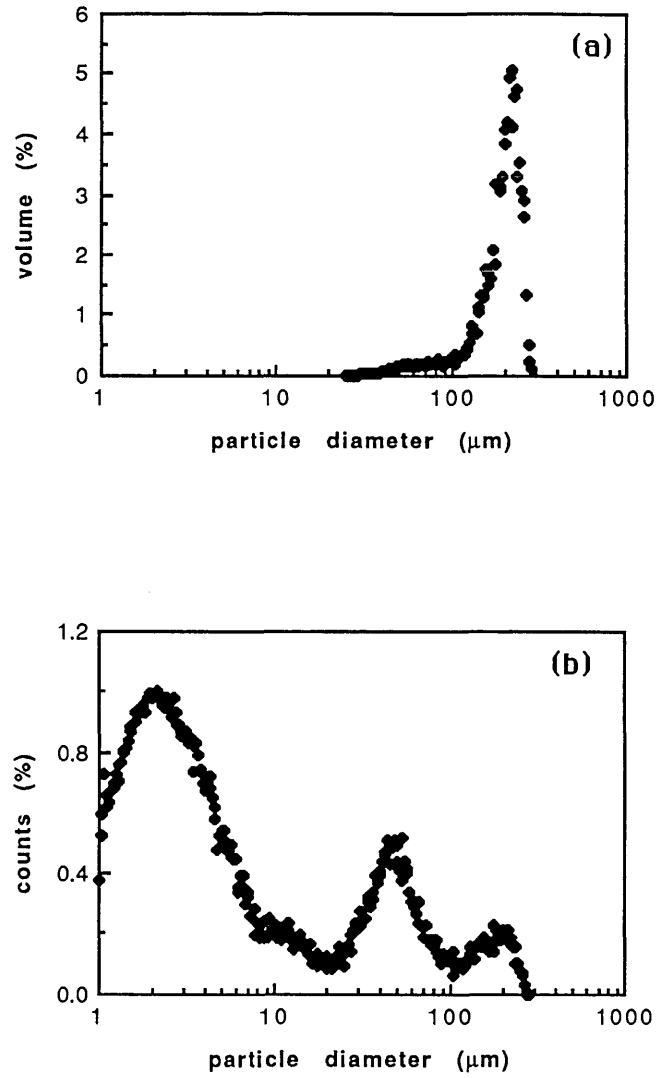


FIGURE 3.4 Size distributions of the 200 μm beads used in the experiment; (a) volume (%) and (b) counts (%) of new beads.

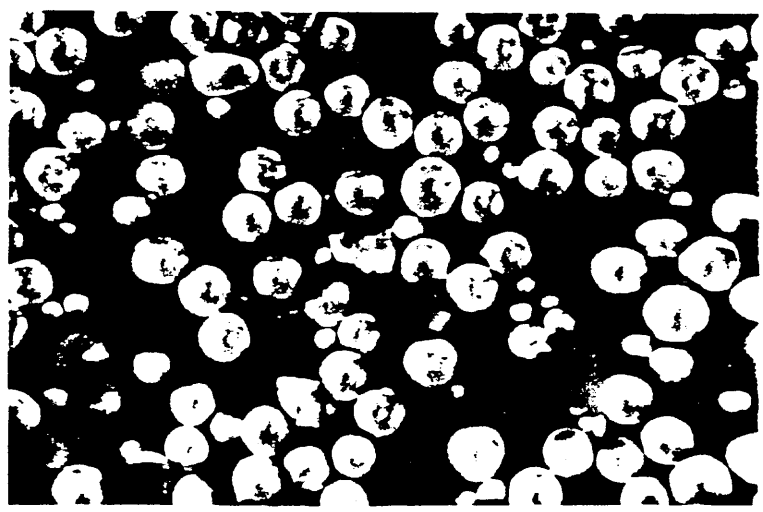


FIGURE 3.5 40 µm beads viewed by a scanning electron microscope at a magnification of ≈ 200.

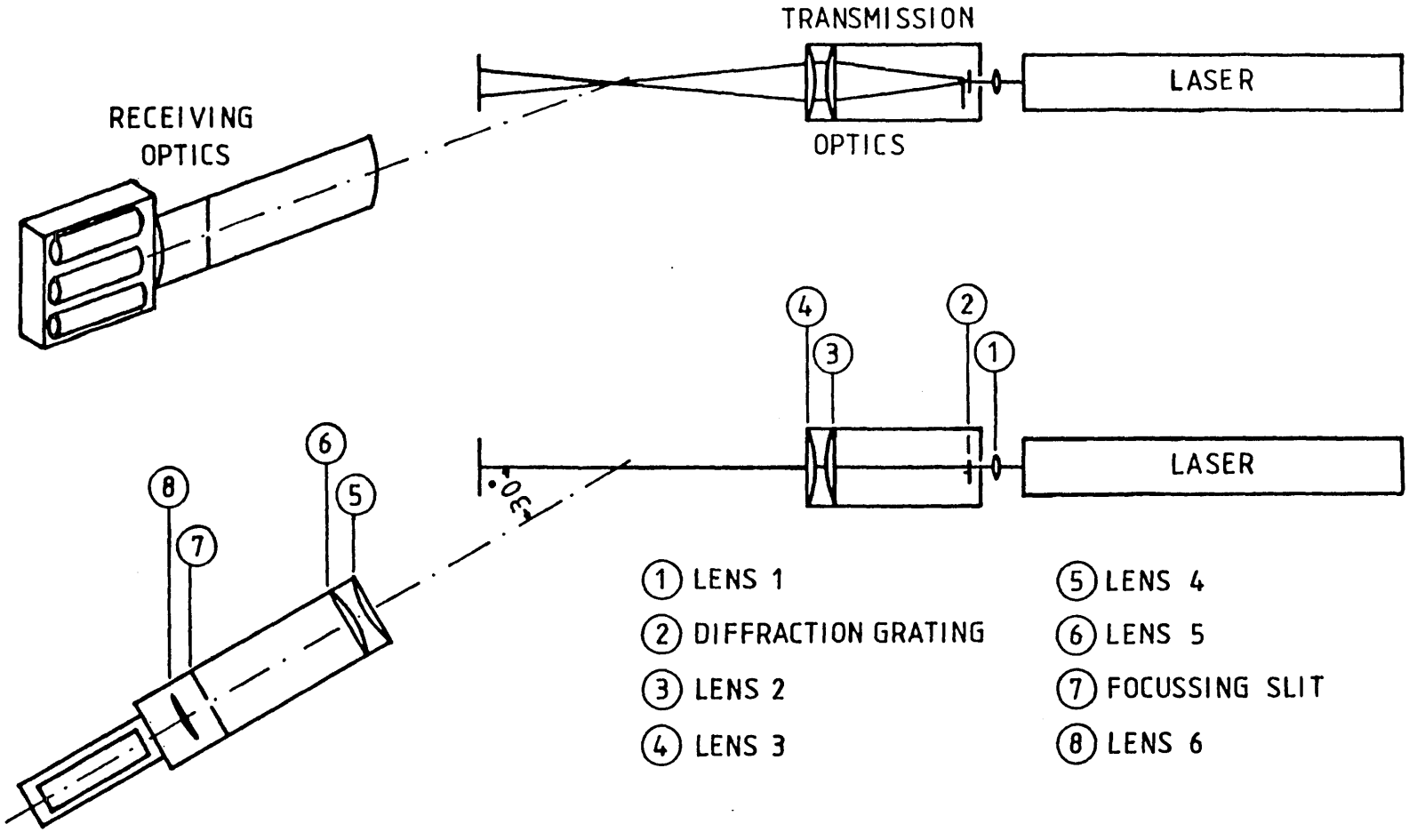


FIGURE 3.6 Optical configuration.

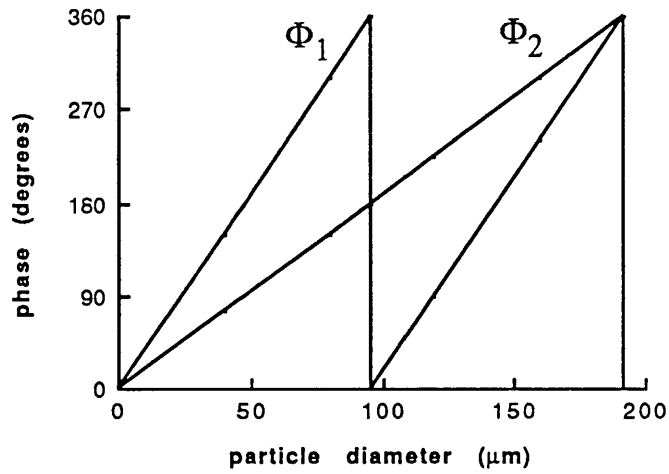


FIGURE 3.7 Phase-Doppler calibration curve.

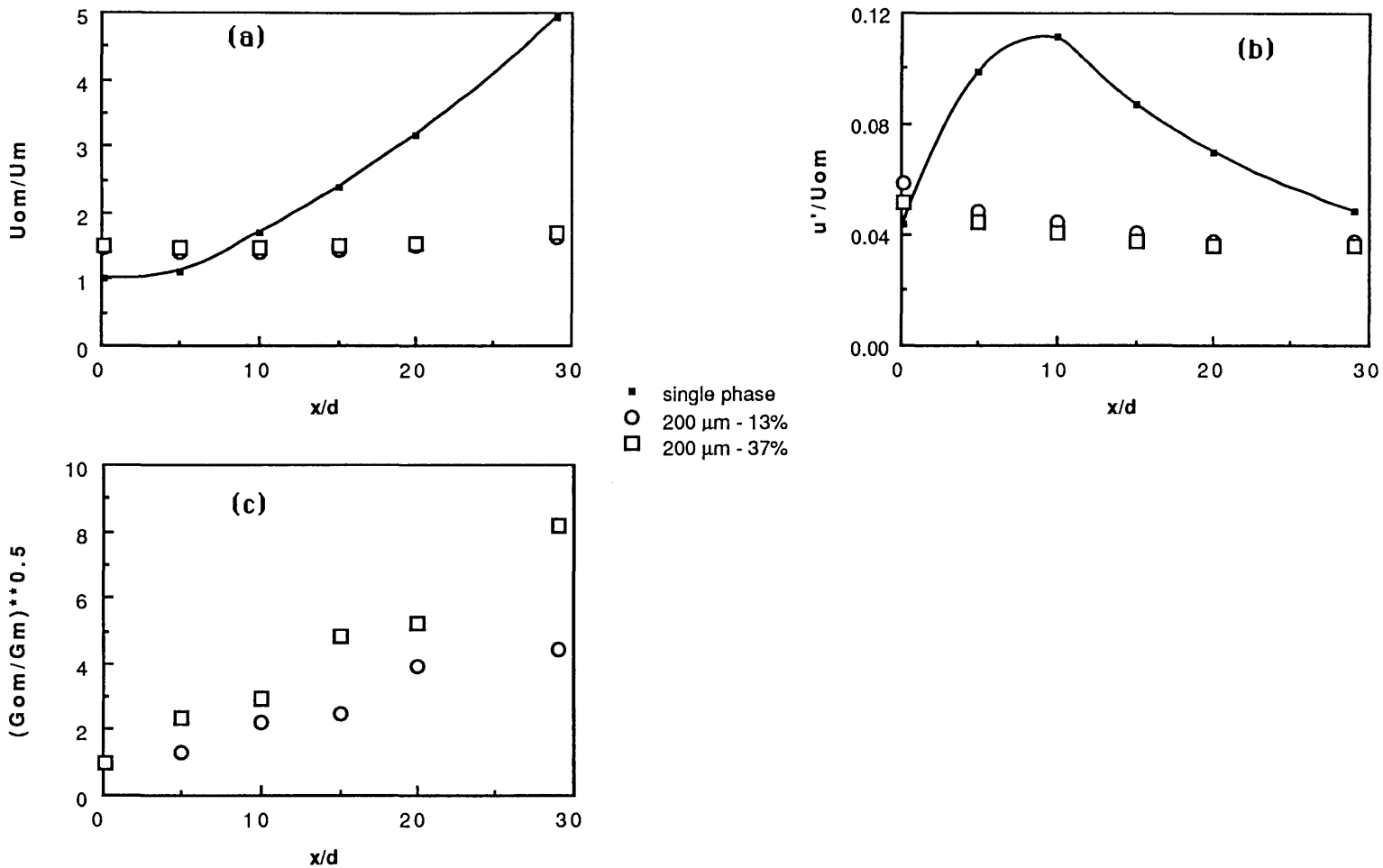


FIGURE 3.8 Centreline profiles of (a) mean and (b) rms axial velocity (U, u') and (c) flux normalised by the exit centreline flux, Gom, for 200 µm beads for mass loadings of 13% (circle) and 37% (square) compared to the single phase. Normalisation of velocities is by the single phase exit velocity, Uom.

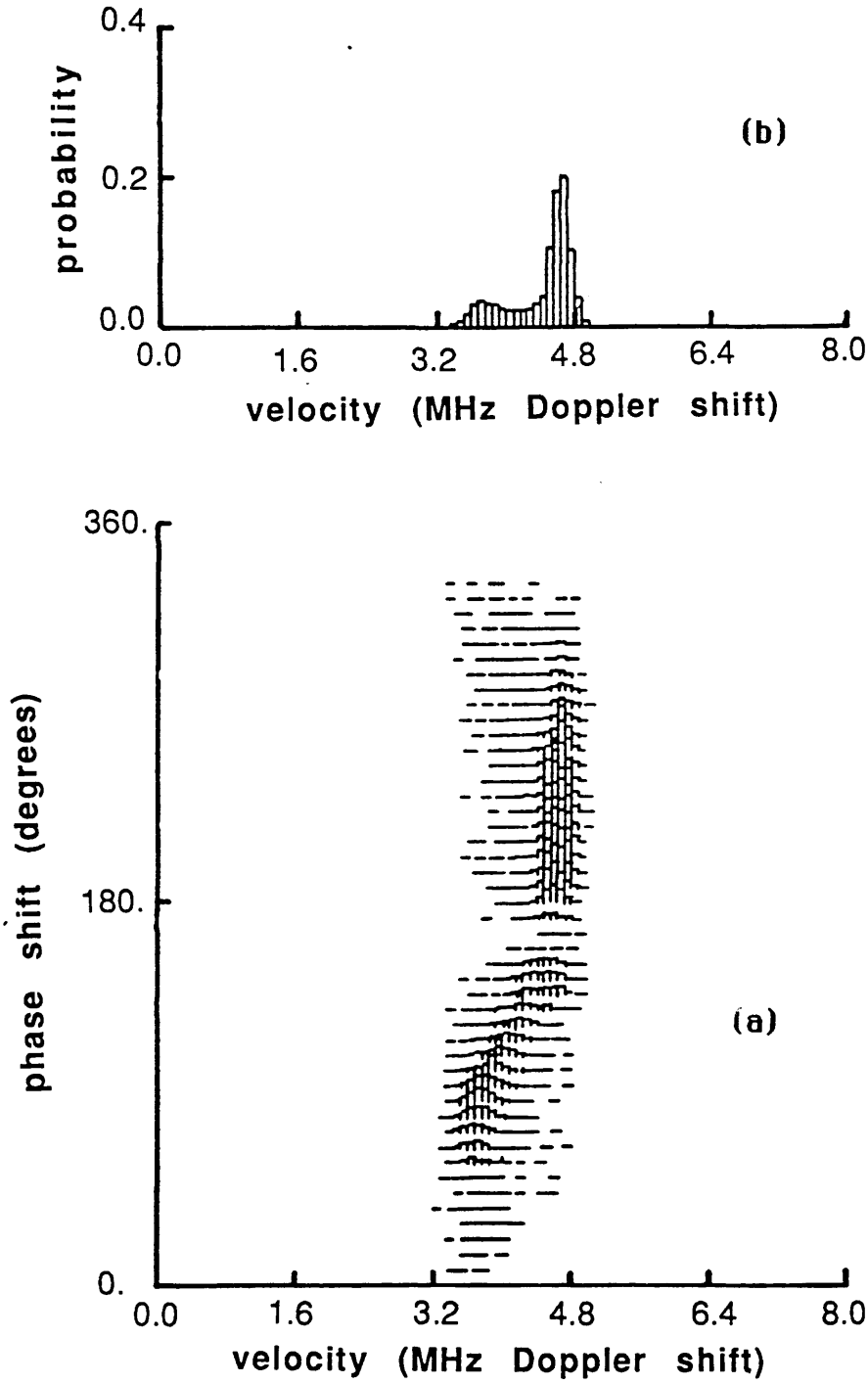


FIGURE 3.9 Velocity and size distributions for the 200 μm beads measured by the phase-Doppler anemometer; (a) size-velocity probability distribution showing correlation between low velocities and small bead diameter, (b) velocity probability distribution corresponding to (a) showing bimodal distribution due to small beads.

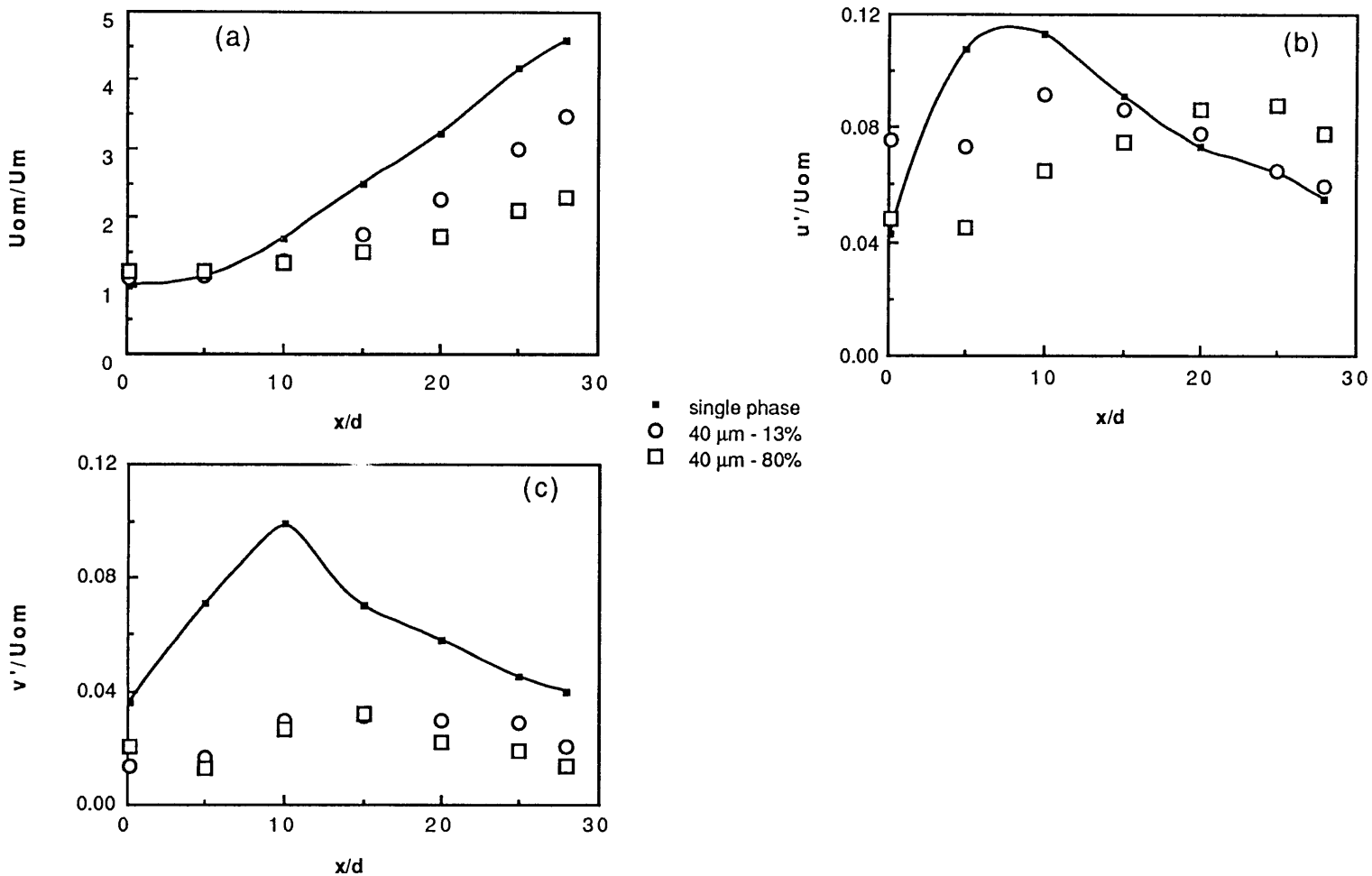


FIGURE 3.10 Centreline profiles of (a) mean axial, U, (b) axial rms, u', and (c) radial rms, v', velocities for 40 µm beads for mass loadings of 13% (circle) and 80% (square) compared to the single phase. Normalisation is by the single phase exit mean velocity, Uom.

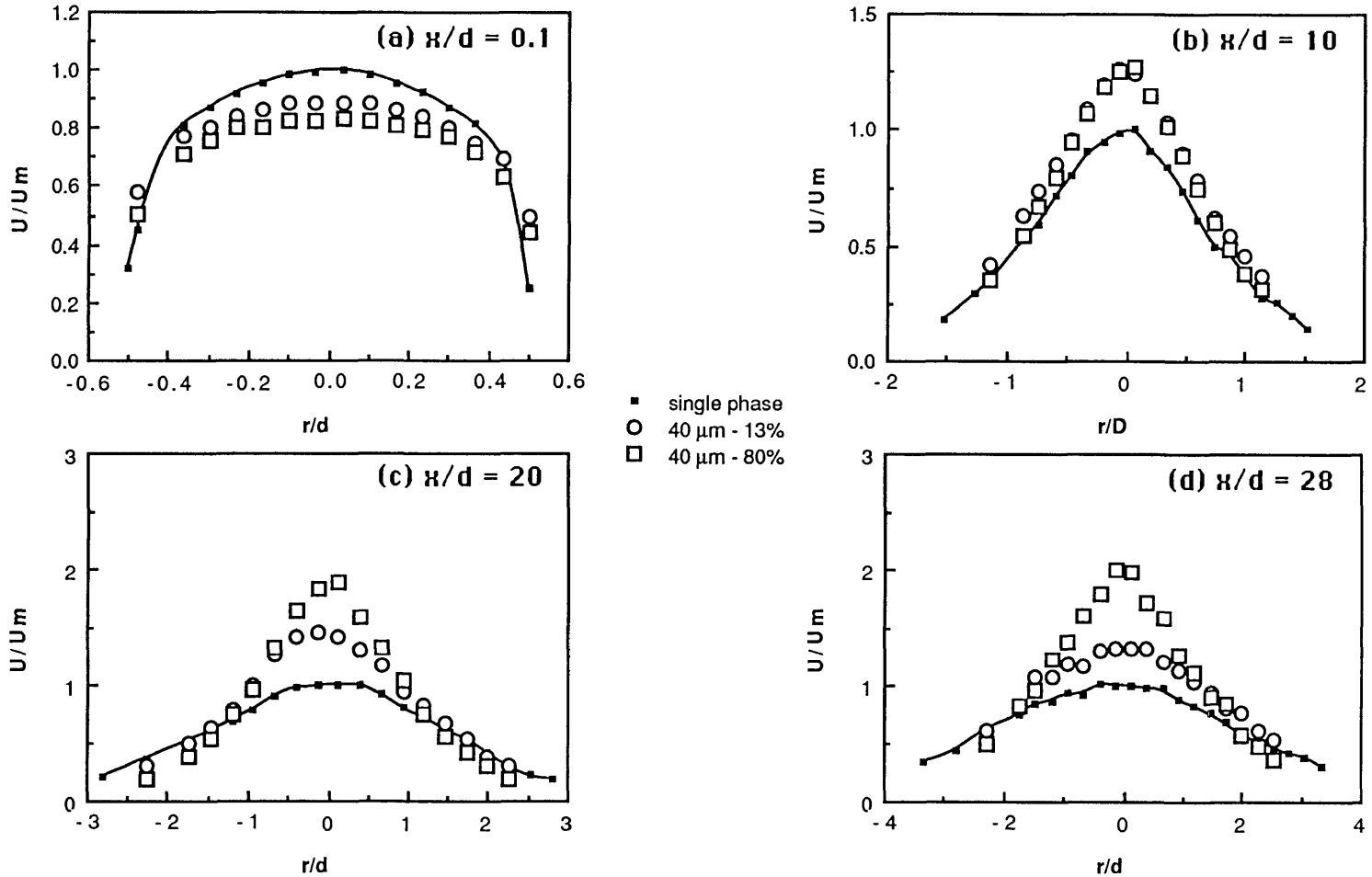


FIGURE 3.11 Radial profiles of mean axial velocity (U) for 40 μm beads at x/d = 0.1, 10, 20 and 28 for mass loadings of 13% (circle) and 80% (square) compared to the single phase. Normalisation is by the single phase centreline velocity, Um.

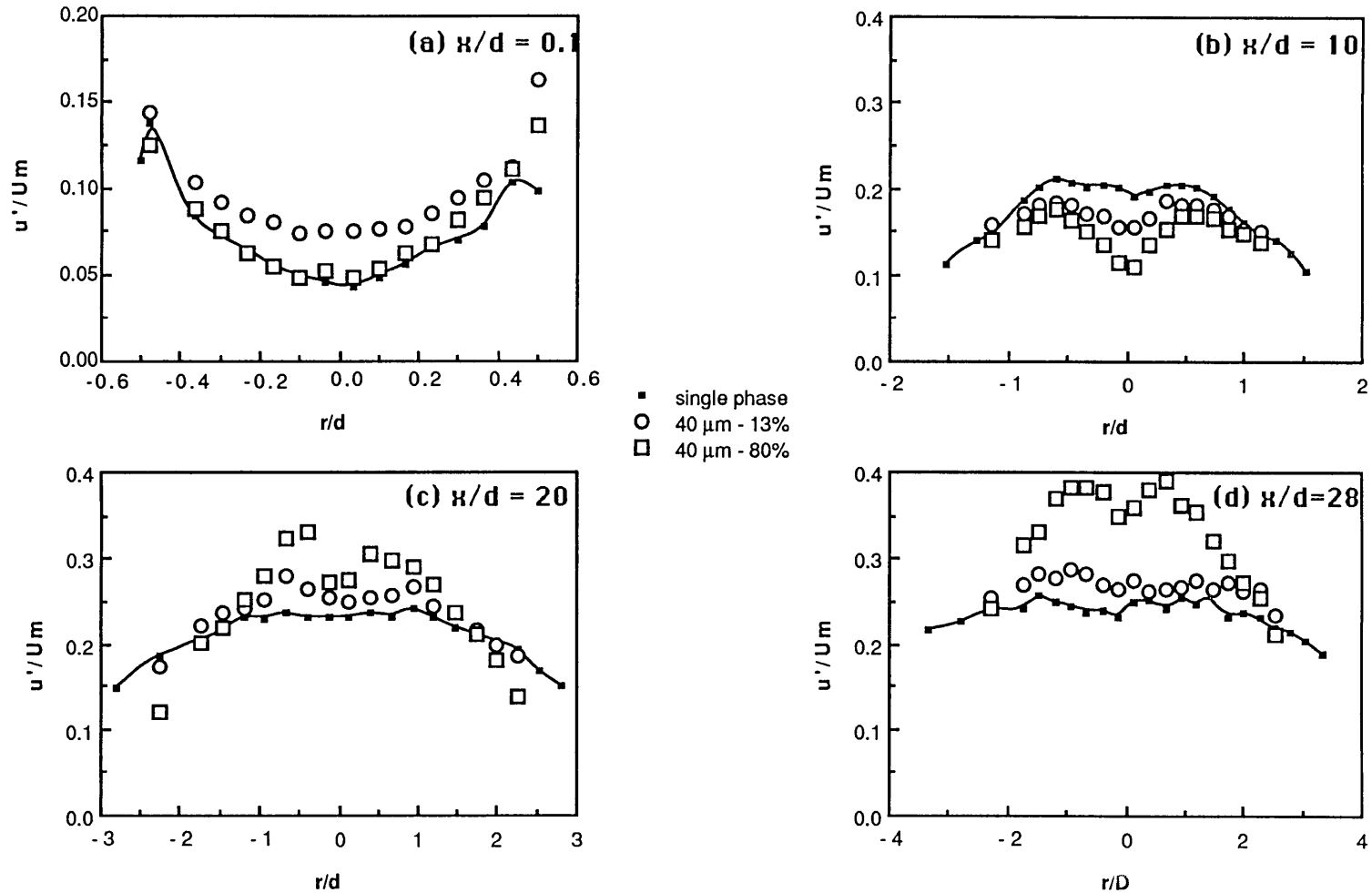


FIGURE 3.12 Radial profiles of axial rms velocity (u') for 40 µm beads at x/d = 0.1, 10, 20 and 28 for mass loadings of 13% (circle) and 80% (square) compared to the single phase. Normalisation is by the single phase centreline velocity, Um.

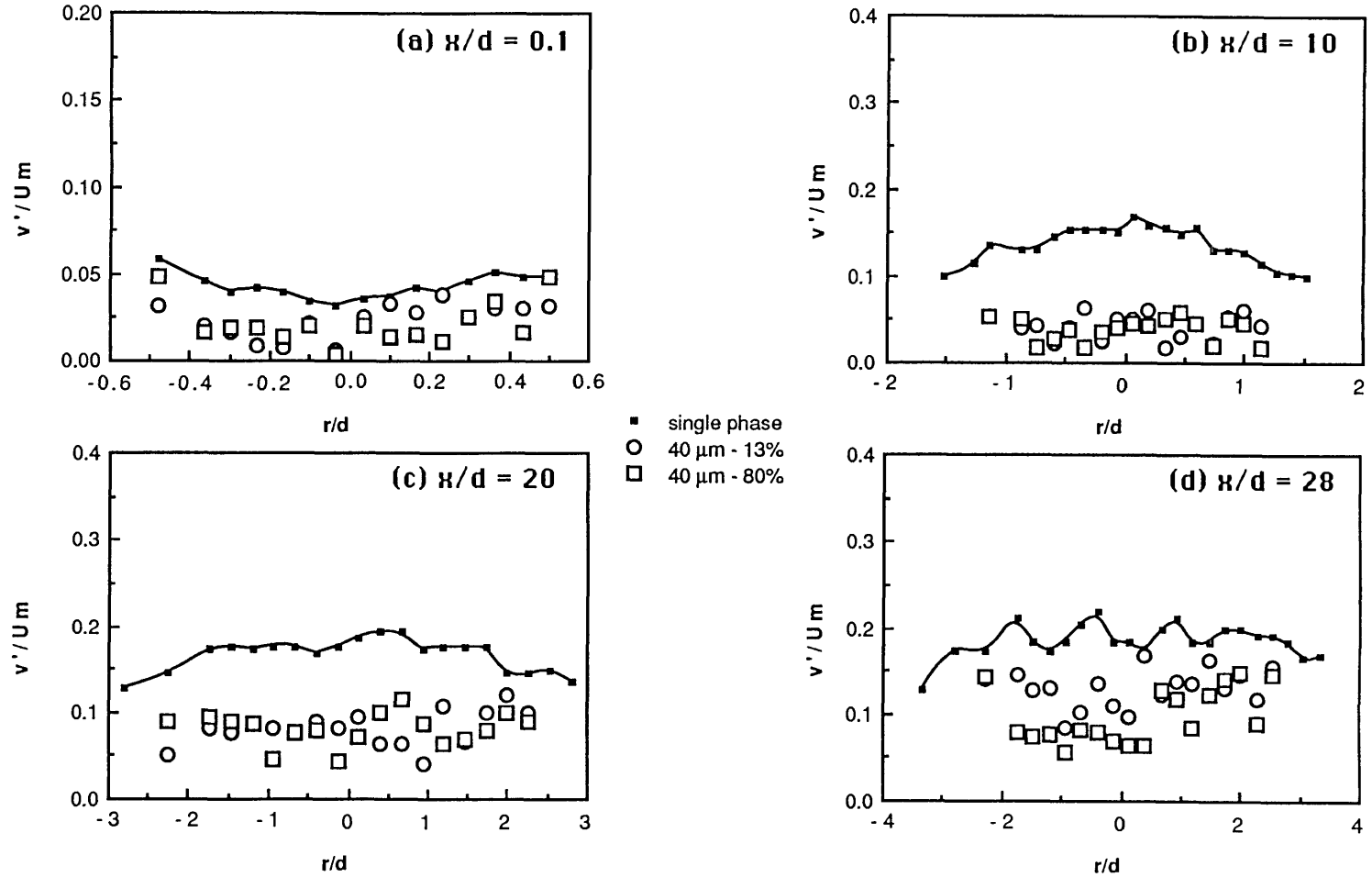


FIGURE 3.13 Radial profiles of radial rms velocity (v') for 40 μm beads at x/d = 0.1, 10, 20 and 28 for mass loadings of 13% (circle) and 80% (square) compared to the single phase. Normalisation is by the single phase centreline velocity, Um.

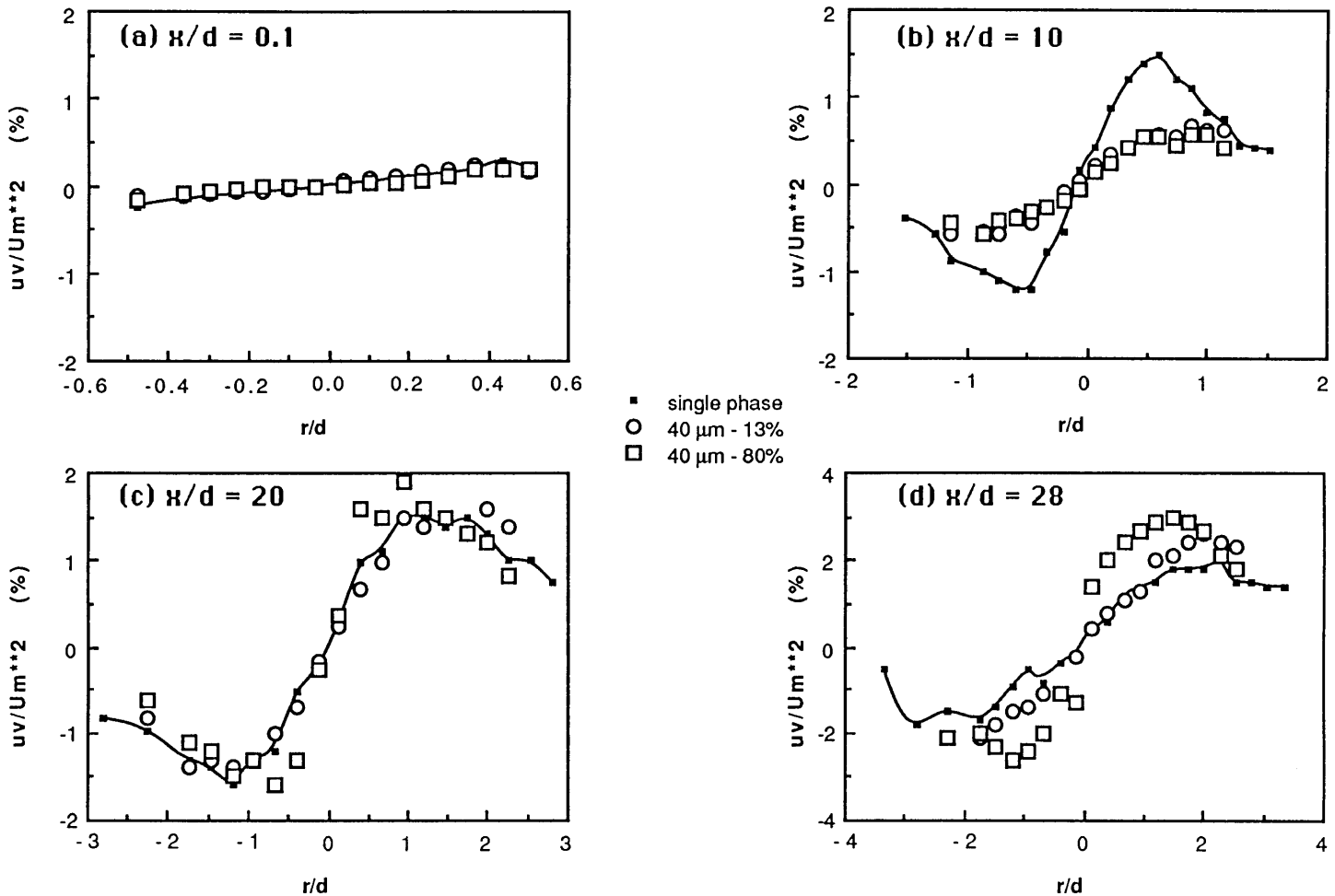


FIGURE 3.14 Radial profiles of (uv) for 40 µm beads at x/d = 0.1, 10, 20 and 28 for mass loadings of 13% (circle) and 80% (square) compared to the single phase. Normalisation is by the single phase centreline velocity, Um.

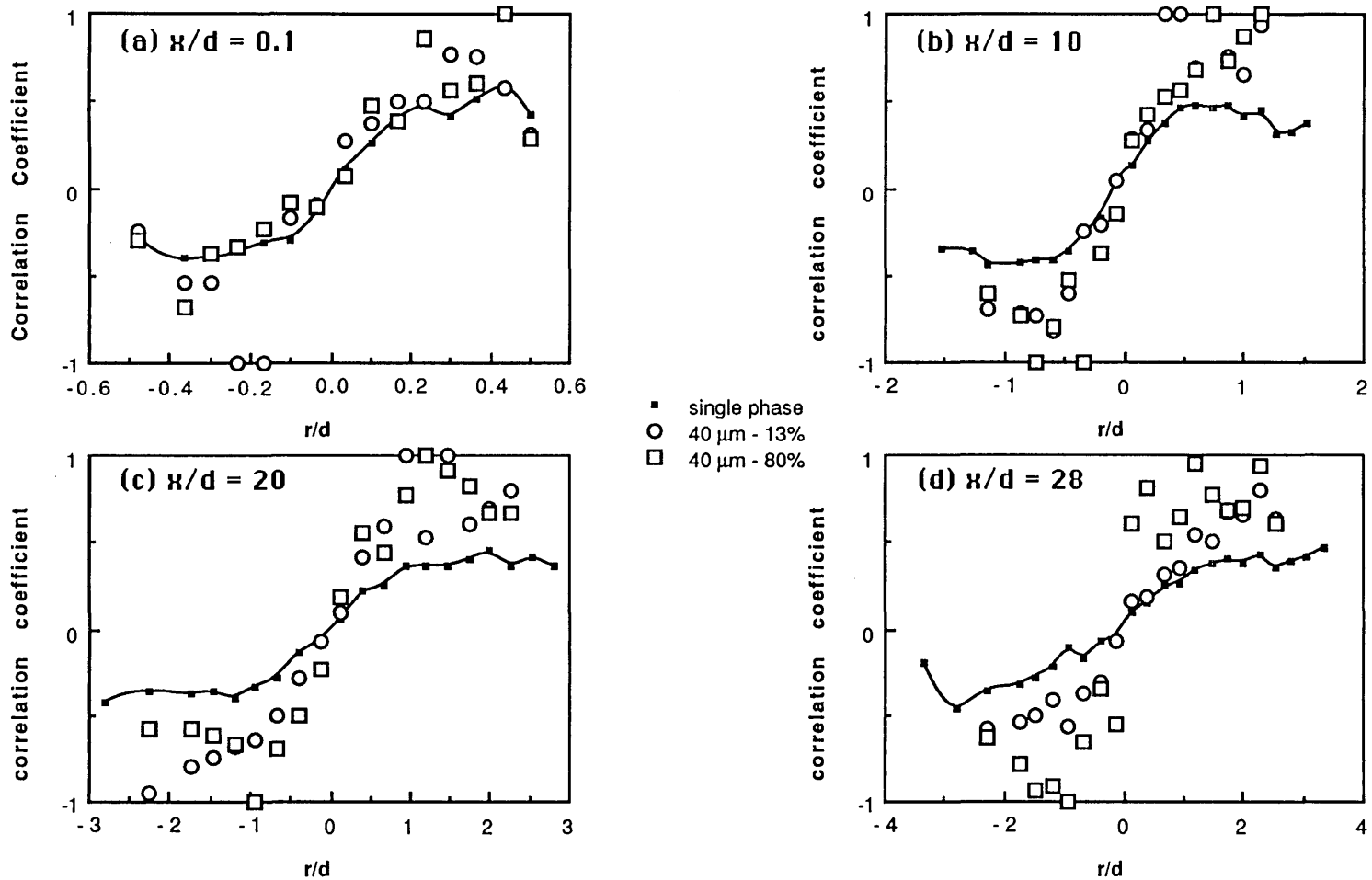


FIGURE 3.15 Radial profiles of correlation coefficient of uv for 40 μm beads at x/d = 0.1, 10, 20 and 28 for mass loadings of 13% (circle) and 80% (square) compared to the single phase.

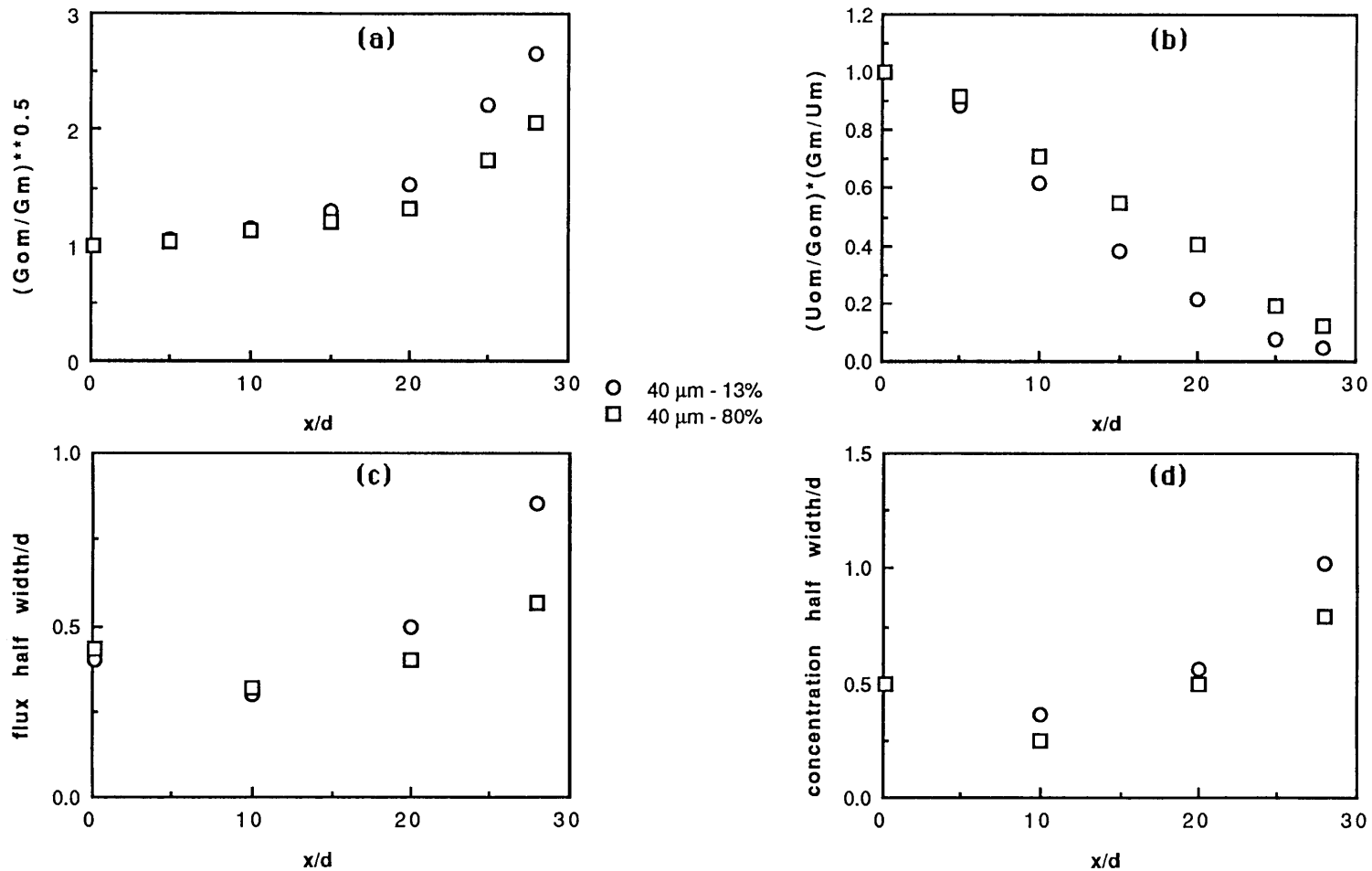


FIGURE 3.16 Effect of mass loading 13% (circle) and 80%(square) on centreline profiles of (a) 40 µm bead flux Gm, normalised by exit centreline flux, Gom, (b) 40 µm bead concentration Gm/Um, normalised by exit centreline concentration, (c) flux half-width and (d) concentration half-width normalised by nozzle exit diameter, d.

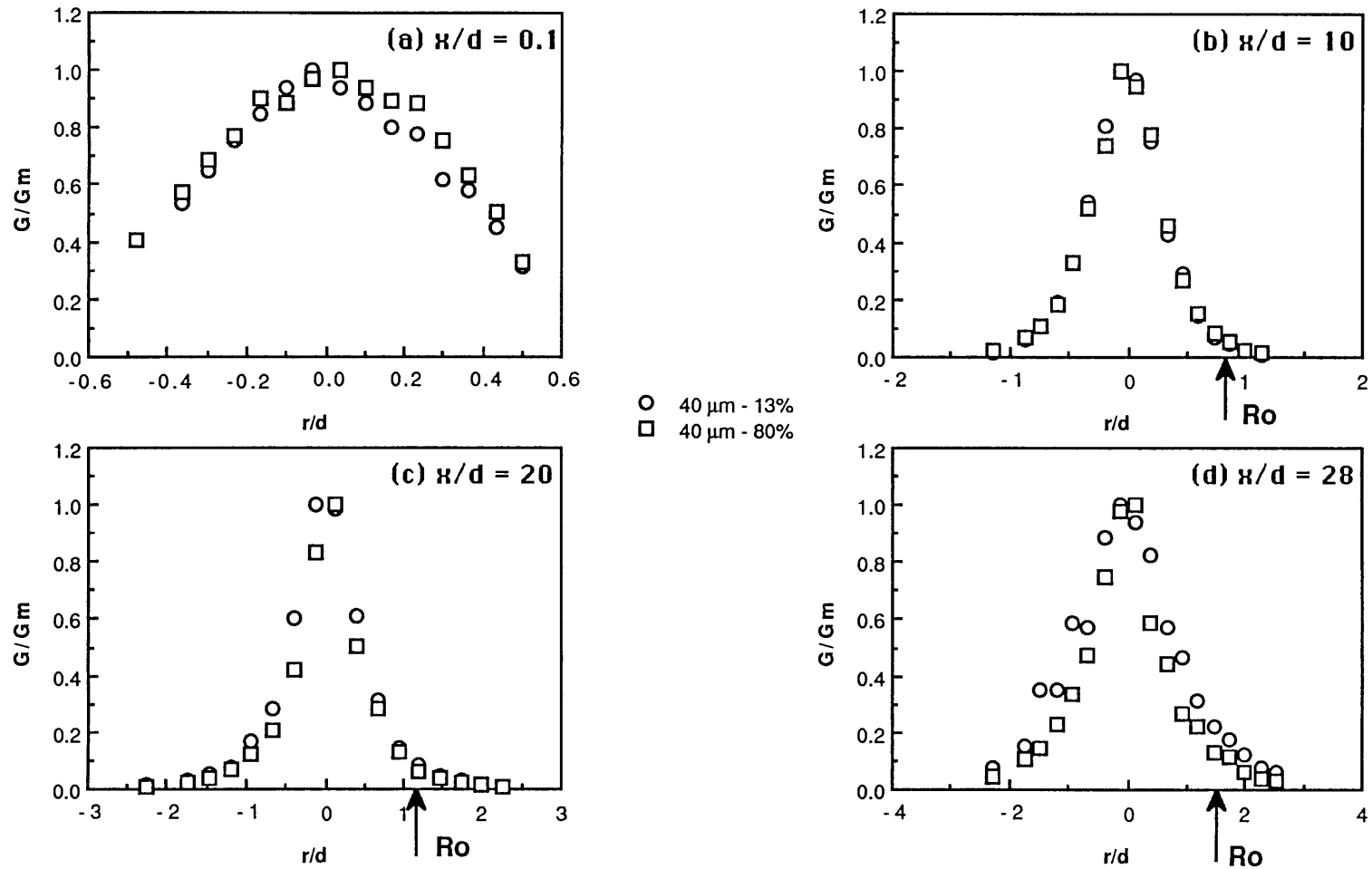


FIGURE 3.17 Effect of mass loading 13% (circle) and 80% (square) on radial profiles of flux G of 40 µm beads at x/d = 0.1, 10, 20 and 28. Normalisation is by centreline flux Gm. Ro is the half-width of the single phase jet.

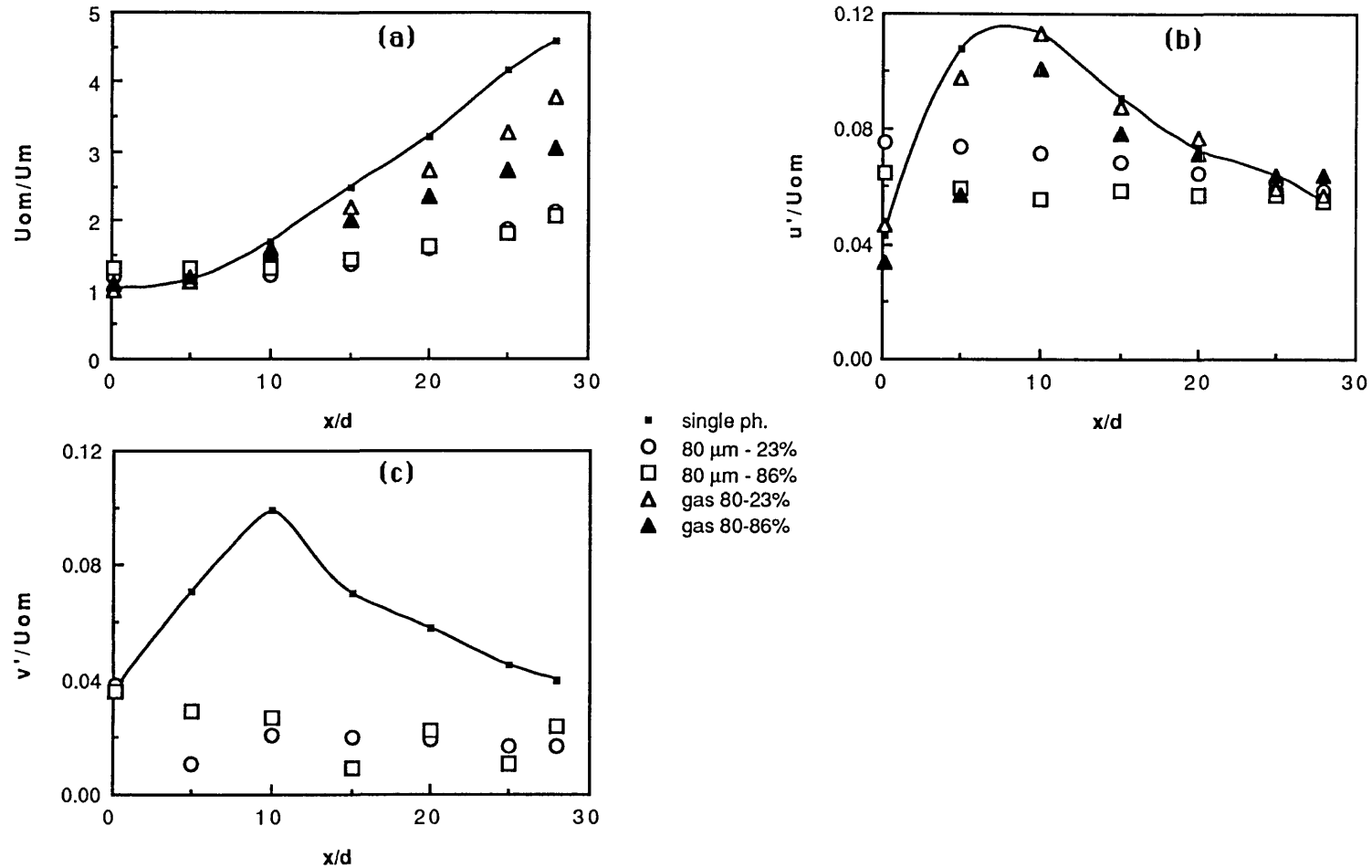


FIGURE 3.18 Centreline profiles of (a) mean axial, U, (b) axial rms, u', and (c) radial rms, v', velocities for gas phase and 80 µm beads for mass loadings of 23% and 86% compared to the single phase. Normalisation is by the single phase exit mean velocity, Uom.

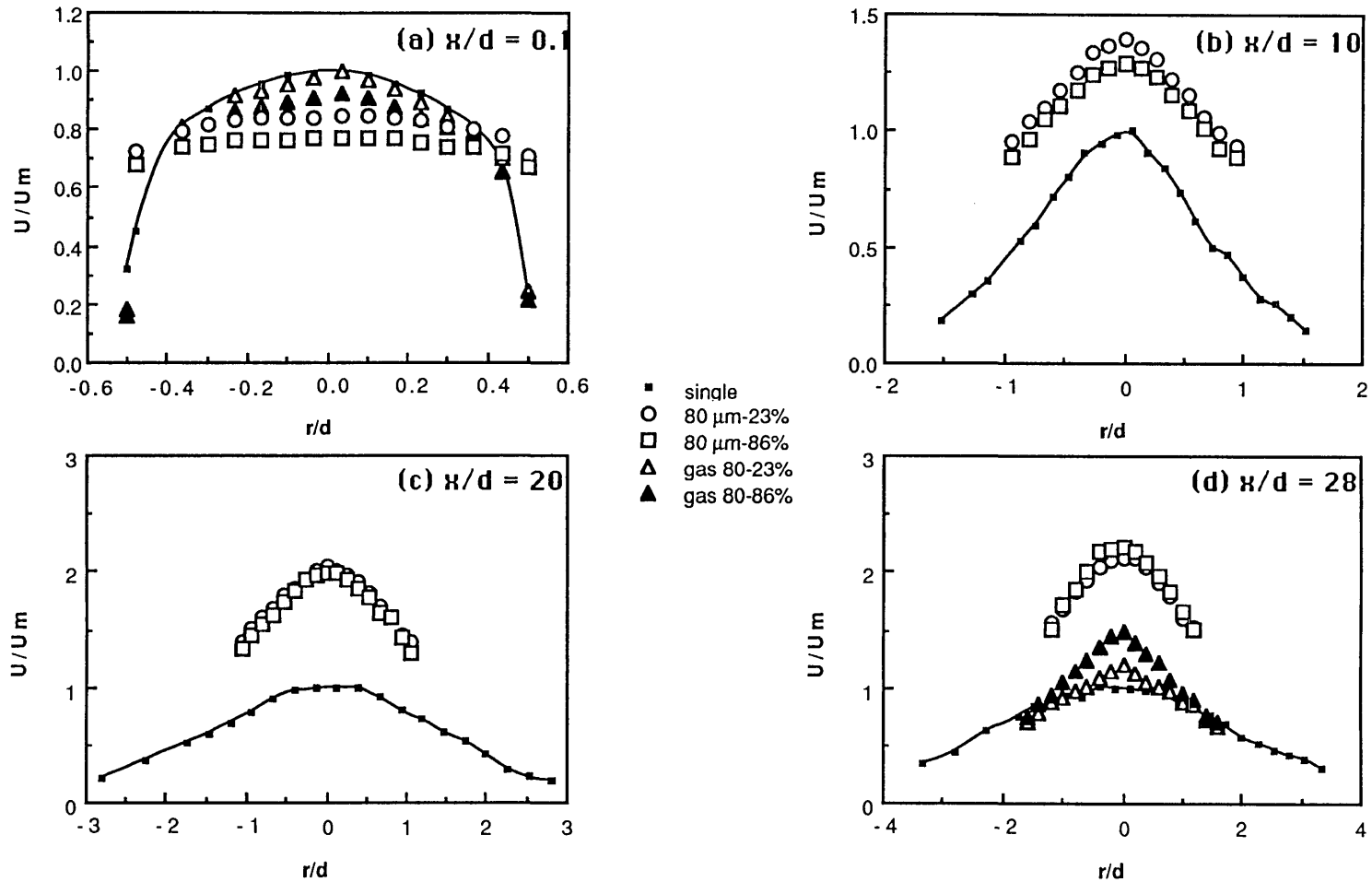


FIGURE 3.19 Radial profiles of mean axial velocity (U) for gas phase and 80 µm beads at x/d = 0.1, 10, 20 and 28 for mass loadings of 23% and 86% compared to the single phase.
Normalisation is by the single phase centreline velocity, Um.

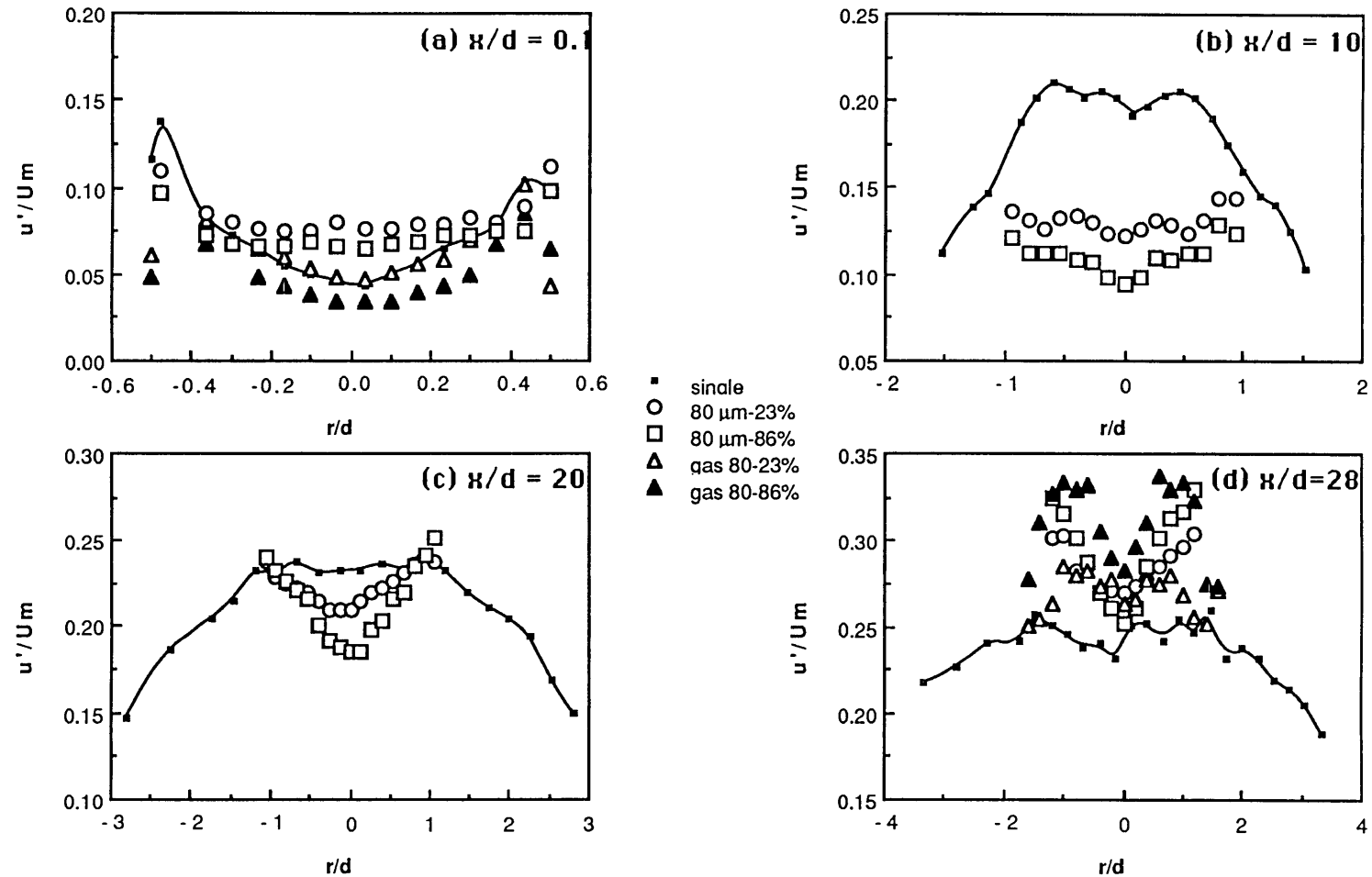


FIGURE 3.20 Radial profiles of axial rms velocity (u') for gas phase and 80 µm beads at x/d = 0.1, 10, 20 and 28 for mass loadings of 23% and 86% compared to the single phase.
Normalisation is by the single phase centreline velocity, Um.

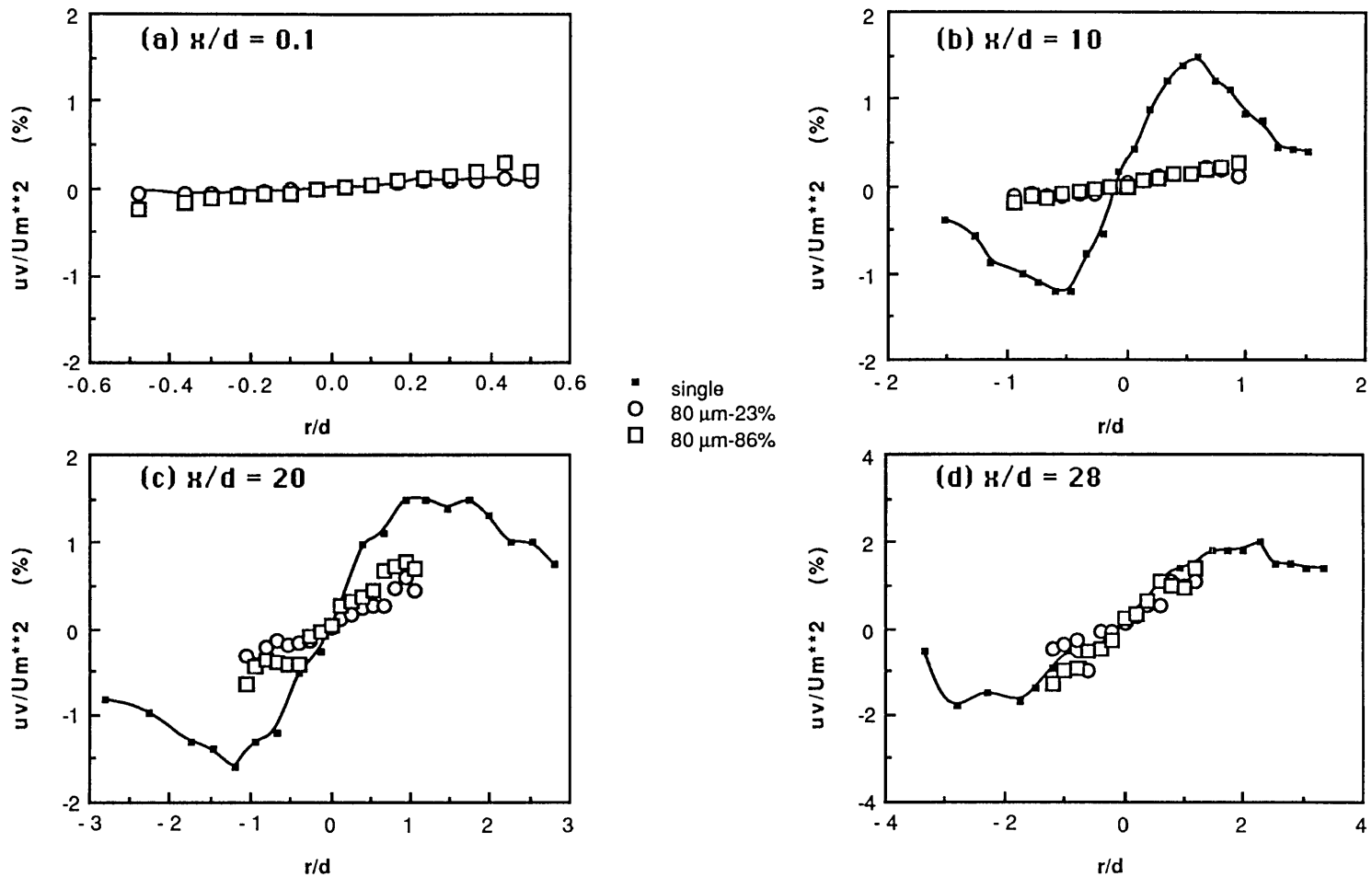


FIGURE 3.21 Radial profiles of uv for 80 µm beads at x/d = 0.1, 10, 20 and 28 for mass loadings of 23% (circle) and 86% (square) compared to the single phase.
Normalisation is by the single phase centreline velocity, Um.

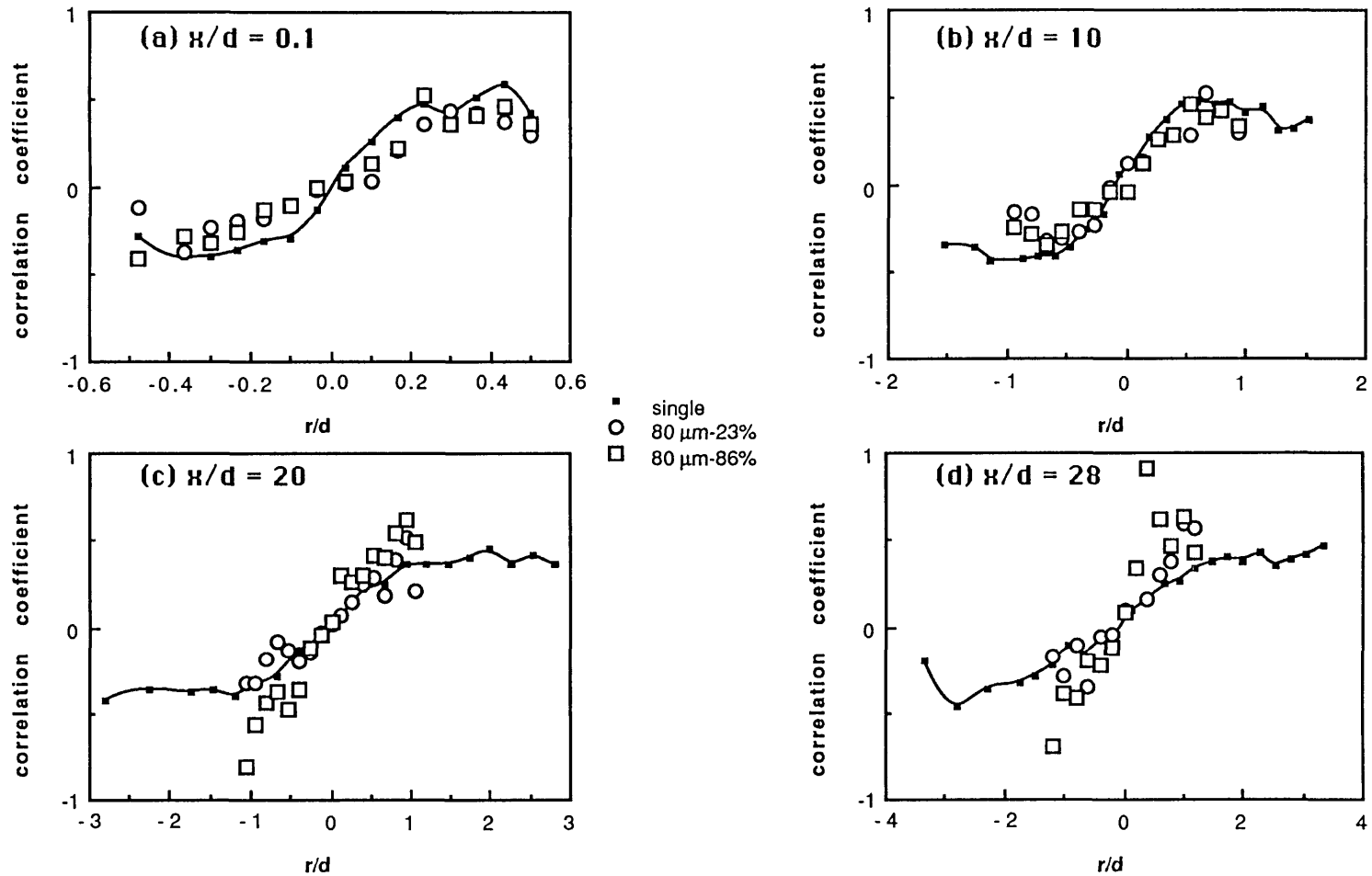


FIGURE 3.22 Radial profiles of correlation coefficient of uv for 80 μm beads at x/d = 0.1, 10, 20 and 28 for mass loadings of 23% (circle) and 86% (square) compared to the single phase.

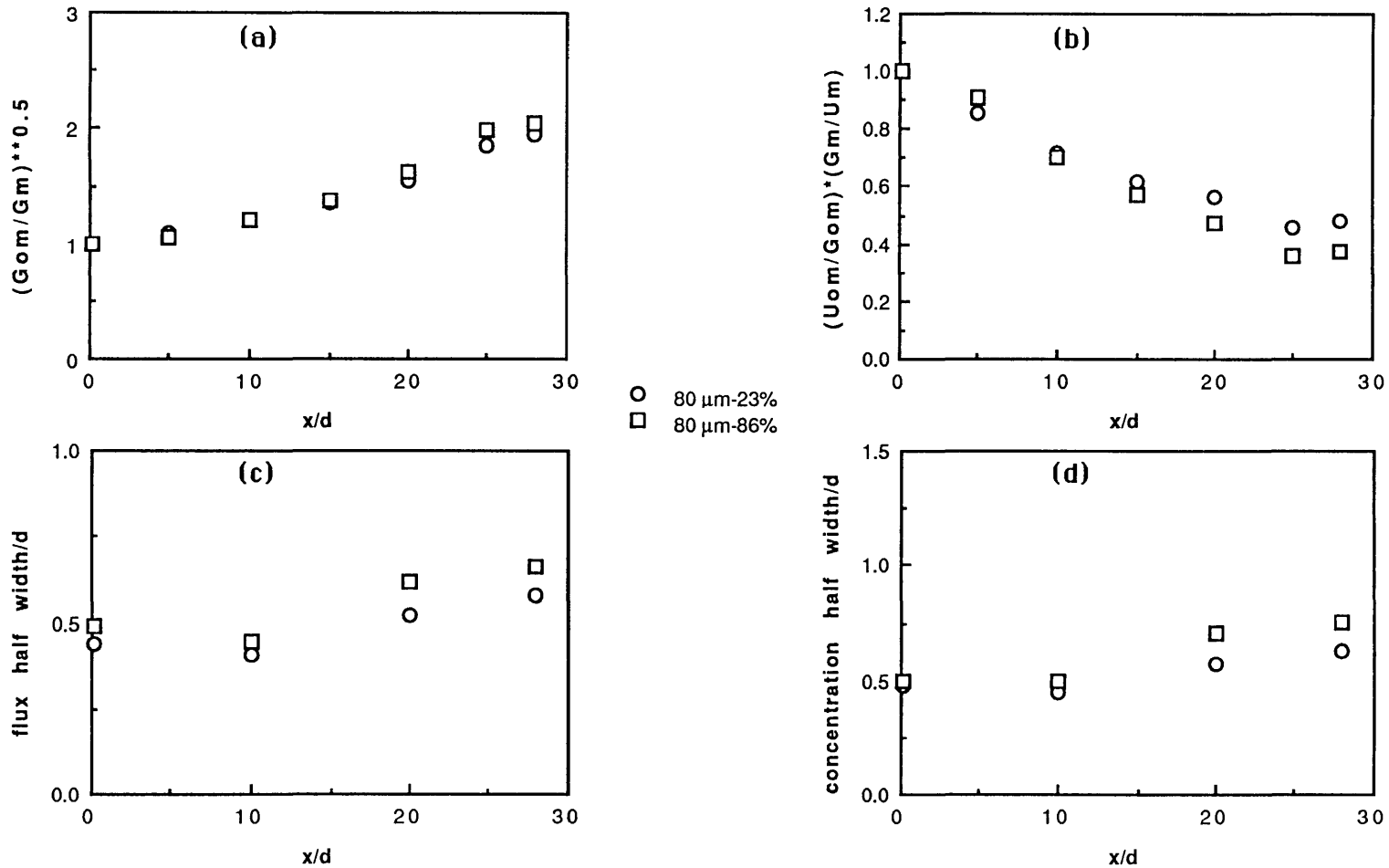


FIGURE 3.23 Effect of mass loading 23% (circle) and 86%(square) on centreline profiles of (a) 80 µm bead flux Gm, normalised by exit centreline flux, Gom, (b) 80 µm bead concentration Gm/Um, normalised by exit centreline concentration, (c) flux half-width and (d) concentration half-width normalised by nozzle exit diameter, d.

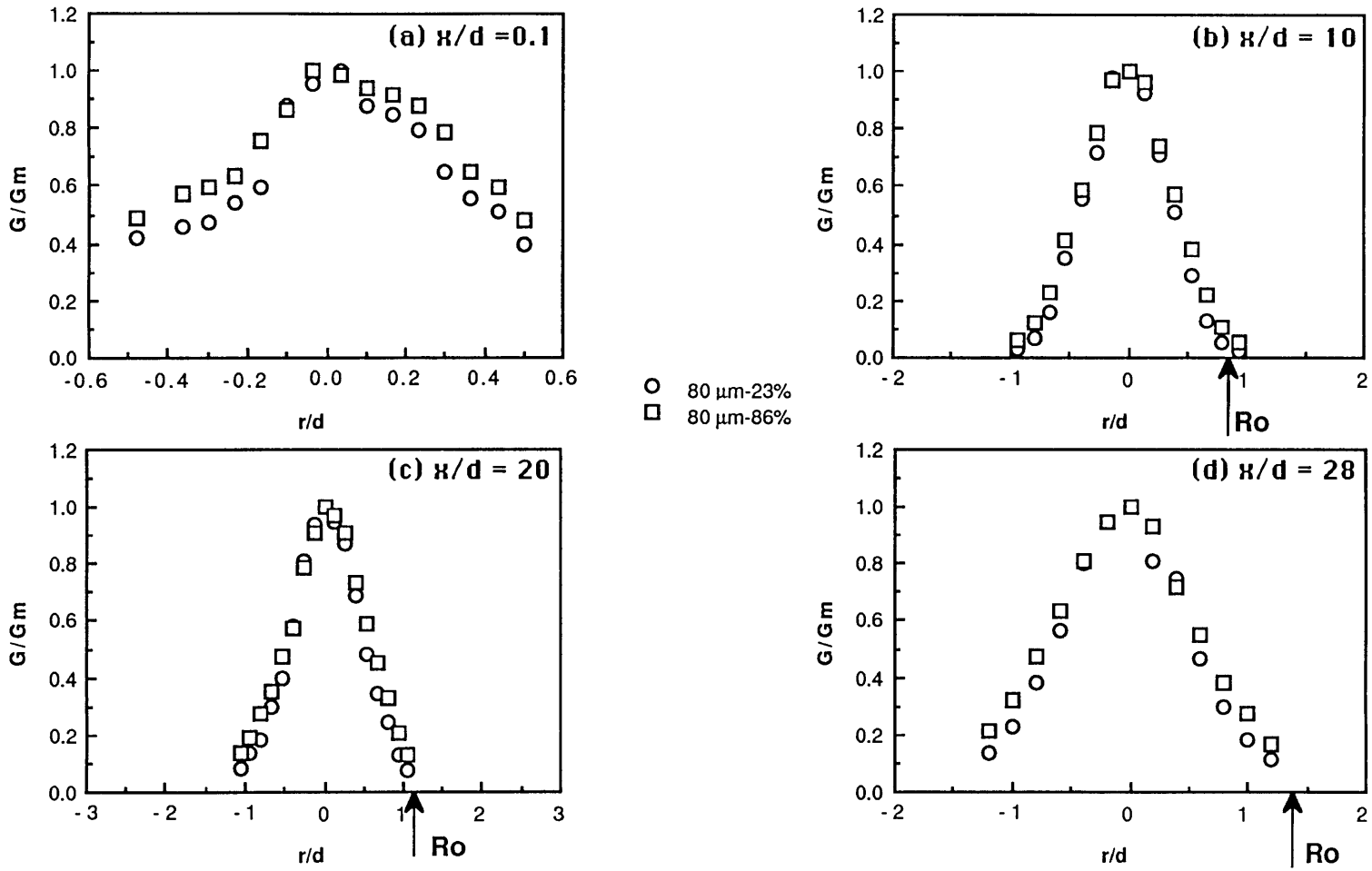


FIGURE 3.24 Effect of mass loading 23% (circle) and 86% (square) on radial profiles of flux G of 80 µm beads at x/d = 0.1, 10, 20 and 28. Normalisation is by centreline flux Gm. Ro is the half-width of the single phase jet.

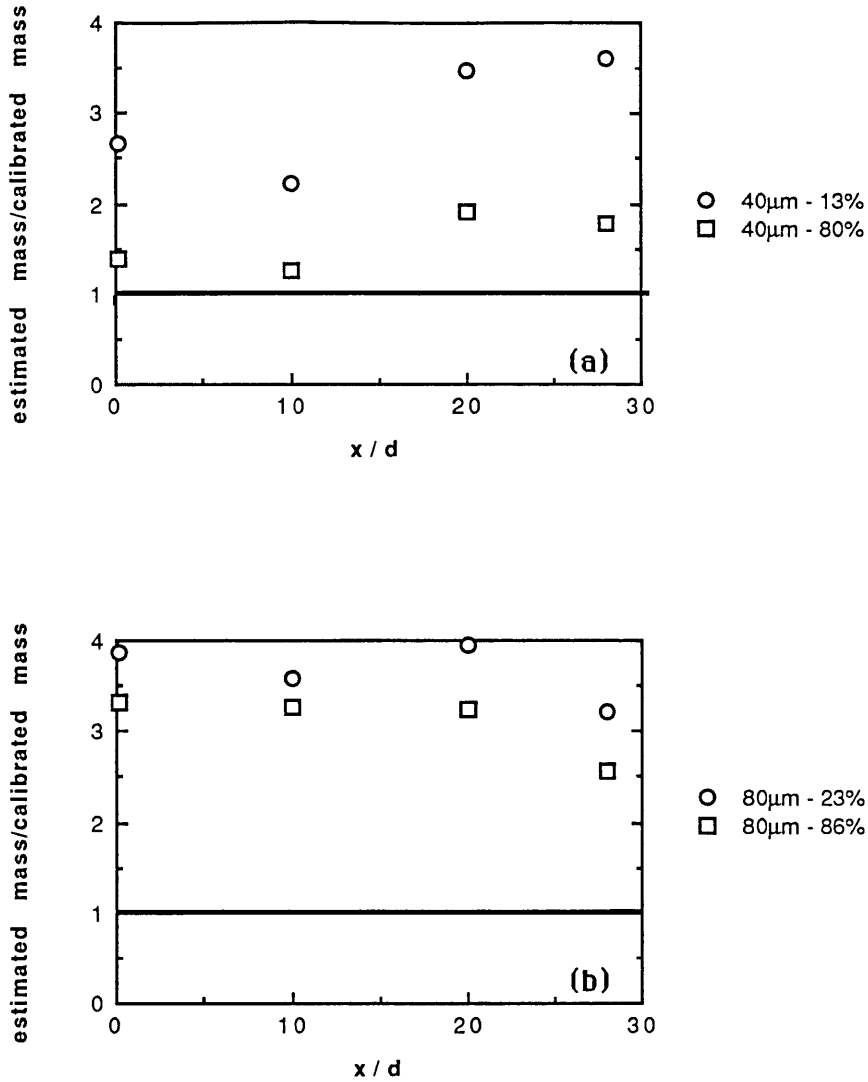


FIGURE 3.25 Comparison of the estimated mass flowrate of the beads at four stations along the axis of the jet to the calibrated mass flowrate of the screw-feeder; (a) 40 μm beads for mass loadings of 13% and 80% and (b) 80 μm beads for mass loadings of 23% and 86%.

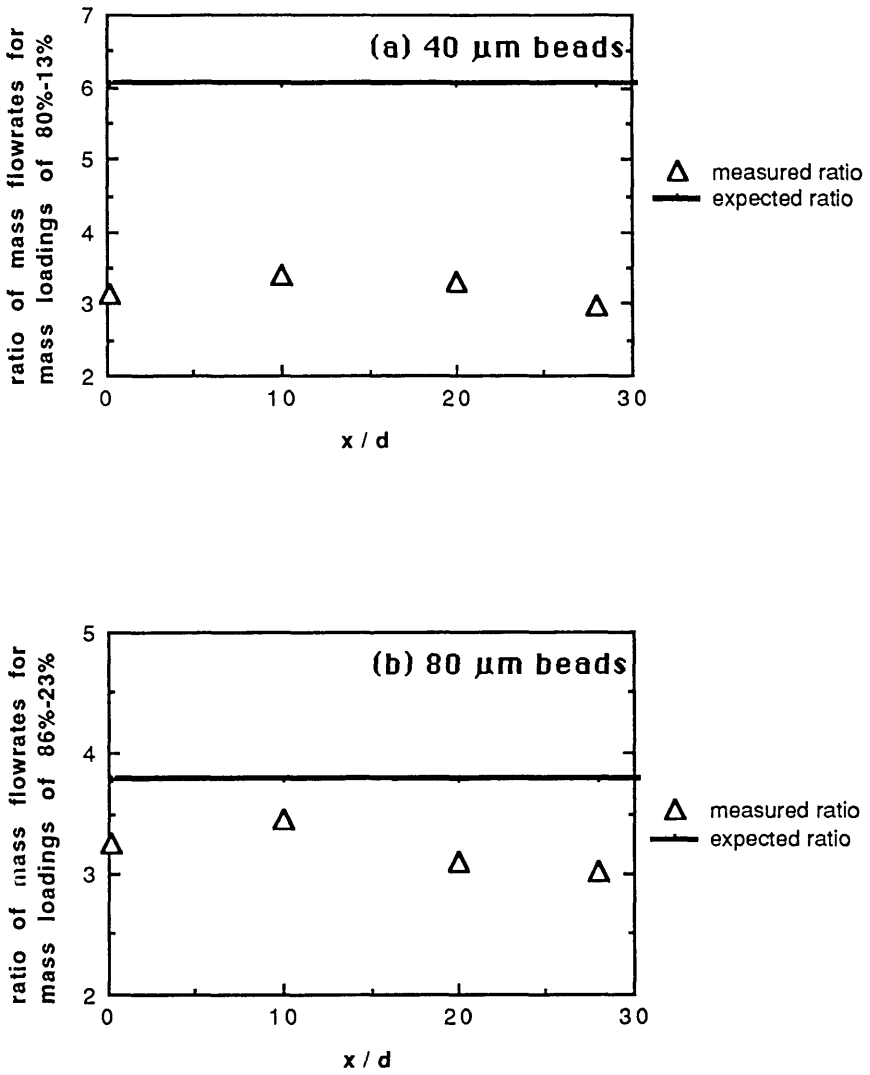


FIGURE 3.26 Comparison of the ratio of the estimated mass flowrates of the beads for two mass loadings at four stations along the axis of the jet to the expected ratio; (a) 40 μm beads for mass loadings of 80% and 13% (expected ratio of 80/13 = 6.1) and (b) 80 μm beads for mass loadings of 86% and 23% (expected ratio of 86/23 = 3.7).

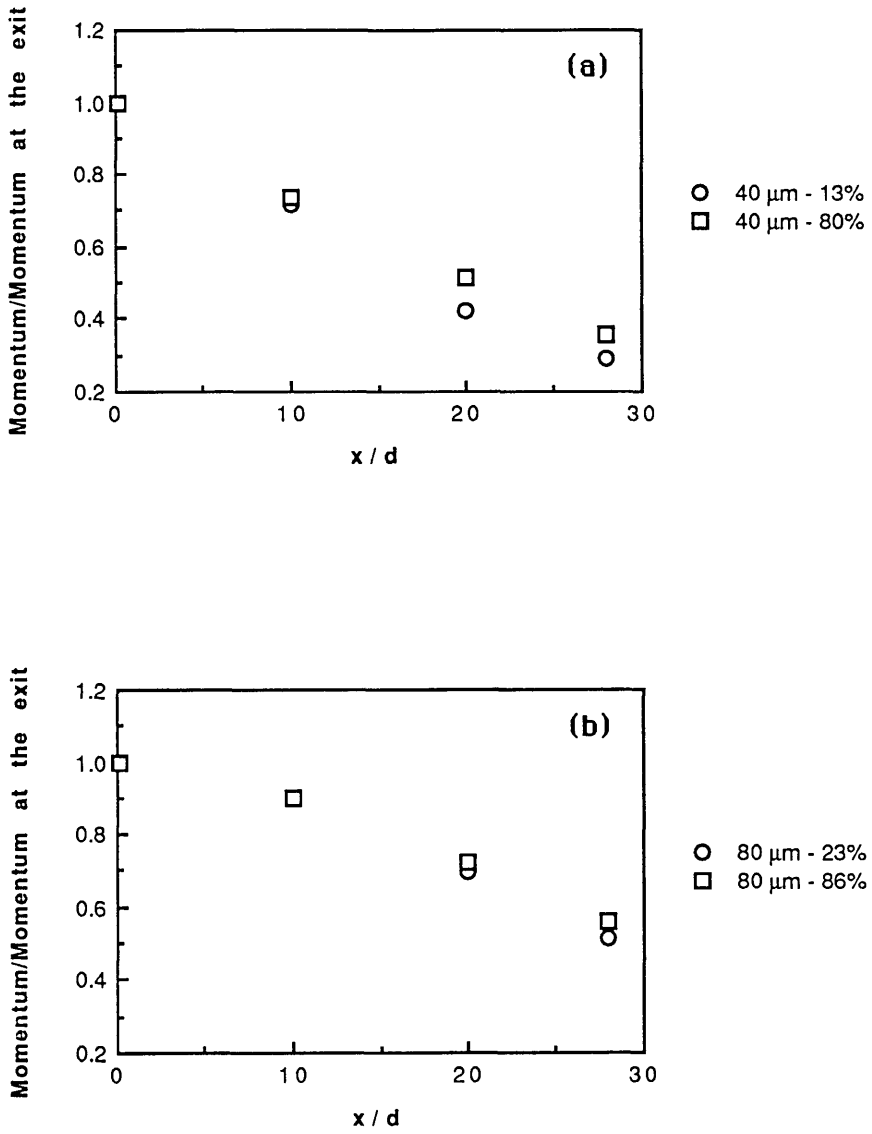


FIGURE 3.27 Integral of momentum flux along the axis of the jet normalised by the exit momentum flux of (a) 40 µm beads and (b) 80 µm beads.

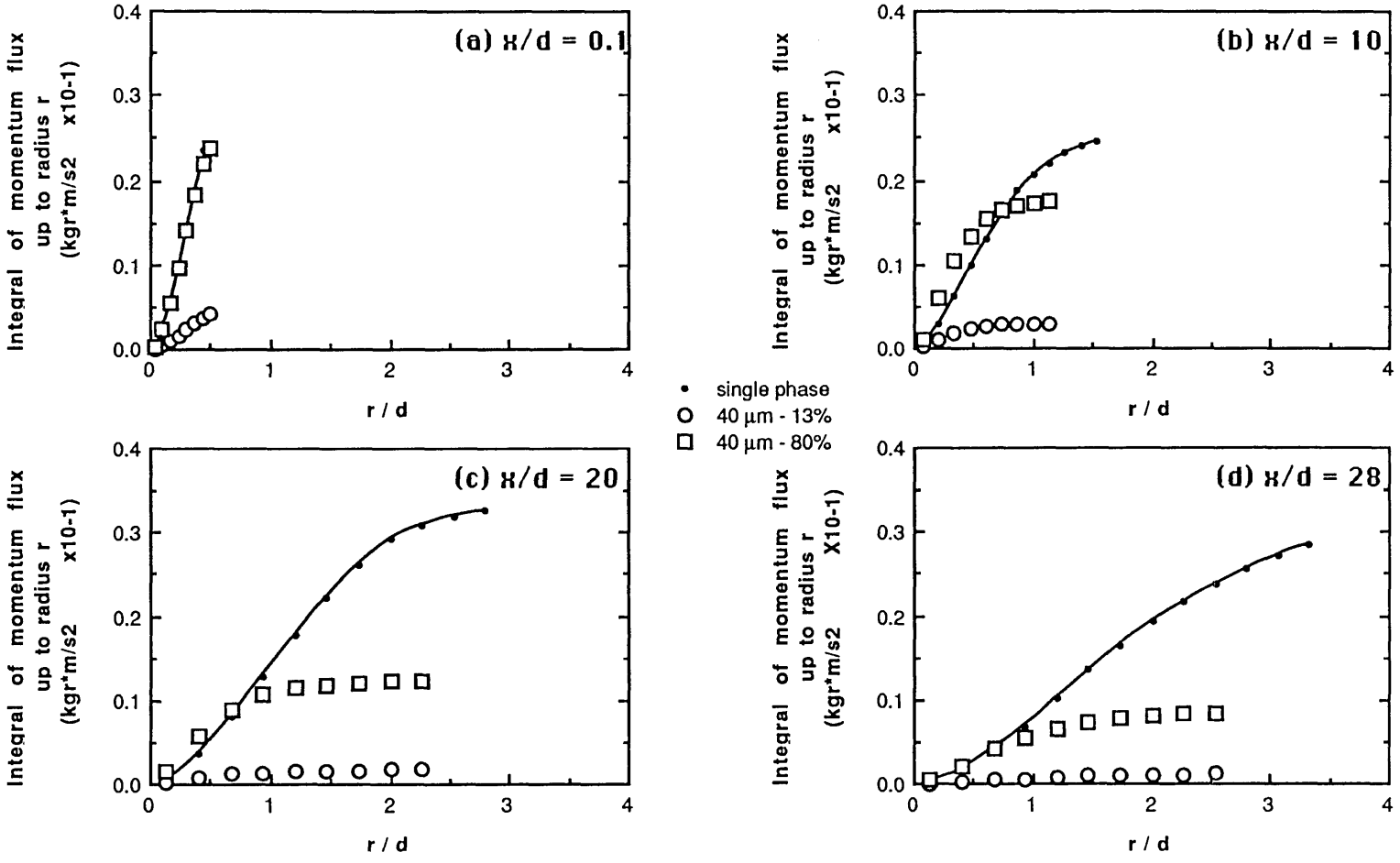


FIGURE 3.28 Radial profile of the value of the integral of momentum flux up to radius r at x/d = 0.1, 10, 20 and 28 for 40 µm beads for mass loadings 13% (circle) and 80% (square) compared to the single phase.

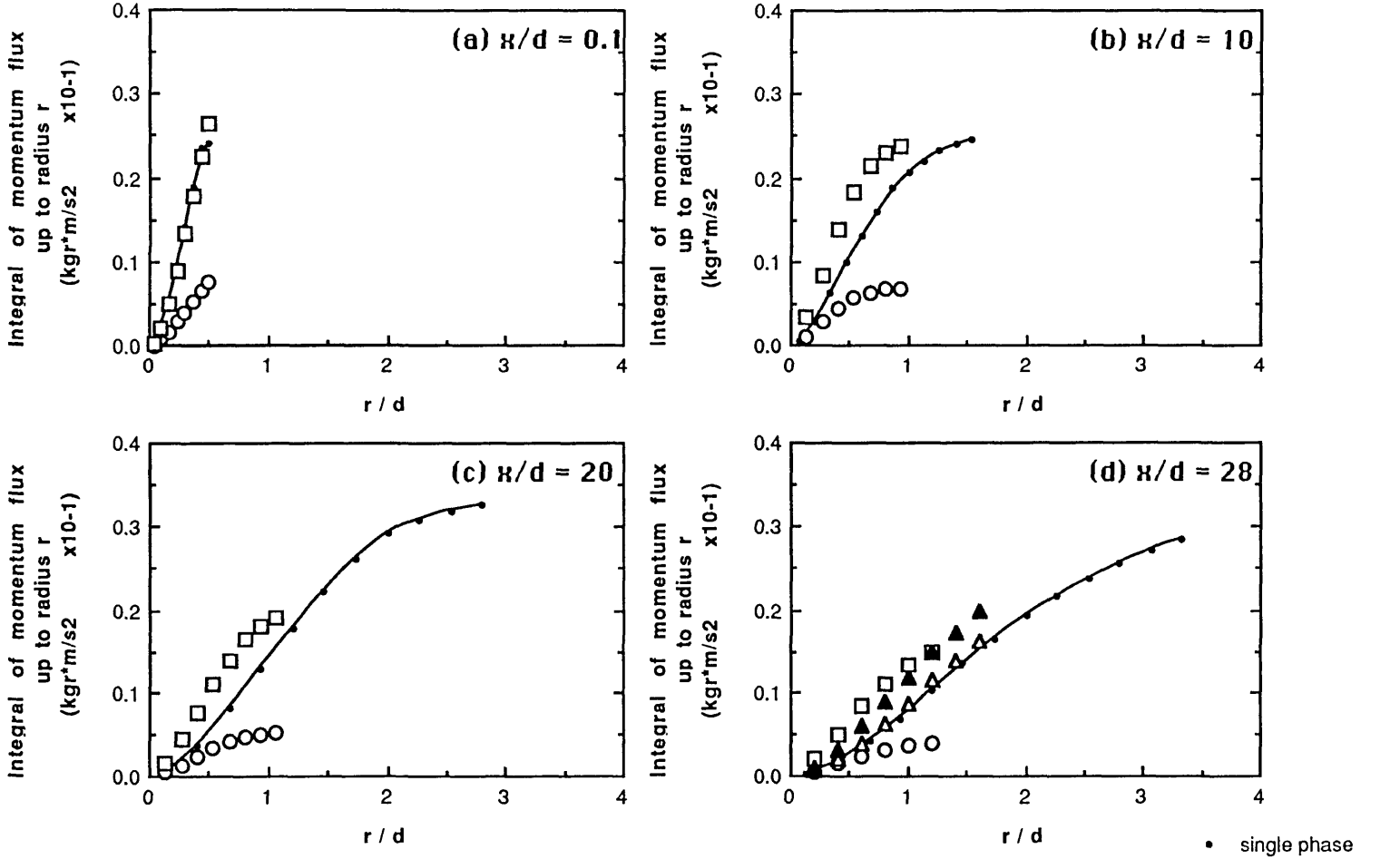


FIGURE 3.29 Radial profile of the value of the momentum flux integral up to radius at x/d = 0.1, 10, 20 and 28 for gas phase and 80 µm beads for mass loadings 23% and 86% compared to the single phase.

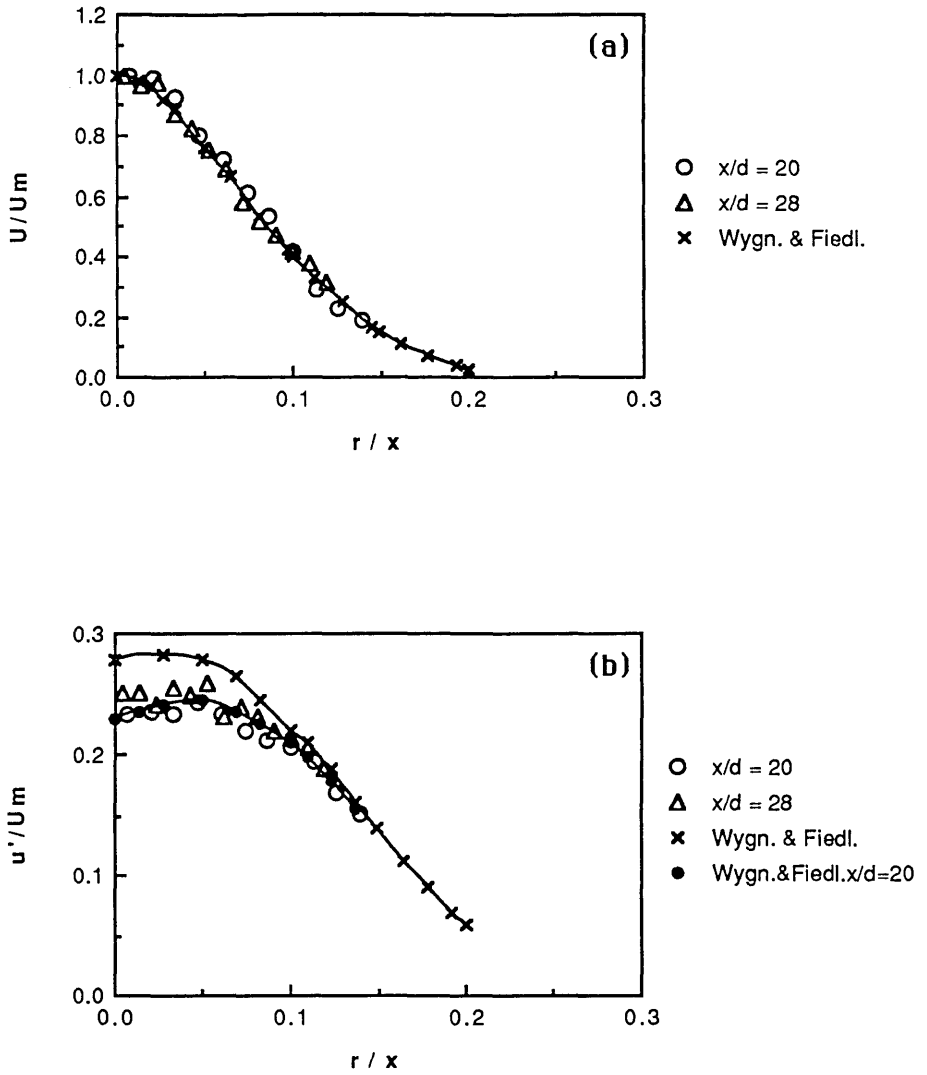


FIGURE 3.30 Comparison of the single phase results of the present experiment at x/d = 20 and 28 to these of Wygnanski and Fiedler, 1969; (a) mean axial velocity and (b) axial rms velocity. Normalisation of velocities is by the local centreline velocity.

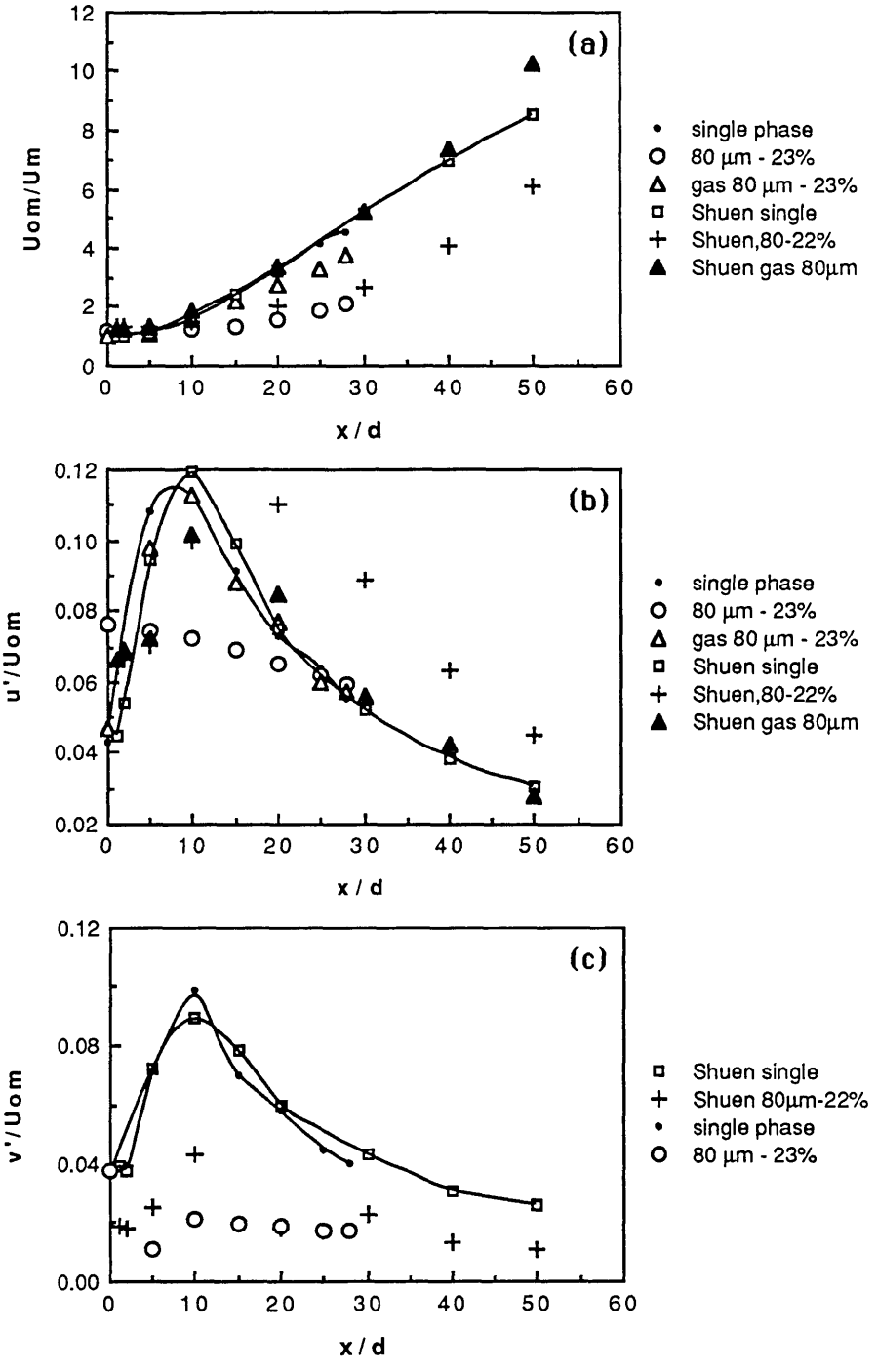


FIGURE 3.31 Comparison to the experiment of Shuen et al, 1985; (a) mean and (b) rms axial velocity of single phase and gas phase (open triangle) and 80 μm beads-mass loading 23% (open circle) compared to single phase and gas phase (closed triangle) and 80 μm beads-mass loading 22% (cross) of Shuen et al. and (c) radial rms velocity of single phase and 80 μm-mass loading 23% compared to single phase and 80 μm beads-mass loading 22% of Shuen et al.

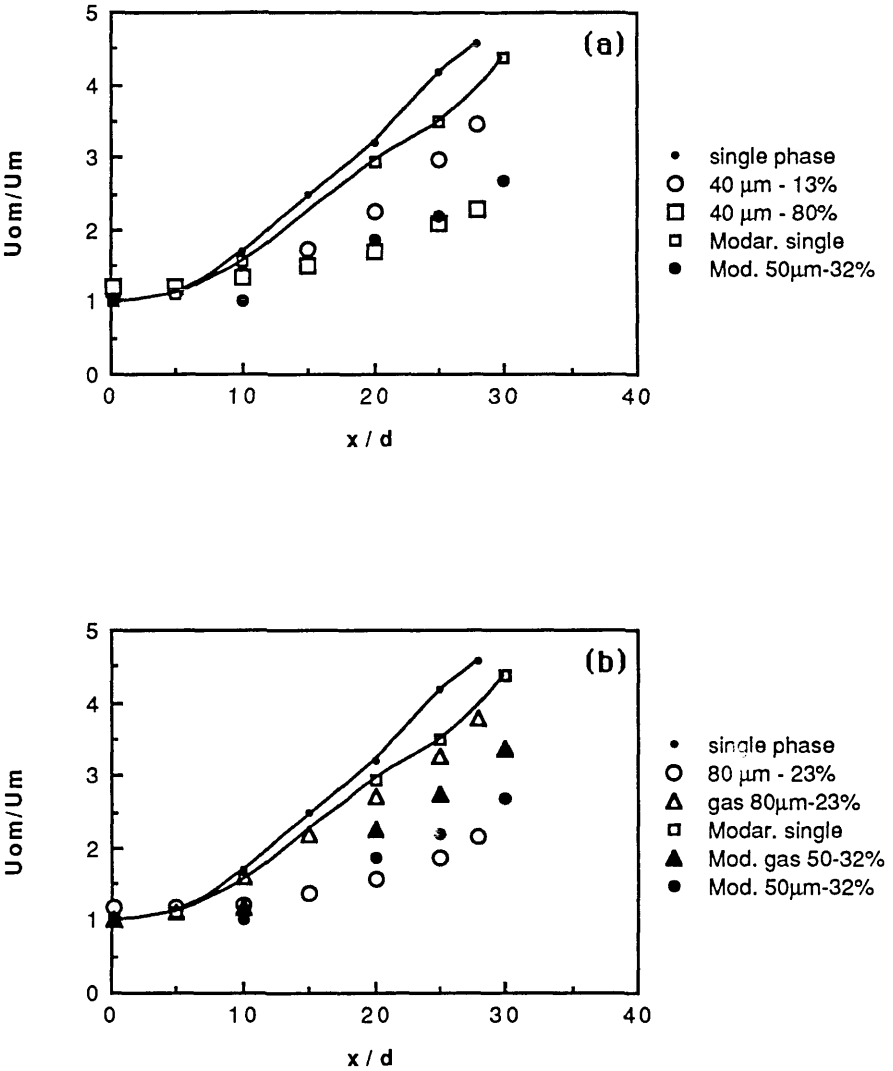


FIGURE 3.32 Comparison to the experiment of Modarress and Tan, 1984; (a) Centreline profile of mean axial velocity of single phase and 40 μm beads for mass loadings of 13% (open circle) and 80% (open square) compared to the single phase and 50 μm beads for mass loading of 32% (closed circle) of Mod. & Tan and (b) Centreline profile of mean axial velocity of single phase and gas phase (open triangle) and 80 μm beads-mass loading 23% (open circle) compared to single phase and gas phase (closed triangle) and 50 μm beads-mass loading 32% (closed circle) of Mod. & Tan.

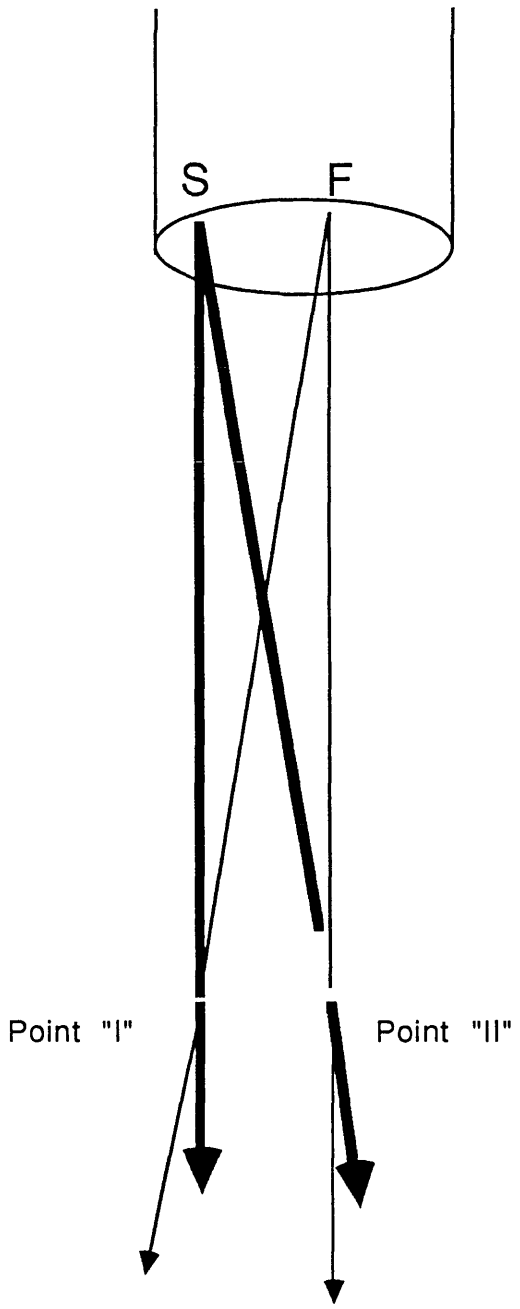


FIGURE 3.33 Schematic representation of "fan-spreading" phenomenon which accounts for large values of u'b even though beads are too large to respond to turbulent frequencies in the gaseous phase. At low Stokes numbers, bead trajectories are close to being straight lines and figure shows superposition of bead trajectories at arbitrary measurement locations "I" and "II". Points "S" and "F" are the two initial positions considered at the exit of the jet: point "S" corresponds to a location, which has slower Ub than does "F". The bold vectors denote velocity of bead which originates from "S" and lighter vectors are from "F". Measurement of bead turbulence at points "I" and "II" is due to superposition of fast and slow trajectories.

CHAPTER 4

ROUND SUDDEN STEP EXPANSION

4.1 Introduction

The dispersion of particles in recirculating flows is of interest for many technical applications, for example, liquid and solid fuels combustion in industrial burners or in internal combustion engines. The present investigation examines the response of different particle sizes to the air flow generated by a round sudden step expansion. Measurements of the velocity and flux characteristics of the 40, 80 and 200 μm glass beads at different mass loadings and the velocity of the gas phase in the presence of the beads are reported for a jet flow expanding in two larger tubes with diameter ratios of 3.33 and 5.

Available information of the detailed characteristics of two phase flows involving recirculating regions is slight due to the difficulty of the corresponding measurements. Concentration measurements of particles in recirculation zones based on light scattering methods are available and for example studies of the transport of small particles in the recirculation zone generated by discs have been reported by Humphries and Vincent, (1976) & (1978). Visualisation and photographic methods have been used to study the behaviour of droplets in a recirculation zone, as for example the reacting flow of McCreath & Chigier (1973), but without size resolution and in flows which are so complex that it is difficult to draw conclusions on the aerodynamic behaviour of particles. Only recently have advanced laser diagnostics been used to study two phase recirculating flows as for example the two-phase flow at the exit of an annular jet (Hardalupas et al, 1986), a fuel injector in a swirl-stabilised combustor (McDonell et al, 1986) and the single-sided backward-facing step two-phase flow (Ruck et al, 1988). However, the physics of the dispersion of particles in recirculation zones remains unknown.

Sudden changes in test section geometries have been used extensively to study flow separations downstream of the step, as for example, on single steps of Bradshaw & Wong (1972), Etheridge & Kemp (1978) and Armally et al. (1983) or on symmetric steps of Abbot & Kline (1962) and Cherdron et al (1978). The simplicity of the

sudden expansion geometry and the reported measurements of single phase flows provide an appropriate flow for the study of the behaviour of the particles in the recirculation zone existing downstream of the step and their development downstream of the recirculation zone.

The present results show that particle size and flow geometry are critical parameters for the dispersion of the particles in the recirculation zone and have been examined on the basis of mean and turbulent flow Stokes numbers, as defined in the previous chapter. Thus, the reattachment length of the gas flow recirculation zone was found to increase in the presence of the beads and is longer for the higher particle mass loading. So a "two-way" interaction exists between the particles and the gas and the effect is more pronounced for the higher mass loadings.

Section 4.2 describes the flow arrangement and refers to chapter 3 for the description of the measurement method used and estimates of uncertainties. Section 4.3 presents the results for the two expansion ratios 3.33 and 5. and section 4.4 compares the centreline development of the jet flow reported in chapter 3 and this of the expansion flow arrangement to find the effect of the confinement of the flow on the dispersion of the beads. The results are analysed and discussed in section 4.5 and the main conclusions are summarised in section 4.6.

4.2 Experimental arrangement.

The jet flow described in the previous chapter and shown in figure 3.1 formed the pipe upstream of the expansion. The Reynolds number at the exit of the upstream pipe was around 13000, corresponding to a bulk exit velocity of about 13.2 m s^{-1} at the exit of the 15 mm pipe. The air was supplied by a compressor and divided to provide pneumatic transport for the glass beads and for the seeding tracer for the gas phase measurements. The rotameters metering the two streams operated at gauge pressures between 0.1 and 0.3 atmospheres and the flowrates were corrected to N.T.P. from calibration charts provided by the manufacturer. The two streams recombined as described in chapter 3 developed along about 100 diameters to a fully turbulent pipe flow exhausting vertically downwards in the round sudden step expansion produced by co-axial

precision bore glass tubes with internal diameters of either 50 or 75 mm at the exit of the upstream pipe (figure 4.1). The top of the glass tubes was closed by aluminium plates and sealed by o-rings.

The precision bore glass tubes ensured the transparency needed for the optical measurements but the seeding powder (kaolin) used for the gas phase measurements eventually built up on the glass wall, resulting in attenuation of the laser beams. The tube was treated often with "antistatic" cleaner, which helped to keep the tube clean for long periods. No problem of electrostatic attraction of the glass beads was observed on the glass tube or the metal plates, as reported by McDonell (personal communication).

The glass beads were supplied to the flow and metered by the screw feeder described in the previous chapter. The air flowrate through the screw feeder box was maintained at around 1 $dm^3\ s^{-1}$. The seeding powder was kaolin supplied to the flow by the reverse cyclone arrangement (Glass & Kennedy, 1977) and the flowrate through the reverse cyclone was kept constant at around 1.5 $dm^3\ s^{-1}$. The chosen flowrate was a compromise between the requirement for high mean Stokes number in the upstream pipe (small flowrate) and the requirement for a Reynolds number based on the diameter of the downstream tube higher than 2500 to ensure turbulent flow. The flow conditions for all the cases measured are given in table 4.1.

The seeded air and the beads were discharged from the glass tube to the laboratory before the flow was captured by a collection hopper that was placed on the inlet of a large fan to provide a suction flow. The particles were recovered by passing the flow through a cyclone and collecting them in a bin at the base of the cyclone. The beads were returned to the hopper of the screwfeeder from time to time to be used again. The particles used were glass beads with the same properties as those of chapter 3, see table 3.1. The phase-Doppler instrument of chapter 3 and table 3.2 was again used with uncertainties similar to those of table 3.3.

4.3 Results

The results are divided into four sub-sections and are presented for both expansion ratios for the 40, 80, 200 μm beads in the following order. Sub-section (a) presents the velocity and the flux

characteristics of the 40 μm; sub-section (b) reports the velocity and the flux characteristics of the 80 μm beads as well as the gas phase velocity characteristics; sub-section (c) presents the velocity characteristics of the 200 μm beads and sub-section (d) presents the separation streamline of the single phase flow and the zero axial velocity contours of the beads and the gas phase. Although the mean flow Stokes exit number suggests all particles would be unresponsive to the mean flow, it will be shown that the 40 μm beads are responsive to the recirculation zone generated at the corner downstream of the step for both expansion ratios and that the 80 μm are semi-responsive as they enter the recirculation zone of the large expansion ratio flow but they do not for the small expansion ratio. The 200 μm beads, however, are unresponsive to the recirculation zone for both expansions.

The bulk velocity, U_0, (tables 4.2 & 4.3) in the downstream tube was used to normalise the velocity profiles and was chosen because the integrals of the normalised single phase velocity profiles become unity. The diameter of the downstream tube was used as the corresponding length-scale parameter of the flow to normalise the radial and the axial distance from the centreline and the inlet respectively. The coordinate system used in this chapter relative to the position of the laser can be seen at figure 4.1.

a) Velocity and flux characteristics of 40 μm beads.

The results for the 40 μm beads are presented separately for different expansion ratios and in the following order for each case : centreline mean and turbulent velocities, radial profiles of mean and turbulent velocities, flux characteristics.

Expansion ratio of 3.33

i) Centreline velocities

The centreline mean axial velocity and the mean turbulent r.m.s. velocity fluctuations in the axial and radial direction are shown in figure 4.2 normalised by the bulk velocity in the downstream pipe. The mean axial velocity decay of the single phase fluid is rapid and becomes approximately equal to the bulk velocity U_0 within four tube

diameters. The 40 μm beads leave the upstream tube with lower velocity than the single phase and as their inertia causes their velocity decay to be slower, they move faster than the single phase after one tube diameter. The mean slip velocity between the two phases decreases farther downstream and the beads have nearly the same velocity as the single phase flow at about z/D = 8. For the smallest mass loading (13%), the gas phase can be assumed unaffected by the beads, so the interaction is one way from the gas to the beads. As the mass loading increases, the beads leave the inlet with smaller velocity (figure 4.2(a)) and the velocity of the beads decays at a lower rate. It is likely that this is due to the increased gas phase velocity relative to the single phase at higher mass loadings, as the interaction between the two phases is "two way", and this has been measured for the 80 μm and is presented later.

The 40 μm beads leave the upstream pipe with larger r.m.s. fluctuations than the single phase, which is a result of the behaviour of the beads inside the tube, but not due to turbulent movement of the beads as the mean flow Stokes number is small at the exit (chapter 3). The maximum of the r.m.s. fluctuations of the beads is shifted downstream relative to the single phase and the effect of mass loading is to "delay" the occurrence of the maximum. The velocity r.m.s. fluctuations of the beads downstream are always larger than the single phase, and this apparently paradoxical result is due to the fan-spreading effect explained in chapter 3 rather than abnormally large response of the beads to the axial gas phase turbulence.

The radial r.m.s. fluctuations of the beads along the centreline remain approximately constant, equal to their exit value and much smaller than the axial r.m.s. fluctuations and this observation supports the fan-spreading effect. The beads at the exit of the upstream tube have smaller radial r.m.s. fluctuations than the single phase, while the reverse is observed in the axial direction. The single phase radial r.m.s. has a similar variation as in the axial direction although its maximum value is around 20% lower, due to the known anisotropy. The beads appear to have larger r.m.s. values in the radial direction than the single phase flow farther downstream, a strange result, which could be due to a fan spreading effect in the radial direction.

ii) Radial profiles of mean and turbulent velocities.

The radial velocity profiles show that the response of the beads to the gas turbulence is enough to enter the recirculation zone, which is not obvious from their centreline behaviour. The mean velocity profiles, figure 4.3, show that the 40 μm beads respond to the gas phase and follow the flow in the recirculation zone quite well. Figures 4.3 (a) and (b) show that the single phase flow and the beads mean negative velocities are indistinguishable in the recirculation zone and even close to the wall, where there is a trapped corner vortex, the beads and the single phase have positive velocities. For the main jet stream, the beads move slower than the single phase and only at z/D=1.5 the mean velocities at the central part of the flow are equal. At this position the single phase negative velocity in the recirculation zone has its maximum value and the beads follow this trend. However, the zero mean axial velocity of the beads occurs closer to the centre of the tube than for the single phase, which implies a wider recirculation zone for the beads and suggests a longer reattachment length. The beads slide down the wall due to gravity and their velocity is positive as their terminal velocity is not negligible in the recirculation zone and should be taken into account in the interpretation of the results. The mass loading appears to have an effect and the velocities of the beads in the shear layer are smaller for the higher loading. This observation becomes more obvious for the higher loading farther downstream, where beads move faster on the centreline and slower in the shear layer and in the recirculation zone than the beads at lower loadings. So the length of the beads' recirculation zone is larger for the higher loadings (figure 4.3 (d), (e), (f)) as quantified in sub-section (d) and the recirculation zone of the single phase flow is always shorter than that of the beads. Although the single phase flow mean velocity profile is flat at z/D=6 (figure 4.3(g) and (h)), those at higher mass loading beads are far from flat, moving faster at the centre and having small negative velocities close to the wall.

The radial profiles of the axial r.m.s. fluctuations are presented in figure 4.4. In the shear layer, close to the step (z/D=0.06 and 0.3) the beads have larger r.m.s. values than the single phase and the velocity probability function of the beads is bimodal close to the separation streamline, implying large scale structures in the gas flow. The bimodal velocity p.d.f. is more obvious for the 80 μm beads and

will be explained later. At the centre, the profile corresponds closely to the fully turbulent pipe flow coming out of the upstream pipe. In the recirculation zone the beads have smaller r.m.s. values than the single phase, expected as the beads cannot respond to the complete frequency spectrum of turbulence and since there are no fan-spreading effects. At z/D=2.4, the r.m.s. fluctuations at the centre and in the recirculation decrease as the mass loading increases. This sequence becomes different farther downstream, and after z/D= 6 the r.m.s. fluctuations increase with the increase of mass loading except close to the wall. The r.m.s. fluctuations of the beads close to the wall are always lower relative to the single phase, which is due to the extension of their recirculation zone. The longer recirculation zone of the beads implies that the gas phase flow has been affected by the presence of the beads in that the length of the recirculation zone is also longer for the gas phase and this will be demonstrated later for the 80 μm beads. However, it can be argued here that if the beads have negative velocities close to the wall, so must the air. So the length of the recirculation zone of the gas phase is at least as long as that of the beads.

iii) Bead flux characteristics.

The bead flux was measured as the number of valid Doppler signals in the 35-45 μm size range per second per effective probe volume area normal to the flow of the beads at each point. The arguments made in chapter 3 for the flux measurement are valid here only in the central region, which is similar to the jet flow. The area of the control volume has to be approximated again by the width of the control volume at the e^{-2} point of the Gaussian light distribution of the beam, b, multiplied by the width of the image of the collection optics spatial filter, s, which limits the length of the control volume because the optics are positioned off-axis. So the effective area of the control volume is $A = s \times b = 200 \times 55\ \mu m^2$

It is shown in table 4.2 that the absolute values of the flux centreline at the exit of the upstream pipe, G_{om}, are not proportional to mass loading. This is due to the turbidity of the flow which is higher here than in the free jet flow, due to the confinement of the flow. The beads which recirculate generate a "wall film" on the glass tube, which attenuates the incident and the scattered light and

thus the effective area A of the control volume, which was assumed constant, may vary with mass loading and location. The lack of knowledge of the variation of the effective area of the probe volume during the measurement, because of the absence of the necessary electronic instrumentation at the time of this experiment, limits the flux results to relative comparison for each mass loadings and precludes comparison of absolute values.

In chapter 3, flux was defined as the particle arrival rate per unit area of the probe volume and this is appropriate when the beads are moving in one direction, as in the jet flow of chapter 3. For the recirculating flow described here, the axial bead flux G(x,z) at a point (x,z) of the flow is defined as :

$$G(x,z) = F_{+}(x,z) - F_{-}(x,z) \qquad (4.1)$$

where $F_{+}(x,z)$ and $F_{-}(x,z)$ are the arrival rate at the probe volume of the laser Doppler of the beads moving with axial velocity $U > 0$ and $U < 0$ respectively and normalised by the area of the probe volume (# s^{-1} m^{2}). So $G(x,z) < 0$, when the net fraction of all beads passing through a point (x,z) is moving in the defined negative direction of the flow.

It was not made possible to take into account the directional ambiguity here and this is the subject of future work combined with improved instrumentation, as described in chapter 2, which will measure the flux and the concentration of the beads. The bead flux is presented here as the number of occurrences per second without taking into account the directional ambiguity. At the central part of the flow there are no beads with negative velocities, so the bead arrival rate is equal to the bead flux G(x,z). This is not correct in the neighbourhood of the separation streamline and inside the recirculation zone, where beads are moving in both directions, so the results obtained there show the time average number of beads present at each point and not the bead flux.

The centreline flux development is given in figure 4.5 normalised by the flux centreline value at the exit of the upstream pipe, G_{om}, and plotted as the reciprocal of the dependent variable. The normalisation parameters are given in table 4.2. The flux decay along the centreline is faster for the lower mass loading beads

suggesting that beads at lower mass loadings disperse faster and this agrees with the velocity results presented earlier.

The radial profiles of the bead flux are shown in figure 4.6 and are normalised by the centreline value at each station. The flux of beads in the recirculation zone, close to the step, is 90% smaller than that at the centreline and the profiles are similar for different mass loadings. Further downstream, at z/D=1.5 & 2.4, the flux profile has a minimum in the shear layer and increases close to the wall, but is always smaller than the value at the centre. The profiles are asymmetric for the higher mass loadings (40% & 80%), probably due to the effect of turbidity on the measurements rather than asymmetry in the flow, as is explained in the following section. The measurements were obtained by traversing the phase-Doppler instrument along its axis, as refraction through the cylindrical glass tube made the measurements along the normal direction to the optical axis difficult. As a consequence, negative values of y/D are closer to the laser (figure 4.1) and the measurements are less affected by turbidity.

Approaching the end of the recirculation zone the near-wall flux increases and at the farthest downstream location the maximum is close to the wall and the central part is nearly flat. This allows the speculation that the majority of the beads leave the recirculation zone due to their weight by sliding down the wall. The profiles become symmetrical farther downstream, where the turbidity effect is lower and this supports the explanation that the asymmetry closer to the step is due to the measuring system rather than the flow.

Expansion ratio of 5

i) Centreline velocities

With the larger expansion, the bulk velocity, U_o, (table 4.3) of the gas flow is smaller as the initial flowrate is the same for both geometries. The single phase mean axial velocity reaches its steady state 4.5 tube diameters from the inlet of the large pipe similar to the observation for the other expansion (figure 4.7(a)). For low mass loading, the velocities are again closer to those of the single phase but there is always a mean slip velocity between the two phases (figure 4.7 (a)). The axial r.m.s. velocity characteristics (figure 4.7 (b) and (c)) are

similar to those discussed earlier and the location of the maximum r.m.s. fluctuations of the single phase appears to scale with the downstream tube diameter and is the same for both expansion ratios. The location of the maximum value of r.m.s. of the fluctuations of the beads does not scale with the downstream tube diameter and further downstream the beads have different fluctuation levels for each expansion ratio. This may be due to partial response to the gas flow turbulence, which appears to be possible as the turbulent Stokes number of the beads increases far downstream from the exit. However, the centreline development of the radial r.m.s. fluctuations confirms the weak response of the beads to gas turbulence along the centreline.

ii) Radial profiles of mean and turbulent velocities.

Radial profiles of the mean and r.m.s. axial velocity are presented in figures 4.8 and 4.9 respectively and show similar features to those for the other expansion ratio. In order to find the response of the beads to the gas turbulence, it is necessary to eliminate the fan-spreading effect and this is the case when the mean velocity in the direction of the measurements is around zero. Thus, the azimuthal r.m.s. fluctuations were measured because the mean azimuthal velocity is zero for the axisymmetric sudden expansion and the fan spreading effect is eliminated, see figure 4.10. The profile close to the exit of the upstream pipe shows that there is a maximum in the shear layer for the single phase and for the beads (figure 4.10(a)), but the azimuthal r.m.s. fluctuations of the beads are smaller. Farther downstream, the beads' radial profiles have a maximum which always occurs at the same radial location as the maximum of the axial r.m.s. fluctuations, but is smaller than the corresponding axial value by a factor of around 2.5, which suggests that the beads acquire about 40% of the gas turbulence (figure 4.10 (b) and (c)). Also, for the single phase jet there is anisotropy between the axial and azimuthal turbulent velocities of the order of 0.30 while for the beads the anisotropy is much larger and of the order of 0.80. So only a small amount of radial turbulence can be acquired by the beads and is enough to generate the large axial r.m.s. values due to the fan spreading effect and also their fan-like trajectories make them cross the separation streamline. At z/D=5.33, the beads' azimuthal r.m.s. fluctuations are constant and

larger than those of the single phase despite their reduced response to the gas turbulence due to their inertia and they increase as mass loading increases (figure 4.10(d)). This strange result can be due to the ability of the beads to maintain their conditions for a longer period than the gas phase due to their inertia, although the axial gas phase turbulence may be increased here also as was measured in the presence of the 80 μm beads and is presented later in this section.

Finally, the radial variation of the r.m.s. fluctuations normal to the main direction of the flow was measured at z/D=1.33. The complete radial profile could not be measured because the beams were totally reflected at the surface of the tube and the existence of the steel bar, which supports the tube, prohibited optical access to part of the tube. The mean and the r.m.s. of the radial velocity are shown in figure 4.11, with the former very small relative to the axial velocity of the single flow and of the beads. The scale of figure 4.11(a) is different from that of the axial velocity profile (figure 4.8(c)), in order to show the sign of the radial velocity which is negative at the neighbourhood of the separation streamline and implies beads moving towards the wall. The radial r.m.s. fluctuations show the same trends as the azimuthal r.m.s. fluctuations and their values are approximately equal. This result supports the supposition that the response of the beads to the gas phase turbulence is partial, although it is enough to cause bead transport along the separation streamline.

iii) Bead flux characteristics

The centreline flux, normalised by G_{om}, table 4.3, shows that the decay of the flux along the centreline is faster than that of the beads with the expansion ratio of 3.33 (figure 4.12). This result is expected as the timescale of the larger expansion ratio is larger and the beads have more time to react to the gas turbulence, so more beads enter the recirculation zone.

The asymmetry of the radial profiles of the flux is smaller than for the smaller expansion ratio, since the turbidity effect is lower with the beads dispersed over a larger area. The profiles of figure 4.13 show that the behaviour of the beads is similar to that with the smaller expansion ratio.

b) Velocity flux characteristics of the 80 μm beads and gas phase flow

The characteristics of the 80 μm beads are presented separately for each expansion ratio. The gas phase velocity characteristics in the presence of the beads are also presented. The following order will be followed: centreline velocity characteristics of the beads and the gas phase, radial profiles of mean and turbulent velocities of the beads and the gas phase and finally the bead flux characteristics.

Expansion of 3.33

i) Centreline velocities

Figure 4.14(a) shows that the mean axial centreline velocity of the 80 μm beads is lower than that of the single phase at the exit of the upstream pipe but becomes larger than the gas at one tube diameter downstream, as the gas phase decelerates rapidly and reaches the bulk velocity of the downstream pipe after 4.5 tube diameters. The 80 μm beads maintain their initial velocity up to two diameters downstream of the exit of the upstream pipe before starting to lose momentum to the gas. However, it is not before four tube diameters that the gas phase has a larger velocity than the single phase because of the momentum transfered from the beads to the gas. The velocity characteristics of the beads along the centreline for different mass loadings are nearly the same, so the only parameter which could affect the amount of momentum transfered to the gas is the mass loading of the beads. At the last measured location the gas phase for all three mass loadings is moving faster than the single phase on the centreline and appears to be fully developed, although the beads still decelerate.

The bead axial r.m.s. fluctuations, shown in figure 4.14(b), are larger than these of the single phase at the exit of the upstream pipe and are constant along the centreline, without any distinguishable maximum but with the lower loading, they have larger fluctuations up to four diameters from the inlet and gradually downstream the reverse effect is observed, as was the case for the 40 μm beads. The turbulence modification of the gas phase in the presence of the beads is not monotonic. Near the inlet, it is reduced relative to the single

phase and this effect is more pronounced for the higher mass loadings, while further downstream it is increased relative to the single phase. For the particulate phase, fan-spreading is likely to explain the larger axial r.m.s. fluctuations relative to the single phase. The results for the gas phase agree with observations made in chapter 3. The 80 μm bead lose momentum at a slower rate than the 40 μm beads as expected from their larger time constant.

ii) Radial profiles of mean and turbulent velocities

The mean axial velocity profile at the exit shows that there are no beads in the recirculation zone and the profiles of the 80 μm beads at z/D=0.06 and z/D=0.3 (figure 4.15 (a) and (b)) are nearly flat and confined to the central region of the tube. The velocities of the beads are lower than those of the single phase with the exception of the shear layer, where the beads move much faster than the gas. At the higher mass loadings, the beads move slower than the lower loading. At z/D=2.4 the gas phase mean velocity has been measured in the presence of the beads and there is nearly no change in the axial mean velocity relative to the single phase for all three mass loadings. The beads move faster than the single phase as the gas decelerates. The gas phase moves faster at z/D=5 and z/D=8 (figure 4.15 (e) and (f)) than the single phase at the centre but slower close to the wall as required by mass continuity. In consequence, the recirculation zone of the gas phase is longer in the presence of the beads and this effect is more obvious for the larger mass loading.

The mean axial velocity profile of the beads is asymmetric in that the beads reach the wall of the tube first on the side of the negative y/D and the location of the maximum velocity is not on the geometrical axis of the tube but at y/D=-0.1 at the farthest downstream measured profile. It seems that this happens because the axis of the upstream tube is inclined to the axis of the downstream tube by an angle of around 1°. This also might explain the asymmetry of the single phase profiles and the 20% difference between the reattachment lengths at ±y/D. However, it is quite common in the literature to observe asymmetries in sudden expansions for reasons independent of the geometry of the flow (e.g. Cherdron et al., 1978) and it is possible that this is the case here.

The axial r.m.s. fluctuations are shown in figure 4.16 and at the inlet to the section the beads have larger fluctuations than the single phase at the centre but in the shear layer, the single phase has much larger r.m.s. values. The small axial r.m.s. fluctuations of the beads in the shear layer suggest even smaller radial r.m.s. fluctuations, so there is not enough response to the turbulence to make them cross the separation streamline. The gas phase turbulence is the same as that of the single phase at the centre but it is reduced in the shear layer and inside the recirculation zone at z/D=2.4 (figure 4.16(c)). Although the presence of the beads does not modify the mean gas velocity characteristics, the turbulence is suppressed even in the recirculation zone where there are no beads present. This implies that the effect of the presence of the beads on the fluid is not local, but modifies the gas flow field everywhere even in regions where no beads are present. The beads disperse due to their initial radial r.m.s. values and, in lesser part, because of their very small response to gas turbulence, and reach the wall of the tube at z/D=5 where their r.m.s. fluctuations have a maximum close to the wall and are everywhere larger than those of the gas phase. At this axial station, the gas phase turbulence is larger than that of the single phase for all mass loadings and this effect is more pronounced for the higher mass loading (figure 4.16(e)) due to the increased production by the greater mean rate of strain. Finally, at z/D=8 (figure 4.16(f)), the r.m.s. fluctuations of the beads are constant at the centre and decreases close to the wall with the former result suggesting that the beads do not bounce on the wall but remain close to it. The difference between the gas phase and the single phase r.m.s. values is larger here than farther upstream, although the effect of mass loading is smaller (figure 4.16(f)).

iii) Bead flux characteristics

The centreline flux, shown in figure 4.17, decays slower for the 80 μm beads than for the 40 μm beads since the former do not follow the recirculation zone. The flux of the higher mass loading 80 μm beads decays faster in agreement with observations in the free jet of chapter 3. It is unlikely that this is an artefact introduced by the turbidity of the flow, because of the consistency of the results for this flow and for the free jet.

The radial flux profiles for the 80 μm beads are shown in figure 4.18, normalised by the local centreline value. At the inlet to the section, most of the beads are close to the centre, but at z/D=2.4 they have spread out. The rate of spread may be quantified by the axial development of the flux half width (figure 4.17(b)) which shows that the beads spread faster at the higher mass loading and this is consistent with the centreline results. The profiles at z/D = 3.2, 5 and 8 show also that the higher loading beads spread faster and as the beads reach the wall remain in the near wall region (figure 4.18(f)). A qualitative difference between the 80 μm beads and the 40 μm beads is that most of the flux of the 40 μm beads is close to the wall downstream of the recirculation zone.

Expansion ratio of 5

The main difference between the two expansions of the 80 μm beads is that the particles follow the recirculation zone in the larger expansion ratio. This will be established in the results below, which are presented in the same order as before.

i) Centreline velocities

The centreline development of the beads shows a similar trend to that of the smaller expansion ratio. The beads start with smaller velocity than the single phase at the exit, which is maintained up to 1.5 tube diameters before decaying. The mass loading effect is more obvious in this expansion as the higher loading beads start with smaller velocities and, at the farthest downstream location, have larger velocities than the lower loadings. The gas phase moves faster than the single phase after z/D = 2 (figure 4.19(a)). The r.m.s. fluctuations of the gas phase are modified in the same way as for the smaller expansion ratio and are lower than the single phase close to the inlet and larger after four tube diameters (figure 4.19(b)).

The r.m.s. fluctuations of the beads are larger than that of the single phase at the exit of the upstream pipe and remain constant up to three tube diameters where there is a slight increase and a maximum at around four tube diameters. The axial location of the maximum is "delayed" as the mass loading increases and is the reason for the larger r.m.s. fluctuations at higher mass loading beads far

downstream even though they leave the upstream pipe with smaller r.m.s. than the lower loadings.

The centreline results show small differences between the behaviour of the 80 μm beads in the two expansion ratios and there is nothing to indicate that the beads disperse in the recirculation zone at the larger expansion.

ii) Radial profiles of mean and turbulent velocities

The beads leave the upstream pipe with smaller velocities than the single phase at the centre and larger in the shear layer (figure 4.20(a)). They enter the recirculation region and their mean velocities there are small and negative but larger than these of the single phase. The higher loading beads leave the upstream pipe with smaller velocity but there is no corresponding effect in the recirculation zone. At z/D=0.66 and in the central region the beads still have smaller velocities than the single phase, but the beads' shear layer is farther from the axis and the velocity gradient much larger than that of the single phase. This effect is more obvious at z/D=1.33 and 2.66 (figures 4.20(c) and (d)), where the beads move faster than the single phase everywhere along the radial profile. At this axial station, the beads at high mass loading move with lower velocity than the lower mass loadings even into the recirculation zone. The larger velocity of the beads relative to the single phase suggests that the beads' recirculation region is shorter than that of the single phase, and in contrast to the 40 μm beads it is likely that the gravitational forces which oppose the drag forces are sufficiently large to stop the negative movement of the 80 μm beads. At higher mass loadings, the beads always move slower close to the wall and the gas phase moves faster than the single phase in the central region with smaller velocities close to the wall and a longer recirculation zone as was observed at the smaller expansion flow. At z/D=4, figure 4.20(e), the beads at higher loading still have negative velocities close to the wall and move faster at the centre. At the last measured station downstream from the step, z/D=5.33, the gas phase is faster than the single phase at the centre and the recirculation zone is extended and is larger for the higher loadings. The 80 μm beads have a large velocity gradient in the radial direction which was not observed for the 40 μm beads and move faster than the gas phase everywhere (figure 4.20(f)).

The radial profiles of the axial r.m.s. fluctuations are shown in figure 4.21. The exit profile for the 80 μm beads is similar to that of the 40 μm beads, although flatter at the centre and both have lower r.m.s. fluctuations in the recirculation zone than the single phase. So there is no particular characteristic of the r.m.s. fluctuations profile which distinguishes the 40 and 80 μm beads at the exit of the upstream pipe. This changes at z/D=0.66 where the 80 μm beads have larger r.m.s. fluctuations than both the 40 μm beads and the single phase inside the recirculation zone. The fluctuations of both bead sizes are the same in the central region of the flow and lower than those of the single phase. So the 80 μm beads appear to disperse better than the air in the recirculation zone, which is a strange result as the 80 μm beads did not enter the recirculation zone at the smaller expansion-ratio flow. The beads at the higher mass loading have smaller r.m.s. fluctuations in the centre and in the recirculation zone and no particular effect of mass loading exists in the shear layer (figure 4.21(b)). At z/D=1.33, figure 4.21(c), the 80 μm beads have larger r.m.s. values than the single phase over a wide region of the shear layer and only in a small region of the recirculation zone close to the wall have smaller values. The maximum of the axial r.m.s. fluctuations occurs in the shear layer, closer to the centre for the higher mass loading and shifted towards the wall as the mass loading decreases. The 40 μm beads at the same station have smaller r.m.s. values than the single phase. At z/D=2.66, the beads have larger r.m.s. values than the single phase in the recirculation zone and close to the wall but lower values in the centre. The gas phase turbulence is not affected by the presence of the beads for the lower mass loading but is suppressed as the mass loading increases, figure 4.21(d). The reduction of the gas axial turbulence is expected as the beads introduce an extra mechanism for the dissipation of the turbulent kinetic energy (Owen, 1969). At z/D=5.33, the axial r.m.s. fluctuations of the 80 μm beads are larger than that of the single phase and the gas phase in the presence of the beads, which is explained by the fan spreading effect. The gas phase turbulence is everywhere larger than that of the single phase for all three mass loadings, which is similar to the observation for the smaller expansion ratio and for the free jet flow.

The 80 μm beads have larger r.m.s. fluctuation values than the single phase and the 40 μm beads, so it seems that they disperse

more. This unexpected result is an artefact of the presence of high and low velocity beads at the same point in the shear layer. The large axial velocities of the 80 μm beads belong to the main jet flow and have been transported there by the large eddies of the flow, while the low axial velocity beads belong in the instantaneous recirculation zone region and exist at the same position in the flow but not at the same time. So the time averaged axial velocity probability function of the 80 μm beads is bimodal over a large region of the shear layer of the flow which is not observed for the single phase flow, where a skewed velocity probability function was measured, or for the 40 μm beads. Figure 4.22 shows the velocity p.d.f. of the single phase flow and of the 40 and 80 μm beads measured at z/D = 1.33 and for y/D = 0.24 in the large expansion ratio. The width of the skewed p.d.f. of the 40 μm beads is smaller than that of the single phase as should be expected for the beads which can acquire only a portion of the gas phase turbulence.

The radial r.m.s. fluctuations along the centreline of the beads were constant and are not presented here. At z/D=2.66, the mean azimuthal velocity is zero for both the beads and the single phase, figure 4.23(a). The azimuthal r.m.s. fluctuations have a maximum value at the radial location where the axial r.m.s. fluctuations of the beads have a maximum. However, the azimuthal r.m.s. is around 30% of the single phase value, which is lower than the observed value for the 40 μm beads by a factor of 10%, while the difference between the response of the 80 and the 40 μm should be around a factor of 4, the ratio of the relaxation times.

iii) Bead flux characteristics.

The centreline flux decay, figure 4.24, shows that the 80 μm beads at this expansion ratio disperse faster for the higher mass loading and relative to the smaller expansion. The flux decay of the 80 μm beads is lower than that of the 40 μm beads for the same expansion ratio.

The radial profiles of flux show that the relative concentration of 80 μm beads in the recirculation zone is smaller than of 40 μm. The flux of the 80 μm beads in the reverse flow region is small close to the step and increases farther downstream, relative to the local centreline value. This happens, because gravitational forces are

important for the 80 μm beads as the bead velocity in the recirculation zone is approximately 1 m/s which is only twice their terminal velocity. So the beads stop in their reverse flow movement due to gravity before reaching the step. The profiles appear symmetrical in contrast to those of the 40 μm beads and this is expected because the turbidity effect on the measurements is smaller for the 80 μm beads. The radial profiles show that the relative number of 80 μm beads in the recirculation zone is larger for the higher mass loading, which means that the beads for this case disperse faster and this agrees with the centreline results although they could be some effect of turbidity on the measurements. The radial profile of flux at z/D=5.33, figure 4.25(f), is further evidence that the 80 μm disperse less than the 40 μm beads, as the flux profile of the 80 μm beads has a maximum at the centre, a minimum in the shear layer and a second maximum close to the wall which is always much smaller than the centreline value. This does not happen for the 40 μm beads which have a nearly flat profile at the centre and the flux maximum is close to the wall.

c) Velocity characteristics of 200 μm beads

The velocity characteristics of the 200 μm beads are presented in this section and indicate that they do not recirculate for either expansion ratio. The particle relaxation time for the 200 μm beads is around four times larger than that of the 80 μm beads and is enough to prevent the 200 μm beads from entering the recirculation zone at the larger expansion ratio flow. This underlines the importance of the particle relaxation time for the dispersion of the beads into the recirculation zone. The centreline development and the radial profiles of axial velocities for the smaller expansion ratio is presented at the first subsection, followed by the centreline development for the larger expansion ratio.

Expansion ratio of 3.33

i) Centreline velocities

Figure 4.26 shows the centreline development of the mean flow of the 200 μm beads in comparison to the single phase flow. The beads leave the upstream pipe much slower than the single phase, due

to their inability to interact with the gas inside the tube as the small Stokes number S_m = 0.0032. The beads at the larger mass loading, 58%, have slightly smaller velocity than at the lower mass loading at the exit of the upstream pipe. It can be speculated that the bouncing of the beads on the wall of the pipe (Boothroyd, 1971) is more frequent for the high mass loading and causes the smaller bead velocity at the exit. The velocity of the beads increases slightly up to z/D = 2 because the air flow accelerates them. The decay of the gas mean velocity is rapid after z/D = 2 and downstream of this point the beads move faster than the single phase flow and their velocity decays slowly after z/D = 4 as momentum is transfered from the beads to the gas (figure 4.26(a)).

The axial r.m.s. fluctuations of the beads remain equal to the value at the exit of the upstream pipe up to around z/D = 5 and increases slightly farther downstream, due more to the fan spreading effect than to response to the gas. The velocity fluctuations of the beads at the exit of the upstream pipe are larger than these of the single phase flow probably due to the bouncing of the beads on the wall of the pipe. Also the velocity fluctuations of the beads are larger than the single phase after z/D=5, due to their inertia, which makes them maintain their initial values for a longer period.

ii) Radial profiles of mean and turbulent velocities.

The 200 μm beads do not enter the recirculation zone and the profiles of their mean axial velocity are rather flat. The profiles at z/D = 0.06 and at z/D = 8, figure 4.27, show that the beads at the lower mass loading move everywhere slightly faster than at the high mass loading. The 200 μm beads do not reach the wall of the tube even at z/D = 8, figure 4.27(b), as they disperse less than the 80 μm beads, which reach the wall at z/D = 5. The asymmetry observed with the 80 μm beads is also present with the 200 μm beads.

Figure 4.28 shows that the profiles of the axial r.m.s. fluctuations of the 200 μm beads at z/D = 0.06 and z/D = 8 are flat and without influence of the mass loading. The r.m.s. fluctuations of the beads are larger than those of the single phase at z/D = 8 due to the fan spreading effect.

Expansion ratio of 5

The 200 μm beads do not enter the recirculation zone formed by the expansion ratio of 5 and the results in the radial direction show similar observations as for the smaller expansion. So only the centreline development is presented here. Figure 4.29(a) shows that the centreline velocity of the beads is again much slower than the single phase at the exit of the upstream pipe, followed by modest acceleration up to z/D = 1.5 and deceleration after z/D = 3, as the beads move faster than the single phase after the fast deceleration of the gas flow. The axial r.m.s. fluctuations of the beads, figure 4.29(b), at the centreline are similar to these for the smaller expansion, and there is no indication of better response of the beads to the gas.

d) Separation streamlines and zero velocity contours.

This section presents the locus of zero axial velocity for the 40 and 80 μm beads and the separation streamline for the single phase flow as well as the contours of the zero axial velocity for the gas phase in the presence of 80 μm beads. The modification of the gas phase recirculation zone is quantified and the reattachment length of the beads is presented.

The gas mass flowrate is a conserved quantity for the sudden step expansion flow. Differences of the order of 15 % were found between the air flowrate estimated by integrating the velocity profiles and that measured by the rotameters and are due to the uncertainty involved in the integration close to the wall. The gas flowrate calculations show asymmetry of the flow of the order of 20% in the worst case, which results in a reattachment length difference between the two examined sides of the order of 15 % as can be seen from the separation streamlines which are shown in figures 4.30 and 4.31 for the two expansion flows. The length of the recirculation zone has been measured by placing the laser Doppler probe volume as close to the wall as possible.

The mass flowrate of the beads is not presented for reasons explained in section 3 and the zero mean axial velocity contours for the two expansion ratio flows for the 40 and 80 μm beads are shown in figures 4.30(a) and 4.31(a) and 4.30(b) and 4.31(b) respectively.

The contours of zero velocity are also shown for the single phase and the gas phase in the presence of the 80 μm beads for the three mass loading cases. The main difference between the behaviour of the 40 and 80 μm beads is that the recirculation zone for the latter is shorter for all the examined mass loadings. This suggests larger curvature of the "streamlines" of the beads than those of the air flow and it is not apparent what force would introduce this curvature. The recirculation zone of the 40 μm beads is always longer than that of the single phase by 15, 36 and 57% for the expansion ratio of 3.33 and 13, 23 and 50% for the expansion ratio of 5 respectively for 13, 40 and 80% mass loading. The recirculation zone of the 80 μm beads with the larger expansion ratio is shorter than that of the single phase by 20 and 10 % for the 23 and 40% mass loadings respectively and the same for the 86% mass loading.

The gas phase recirculation zone in the presence of the 80 μm beads has been extended relative to the single phase for all three mass loadings by more than 33 % for the larger expansion ratio and between 10 and 40 % for the smaller.

4.4 Comparison between the centreline velocity of the free jet and the expansion flows.

The effect of the expansion ratio of the flow on the centreline development of the beads is examined here and compared to the free jet results of chapter 3. The free jet flow can be considered an extreme case of a sudden step expansion flow with the wall boundaries being arbitrarily far away. The initial air flowrate and the geometry of the upstream pipe for all three geometries was identical, so that observed differences in the centreline development are due to the interaction between the beads and the gas flow downstream of the nozzle exit. The exit mean axial centreline velocity for each flow, U_{om}, is given in tables 4.2 & 4.3 for the two expansion ratios and in table 3.4 for the free jet, and there were used as normalisation parameters for the single phase velocity profiles and the jet pipe diameter was used to normalise the distance from the nozzle along the centreline.

The mean motion of the beads is affected more by the air in the sudden step expansion flows than in the free jet. The inability of the

beads to respond to the greater deceleration of the mean gas motion in the expansion flows generates larger slip velocity between the two phases close to the nozzle. This results in an increased drag force acting on the beads and decreases the slip velocity between the two phases faster than in the free jet. The centreline development of the single phase flow for the three cases is presented at figure 4.32(a) and certifies the faster deceleration of the flow for the expansion flows. The deceleration timescale is given by :

$$T_{dec} = \left(\frac{dU_m}{dz}\right)^{-1} \qquad (4.2)$$

and may be calculated from the measurements along the centreline. Table 4.4 gives the deceleration timescales of the single phase flow for the three arrangements at different distances from the exit of the upstream pipe as well as the equivalent mean flow Stokes number, which is defined as :

$$S_m = \frac{T_{dec}}{\tau_p} \qquad (4.3)$$

and for $S_m << 1$ there is no response of the beads to the changes of the mean flow, so the mean slip velocity between the beads and the gas increases. The table shows that for the free jet and the 40 μm beads $S_m > 1$, so the beads always follow partly the mean gas flow deceleration and the slip velocity between the two phases remains small everywhere. In the expansion flows after two tube diameters from the nozzle $S_m < 1$, so the slip velocity close to the nozzle is larger for the expansion flows but it is smaller far downstream. The variation of the mean slip velocity along the centreline normalised by the local mean velocity of the single phase, U_m, for the two expansion ratios and the free jet is shown in figures 4.32(b) and 4.32(c) for the 40 and 80 μm beads respectively for the lower mass loading, so that the gas flow can be considered unmodified relative to the single phase. The figures show that the mean slip velocity for the expansion flows is much larger than for the free jet close to the nozzle, but decreases faster downstream and becomes smaller than that of the free jet for the 40 μm beads for the expansion ratio of 3.33. Similar observations

can be made for the 80 μm beads, but there is some delay in the development due to their larger inertia.

So in order to reach equilibrium between the two phases in a required distance from a nozzle, the continuous phase should decelerate rapidly as close to the injecting nozzle as possible and generate a large slip velocity between the two phases, so that the beads can rapidly lose their momentum. This has practical implications for example, at a pulverised coal furnace, where the reverse flow region in the burner, generates large slip velocity between the two phases, which decelerates the coal particles quickly and gives them more chance to burn in the recirculation zone, and thereby helps the stability of the flame.

The axial r.m.s. fluctuations normalised by U_{om} are shown in figure 4.33 and the single phase flow has larger maximum r.m.s. values in the expansion flows than in the free jet. However, far downstream from the step in the expansion flows the turbulence level is smaller and the flows are more "lazy" so that the beads have more time to respond to the flow. Thus the 40 μm beads respond better to the gas flow for the expansion flows, as their r.m.s. fluctuations are larger than in the free jet, figure 4.33(b). Similar observations can be made for the 80 μm beads, figure 4.33(c), although the changes between the different flows are smaller due to the larger inertia of the beads. The radial r.m.s. fluctuations are shown in figure 4.34(a) and (b) for the single phase flow and the 40 μm beads respectively in the expansion flows and the free jet and verify the large anisotropy of the axial and radial direction for all the flows.

Finally, comparison of the flux half width of the 80 μm beads for the free jet and for the expansion ratio of 3.33, figure 4.35, shows that the 80 μm beads disperse faster in the expansion flow for mass loadings (23 and 86 %).

The presented comparison of the free jet and the expansion flows has shown that the larger deceleration rate of the gas flow at the latter is an advantage in that it increases the response of the beads to the mean and turbulent motion of the gas.

4.5 Discussion

Three questions are addressed here. Do the beads disperse in the recirculation zone due to turbulence or due to mean drag and what parameters determine their behaviour ? Do they enter or leave the recirculation zone at "preferred" locations ? How the gas phase characteristics are modified by the presence of the beads during their two-way interaction ?

The first question is considered by summarising observations from the measurements. Two expansion ratios have been examined and it has been shown that the 40 μm beads respond to the recirculation zone of the smaller expansion but the 80 μm do not. With an increase in the expansion ratio by a factor of 1.5, the 80 μm beads have been shown to enter the reverse flow region and the rate of centreline decay of the flux of the 40 μm beads is larger, implying wider dispersion of the 40 μm beads relative to the smaller expansion ratio. So it seems that the beads are more responsive to the larger expansion ratio gas flow, but this does not imply that the larger the expansion the better the particle dispersion, because in the limit of the free jet the dispersion of the particles is smaller, as presented in chapter 3. It was also found that the axial r.m.s. fluctuations of the 80 μm beads in the shear layer, when responsive to the recirculation zone, are larger than those of the 40 μm beads and the gas phase from the wall region to the centreline and this is due to the bimodal form of the velocity p.d.f. observed for the 80 μm beads.

There are three parameters affecting the behaviour of the beads in the neighbourhood of the separation streamline and their relative importance is not clear. Two are connected with the mean flow, namely a "centrifugal" effect due to the curvature of the air streamlines and the transit time of the beads along a distance equal to the reattachment length and the third is connected to the flow turbulence. The beads cannot enter the recirculation zone due to their response to the mean radial velocity because of the shape of the gas separation streamline. As can be seen in figures 4.30 & 4.31, the gas phase separation streamline lies parallel to the wall of the tube close to the step and its curvature gradually increases until the streamline meets the wall at the reattachment location. Virtually by definition of a separation streamline neither the gas nor the beads can

cross the separation streamline due to the mean radial motion. The only available mechanism is turbulent transport and so the turbulent timescale is important for the dispersion of the beads in the recirculation zone.

The curvature of the gas phase streamlines is one of the parameters influencing the trajectories of the beads, which are centrifuged because of their inertia. The centripetal force acting on a bead is due to the slip between the radial components of velocity of the beads and the gas and is the source of beads' curved trajectories, since the "buoyancy" force due to the radial pressure gradient in the air is negligibly small (Kriebel, 1961). The relative magnitude of the centripetal force to the viscous drag force acting on the bead can be estimated by the "centrifuge" Stokes number, defined as (e.g. Kriebel, 1961, Dring & Suo, 1978)

$$S_\omega = \frac{18\,\mu}{\rho_p\,\omega\,d_p^{\,2}} \qquad (4.4)$$

where ρ_p and d_p are the density and the diameter of the bead and ω and μ are representative values of the angular velocity of the air and of its viscosity, respectively. Physically, this number represents the ratio of the drag force on a stationary particle to the centripetal force necessary for the particle to describe circular motion with the azimuthal velocity of the gas. Appendix 4.A shows the estimate of representative values of the radius of curvature of the separation streamline and the angular velocity corresponding to the gas flow velocity at the exit of the upstream pipe and the values of the "centrifuge" Stokes number, S_ω, are given at tables 4.5 & 4.6 for the two expansion ratios and for 40 and 80 μm beads. As S_ω decreases, the bead departs from the curved path of a fluid element, here the separation streamline, and generates an outwardly-directed drift component of mean radial velocity. This is the basis for the earlier argument that the beads cannot enter the recirculation zone due to the drag from the mean slip velocity and proves that the beads cannot have larger streamline curvature than the gas. The centrifuge Stokes number for the 40 μm beads, for all mass loadings examined here, is of the order of 10, suggesting that the influence of the centrifugal force on the behaviour of the 40 μm beads is small. For the 80 μm

beads, S_ω is of the order of unity and the effect of the centrifugal force is not negligible. For the same initial velocity of the beads, the centrifugal effect is more important for the smaller expansion ratio due to the smaller radius of curvature of the gas flow streamlines there and may be partly responsible for the unresponsiveness of the 80 μm beads to the recirculation zone. However, the difference between the centrifuge Stokes numbers for the two expansion ratios for the 80 μm beads is of the order of 2, which is not sufficiently different to be solely responsible for the responsiveness of the beads to the recirculation zone of the larger expansion.

A second feature that is important for the beads is the mean transit time Stokes number, S_{tr}, which is defined as :

$$S_{tr} = \frac{T_{tr}}{\tau_p} \qquad (4.5)$$

where T_{tr} is the transit time of the beads along a distance equal to the length of the recirculation zone. Values of transit time and of the equivalent Stokes number are given in tables 4.5 & 4.6, based on the measured bead velocities along the centreline. For values of $S_{tr} < 1$ the beads do not have enough time to decelerate and the larger the values of S_{tr} above unity, the more chance the beads have to respond to the gas phase recirculation zone. Tables 4.5 & 4.6 show that the 40 μm beads can interact with the gas flow during their transit time for both expansion ratio flows. However, for the smaller expansion ratio there is no time for the 80 μm beads to be influenced, as their transit time Stokes number is much less than unity and the measurements confirm that they do not follow the recirculation zone. At the larger expansion ratio flow the transit time Stokes number of the 80 μm beads is of the order of unity suggesting that there is a chance for the beads to respond to the gas phase and the results show that they disperse into the recirculation zone.

The third parameter which is a measure of the response of the beads to turbulence is the turbulent Stokes number, S_t, defined as :

$$S_t = \frac{t_e}{\tau_p} \qquad (4.6)$$

Here t_e is the timescale of the energy containing eddies of the gas flow and τ_p is the bead relaxation time as before. t_e is the slowest timescale of the gas flow to which the bead should respond to acquire turbulence. The energy containing eddies (Stewart & Townsend, 1951, referenced by Batchelor, 1982, Townsend, 1979) contain about one fifth of the total energy. Lumley (1978) suggests that for homogeneous turbulence

$$t_e \approx 8\, \mathcal{T}_f \qquad (4.7)$$

where $\mathcal{T}_f$ is the Lagrangian integral timescale. For shear layer flows, an estimate of the timescale $\mathcal{T}_f$ can be based on the length scale in the cross-stream direction, L_{22}, and the r.m.s. value of the cross-stream velocity u'_2 (Tennekes & Lumley, 1972)

$$\mathcal{T}_f \approx \frac{4\, L_{22}}{3\, u'_2} \qquad (4.8)$$

so finally

$$t_e \approx \frac{32\, L_{22}}{3\, u'_2} \qquad (4.9)$$

In the present recirculating flow, L_{22} is considered equal to 1/10 of the step height, which corresponds to the width of the shear layer of the radial profile of the axial velocity, and the r.m.s. value u'_2 equal to the cross stream r.m.s. velocity v_s', which is the equal to w_s' in the recirculation zone, where subscript s stands for the single phase. The above relations were used to calculate the turbulent Stokes numbers for the expansion flow as given in tables 4.5 & 4.6. The expectation is that for $S_t > 100$, the response of a particle to air turbulence is excellent and that for $S_t << 1$, there is virtually no response to the turbulence of the air. So the 40 μm beads, which for both expansion ratios have turbulent Stokes number larger than unity, can respond to gas turbulence but the 80 μm beads can respond only to the gas turbulence at the larger expansion ratio. This agrees well with the results, although the value of the turbulent Stokes number and

associated conclusions depend critically on the assumed value of the length scale L_{22}.

The above analysis shows that the turbulent and the transit time Stokes numbers should both be greater than unity if the beads are to enter the recirculation zone. These parameters are independent for most practical applications and for example, in a pulverised coal burner, the injection velocity of the coal particles (and their transit time) can be modified independently of the turbulent timescale of the flow defined by the geometry of the burner. So particle sizes capable of responding to the flow turbulence can be made to enter the recirculation zone by increasing their transit time.

The timescale ratios examined here account for some of the experimental results, but not for others, such as the bimodal velocity probability function of the 80 μm beads. It is therefore likely that other parameters exist which are partially responsible for the explanation of the observations.

Another parameter which could increase the dispersion of the beads is the existence of relatively large amounts of energy at timescales larger than that of equation (4.7), due, for example, to a preferred frequency in the flow. It has been shown that such oscillations exist in plane mixing layer flows and, for example, Cherdron et al. (1978) found that in plane backward-facing steps there are low frequency oscillations with a characteristic Strouhal ($= \frac{f_m \theta}{U_e}$) number of 0.11. These low frequency oscillations can be partially responsible for the dispersion of particles when their period is comparable to the particle relaxation time. For the present flow, a Strouhal number of 0.11 would lead to a period of 85 ms for the expansion ratio of 5, assuming that the shear layer momentum thickness, θ, is half the step height and a characteristic flow velocity, U_e, of 10 m/s, which is of the order of the 80 μm beads relaxation time. A preferred frequency could also be the cause of the bimodal velocity p.d.f. of the 80 μm beads. The low frequency motions could thus transfer high velocity 80 μm beads into the recirculation zone or low velocity beads, from the recirculation zone, towards the centreline.

However, a more probable reason for the existence of high positive-velocity 80 μm beads in the recirculation zone is the fan

spreading effect explained in chapter 3 for the free jet. Figure 4.36 shows different trajectories of the 80 μm beads and involves eddies as shown at the right side of figure 4.36, which have a certain lifetime. Some of these eddies are large enough so that their timescale is comparable to the bead relaxation time. Trajectories denoted by 1 in figure 4.36 enter the reverse flow region with high velocities due to interaction with the wall of the upstream pipe, but the number of these trajectories is limited. Beads with trajectories denoted by 2 travel as straight lines, due to their inertia, between regions of the flow where interaction with the "large" eddies, introduces a small v'_b component and changes their inclination to the vertical direction. The angle of the trajectories is given by $\pm\arctan(\frac{v'_b}{U_b})$, where v'_b is the radial r.m.s. fluctuation of the beads and U_b is the local bead mean axial velocity. This is equal to ±3° at the exit of the upstream pipe and increases downstream, since U_b decreases and the interaction with the large eddies of the flow keeps v'_b approximately equal to the value at the exit of the upstream pipe. The trajectories denoted by 3 are responsible for the large anisotropy existing between the axial and radial r.m.s. fluctuations of the beads, as was explained in chapter 3. Finally, trajectories denoted by 4 are beads which reach the wall and are thrown out by the large eddies of the gas flow to disperse in the recirculation zone upstream of the instantaneous reattachment location. The combination of trajectories 1 or 2 and trajectories denoted by 4 at the same point in the flow is responsible for the bimodal velocity probability function of the 80 μm beads at the neighbourhood of the gas separation streamline. Some of the trajectories denoted by 4 can leave the reverse flow region and reach close to the centreline with small axial velocity and are responsible for the bimodal velocity p.d.f. there. Although the same mechanism applies to the 40 μm beads, it does not produce bimodal velocity p.d.f. because of the initial mean axial velocity profile is not flat as for the 80 μm beads in the shear layer region (see figure 4.8(a)) and their smaller inertia which allows them to decelerate faster and respond better to the gas flow.

The second question, concerning the location where the beads enter or leave the recirculation zone will be tentatively answered here but more work is needed to provide a conclusive answer. The beads

enter the recirculation zone close to the reattachment location and then, as shown by flow visualisation, most of them concentrate close to the wall region from which they are removed by the gas flow eddies as shown in figure 4.36. The beads leave the recirculating region of the flow by sliding down the wall, due to gravity.

The above explanation is supported by the following observations. The dispersion of the 80 μm beads in the larger expansion-ratio flow is larger for the higher mass loading for which the length of the gas recirculation zone is larger (figure 4.31(b)). This causes more beads to enter the recirculation region relative to the smaller mass loadings and smaller reattachment length cases. This also implies that the bead flux into the recirculation zone is largest close to the reattachment location. Two observations support the argument that most of the beads leave the recirculation zone by sliding along the wall; the increased mass flux of the beads near the wall downstream of the recirculation zone and the positive mean velocity of the beads close to the wall inside the reverse flow region. Flow visualisation supports the above observations.

Finally the third question is about the modification of the gas phase characteristics due to the two-way interaction existing between the gas and the beads. The observations agree well with those of chapter 3 for the two phase jet. The central part of the gas flow accelerates relative to the single phase flow due to the higher inlet momentum flux of the particle-laden flow, so lower gas velocities exist close to the wall due to mass conservation, and this leads to an increase of the length of the recirculation zone. So the reattachment length increases with increasing mass loading, which is quite different from the single phase flow, where the reattachment length is constant and independent of the Reynolds number. This observation supports the results of the calculations of Durst et al (1984). The increase in the reattachment length increases the transit time of the beads and the chances of the beads to respond to the recirculation zone. The gas phase turbulence in the central region is reduced close to the inlet relative to the single phase and is increased farther downstream and this effect is more pronounced here than at the free jet. The gas turbulence inside the recirculation zone is also reduced relative to the single phase flow, but downstream of the reverse flow region is increased close to the wall. So the modification of the gas phase

characteristics due to the presence of the beads gives them more chance to respond to the gas flow.

4.6 Conclusions

i) This chapter describes the velocity and the mass flux characteristics of the flows in round sudden step expansions with ratios of 3.33 and 5 for three bead sizes (40, 80 and 200 μm) at three mass loadings for the same upstream pipe Reynolds number of around 13000. The corresponding volume fractions were always small so that bead-bead interactions were negligible.

ii) The response of the beads to the corner recirculation zone existing downstream of the step is characterised by Stokes numbers S_t and S_{tr} based on the timescale of the energy containing eddies and the transit time of the beads along the length of the recirculation zone respectively.

iii) The centrifuging of the beads, as they try to follow the curvature of the gas streamlines, is expressed as a centrifuge Stokes number and suggests that the curvature of the trajectories of the beads cannot be larger than that of the gas streamlines.

iv) The 40 μm beads respond to the recirculation zone for both expansion ratios for all mass loadings. The axial r.m.s. velocity of the beads is smaller than that of the single phase in the recirculation zone and is always much larger than the radial r.m.s. velocity of the beads. The length of the beads' recirculation zone is larger than that of the single phase flow and increases with mass loading. The centreline development is qualitatively similar to that of the jet and is affected by the mass loading. Downstream of the recirculation zone the single phase adjusts quickly to the pipe flow characteristics while with the beads there is a "delay" which increases with loading. The flux of the beads is largest close to the wall of the tube downstream of the recirculation zone for both expansion ratios.

v) The 80 μm beads respond to the recirculation zone only for the larger expansion ratio. Their axial r.m.s. velocity in the recirculation zone is larger than that of the single phase, in contrast to the 40 μm beads, due to the presence of high velocity beads at region with low velocity, which give rise to bimodal axial velocity p.d.f.. The flux of the beads remains larger on the axis than close to the wall at the last

measured location, because their inertia delays their dispersion. The length of the beads' recirculation zone is approximately the same as that of the single phase flow.

vi) The length of the gas phase recirculation zone in the presence of the 80 μm beads increases as the mass loading increases. The gas phase turbulence is reduced close to the inlet to the section and is larger farther downstream relative to the single phase.

vii) The 200 μm beads do not respond to the recirculation zone for either expansion ratios. Their initial velocity is much lower than that of the single phase flow at the exit of the upstream pipe and increases slightly in the downstream tube before starting to decay. There is no effect of mass loading on the centreline velocity decay up to a loading of 58 %.

viii) The rate of spread of the 40 μm beads decreases with increasing mass loading but the opposite happens for the 80 μm beads. More 80 μm beads disperse in the recirculation zone for the larger mass loading, because the gas phase recirculation zone is longer relative to the lower mass loadings and the transit time of the beads along the reattachment length increases.

ix) Gravity acts against the reverse flow in the recirculation zone, particularly for the 80 μm beads and its effects are important. It is expected that, if the beads were injected vertically upwards, gravity would influence the results in a different way and would help the beads to enter the recirculation zone.

x) The beads enter the recirculation zone by crossing the gas separation streamline close to the reattachment point mainly due to response to the gas phase turbulence and partially due to the fan spreading effect. The bead flux on the wall is continuously increasing and the beads leave the recirculation zone by sliding down along the wall.

xi) The "fan-spreading" model for the motion of the beads, chapter 3, refers to straight line trajectories of the beads between interactions with the large eddies of the gas flow existing in the neighbourhood of the separation streamline, which results in beads crossing the separation streamline. It accounts for the large anisotropy of the beads close to the separation streamline, the paradoxical result of u'_b of the 80 μm beads being larger than u'_f and the bimodal velocity p.d.f. of the 80 μm in the recirculation zone.

TABLE 4.1

Flow conditions

Parameters	EXPANSION RATIO OF 5		EXPANSION RATIO OF 3.33	
	40 μm	80 μm	40 μm	80 μm
Flowrate (l/min)	140	150	150	150
Diameters (mm)				
initial tube	15	15	15	15
expansion tube	50	50	75	75
Bulk velocity (m/s)				
initial tube	13.18	14.15	14.15	14.15
expansion tube	1.188	1.273	0.566	0.566
Reynolds number (-)				
initial tube	13084	14047	14047	14047
expansion tube	3925	4213	2809	2809

TABLE 4.2

Values of velocity and flux used to normalise quantities for the expansion ratio of 3.33

For 40 μm beads:

single phase flow:

U_{om}	15.9	ms^{-1}
U_o	1.188	ms^{-1}

13% loading:

G_{om}	569.	$\# s^{-1}$ {area of measurement volume}$^{-1}$
$U_{om,b}$	13.6	ms^{-1}

40% loading:

G_{om}	869.	$\# s^{-1}$ {area of measurement volume}$^{-1}$
$U_{om,b}$	13.2	ms^{-1}

80% loading:

G_{om}	951.	$\# s^{-1}$ {area of measurement volume}$^{-1}$
$U_{om,b}$	12.9	ms^{-1}

For 80 μm beads:

single phase flow:

U_{om}	17.4	ms^{-1}
U_o	1.273	ms^{-1}

23% loading:

G_{om}	127.	$\# s^{-1}$ {area of measurement volume}$^{-1}$
$U_{om,b}$	14.5	ms^{-1}

40% loading:

G_{om}	214.	$\# s^{-1}$ {area of measurement volume}$^{-1}$
$U_{om,b}$	14.3	ms^{-1}

86% loading:

G_{om}	387.	$\# s^{-1}$ {area of measurement volume}$^{-1}$
$U_{om,b}$	13.5	ms^{-1}

TABLE 4.3

Values of velocity and flux used to normalise quantities for the expansion ratio of 5

For 40 μm beads:

single phase flow:

U_{om}	16.6	ms^{-1}
U_o	0.566	ms^{-1}

13% loading:

G_{om}	527.	# s^{-1} {area of measurement volume}$^{-1}$
$U_{om,b}$	14.8	ms^{-1}

40% loading:

G_{om}	882.	# s^{-1} {area of measurement volume}$^{-1}$
$U_{om,b}$	14.4	ms^{-1}

80% loading:

G_{om}	1273.	# s^{-1} {area of measurement volume}$^{-1}$
$U_{om,b}$	13.8	ms^{-1}

For 80 μm beads:

single phase flow:

U_{om}	16.6	ms^{-1}
U_o	0.566	ms^{-1}

23% loading:

G_{om}	587.	# s^{-1} {area of measurement volume}$^{-1}$
$U_{om,b}$	12.4	ms^{-1}

40% loading:

G_{om}	785.	# s^{-1} {area of measurement volume}$^{-1}$
$U_{om,b}$	12.3	ms^{-1}

86% loading:

G_{om}	1185..	# s^{-1} {area of measurement volume}$^{-1}$
$U_{om,b}$	11.7	ms^{-1}

TABLE 4.4

Deceleration rates and mean Stokes numbers for free jet and expansion flows

range of distances from the nozzle (mm)	T_{dec} (ms)	S_m (40μm) (-)	S_m (80μm) (-)
Free jet flow			
1.5 - 75	45.7	3.8	0.9
75 - 150	17.0	1.4	0.3
150 - 225	27.5	2.3	0.6
225 - 300	54.1	4.5	1.1
300 - 375	72.2	6.1	1.5
375 - 420	138.9	11.6	2.9
Expansion ratio of 5			
6 - 30	477.	40.1	10.0
30 - 50	33.5	2.8	0.7
50 - 80	14.5	1.2	0.3
80 - 100	9.7	0.8	0.2
100 - 150	11.4	0.9	0.2
150 - 200	20.6	1.7	0.4
200 - 250	22.3	1.9	0.5
250 - 300	37.3	3.1	0.8
300 - 350	75.2	6.3	1.6
350 - 400	194.	16.3	4.1
Expansion ratio of 3.33			
3 - 15	50.	4.2	1.0
15 - 75	20.2	1.7	0.4
75 - 120	9.2	0.8	0.2
120 - 160	15.2	1.3	0.3
160 - 200	16.9	1.4	0.4
200 - 220	22.4	1.9	0.5
220 - 250	73.6	6.2	1.5
250 - 300	218.3	18.3	4.6
300 - 350	2984.	250.	62.7

TABLE 4.5

Stokes numbers for the expansion ratio of 3.33

Beads	S_ω (-)	T_{tr} (ms)	S_{tr} (-)	t_e (ms)	S_t (-)
40µm-13%	7.4	22.	1.90	20.	1.72
40µm-40%	10.3	27.	2.33	20.	1.72
40µm-80%	13.7	32.	2.76	20.	1.72
80µm-23%	1.0	15.	0.33	20.	0.44
80µm-40%	1.3	17.	0.37	20.	0.44
80µm-86%	1.9	23.	0.50	20.	0.44

TABLE 4.6

Stokes numbers for the expansion ratio of 5

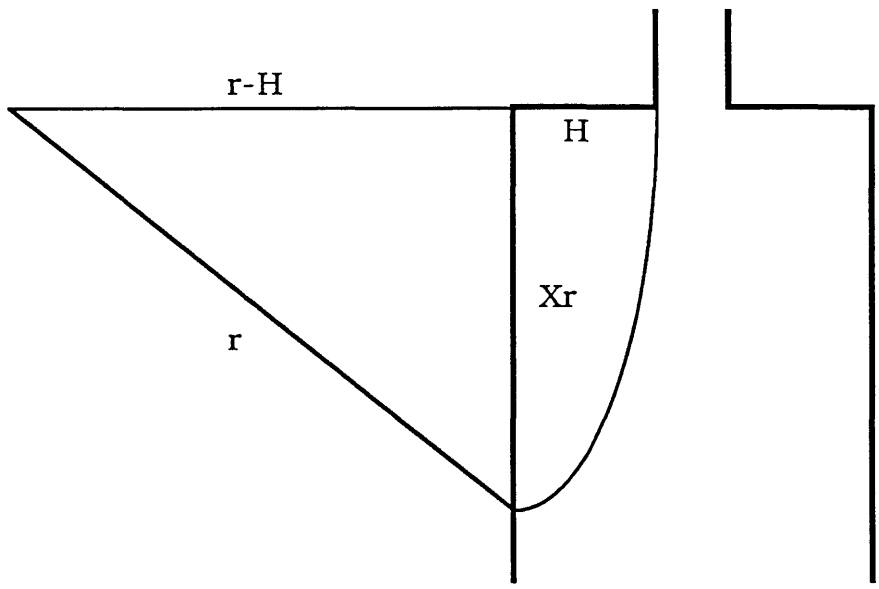
Beads	S_ω (-)	T_{tr} (ms)	S_{tr} (-)	t_e (ms)	S_t (-)
40μm-13%	9.9	38.	3.28	48.	4.14
40μm-40%	11.7	41.	3.53	48.	4.14
40μm-80%	14.4	48.	4.14	48.	4.14
80μm-23%	2.8	45.	0.98	48.	1.05
80μm-40%	3.1	48.	1.05	48.	1.05
80μm-86%	3.6	53.	1.16	48.	1.05

APPENDIX 4.A

Curvature of the separation streamline of the expansion flow.

In order to calculate the curvature of the separation streamline, it is assumed that the streamline is a sector of a circle, so its radius is the radius of curvature of the separation streamline. This assumption does not affect the conclusion because allows the estimate of the relative change of the curvature between various expansion ratio flows.

The figure below shows the geometry of the step and the separation streamline and radius of curvature r will be estimated.



The following relation estimates the radius r :

$$r^2 = X_r^2 + (r-H)^2 \qquad (A.1)$$

where X_r is the reattachment length and H is the step height. So the angular velocity ω can be estimated by dividing the axial velocity of the free stream by the radius r and then the centrifuge Stokes number S_ω.

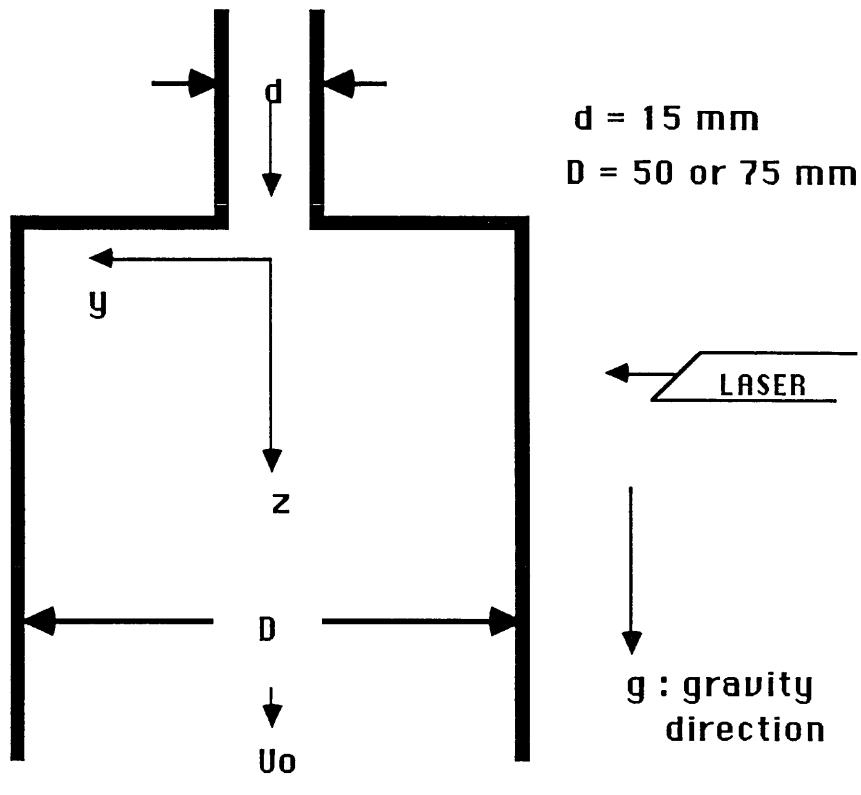


FIGURE 4.1 Experimental arrangement and coordinate system used.

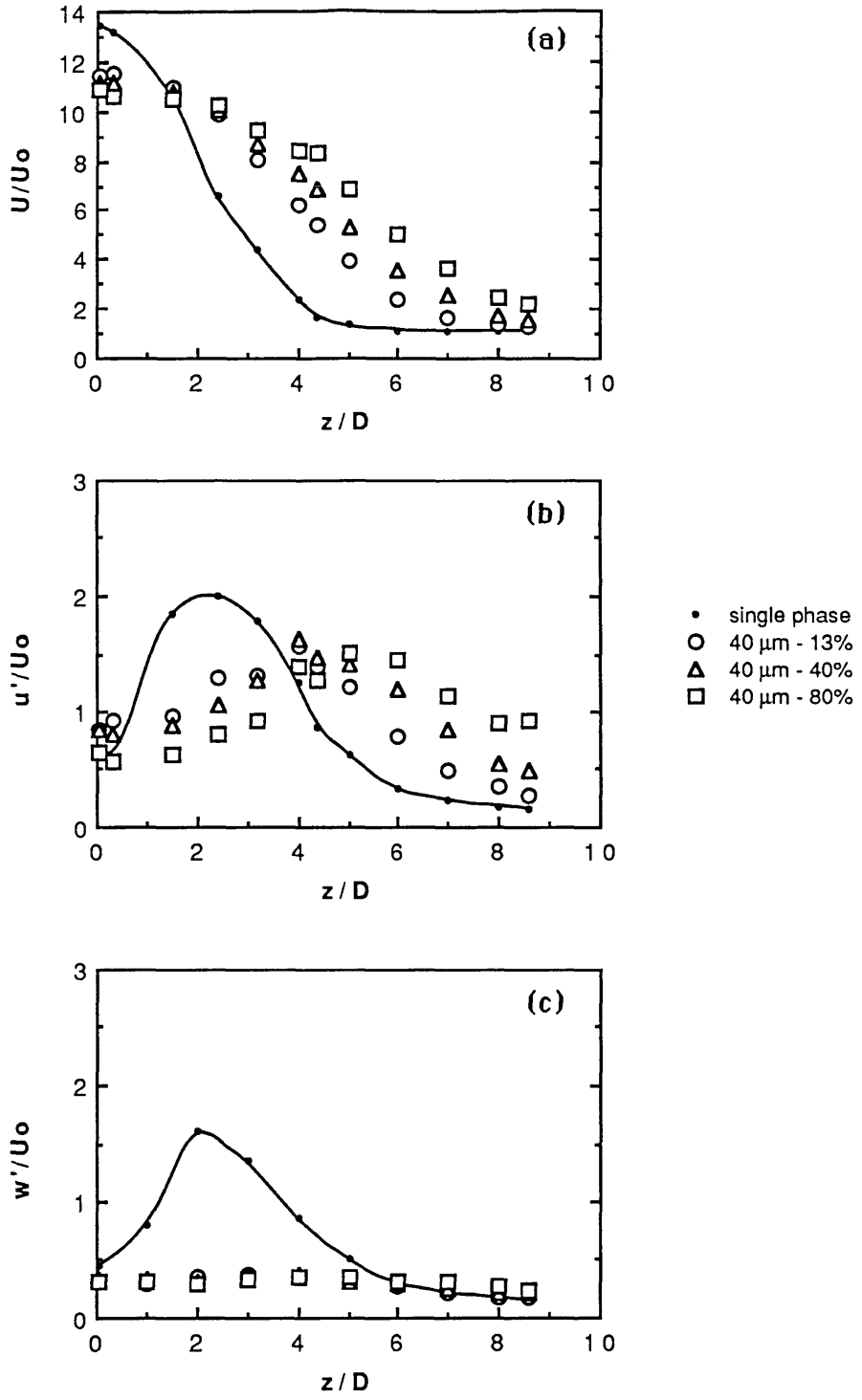


FIGURE 4.2 Centreline profiles in sudden expansion ratio 3.33 for 40 µm beads for mass loadings of 13% (circle), 40% (triangle) and 80% (square) compared to the single phase; (a) mean axial velocity (U), b) axial rms velocity (u'), c) azimuthal rms velocity (w') normalised by the gas bulk velocity in the large tube, Uo.

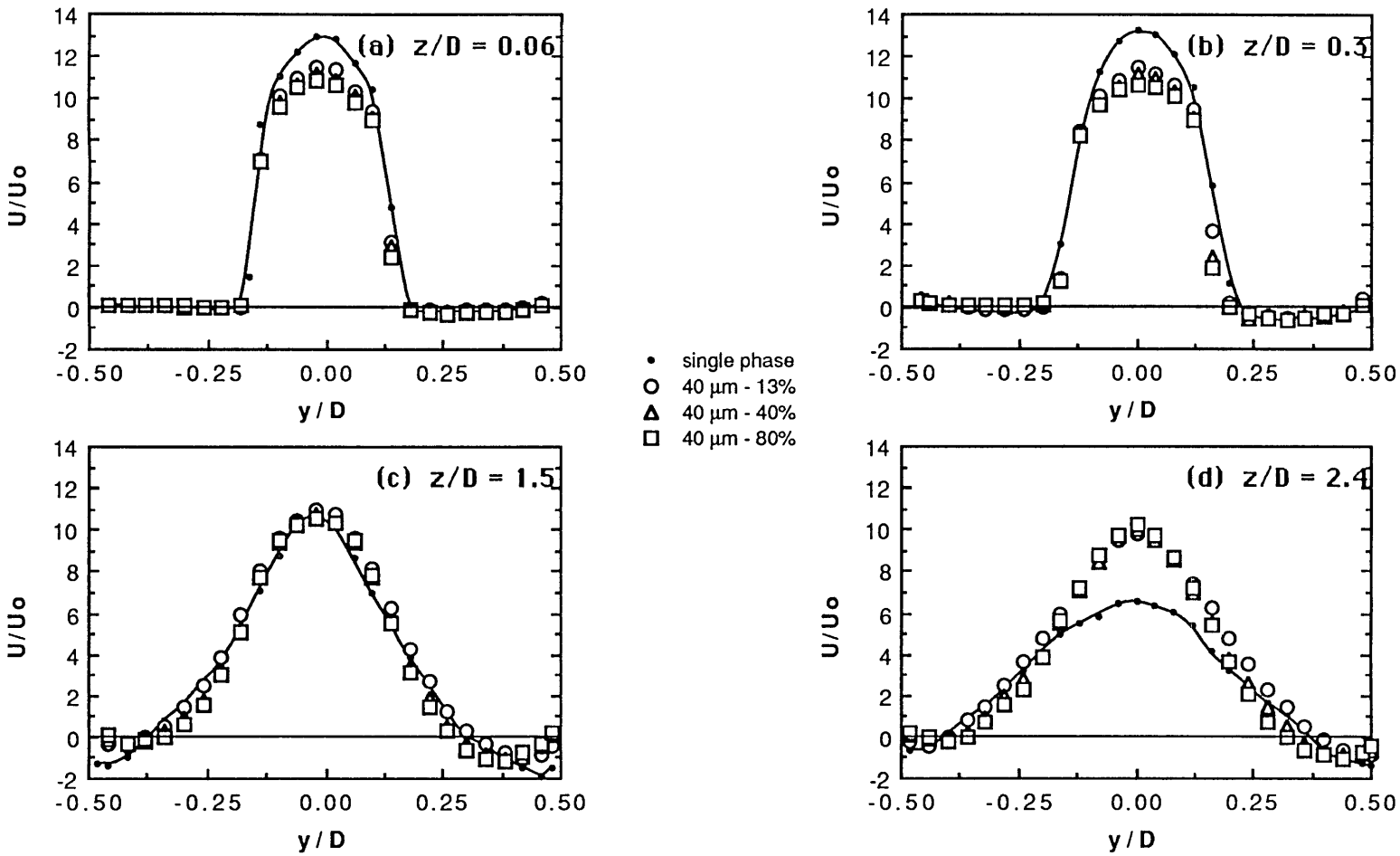


FIGURE 4.3 Radial profiles of mean axial velocity (U) in sudden expansion ratio of 3.33 at z/D = 0.06, 0.3, 1.5 and 2.4 for 40 µm beads for mass loadings 13% (circle), 40% (triangle) and 80% (square) compared to single phase. Normalisation of velocities is by the gas bulk velocity in the large tube, Uo.

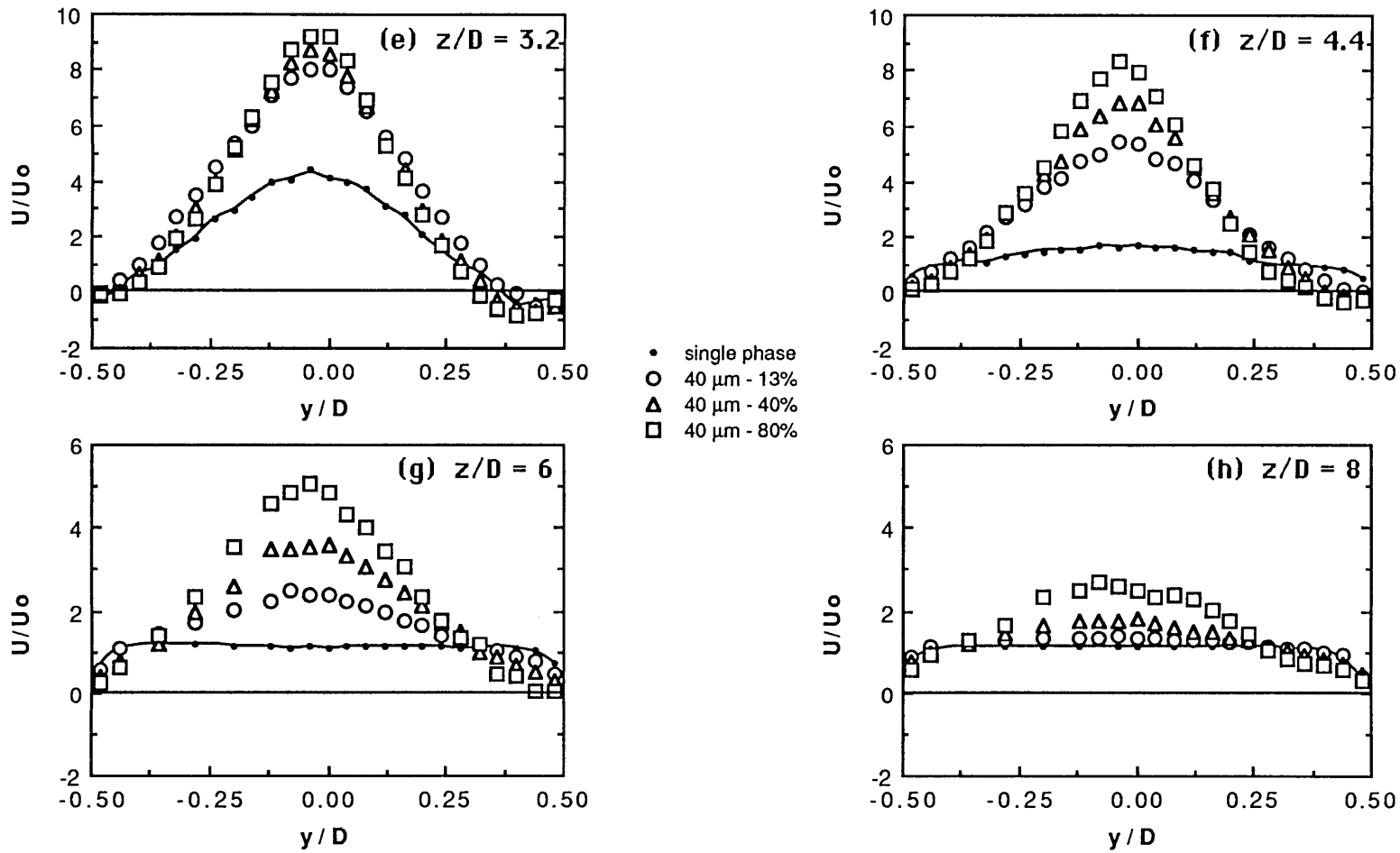


FIGURE 4.3 (Continue) Radial profiles of mean axial velocity (U) in sudden expansion ratio of 3.33 at z/D = 3.2, 4.4, 6 and 8 for 40 µm beads for mass loadings of 13% (circle), 40% (triangle) and 80% (square) compared to the single phase. Normalisation is by the gas bulk velocity in the large tube, Uo.

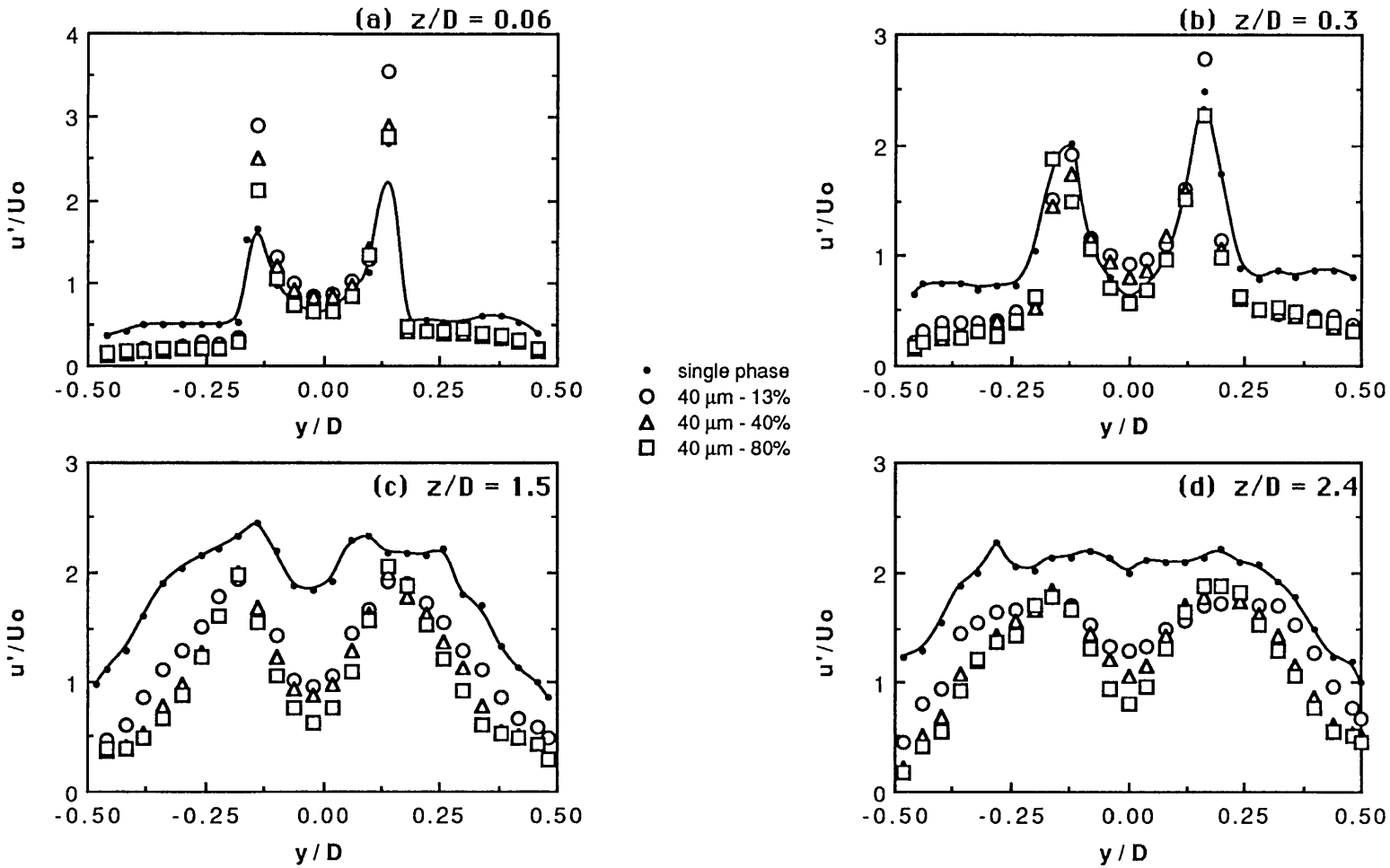


FIGURE 4.4 Radial profiles of axial rms velocity (u') in sudden expansion ratio of 3.33 at z/D = 0.06, 0.3, 1.5 and 2.4 for 40 µm beads for mass loadings of 13% (circle), 40% (triangle) and 80% (square) compared to the single phase. Normalisation is by the gas bulk velocity in the large tube, Uo.

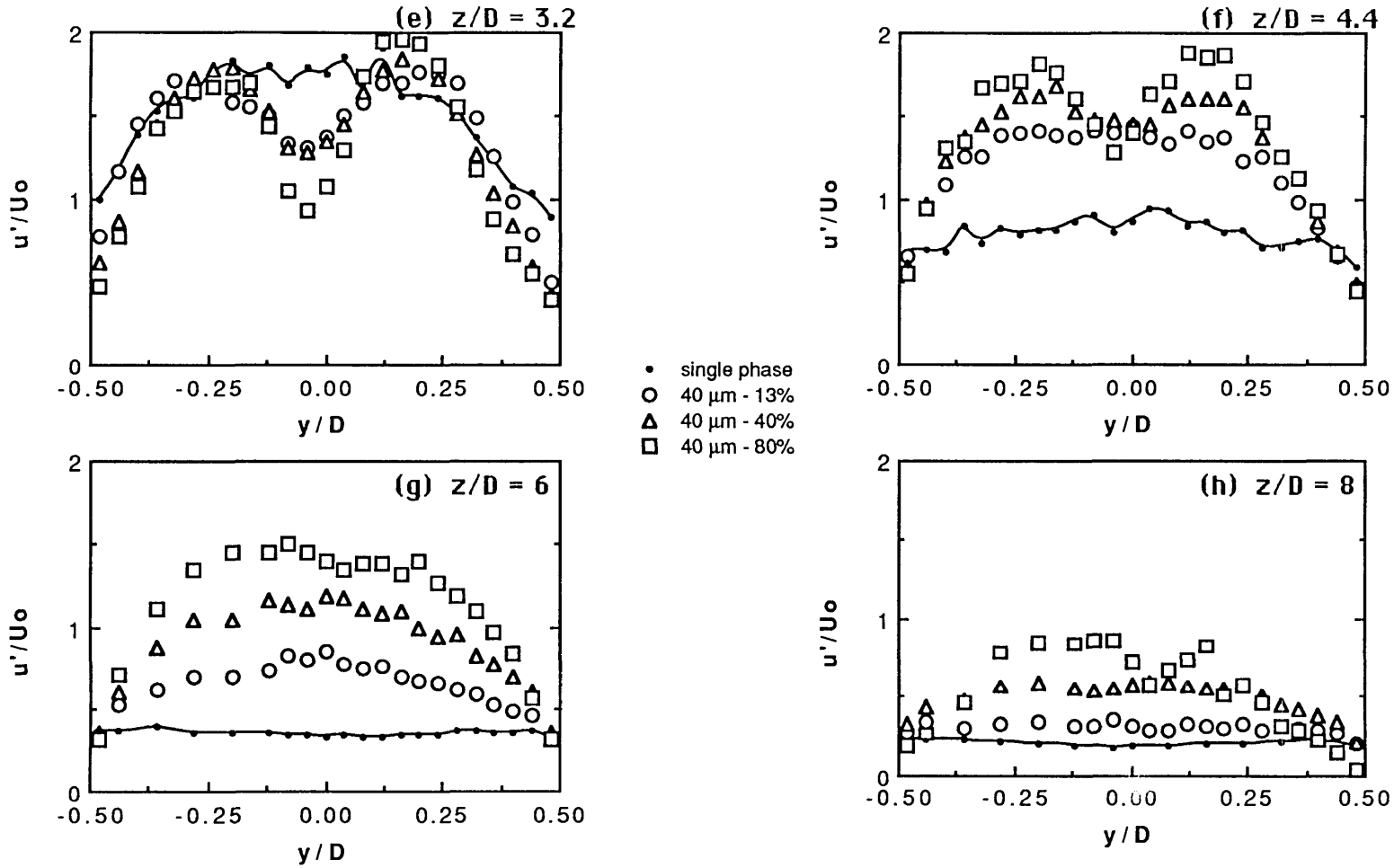


FIGURE 4.4 (Continue) Radial profiles of axial rms velocity (u') in sudden expansion ratio of 3.33 at z/D = 3.2, 4.4, 6 and 8 for 40 µm beads for mass loadings of 13% (circle), 40% (triangle) and 80% (square) compared to the single phase. Normalisation is by the gas bulk velocity in the large tube, Uo.

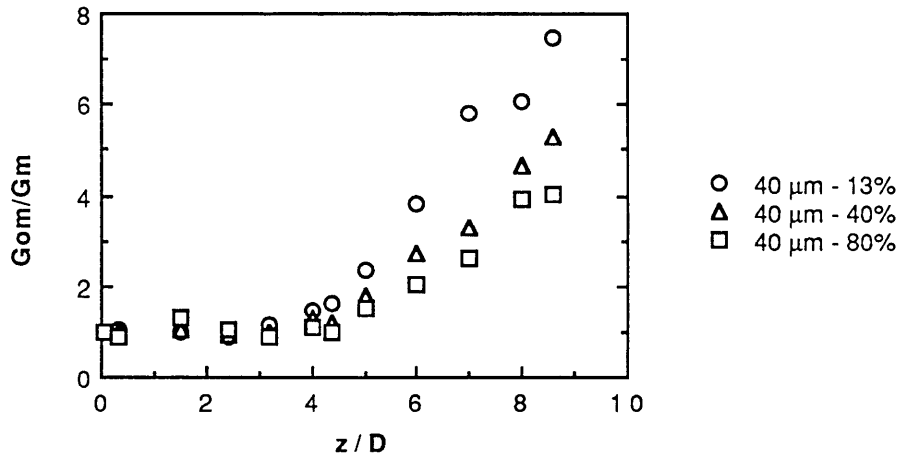


FIGURE 4.5 Centreline profile of volume flux in sudden expansion ratio of 3.33 for 40 µm beads for mass loadings of 13% (circle), 40% (triangle), and 80% (square). Normalisation is by the flux at the exit of the small tube, Gom.

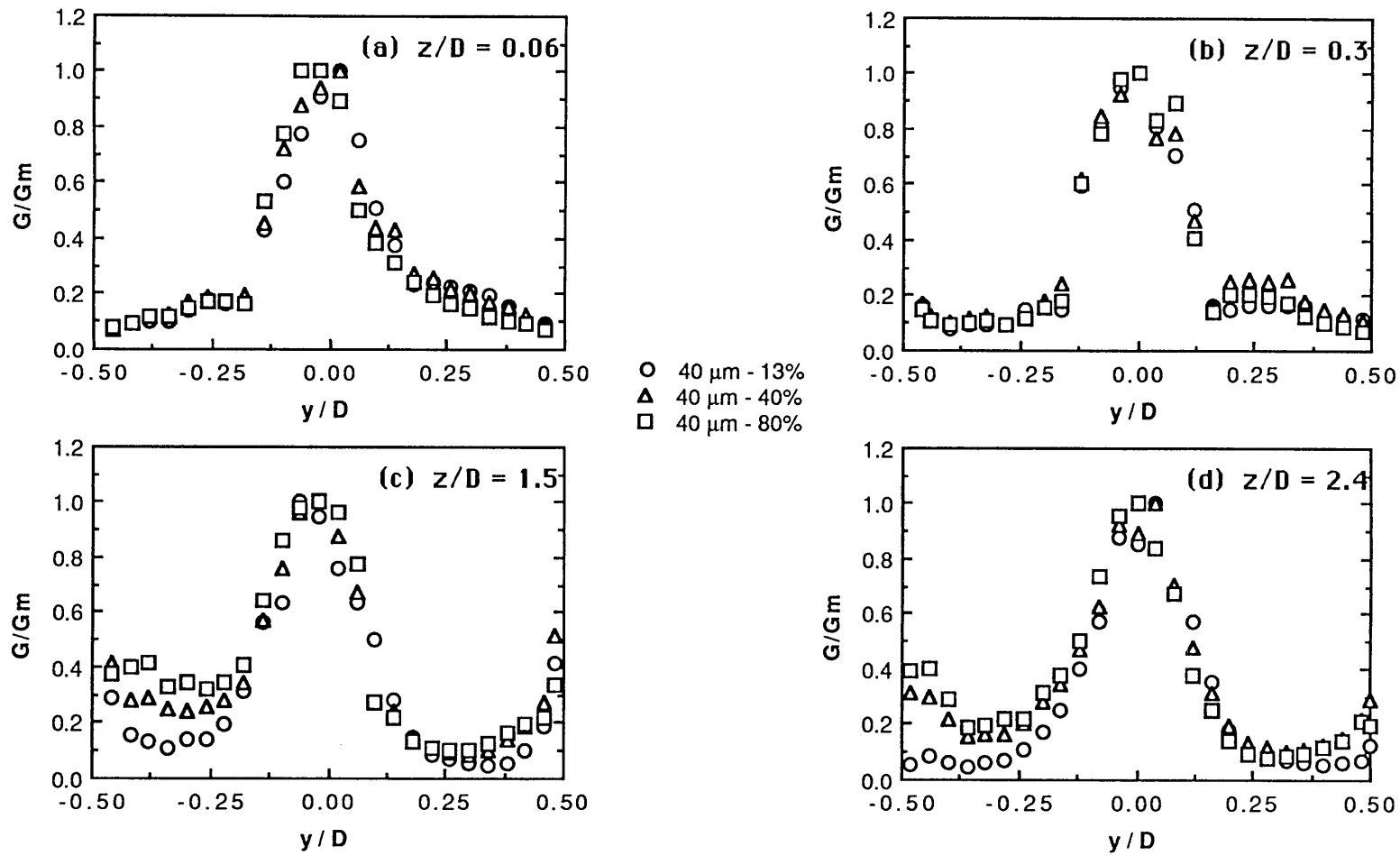


FIGURE 4.6 Radial profiles of volume flux (G) in sudden expansion ratio of 3.33 at z/D = 0.06, 0.3, 1.5 and 2.4 for 40 µm beads for mass loadings of 13% (circle), 40% (triangle) and 80% (square). Normalisation is by the centreline flux, Gm.

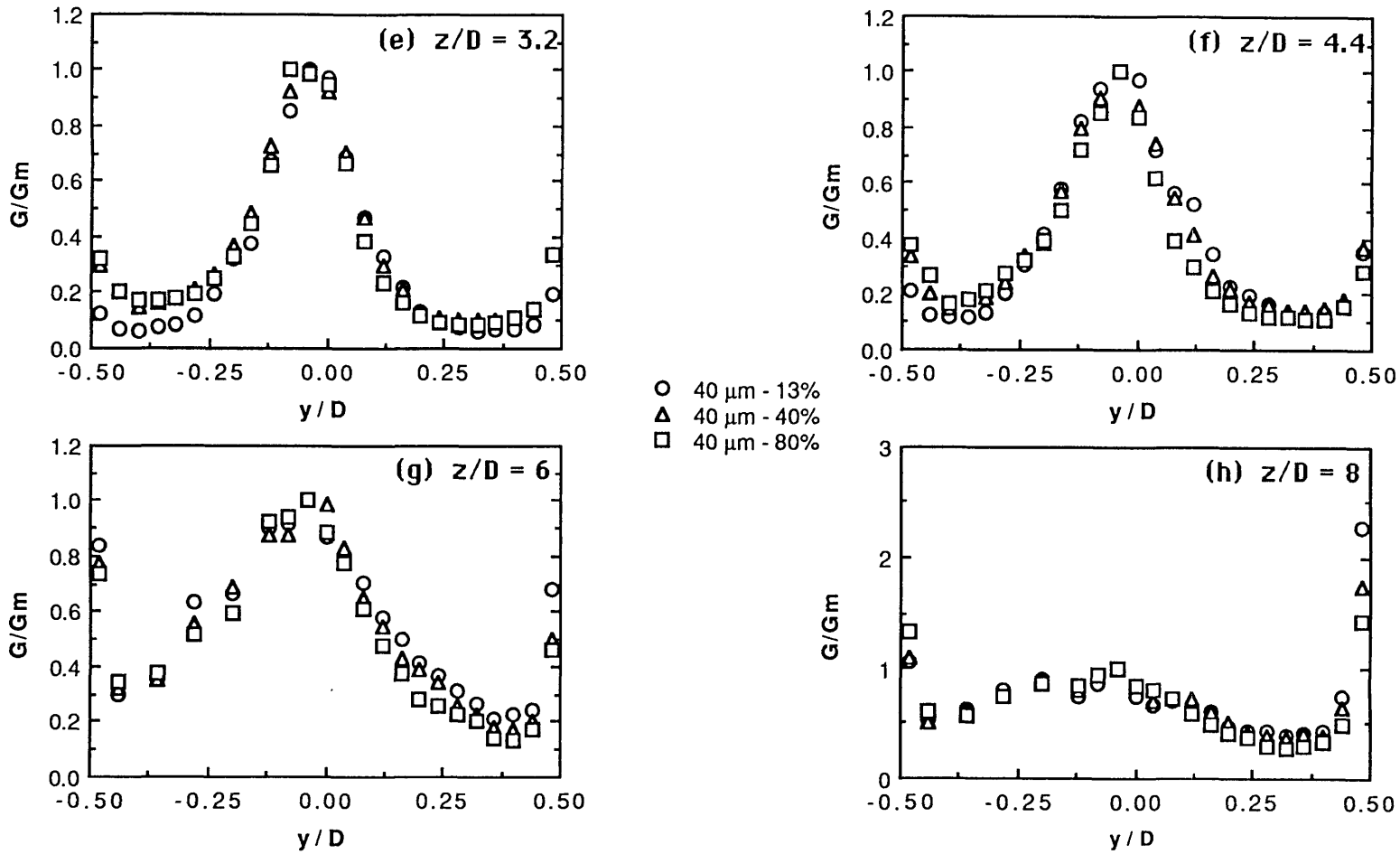


FIGURE 4.6 (Continue) Radial profiles of volume flux (G) in sudden expansion ratio of 3.33 at z/D = 3.2, 4.4, 6 and 8 for 40 µm beads for mass loadings of 13% (circle), 40% (triangle) and 80% (square). Normalisation is by the centreline flux at the exit of the small tube, Gm.

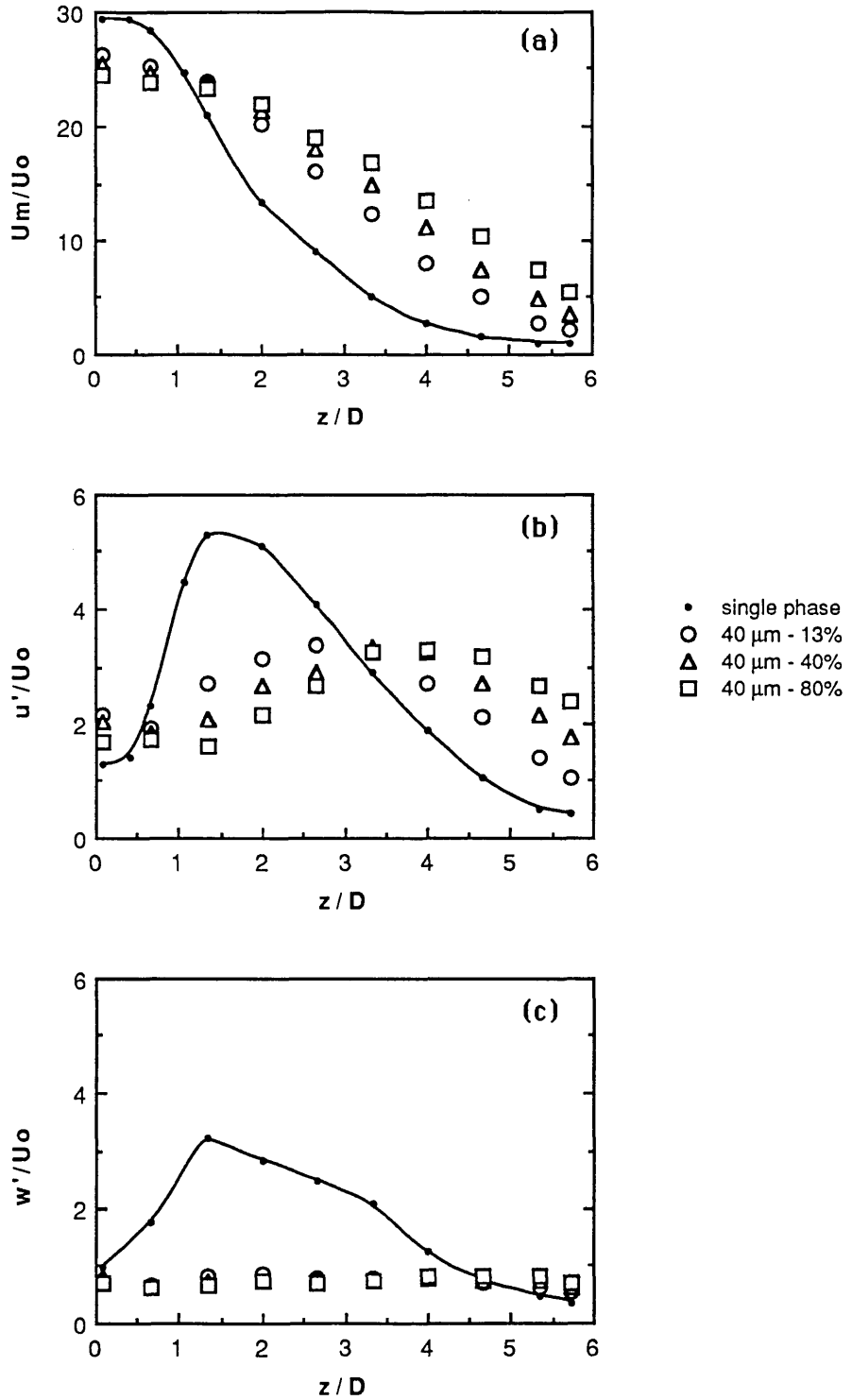


FIGURE 4.7 Centreline profiles in sudden expansion ratio of 5 for 40 µm beads for mass loadings of 13% (circle), 40% (triangle) and 80% (square) compared to the single phase; a) mean axial velocity (U), b) axial rms velocity (u'), c) azimuthal rms velocity (w').

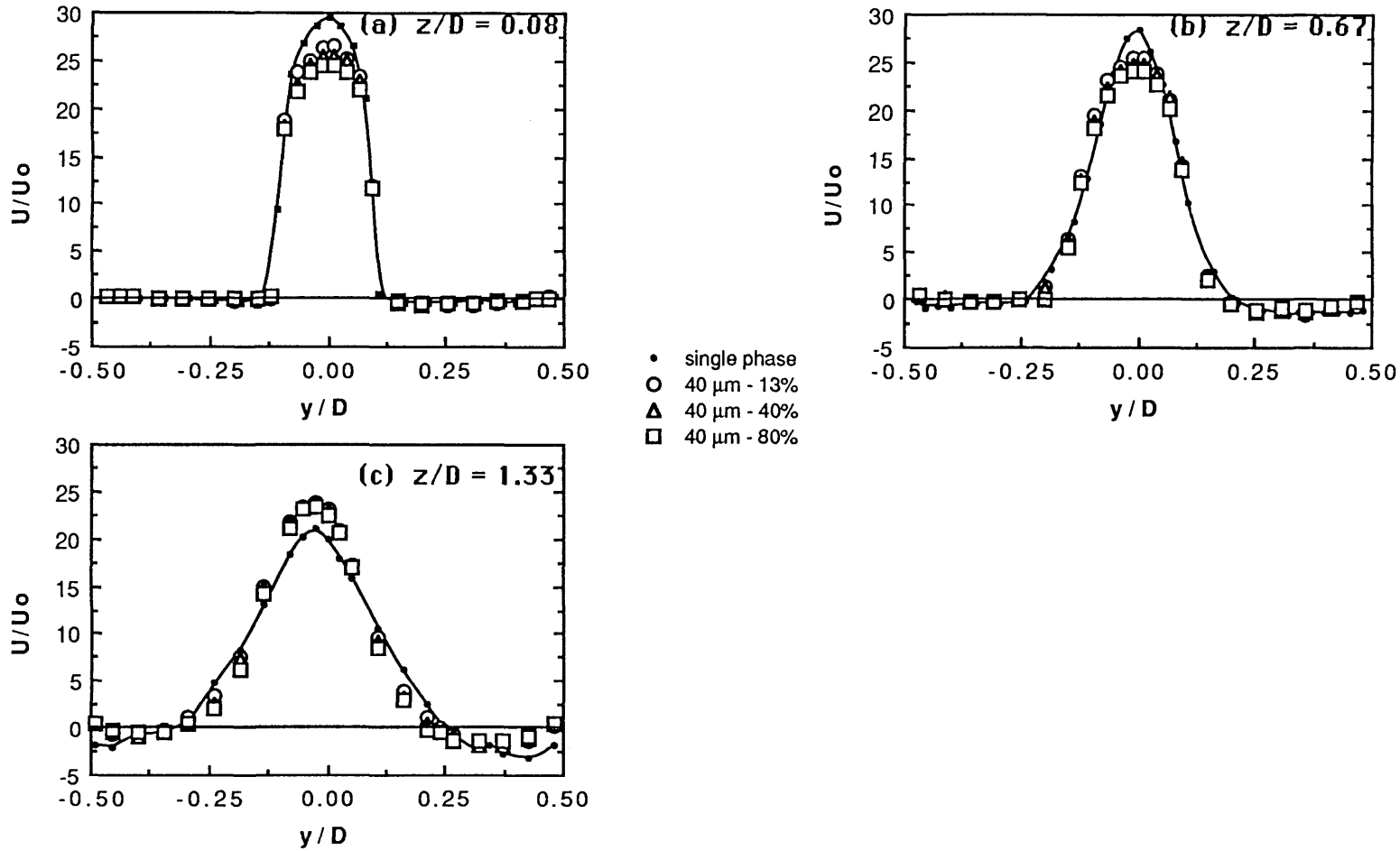


FIGURE 4.8 Radial profiles of mean axial velocity (U) in sudden expansion ratio of 5 at z/D = 0.08, 0.67 and 1.33 for 40 µm beads for mass loadings of 13% (circle), 40% (triangle) and 80% (square) compared to the single phase. Normalisation by the gas bulk velocity in the large tube.

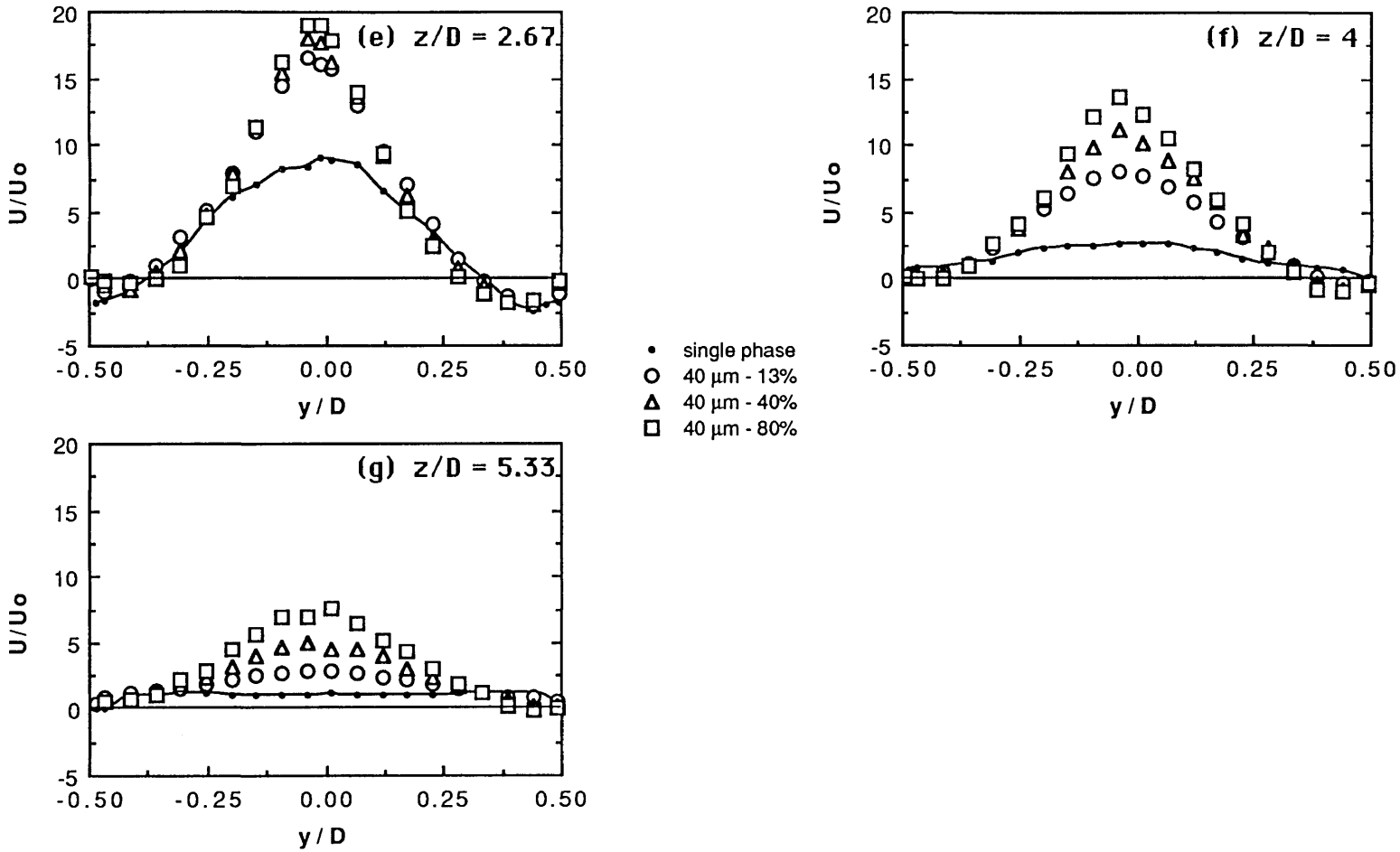


FIGURE 4.8 (Continue) Radial profiles of mean axial velocity (U) in sudden expansion ratio of 5 at z/D = 2.67, 4 and 5.33 for 40 µm beads for mass loadings of 13% (circle), 40% (triangle) and 80% (square) compared to the single phase. Normalisation by the gas bulk velocity in the large tube.

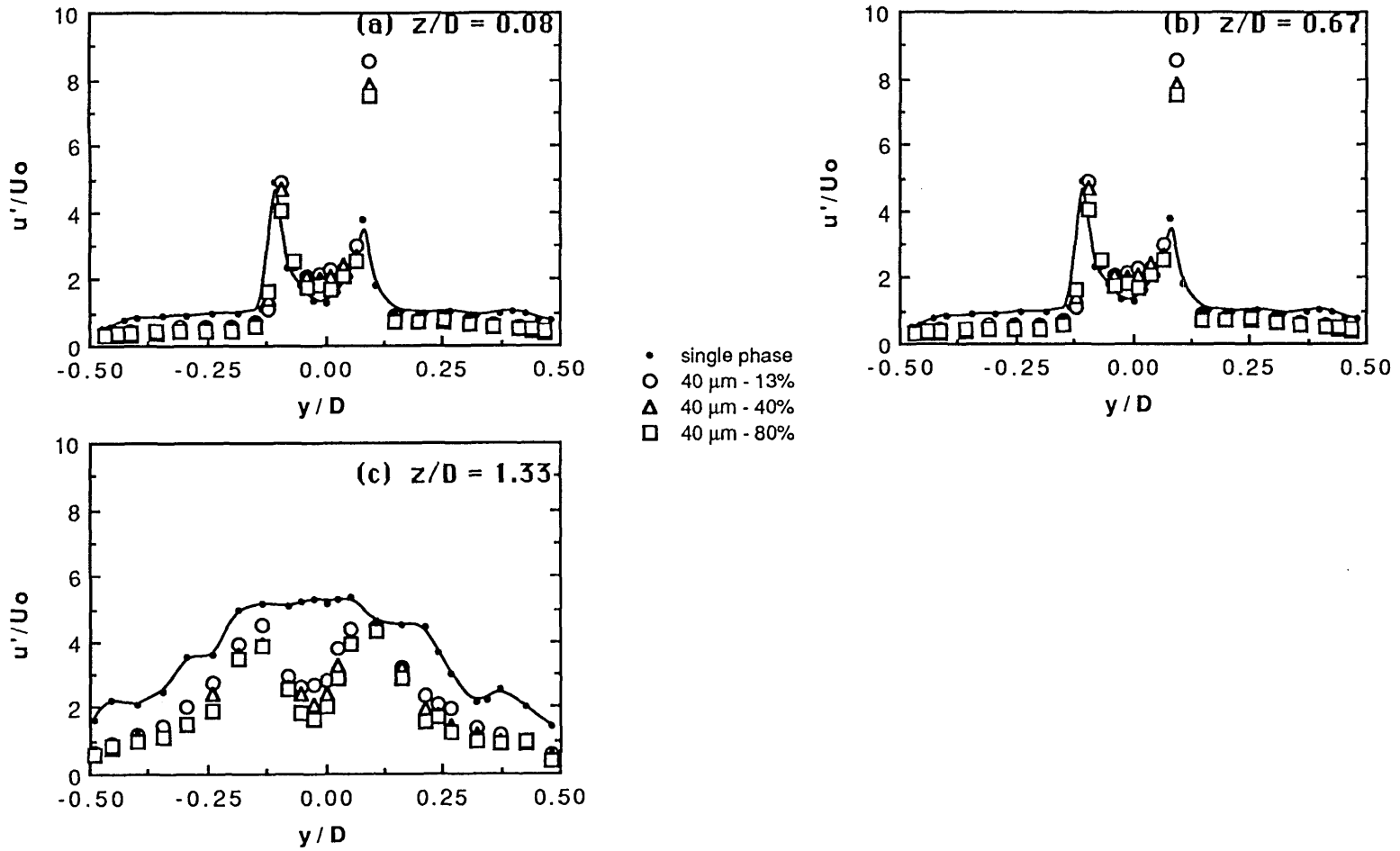


FIGURE 4.9 Radial profiles of axial rms velocity (u') in sudden expansion ratio of 5 at z/D = 0.08, 0.67 and 1.33 for 40 µm beads for mass loadings of 13% (circle), 40% (triangle) and 80% (square) compared to the single phase. Normalisation by the gas bulk velocity in the large tube.

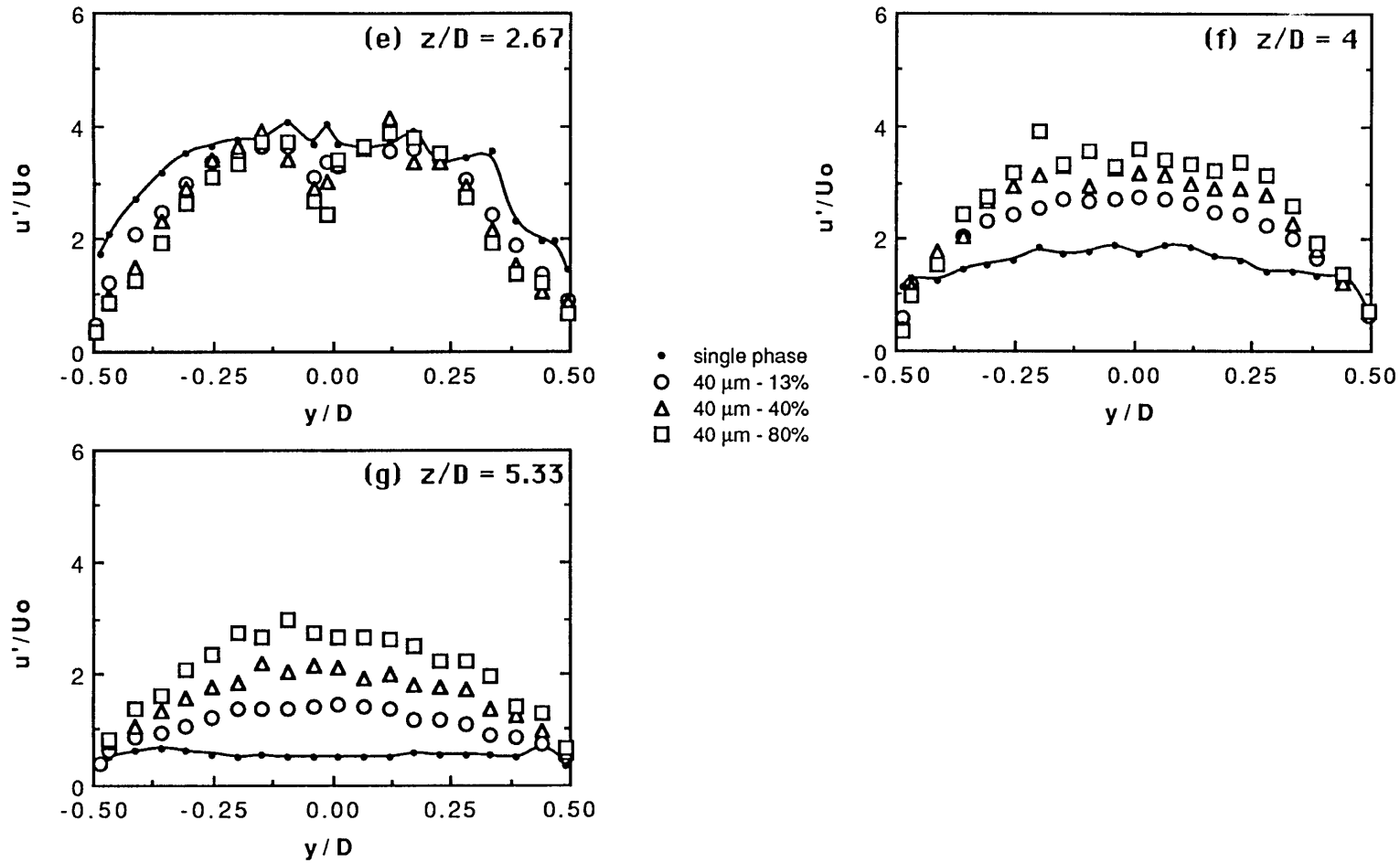


FIGURE 4.9 (Continue) Radial profiles of axial rms velocity (u') in sudden expansion ratio of 5 at z/D = 2.67, 4 and 5.33 for 40 µm beads for mass loadings of 13% (circle), 40% (triangle) and 80% (square) compared to the single phase. Normalisation by the gas bulk velocity in the large tube.

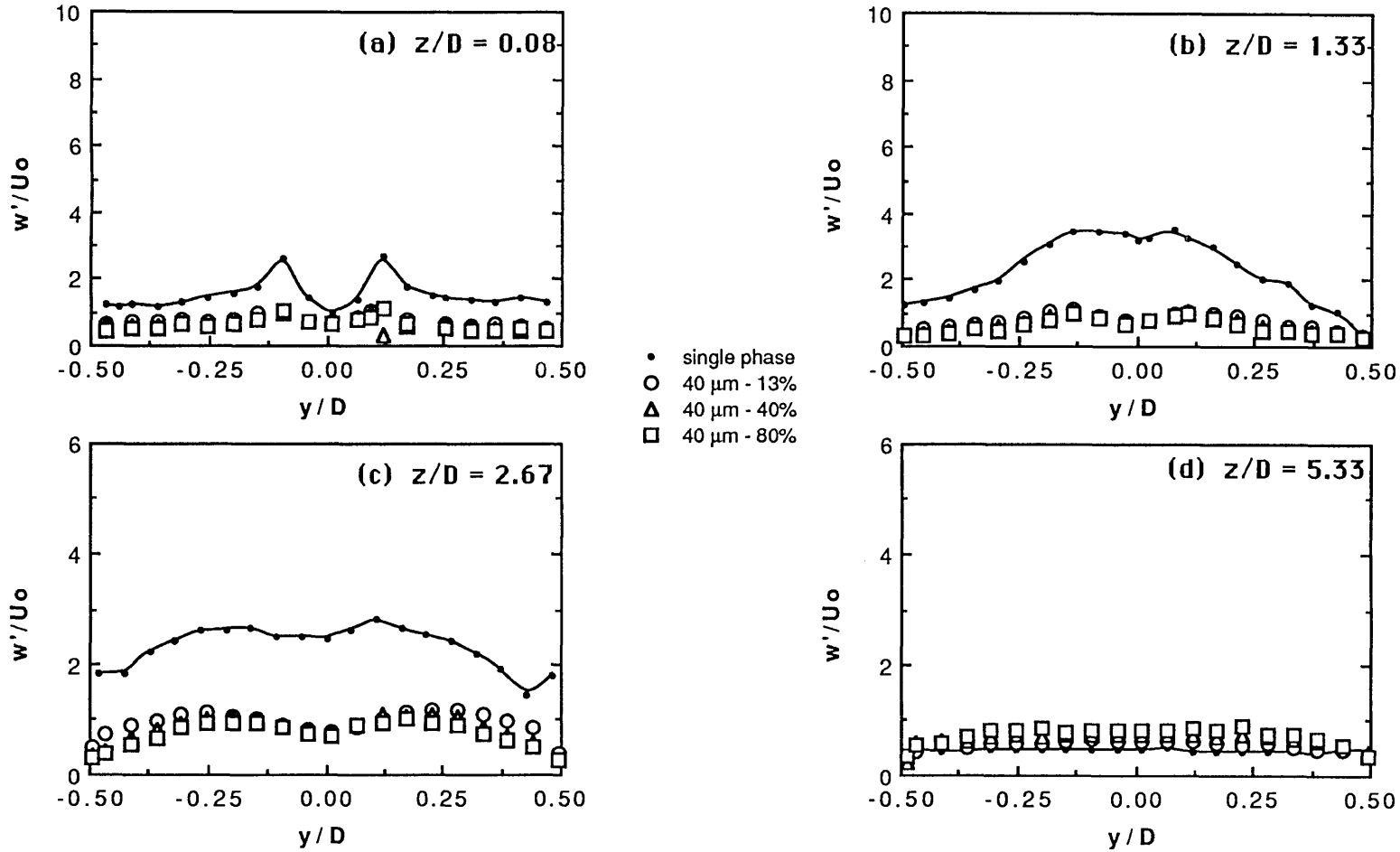


FIGURE 4.10 Radial profiles of azimuthal rms velocity (w') in sudden expansion ratio of 5 at z/D = 0.08, 1.33, 2.67 and 5.33 for 40 µm beads for mass loadings of 13% (circle), 40% (triangle) and 80% (square) compared to the single phase. Normalisation by the gas bulk velocity in the large tube.

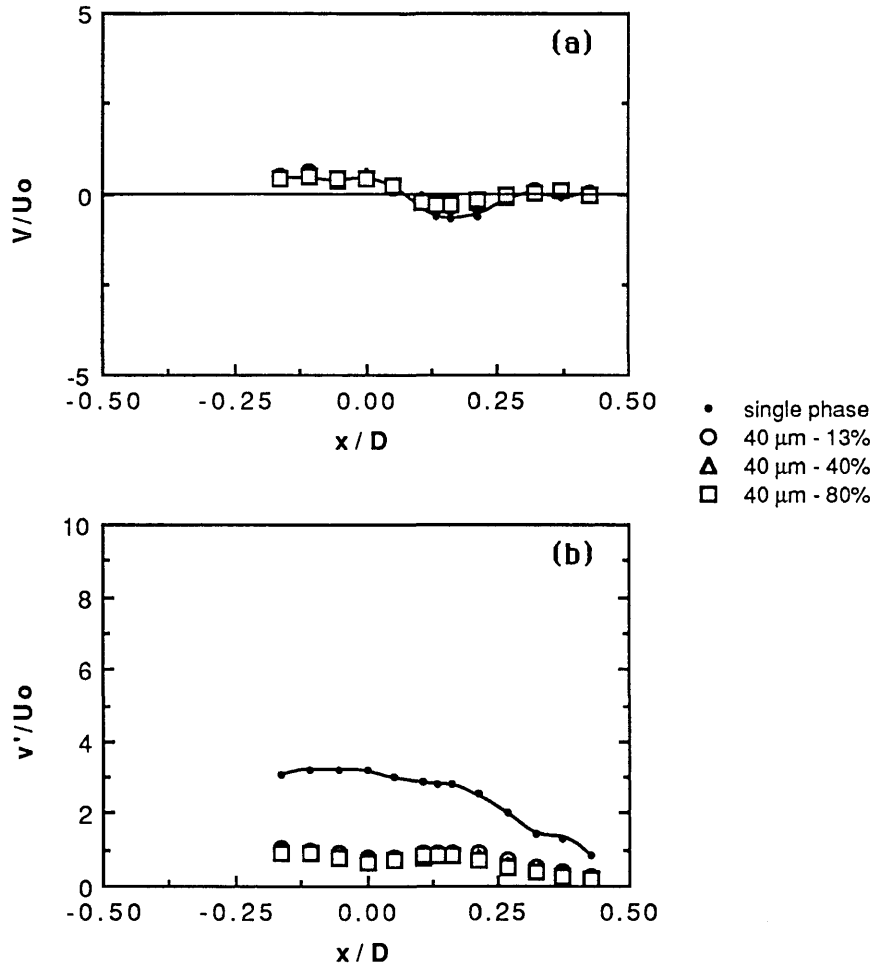


FIGURE 4.11 Radial profiles of (a) mean and (b) radial rms velocity (U, u') in sudden expansion ratio of 5 at z/D = 1.33 for 40 µm beads for mass loadings of 13% (circle), 40% (triangle) and 80% (square) compared to the single phase. Normalisation by the gas bulk velocity in the large tube, Uo.

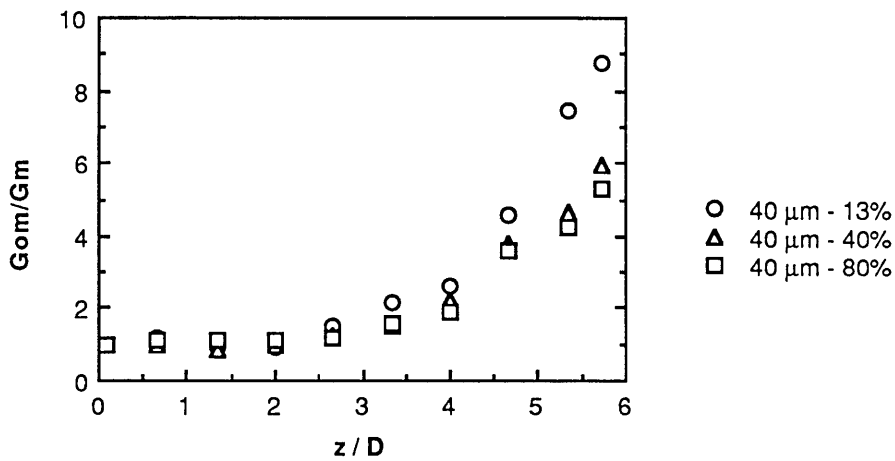


FIGURE 4.12 Centreline profiles of volume flux in sudden expansion ratio of 5 for 40 µm beads for mass loadings of 13% (circle), 40% (triangle) and 80% (square) compared to the single phase. Normalisation is by the centreline flux at the exit of the small tube, Gom.

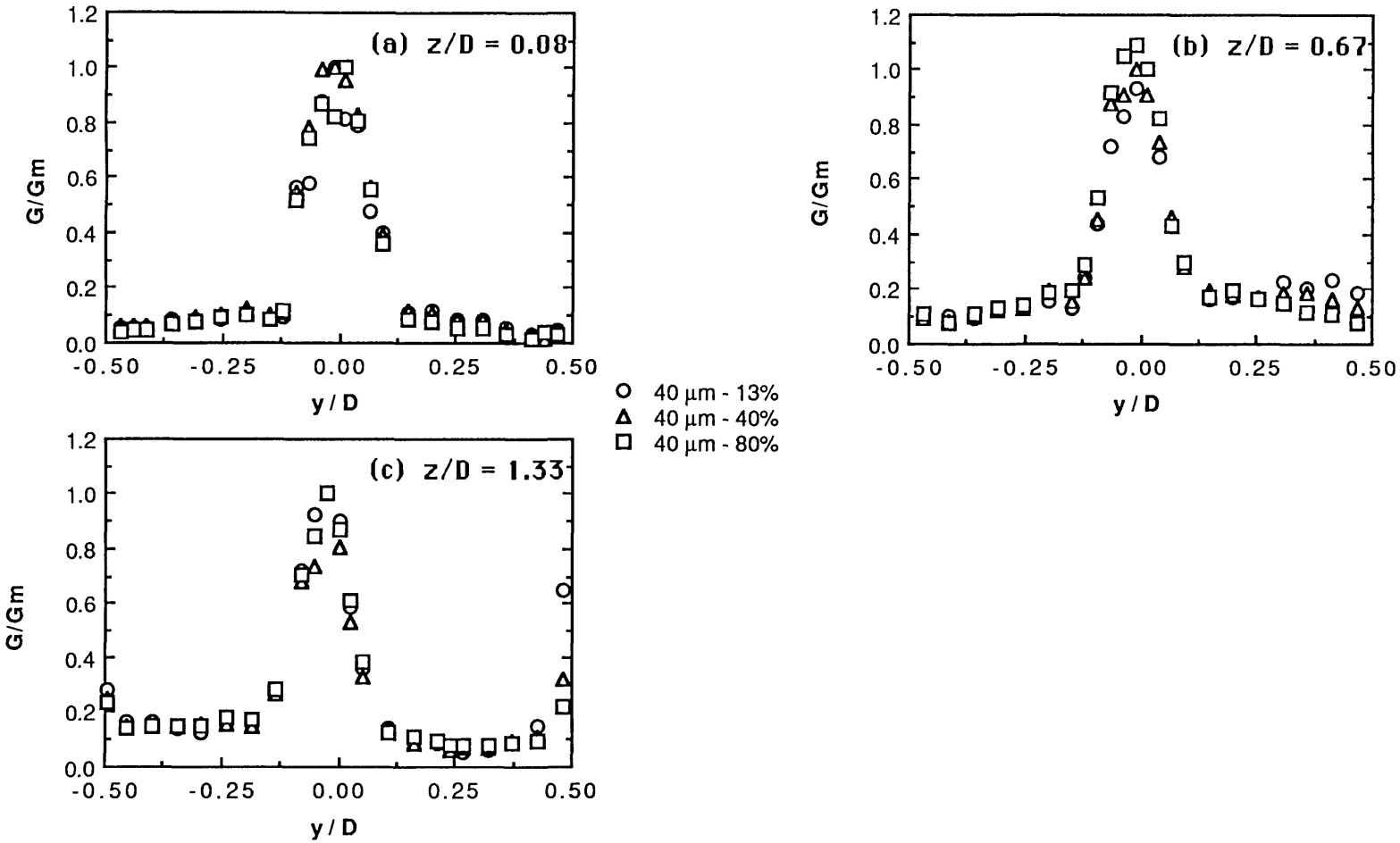


FIGURE 4.13 Radial profiles of volume flux (G) in sudden expansion ratio of 5 at z/D = 0.08, 0.67 and 1.33 for 40 µm beads for mass loadings of 13% (circle), 40% (triangle) and 80% (square). Normalisation is by the centreline flux, Gm.

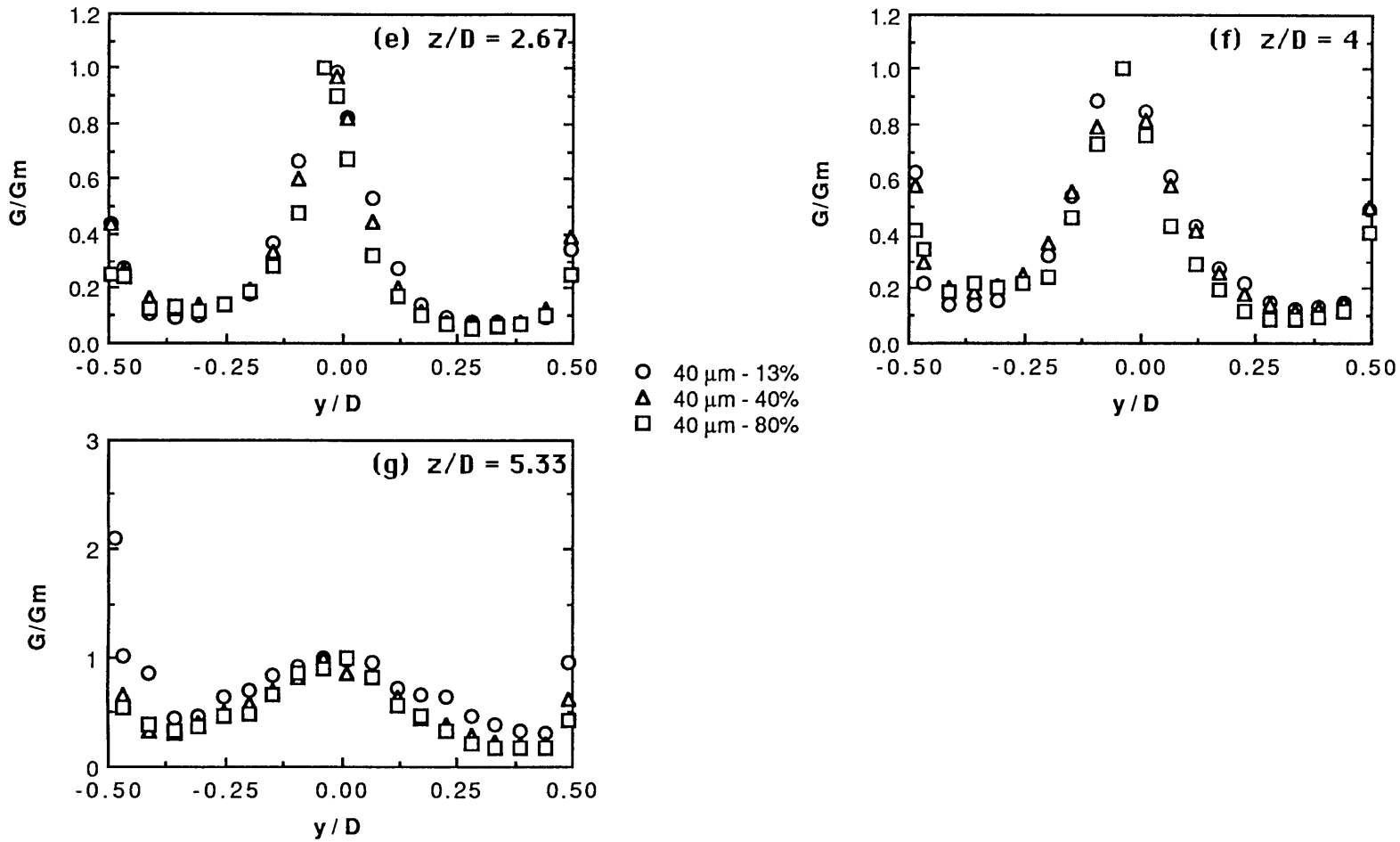


FIGURE 4.13 (Continue) Radial profiles of volume flux (G) in sudden expansion ratio of 5 at z/D = 2.67, 4 and 5.33 for 40 µm beads for mass loadings of 13% (circle), 40% (triangle) and 80% (square). Normalisation is by the centreline flux, Gm.

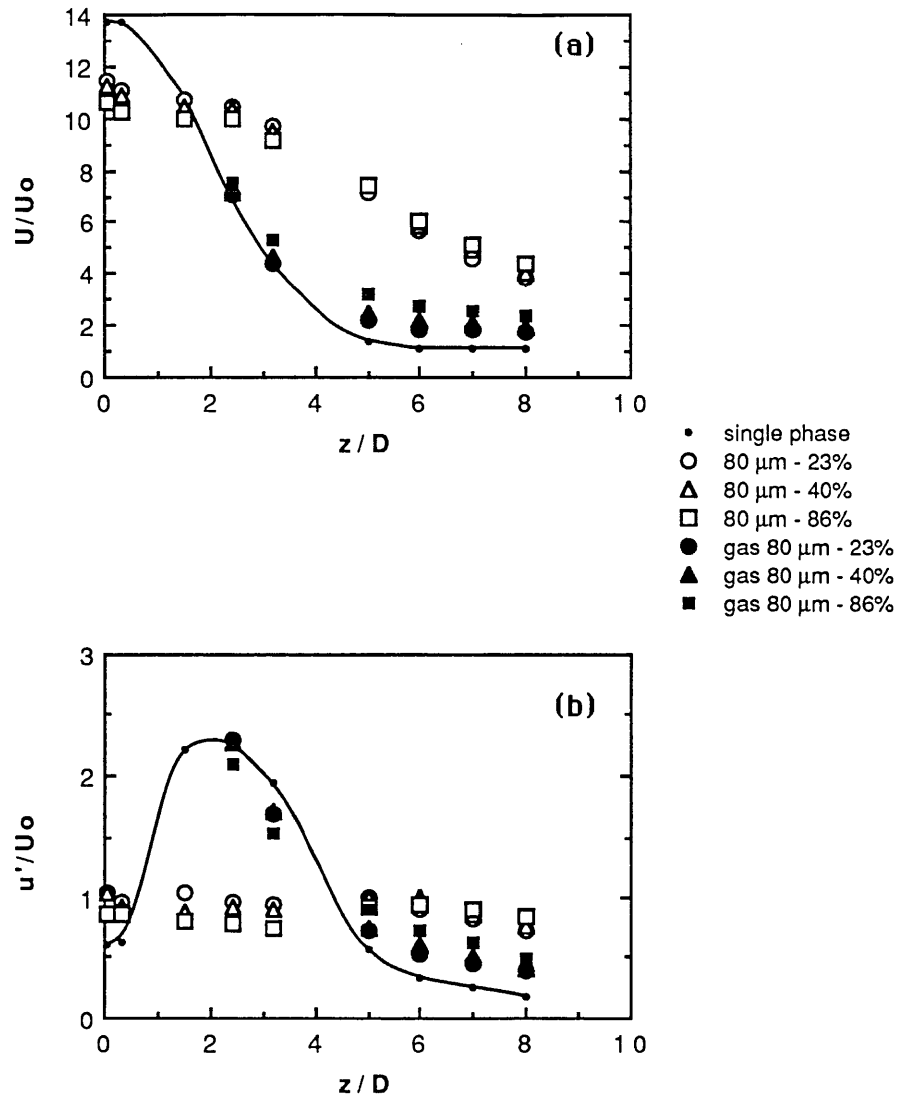


FIGURE 4.14 Centreline profiles of (a) mean and (b) rms axial velocity (U, u') in the sudden expansion ratio of 5 for gas phase and 80 μm beads for mass loadings of 23% (circles), 40% (triangle) and 86% (square). Normalisation is by the gas bulk velocity in the large tube, Uo.

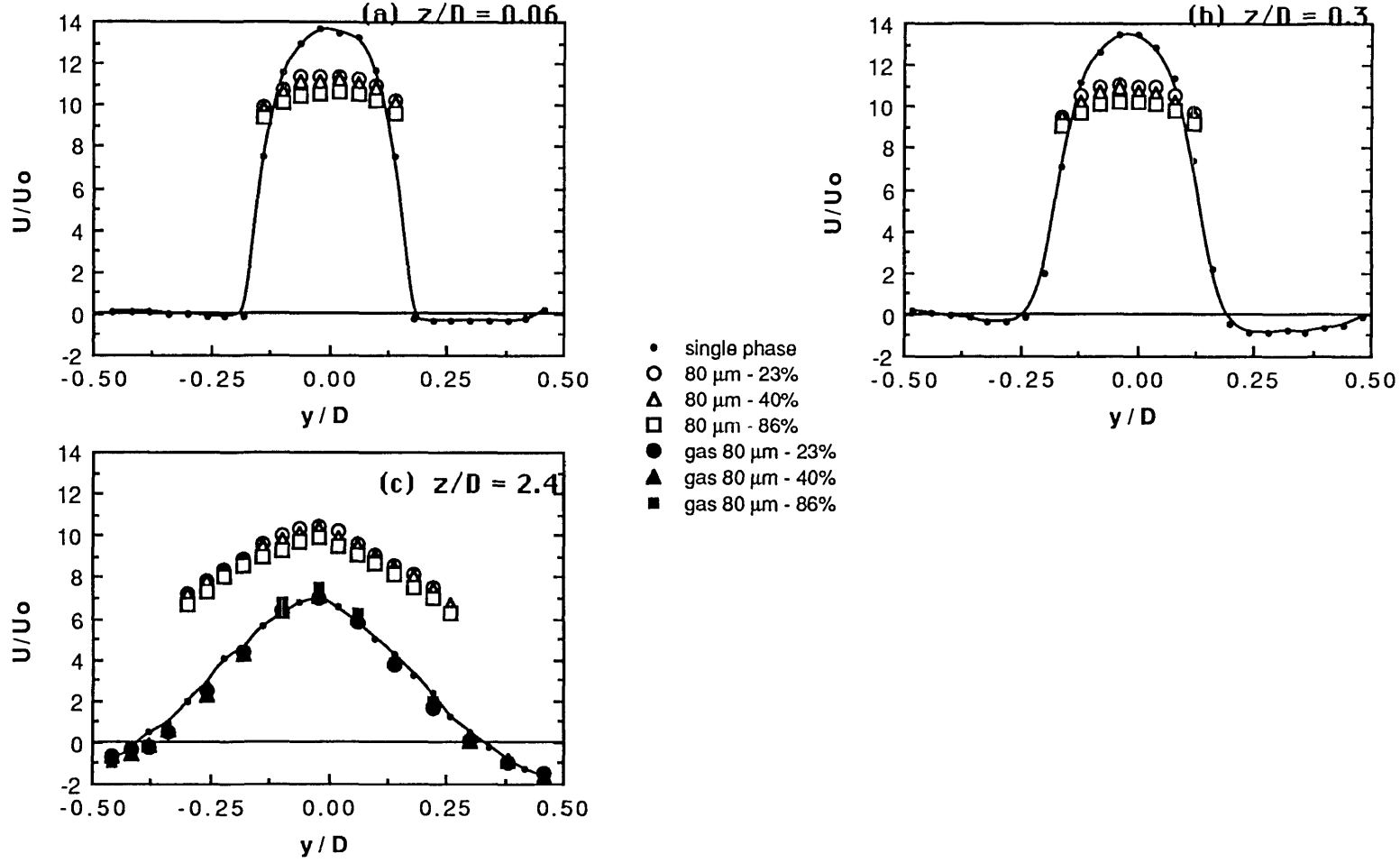


FIGURE 4.15 Radial profiles of mean axial velocity (U) in sudden expansion ratio of 3.33 at z/D = 0.06, 0.3 and 2.4 for gas phase and 80 μm beads for mass loadings of 23% (circle), 40% (triangle) and 86% (square) compared to the single phase. Normalisation is by the gas bulk velocity in the large tube, Uo.

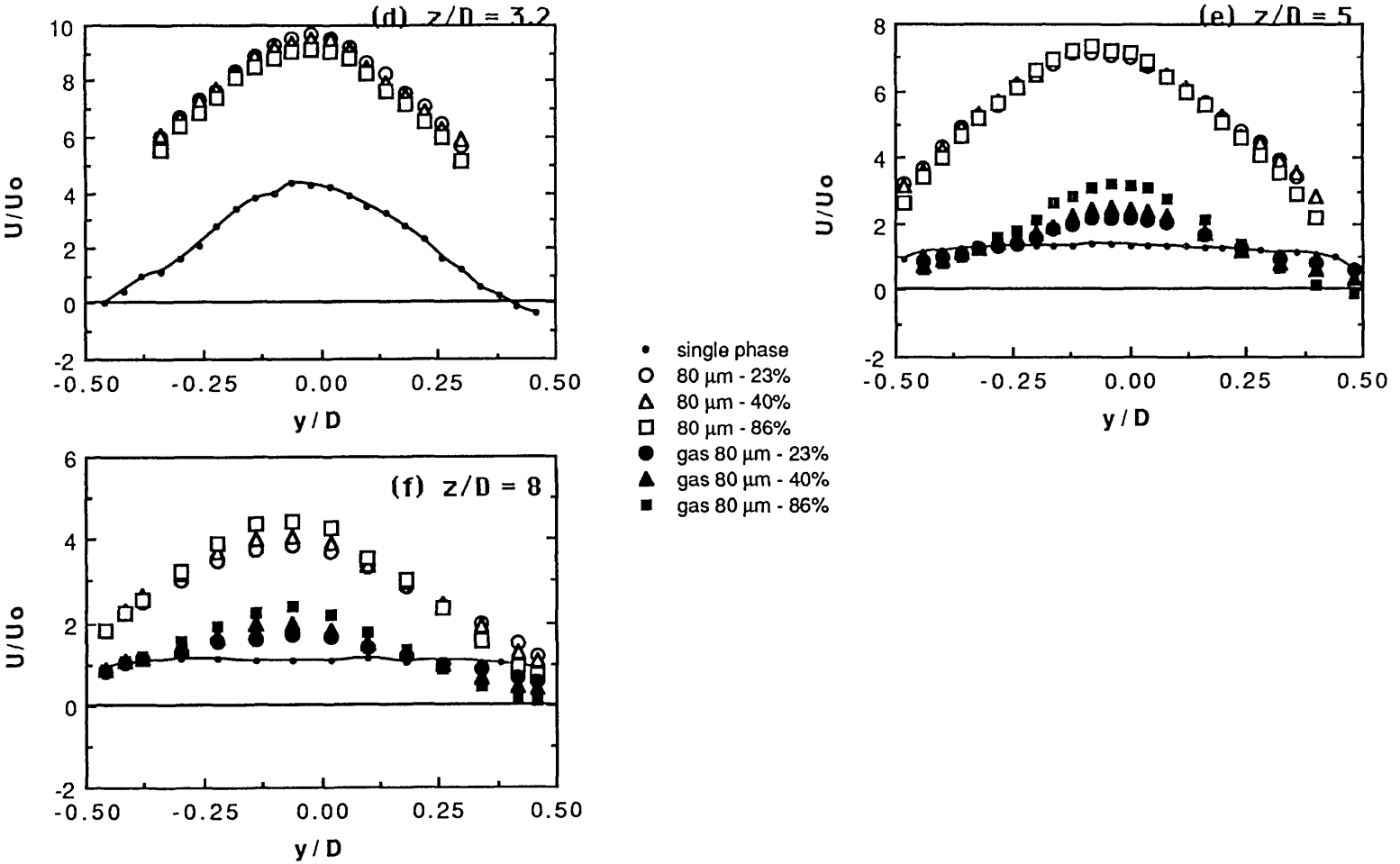


FIGURE 4.15 (continue) Radial profiles of mean axial velocity (U) in sudden expansion ratio of 3.33 at z/D = 3.2, 5 and 8 for gas phase and 80 µm beads for mass loadings of 23% (circle), 40% (triangle) and 86% (square) compared to the single phase. Normalisation is by the gas bulk velocity in the large tube, Uo.

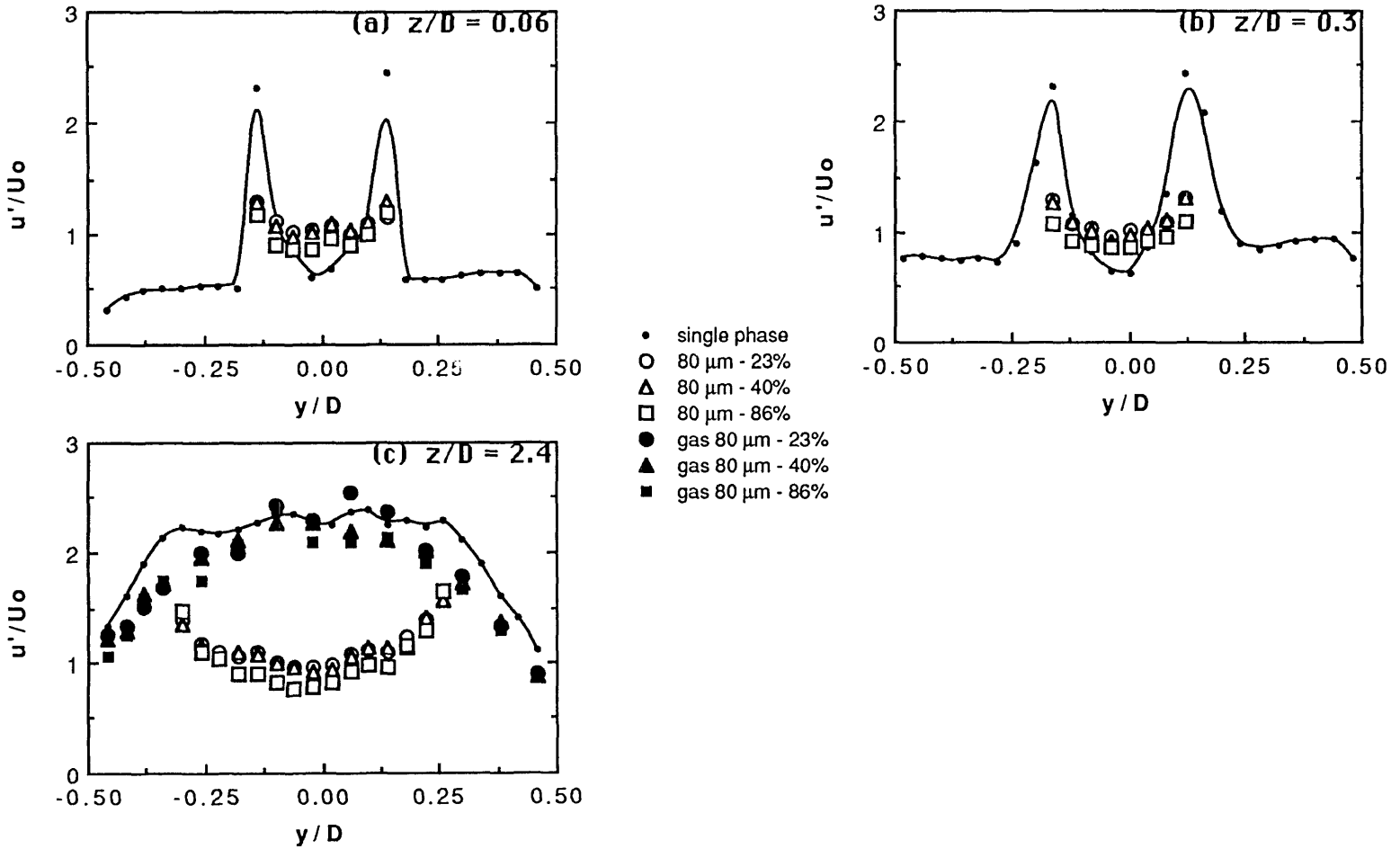


FIGURE 4.16 Radial profiles of rms axial velocity (u') in sudden expansion ratio of 3.33 at z/D = 0.06, 0.3 and 2.4 for gas phase and 80 µm beads for mass loadings of 23% (circle), 40% (triangle) and 86% (square) compared to the single phase. Normalisation is by the gas bulk velocity in the large tube, Uo.

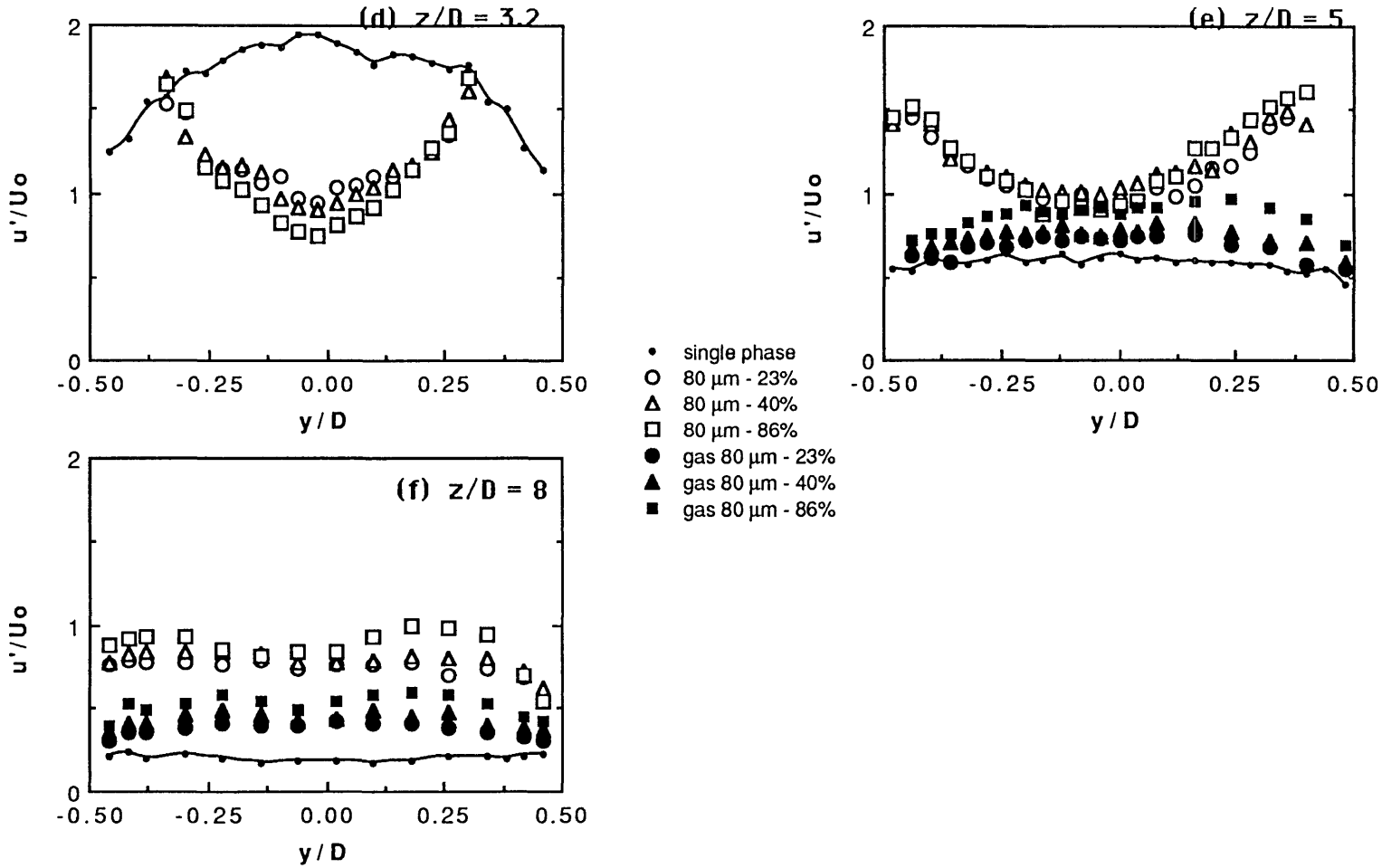


FIGURE 4.16 (continue) Radial profiles of rms axial velocity (u') in sudden expansion ratio of 3.33 at z/D= 3.2, 5 and 8 for gas phase and 80 µm beads for mass loadings of 23% (circle), 40% (triangle) and 86% (square) compared to the single phase. Normalisation is by the gas bulk velocity in the large tube, Uo.

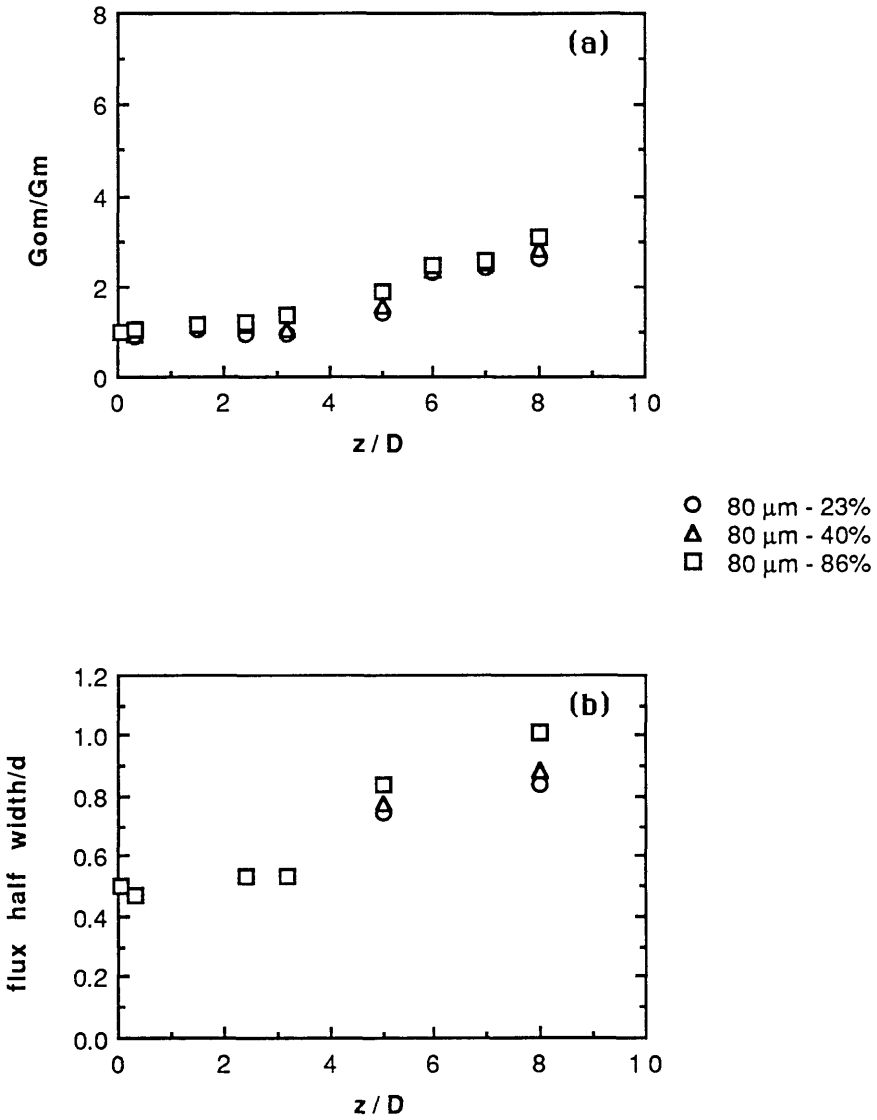


FIGURE 4.17 (a) Centreline profile of volume flux, (b) flux half width in sudden expansion ratio of 3.33 for 80 µm beads for mass loadings of 23% (circle), 40% (triangle) and 86% (square). Flux normalisation is by the centreline flux at the exit of the small tube, Gom, and the flux half width by the diameter of the small tube, d.

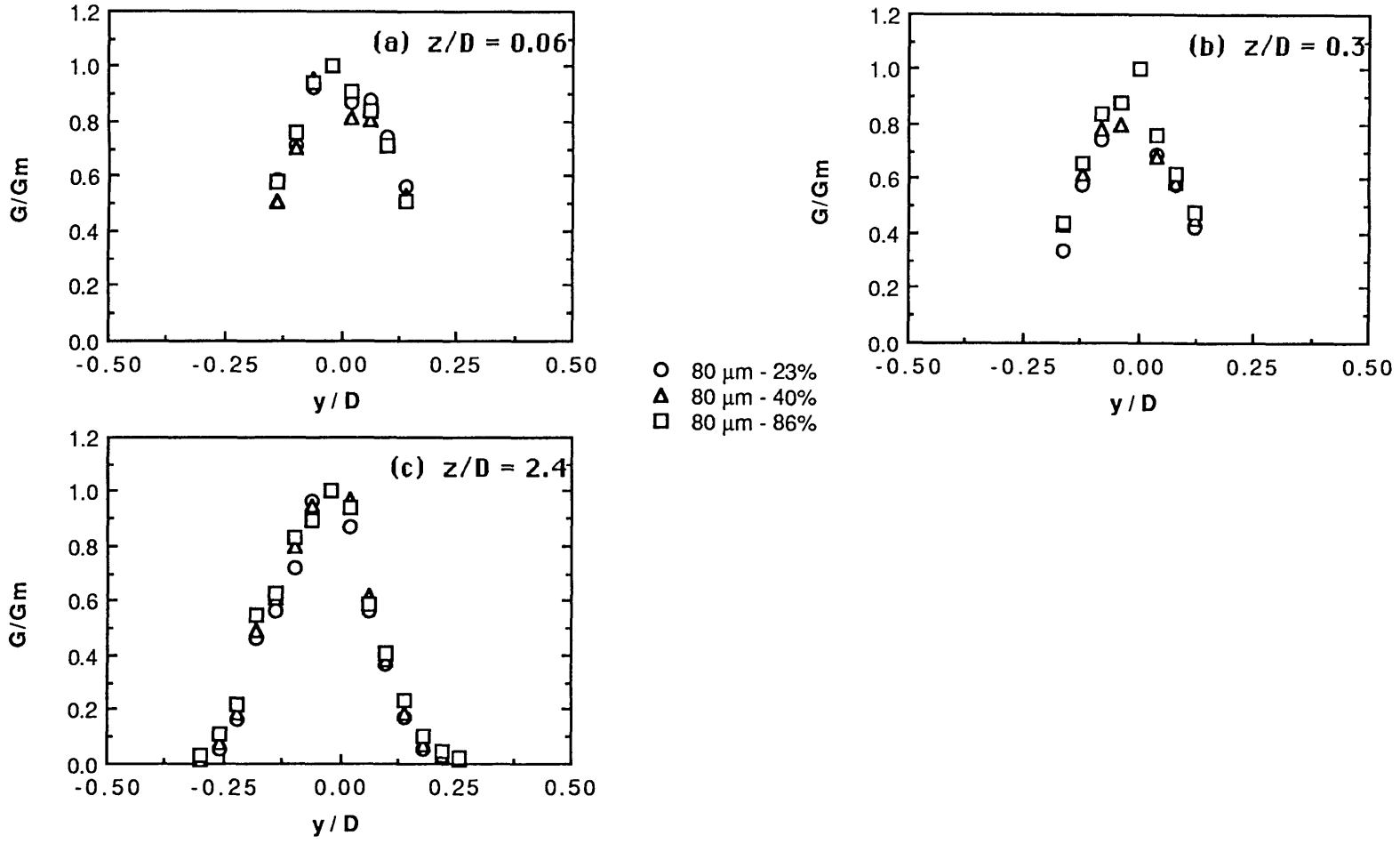


FIGURE 4.18 Radial profiles of volume flux (G) in sudden expansion ratio of 3.33 at z/D = 0.06, 0.3 and 2.4 for 80 µm beads for mass loading of 23% (circle), 40% (triangle) and 86% (square). Normalisation is by the centreline flux, Gm.

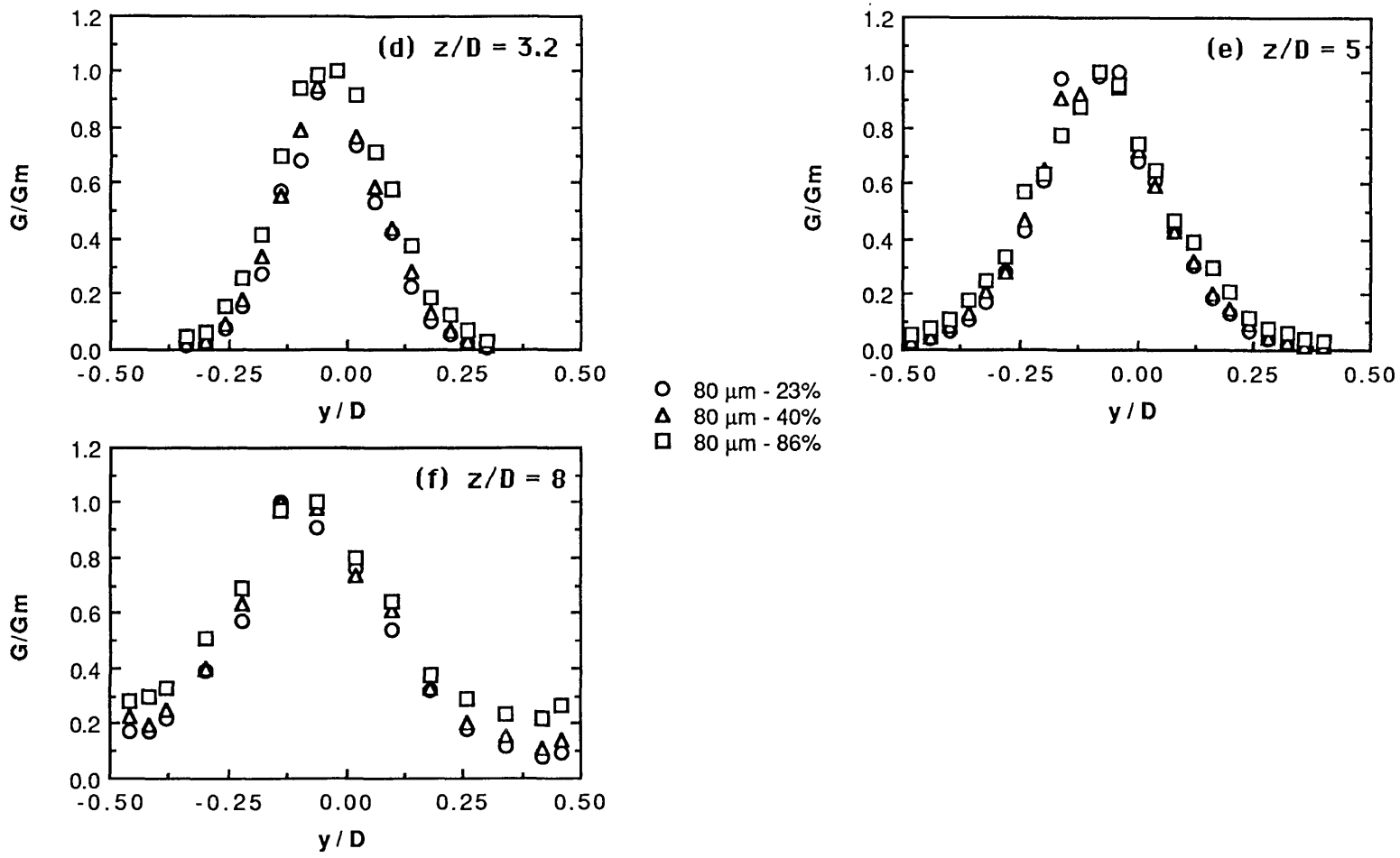


FIGURE 4.18 (continue) Radial profiles of volume flux (G) in sudden expansion ratio of 3.33 at z/D = 3.2, 5 and 8 for 80 µm beads for mass loading of 23% (circle), 40% (triangle) and 86% (square). Normalisation is by the centreline flux, Gm.

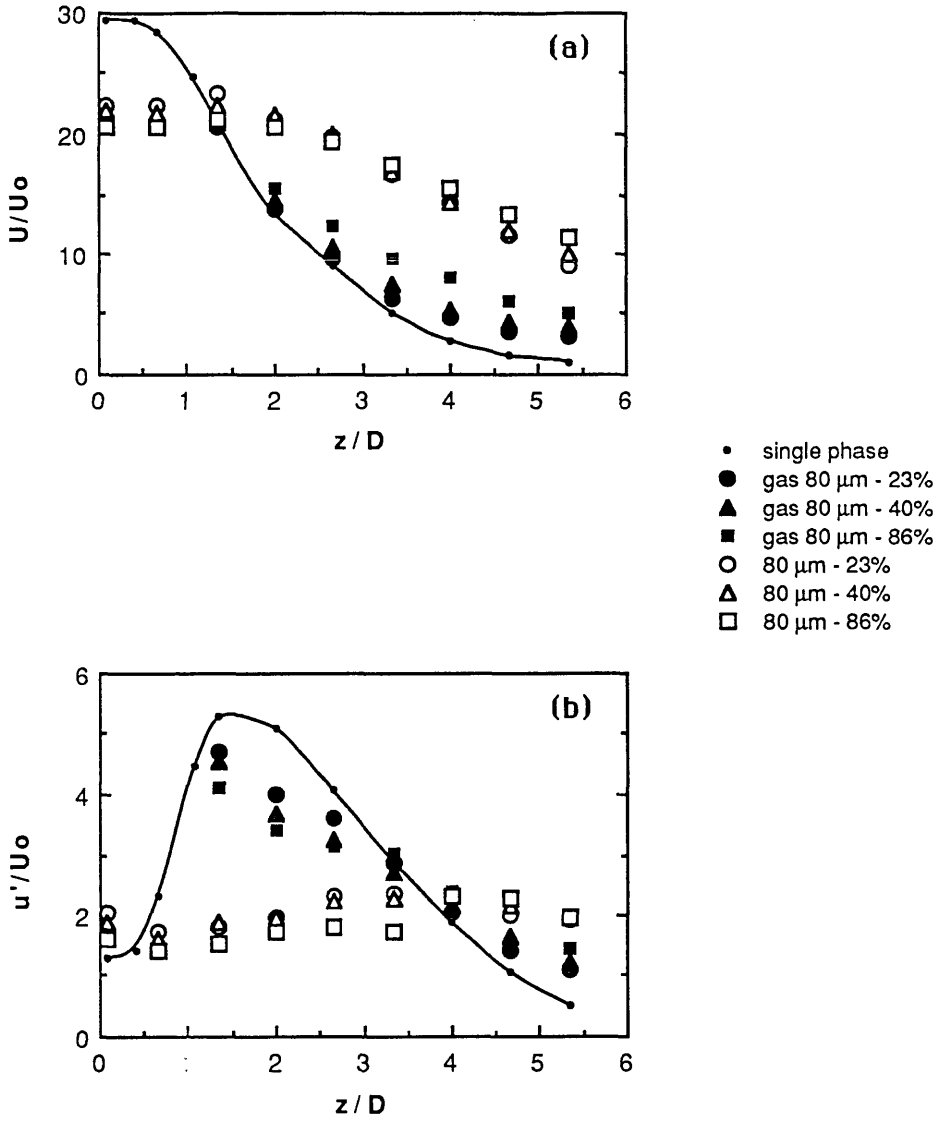


FIGURE 4.19 Centreline profiles of (a) mean and (b) rms axial velocity (U, u') in sudden expansion ratio of 5 for gas phase and 80 µm beads for mass loading of 23% (circle), 40% (triangle) and 86% (square). Normalisation is by the gas bulk velocity in the large tube, Uo.

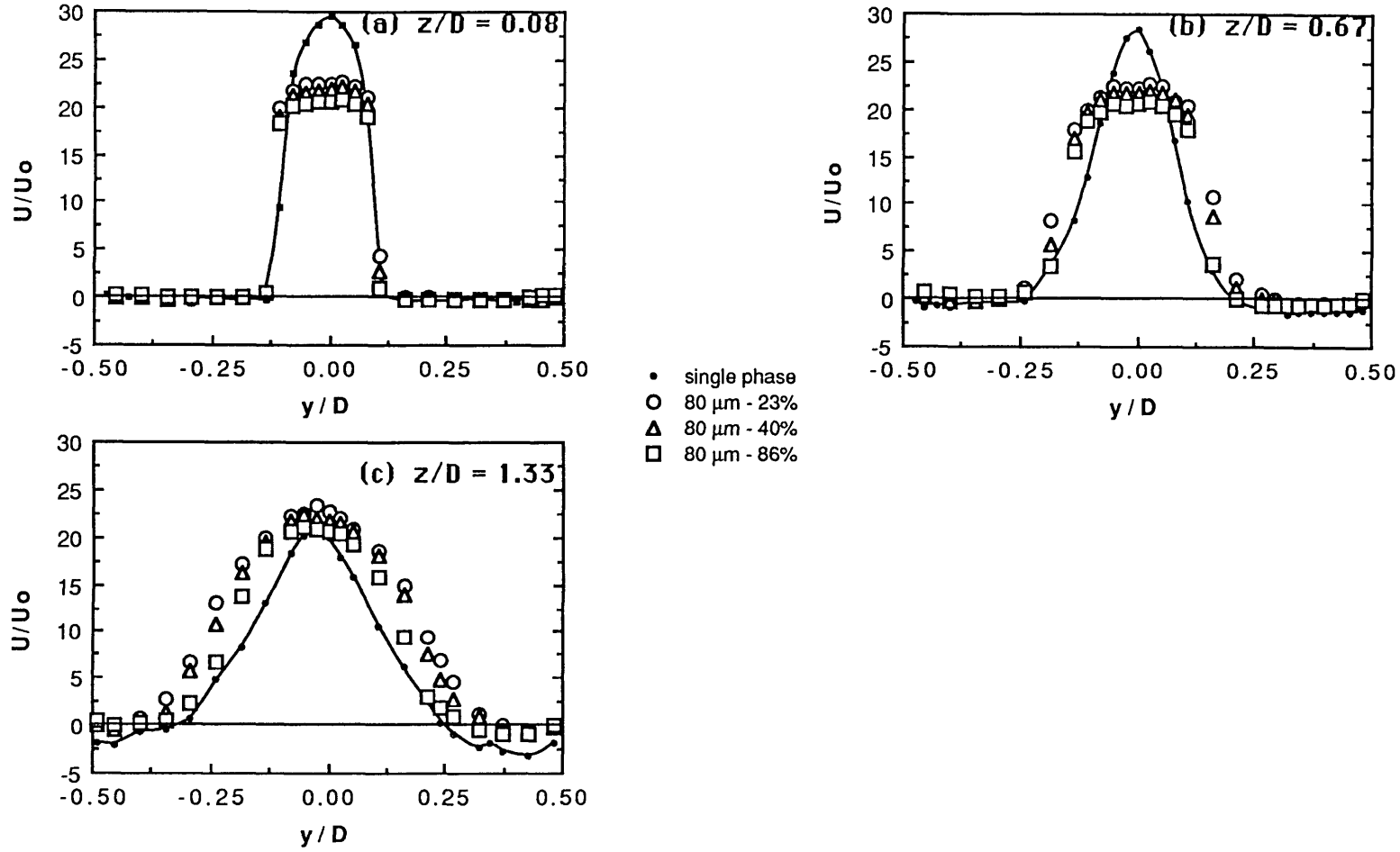


FIGURE 4.20 Radial profiles of mean axial velocity (U) in sudden expansion ratio of 5 at z/D = 0.08, 0.67 and 1.33 for gas phase and 80 μm beads for mass loading of 23% (circle), 40% (triangle) and 86% (square). Normalisation is by the gas bulk velocity in the large tube.

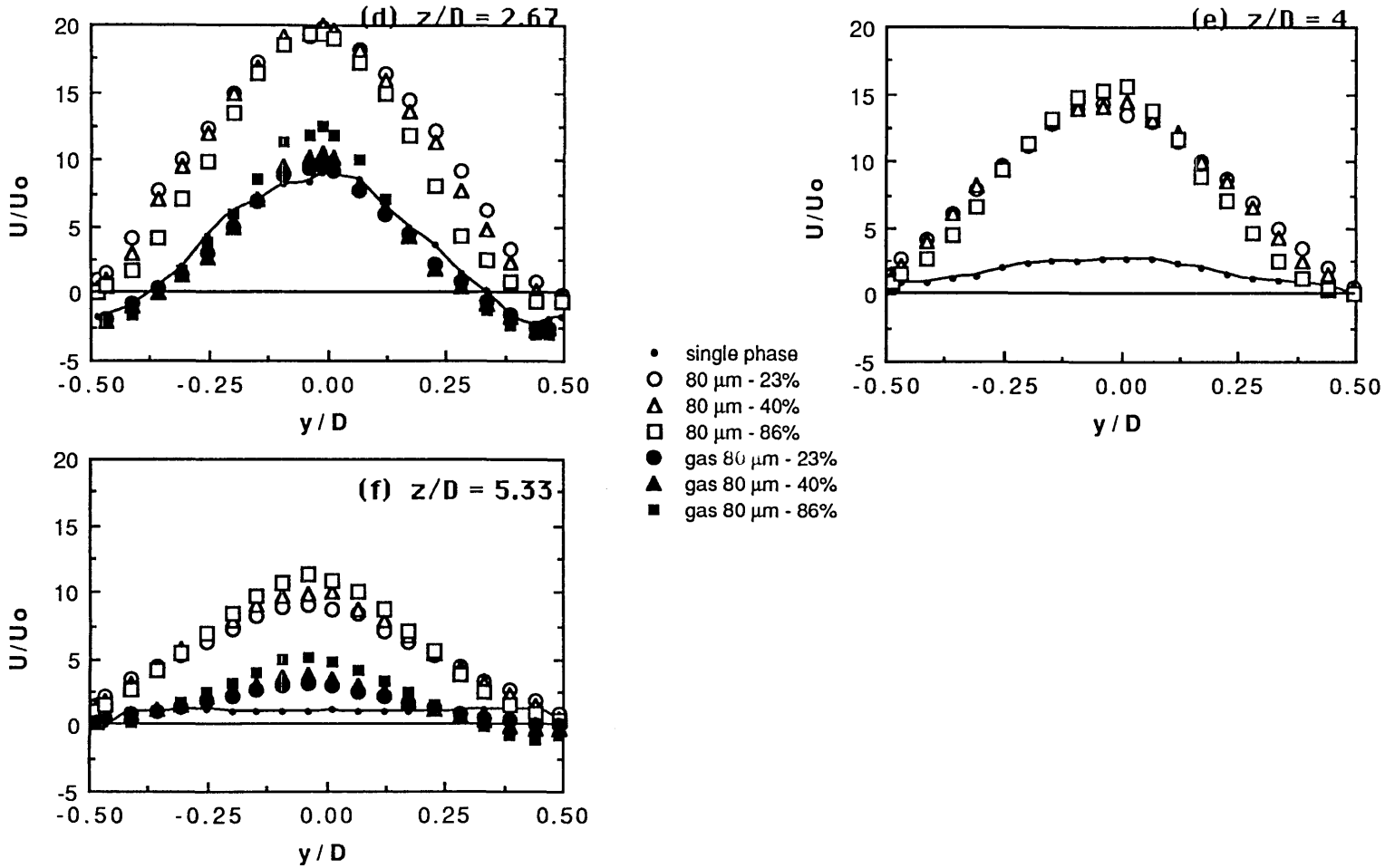


FIGURE 4.20 (continue) Radial profiles of mean axial velocity (U) in sudden expansion ratio of 5 at z/D = 2.67, 4 and 5.33 for gas phase and 80 μm beads for mass loading of 23% (circle), 40% (triangle) and 86% (square). Normalisation is by the gas bulk velocity in the large tube, Uo.

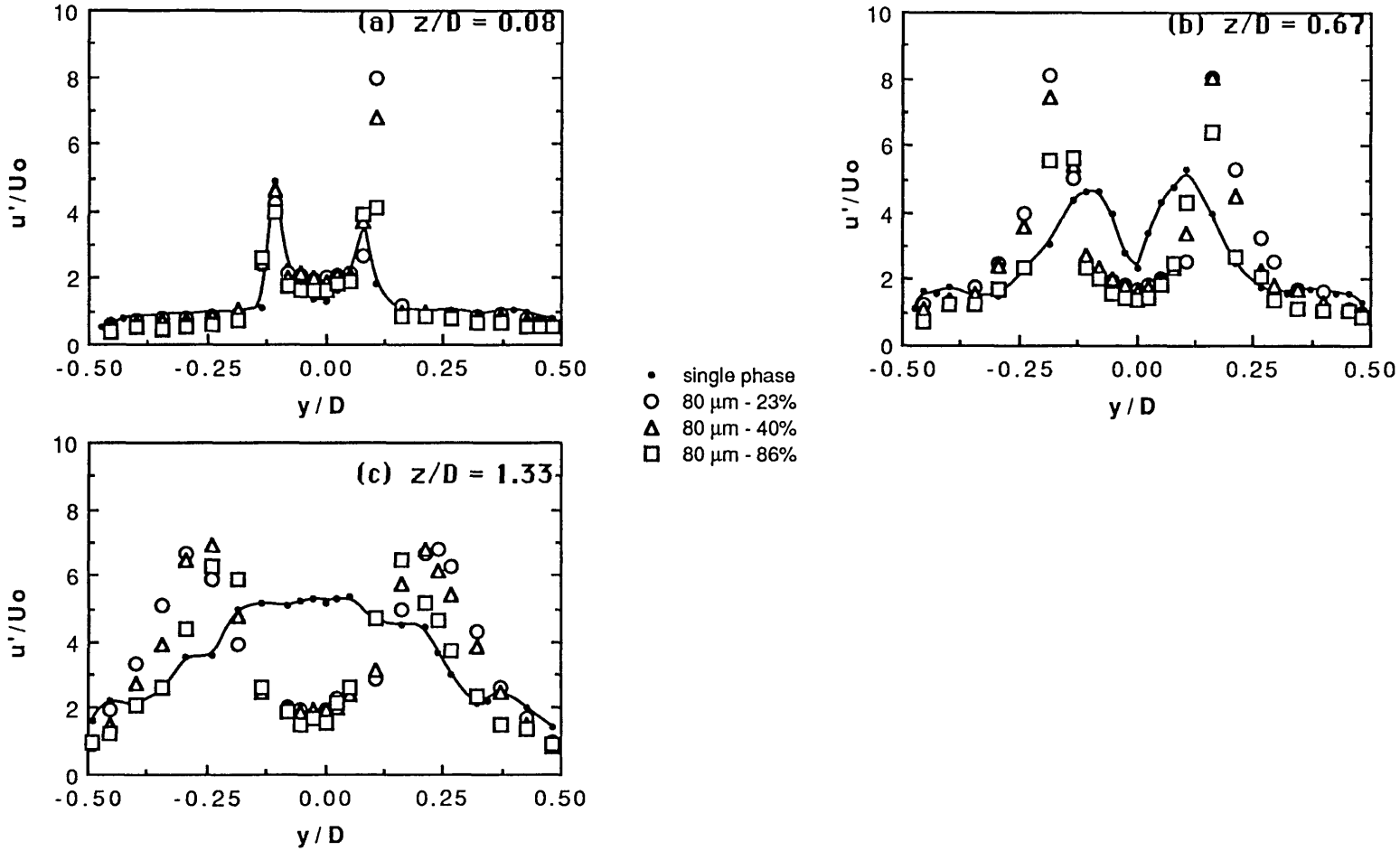


FIGURE 4.21 Radial profiles of rms axial velocity (u') in sudden expansion ratio of 5 at z/D = 0.08, 0.67 and 1.33 for gas phase and 80 µm beads for mass loading of 23% (circle), 40% (triangle) and 86% (square). Normalisation is by the gas bulk velocity in the large tube, Uo.

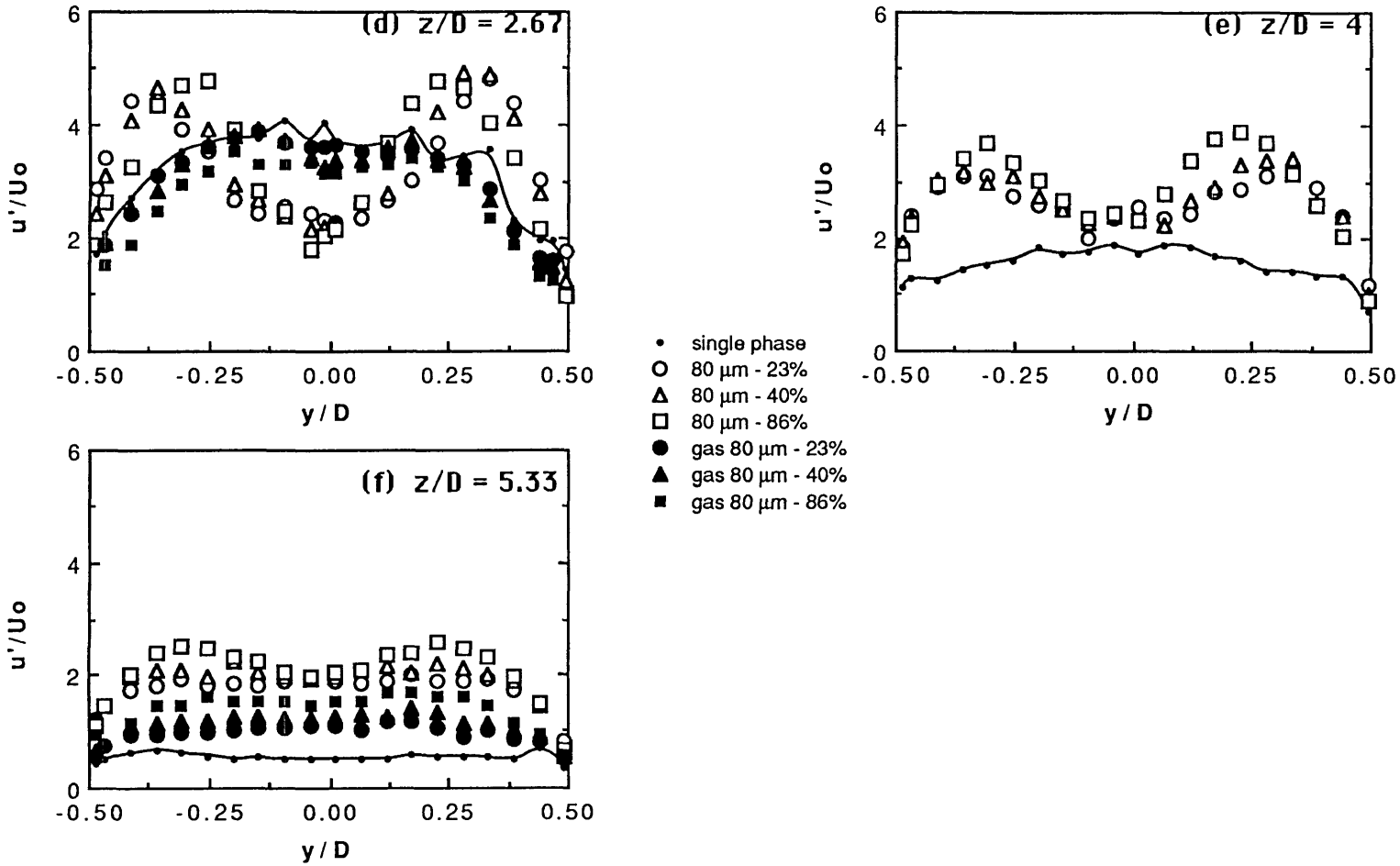


FIGURE 4.21 (continue) Radial profiles of rms axial velocity (u') in sudden expansion ratio of 5 at z/D = 2.67, 4 and 5.33 for gas phase and 80 µm beads for mass loading of 23% (circle), 40% (triangle) and 86% (square). Normalisation is by the gas bulk velocity in the large tube, Uo.

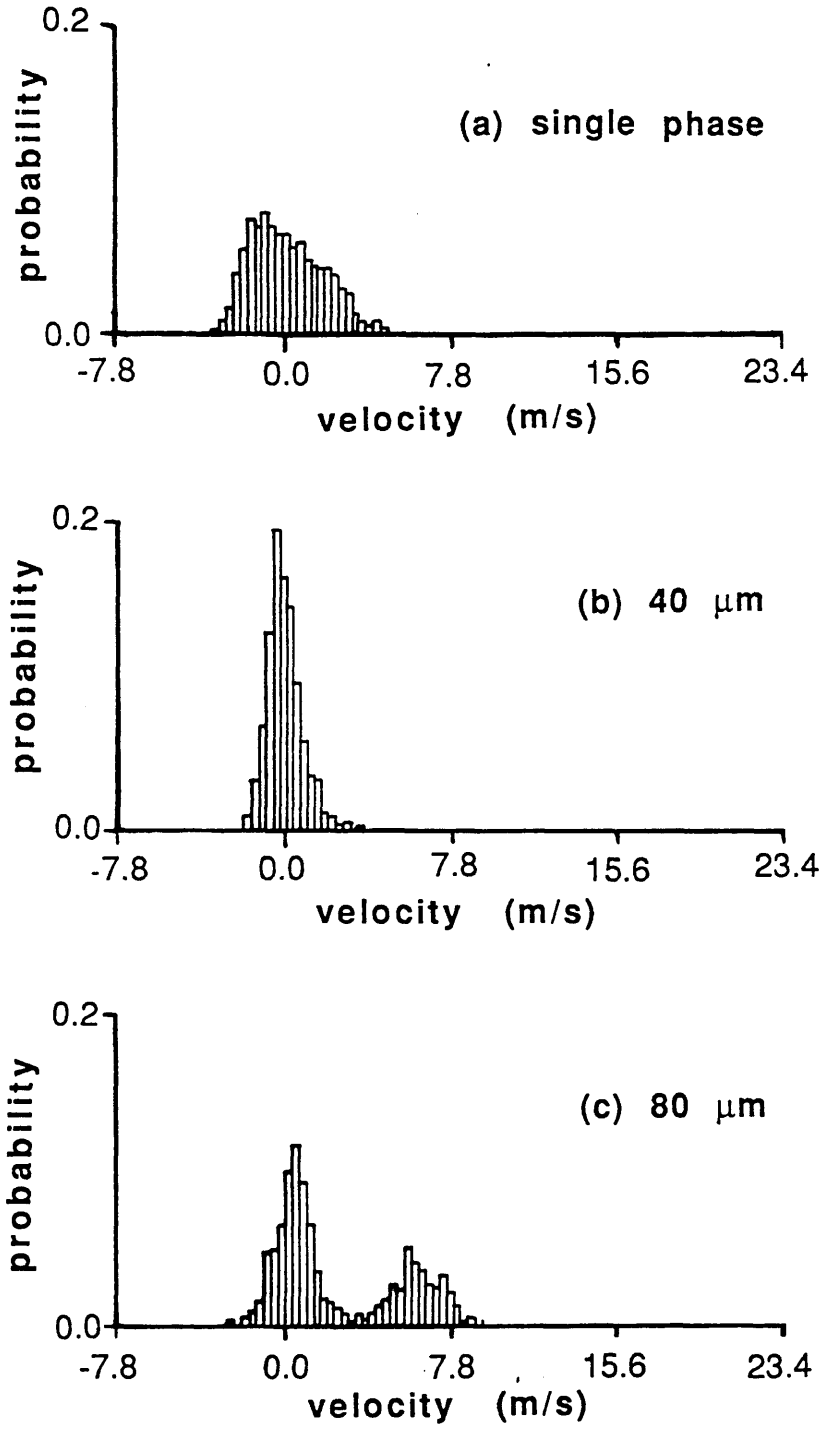


FIGURE 4.22 Velocity probability density functions in expansion ratio of 5 at z/D = 1.33 and y/D = 0.25 for (a) single phase, (b) 40 μm beads and (c) 80 μm beads.

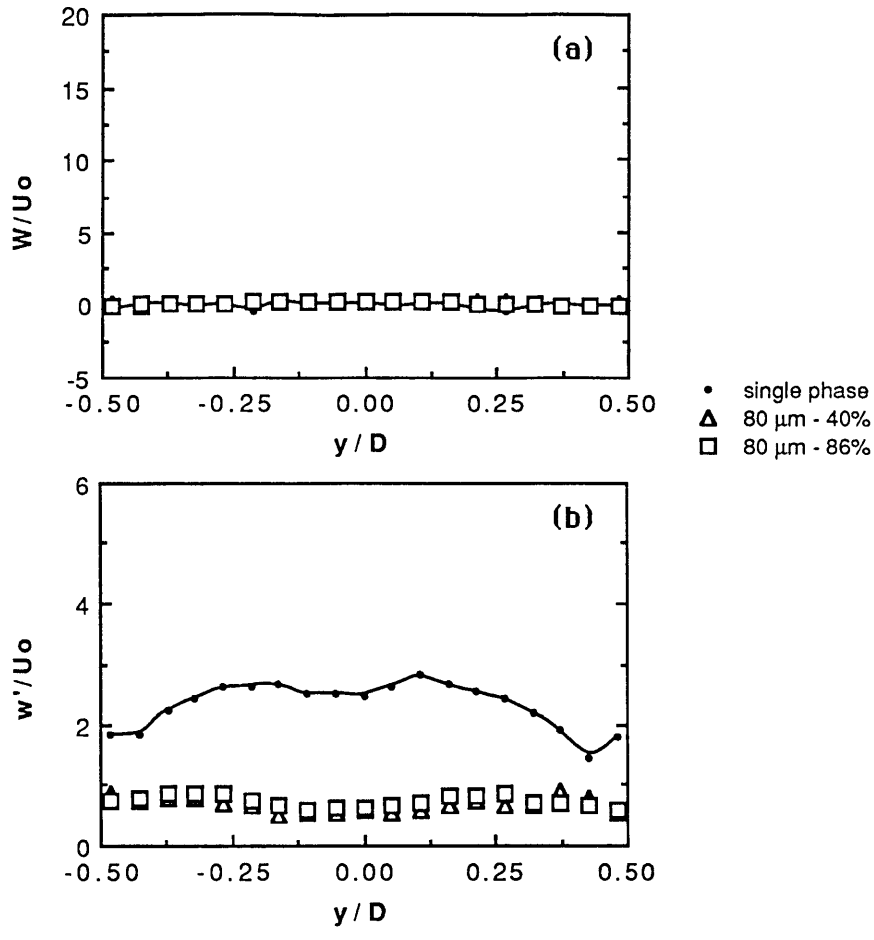


FIGURE 4.23 Radial profile of (a) mean and (b) rms azimuthal velocity (W, w') in sudden expansion ratio of 5 at z/D = 2.67 for 80 μm beads for mass loading of 40% (triangle) and 86% (square). Normalisation is by the gas bulk velocity in the large tube, Uo.

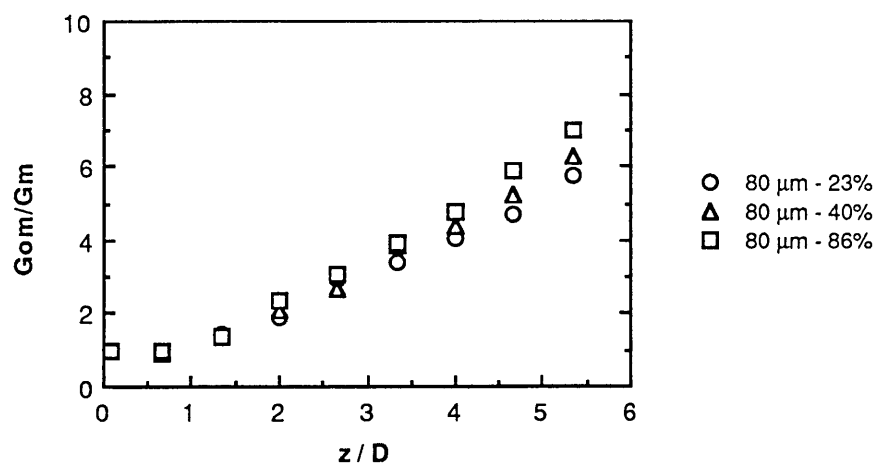


FIGURE 4.24 Centreline profile of volume flux in sudden expansion ratio of 5 for 80 μm beads for mass loading of 23 % (circle), 40% (triangle) and 86% (square). Normalisation is by the centreline flux at the exit of the small tube, Gom.

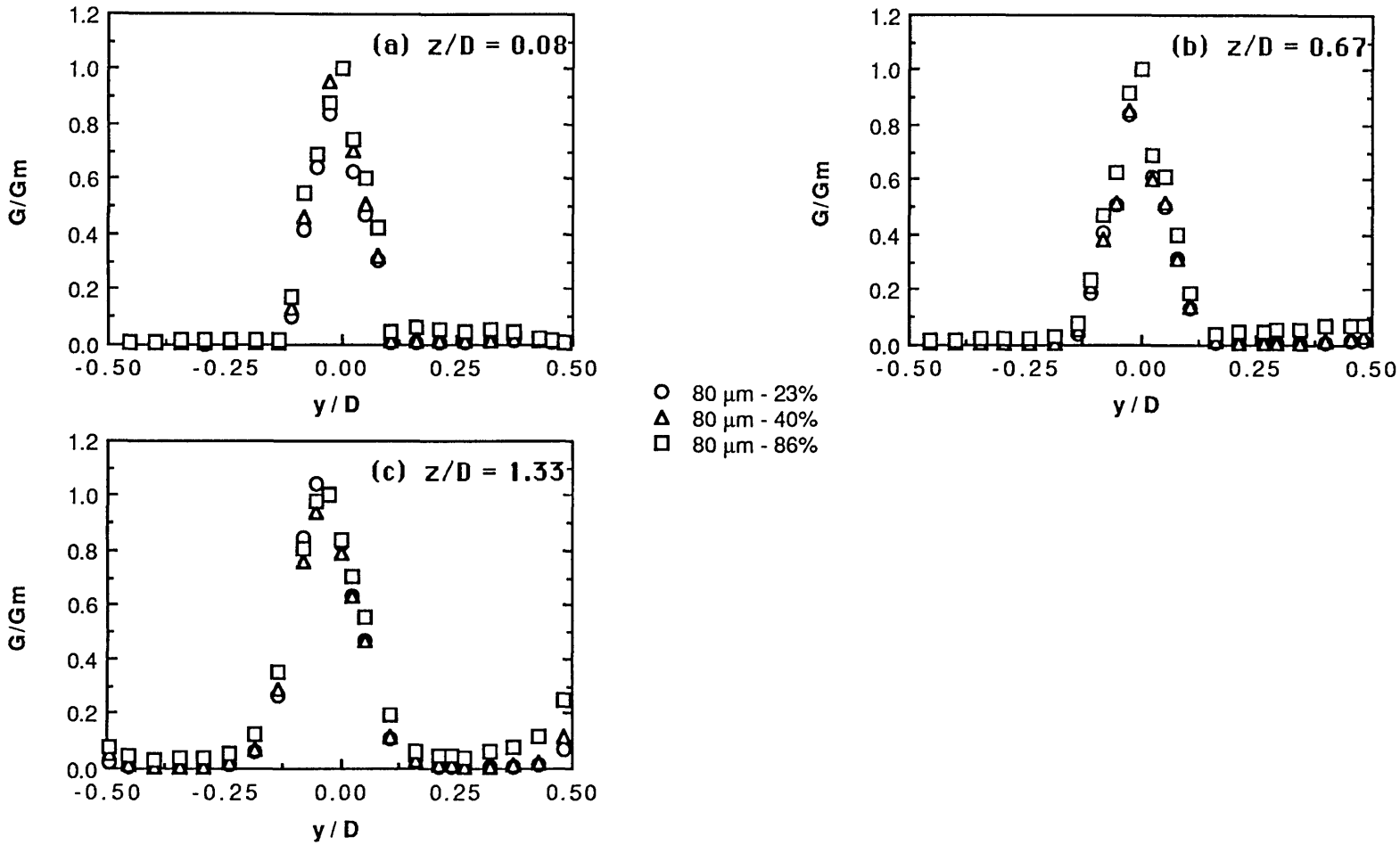


FIGURE 4.25 Radial profiles of volume flux (G) in sudden expansion ratio of 5 at z/D = 0.08, 0.67 and 1.33 for 80 µm beads for mass loadings of 23% (circle), 40% (triangle) and 86% (square). Normalisation is by the centreline flux, Gm.

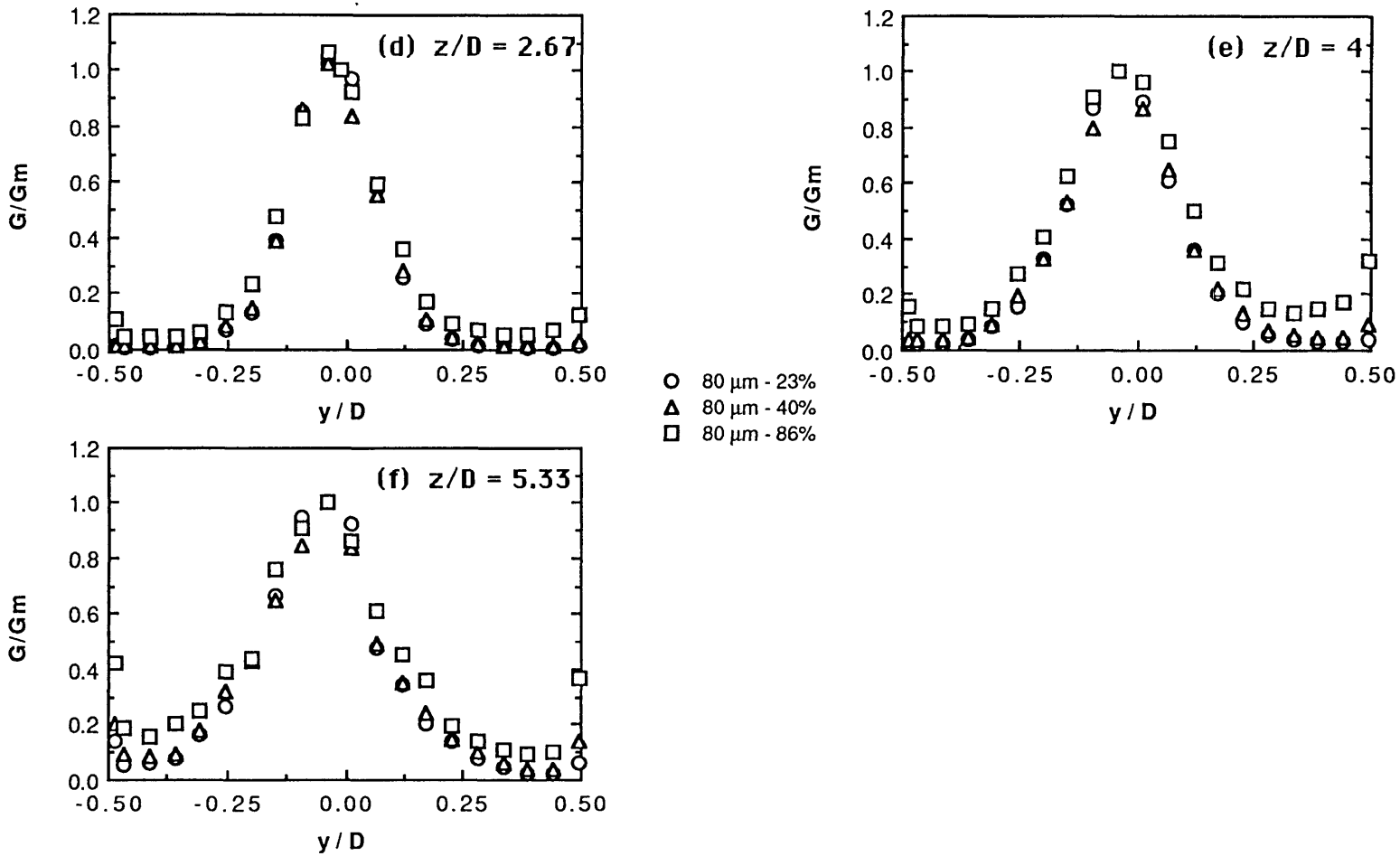


FIGURE 4.25 (continue) Radial profiles of volume flux (G) in sudden expansion ratio of 5 at z/D = 2.67, 4 and 5.33 for 80 µm beads for mass loadings of 23% (circle), 40% (triangle) and 86% (square). Normalisation is by the centreline flux, Gm.

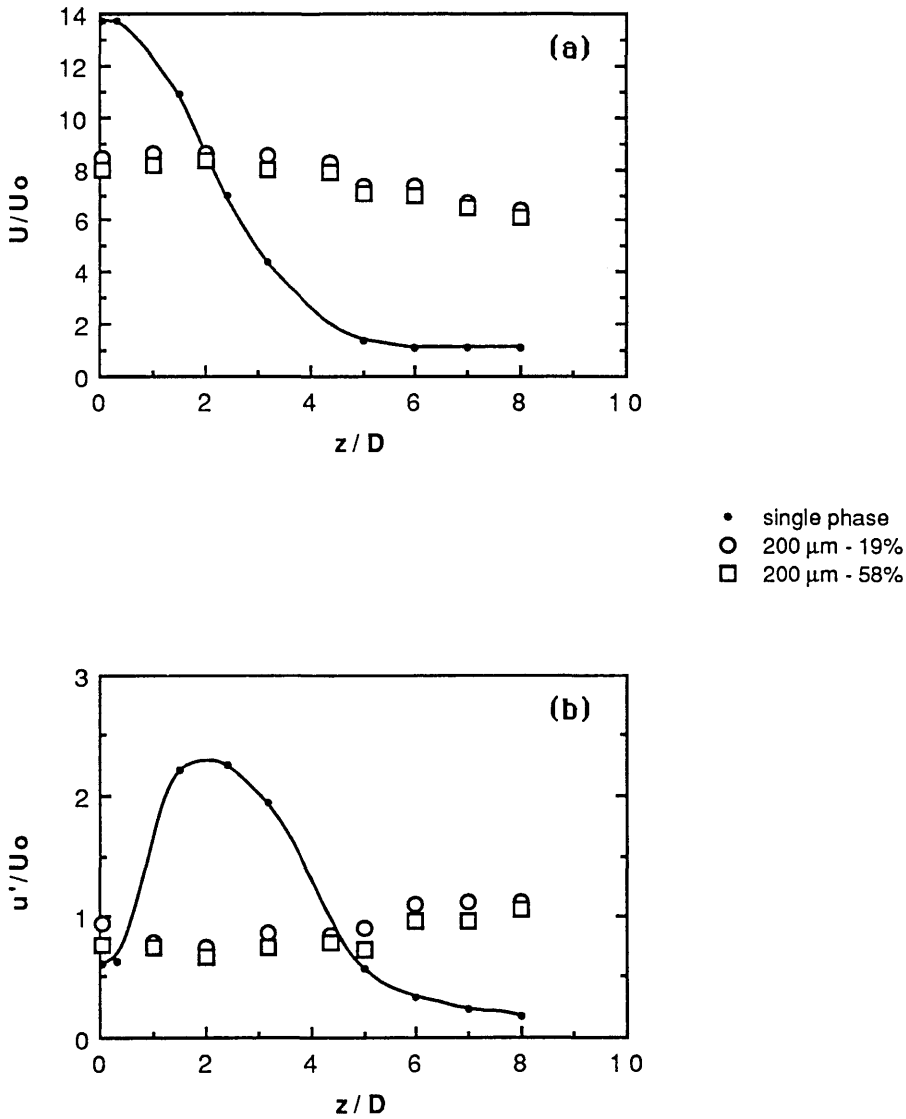


FIGURE 4.26 Centreline profiles of (a) mean and (b) rms axial velocity in sudden expansion ratio of 3.33 for 200 µm beads for mass loadings of 19% (circle) and 58% (square) compared to the single phase. Normalisation is by the gas bulk velocity in the large tube, Uo.

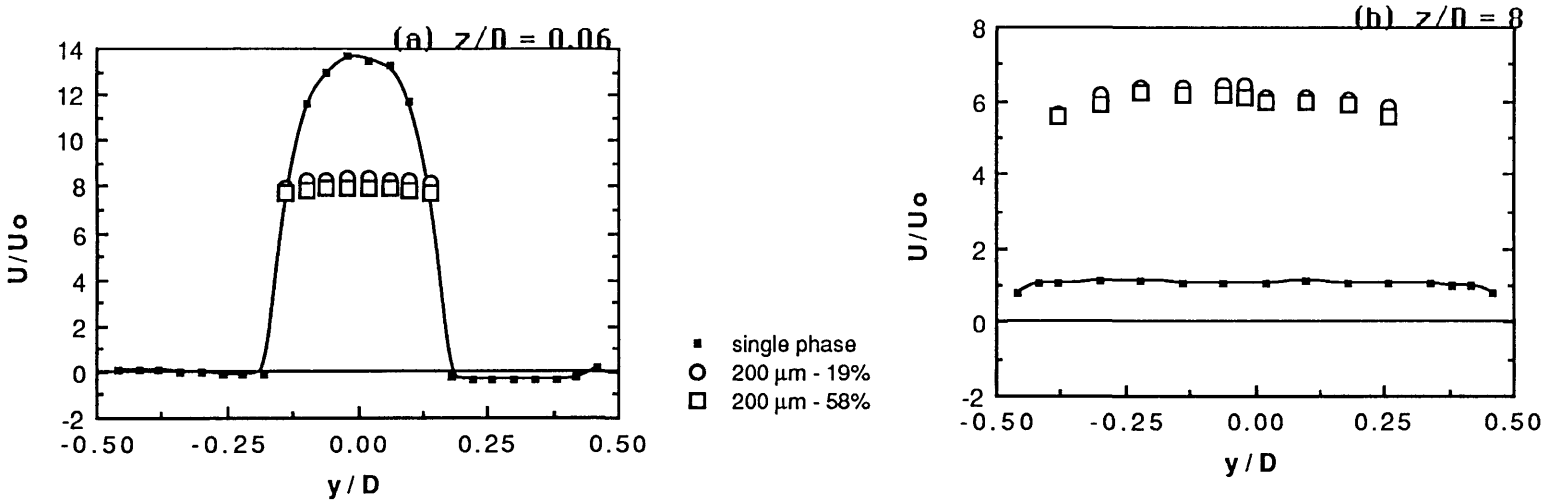


FIGURE 4.27 Radial profiles of mean axial velocity (U) in sudden expansion ratio 3.33 at z/D = 0.06 and 8 for 200 µm beads for mass loadings of 19% (circle) and 58% (square) compared to the single phase.

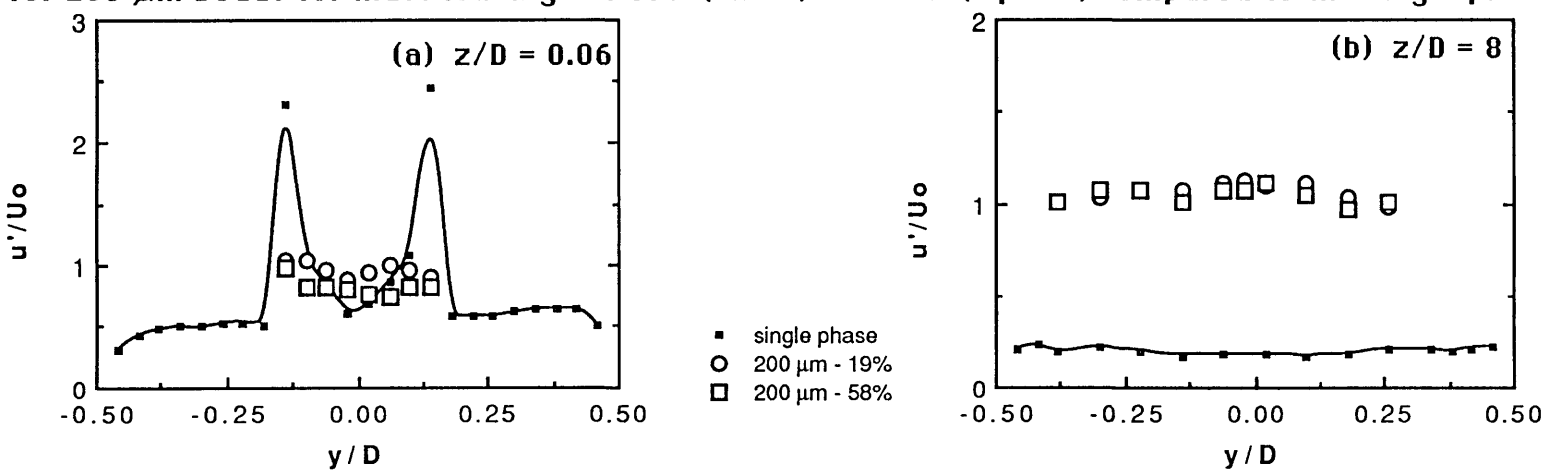


FIGURE 4.28 Radial profiles of rms axial velocity (u') in sudden expansion ratio 3.33 at z/D = 0.06 and 8 for 200 µm beads for mass loadings of 19% (circle) and 58% (square) compared to the single phase. Normalisation is by the gas bulk velocity in the large tube, Uo.

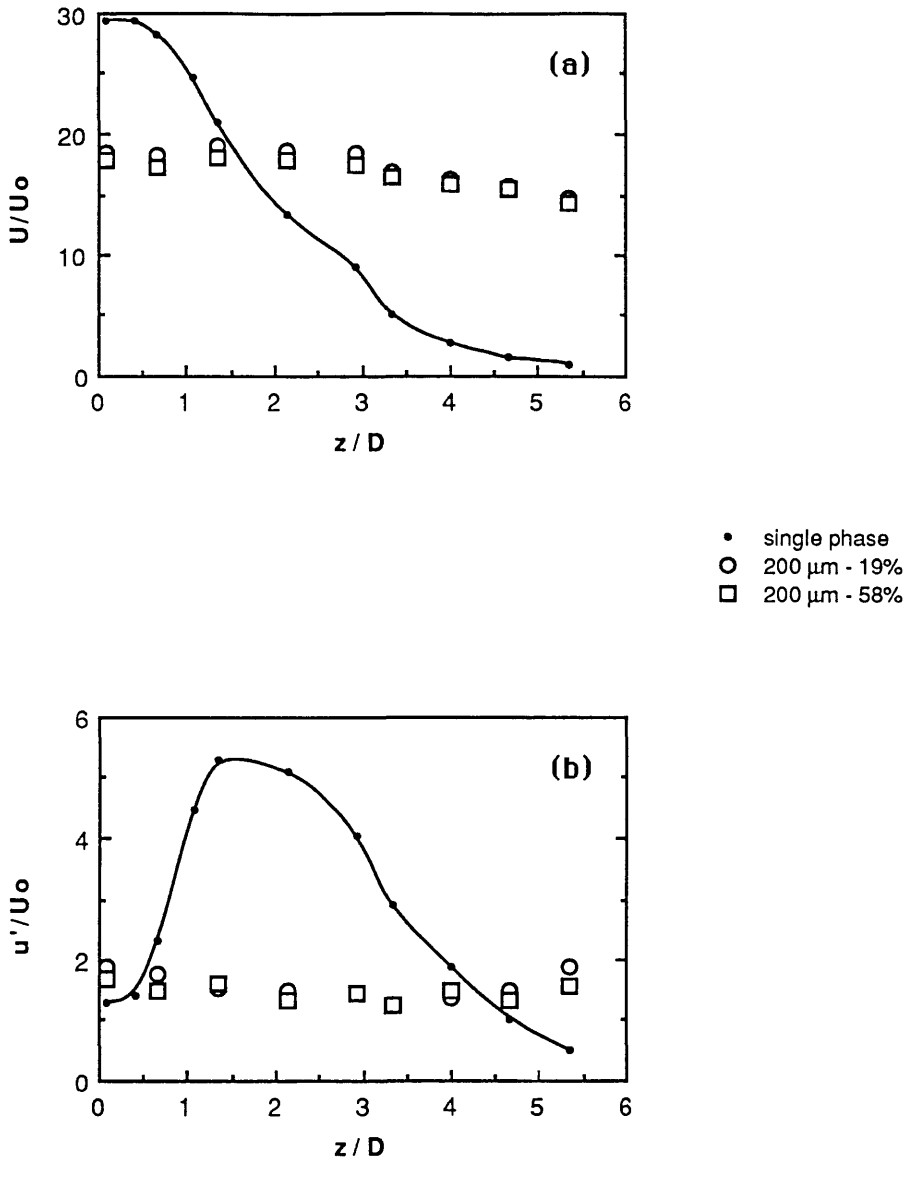


FIGURE 4.29 Centreline profiles of (a) mean and (b) rms axial velocity in sudden expansion ratio of 5 for 200 μm beads for mass loadings of 19% (circle) and 58% (square) compared to the single phase. Normalisation is by the gas bulk velocity in the large tube, Uo.

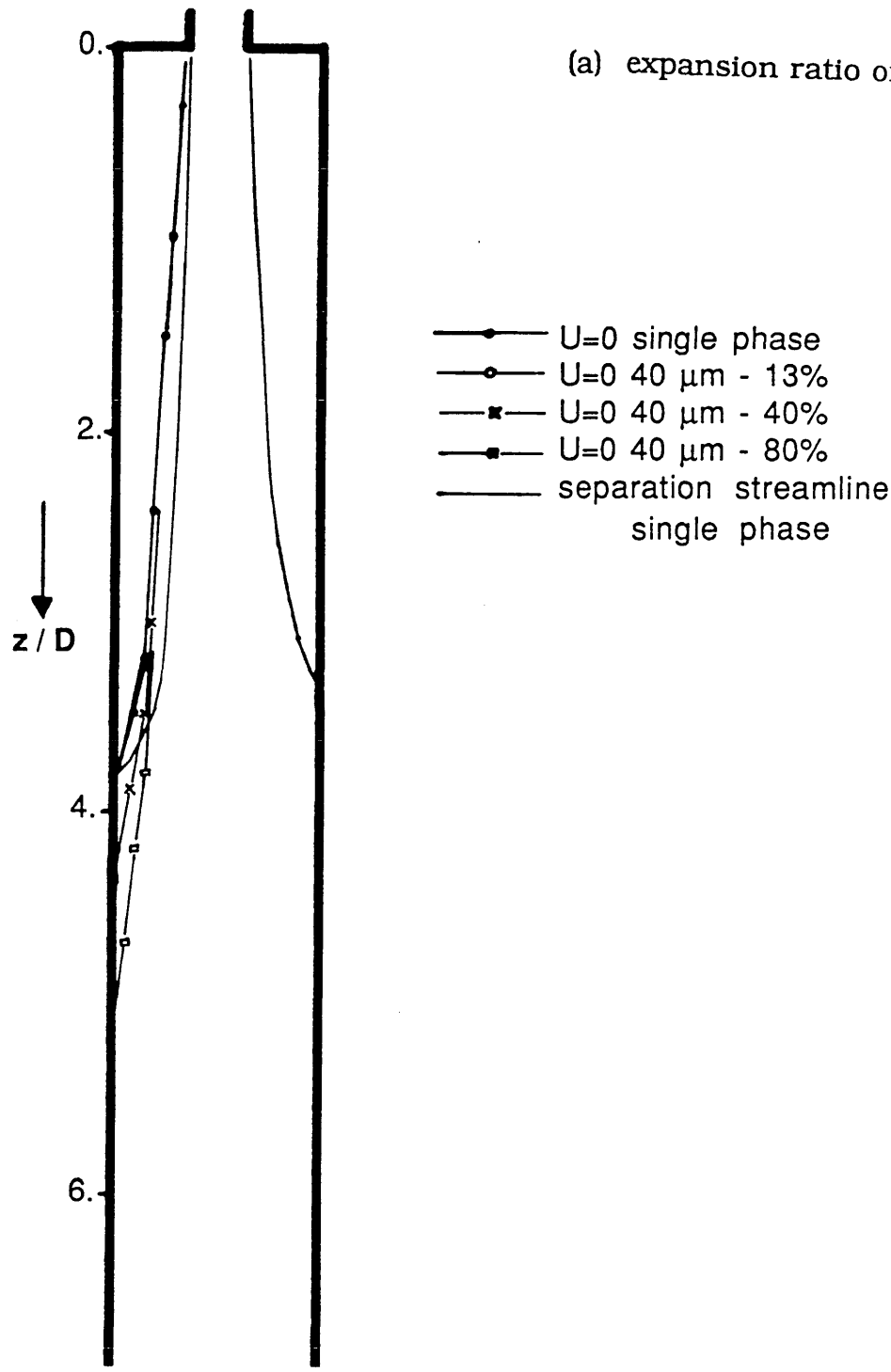


Figure 4.30 Contours of zero velocity for (a) the single phase and 40 µm beads for mass loadings of 13, 40 and 80% and (b) the single and gas phase and 80 µm beads for mass loadings of 23, 40 and 86% and the single phase separation streamline in the expansion ratio of 3.33.

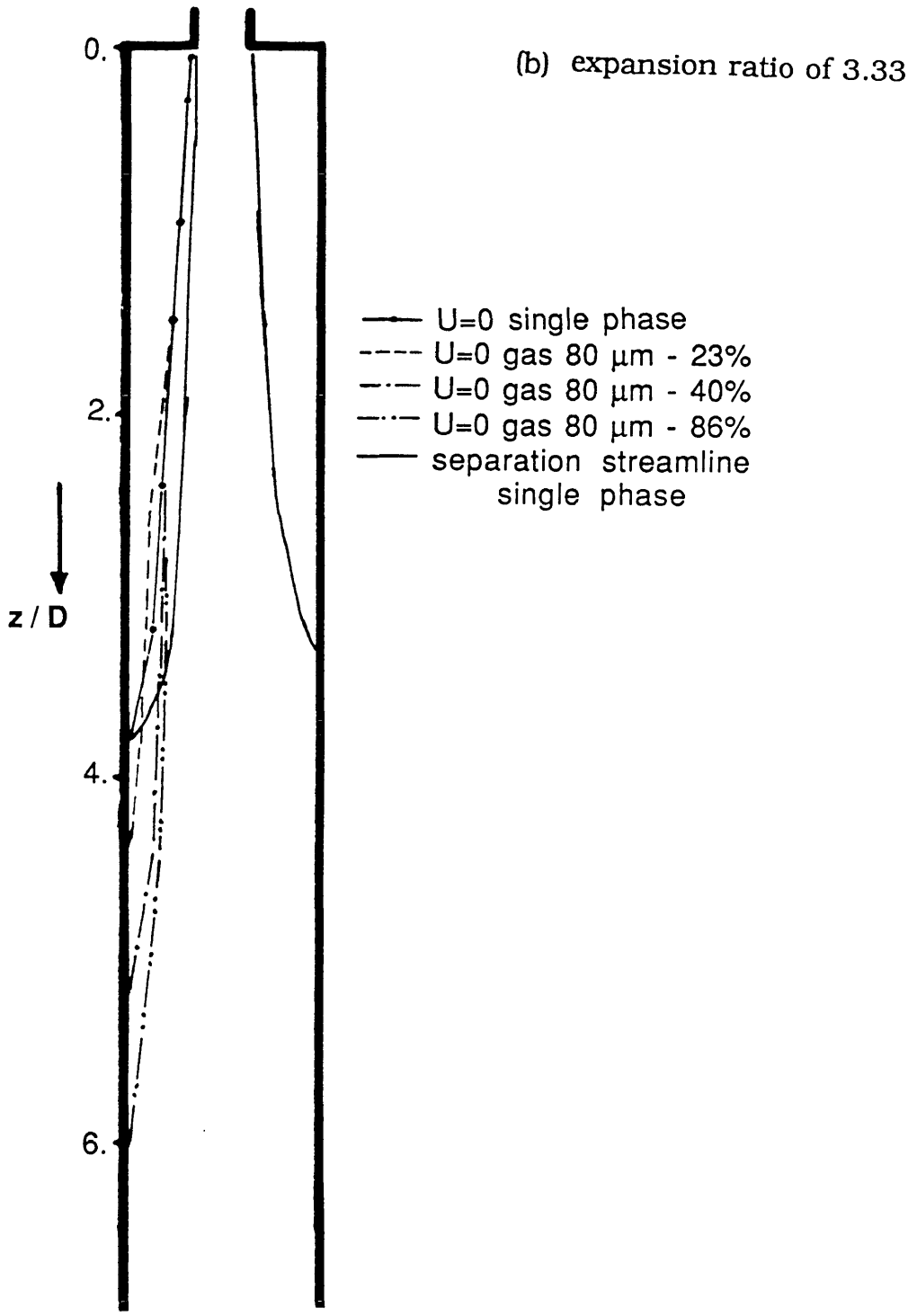


Figure 4.30 Contours of zero velocity for (a) the single phase and 40 µm beads for mass loadings of 13, 40 and 80% and (b) the single and gas phase and 80 µm beads for mass loadings of 23, 40 and 86% and the single phase separation streamline in the expansion ratio of 3.33.

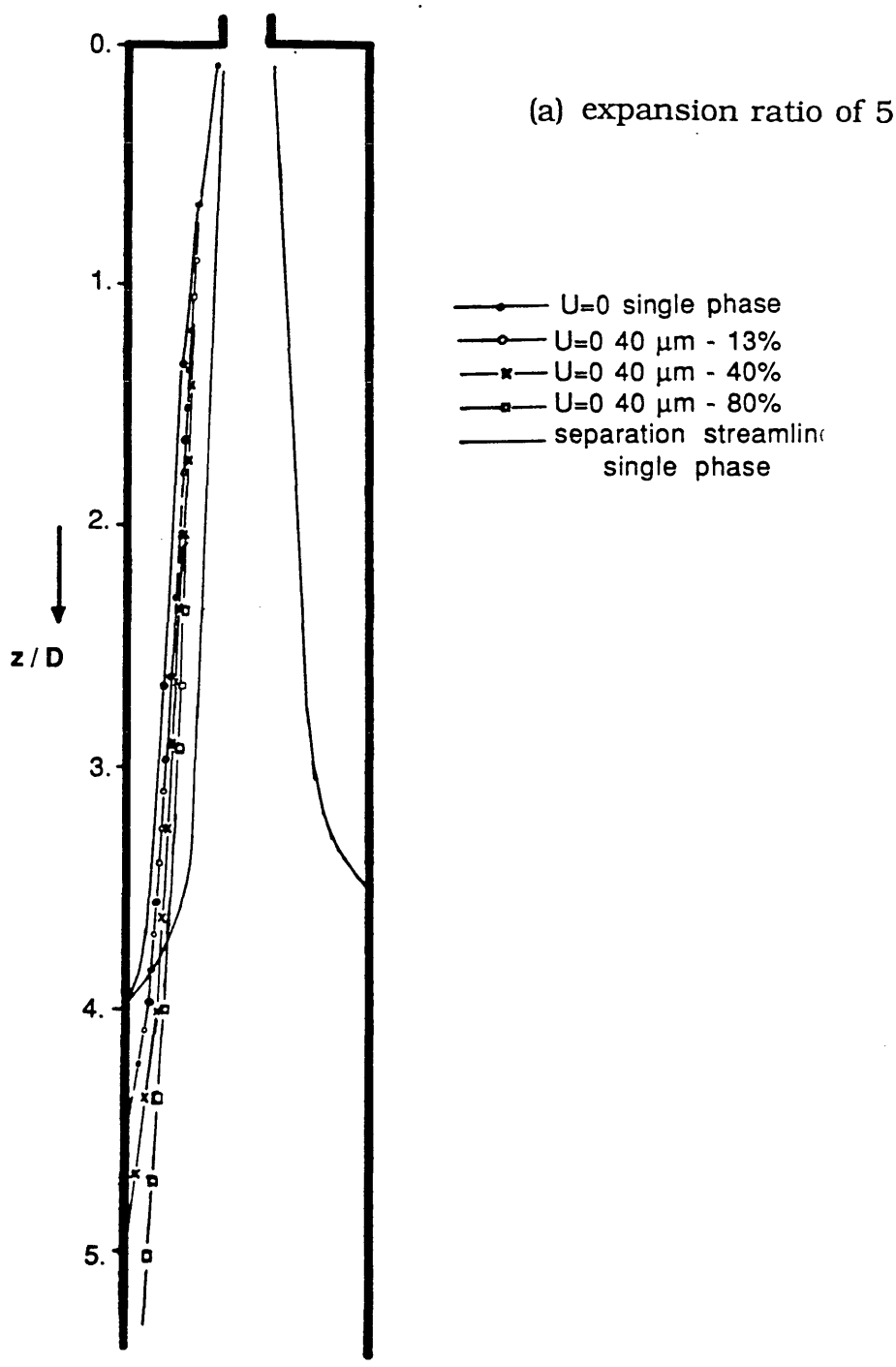


Figure 4.31 Contours of zero velocity for (a) the single phase and 40 µm beads for mass loadings of 13, 40 and 80% and (b) the single and gas phase and 80 µm beads for mass loadings of 23, 40 and 86% and the single phase separation streamline in the expansion ratio of 5.

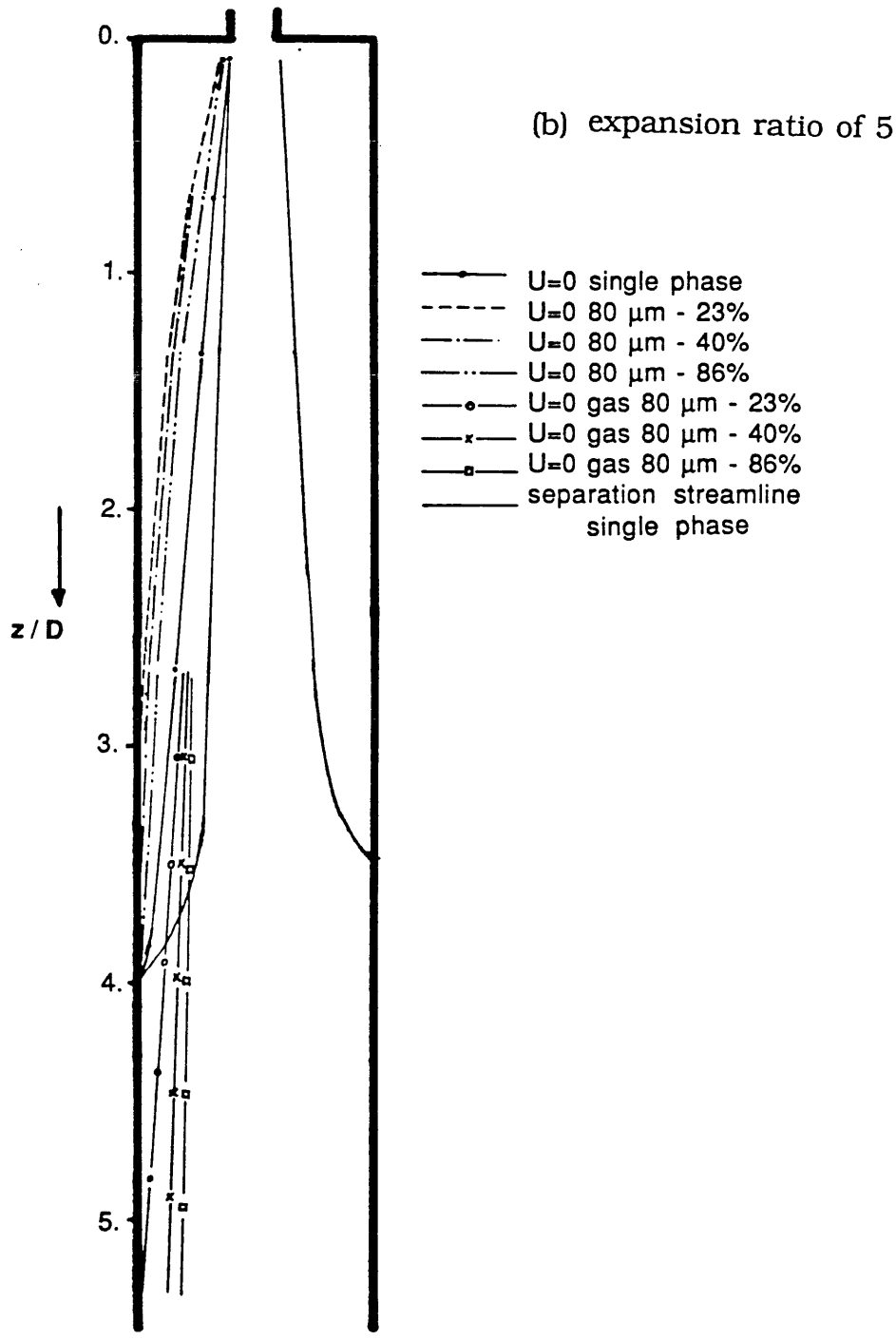


Figure 4.31 Contours of zero velocity for (a) the single phase and 40 µm beads for mass loadings of 13, 40 and 80% and (b) the single and gas phase and 80 µm beads for mass loadings of 23, 40 and 86% and the single phase separation streamline in the expansion ratio of 5.

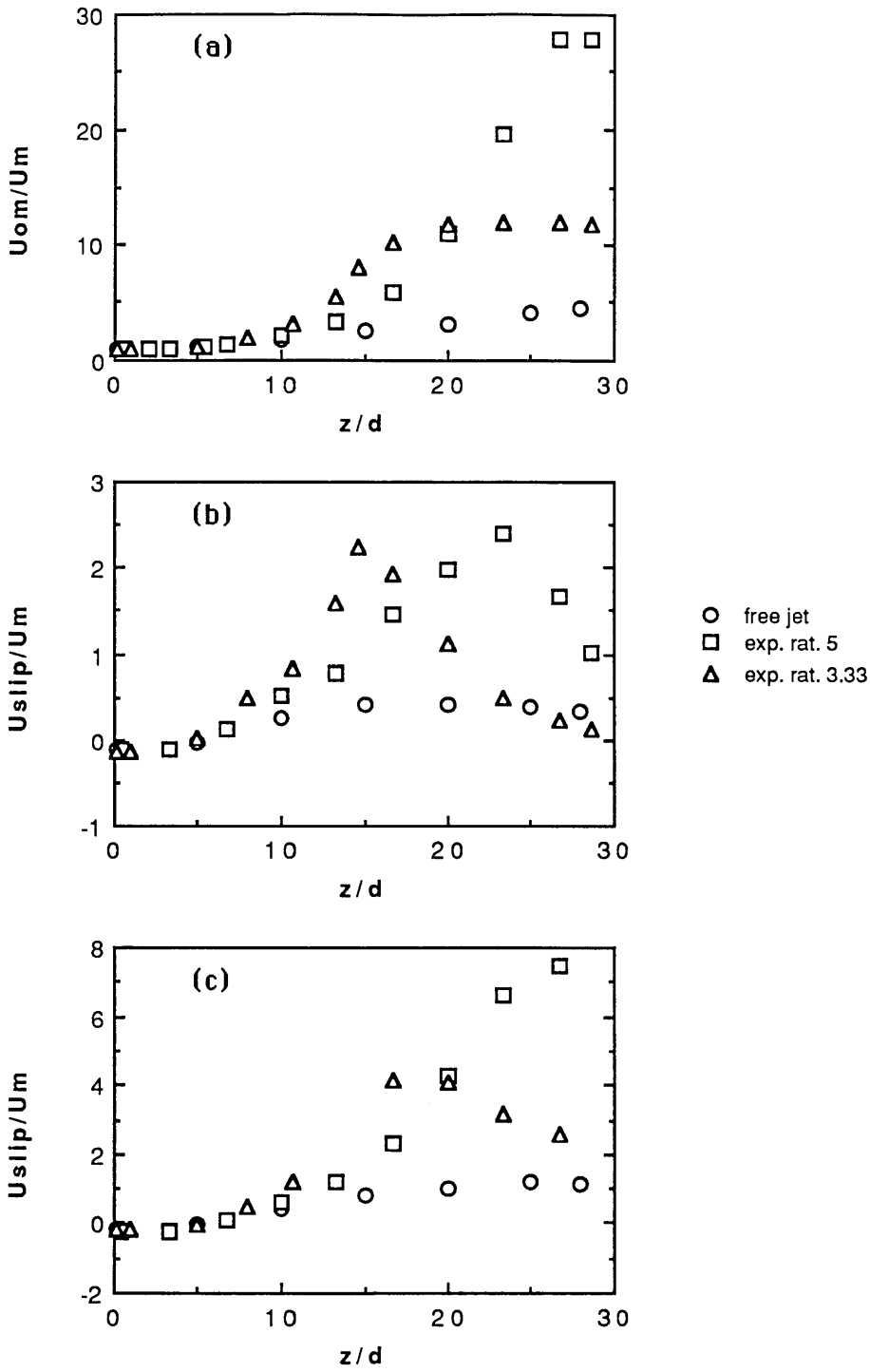


FIGURE 4.32 Centreline profiles of (a) mean axial velocity of single phase, (b) mean slip velocity of 40 μm beads, 13% mass loading normalised by the local gas axial velocity and (c) mean slip velocity of 80 μm beads, 23% mass loading, in the free jet (circle), sudden expansion ratio of 5 (triangle) and 3.33 (square).

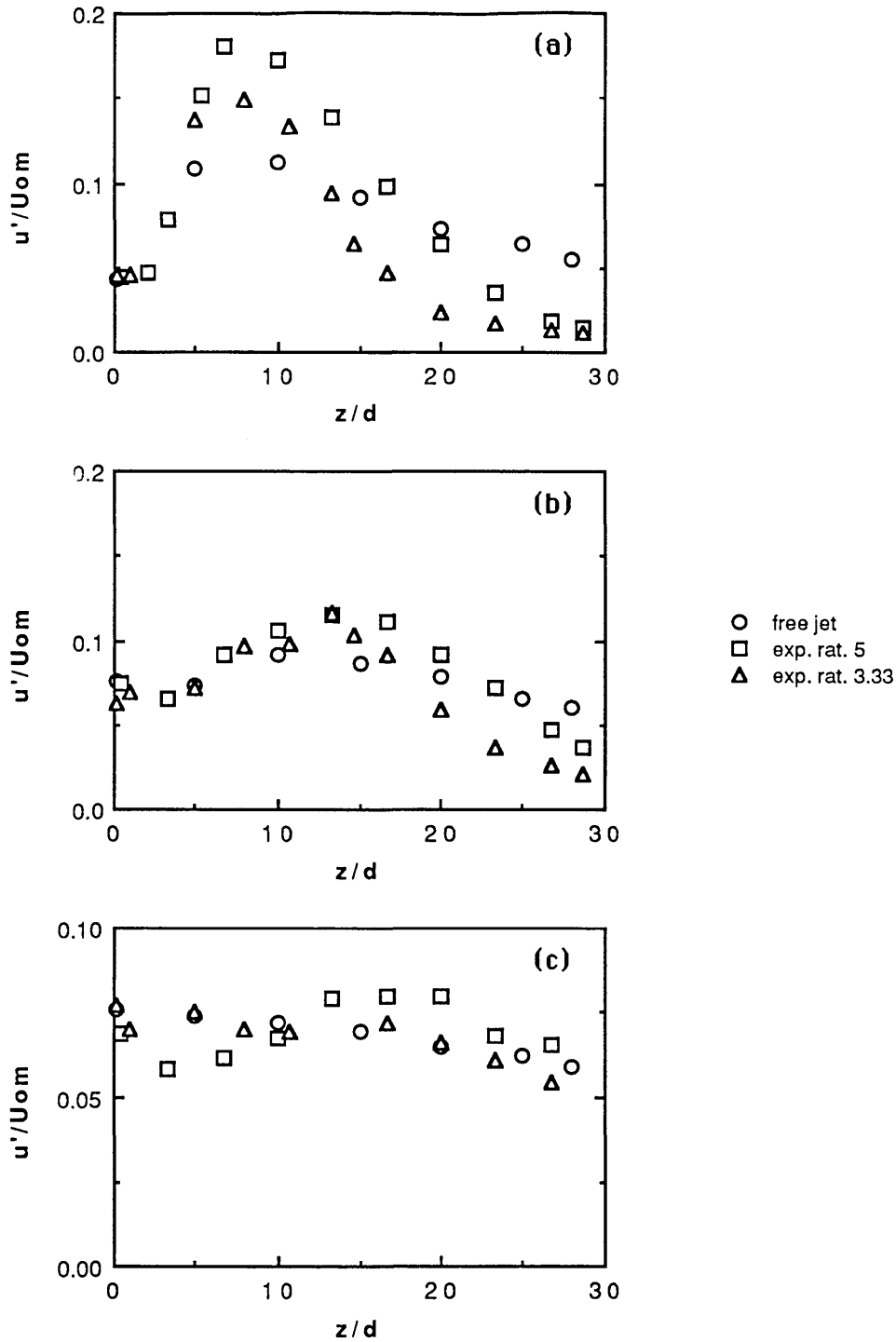


FIGURE 4.33 Centreline profiles of axial rms velocity of (a) single phase, (b) 40 μm beads, 13% mass loading and (c) 80 μm beads, 23% mass loading in the free jet (circle), sudden expansion ratio of 5 (triangle) and 3.33 (square).

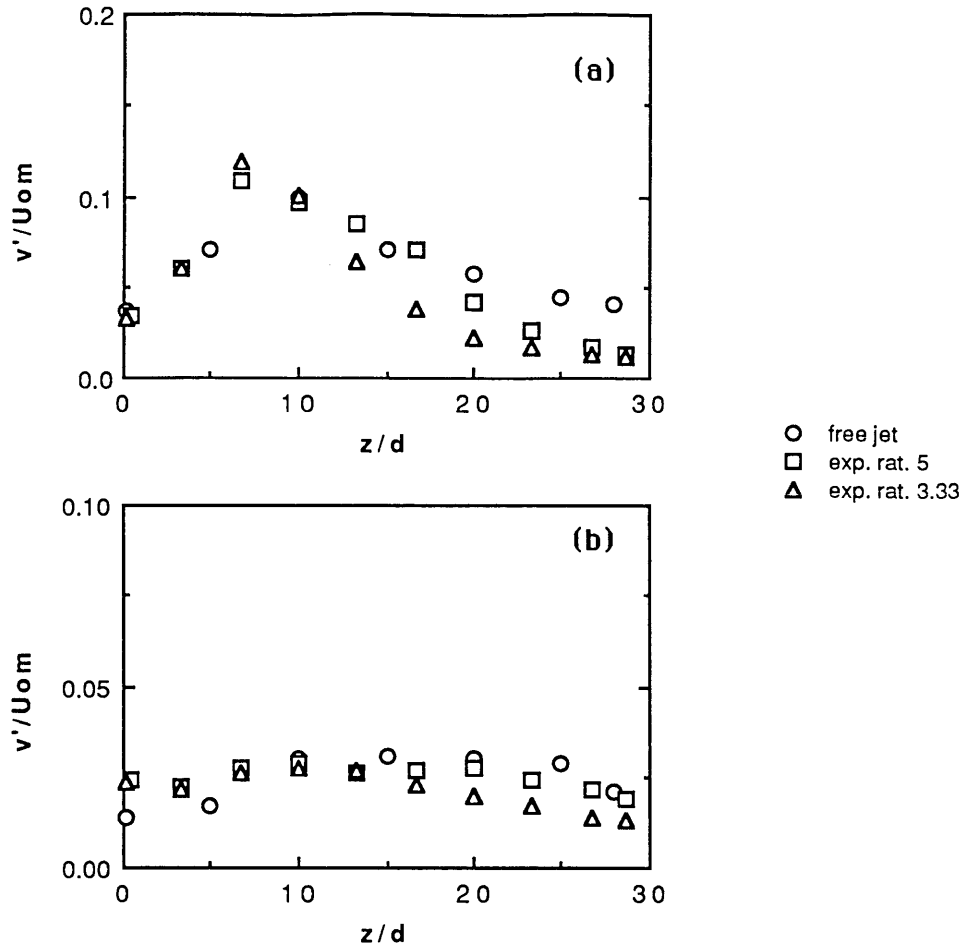


FIGURE 4.34 Centreline profiles of radial rms velocity of (a) single phase and (b) 40 μm beads, 13% mass loading in the free jet (circle), sudden expansion ratio of 5 (triangle) and 3.33 (square).

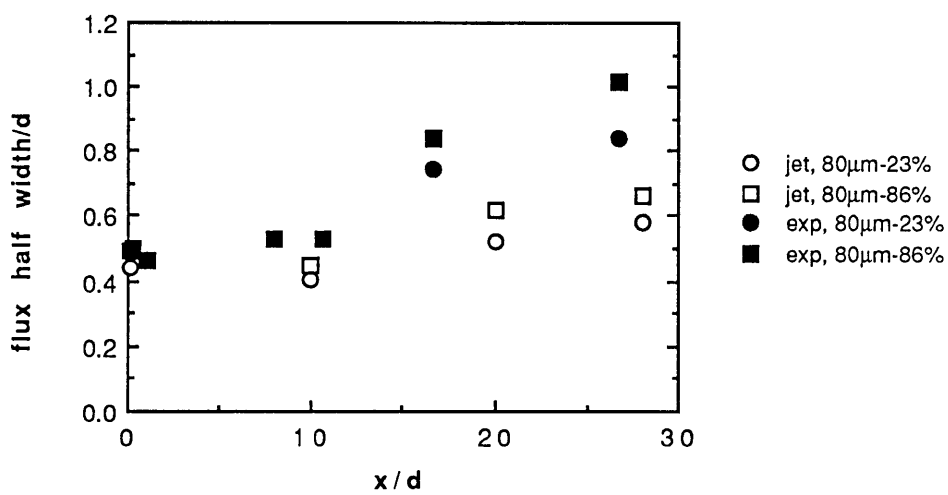
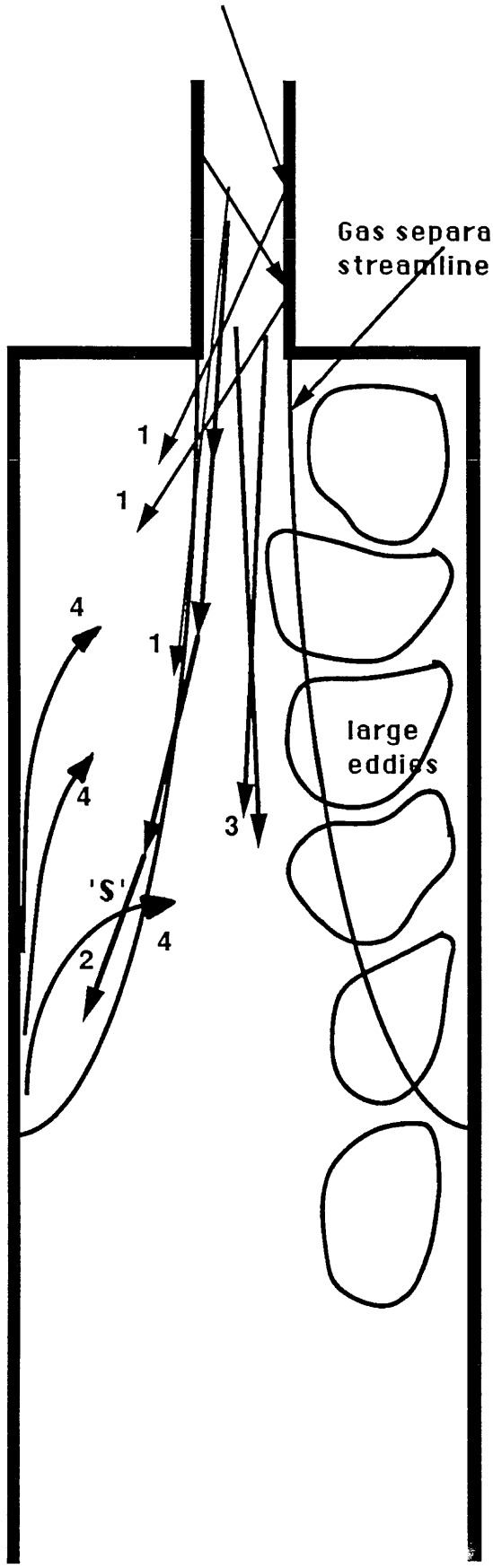


FIGURE 4.35 Flux half width of 80 μm beads for 23 (circle) and 86% (square) mass loadings in the free jet (open symbols) and sudden expansion ratio of 3.33 (closed symbols).



Trajectories :

1 : beads bouncing on the wall of the small tube

2 : beads interacting with the large eddies of the flow

3 : beads responsible for the large axial rms of the beads on the centreline

4 : beads dispersing in the recirculation zone after reaching the wall of the large tube

Point 'S' has a bimodal time average velocity distribution

FIGURE 4.36 Sketch showing the way the beads disperse into the recirculation zone. Page 260 explains the sketch.

CHAPTER 5

CLOSURE TO THE THESIS

5.1 Achievements and Conclusions

The following paragraphs refer to the main findings of the thesis and thereby indicate the way in which the investigation has advanced the understanding of the physics of two phase flows. Contributions have been made in two areas : the instrumentation for the study of two phase flows and the experimental investigation of two simple particle-laden gas flows, a free round jet and a round sudden step expansion. Detailed information concerning the findings and conclusions has been summarised at the end of each chapter and is not repeated here. Section 5.2 puts forward suggestions for further work in both areas.

a) Instrumentation for two phase flows.

The potential of the phase Doppler technique for simultaneous particle size and velocity measurements has been investigated as a part of this thesis. The technique, which was suggested by Durst and Zaré (1975), is based on the phase shift existing between two Doppler signals observed at different positions in space. The theoretical background has been studied and the experimental verification of the theory was established. An instrument based on this sizing principle has been built using the transmission optics of a laser Doppler anemometry and collecting light at three different positions in space using three photodetectors. The signal processing was based on a zero crossing counter, which measures the frequency of the Doppler signal generated by a particle present in the probe volume and the phase shift existing between laser Doppler signals observed at different positions in space.

The relation between phase shift and particle size has been estimated from analysis of light scattering based on geometrical optics and the phase shift between two Doppler signals found to be linearly related to particle size, except for particles smaller than around 10 μm. The main advantages over previous techniques, such as the amplitude and the visibility of the Doppler signal, are the insensitivity

to the turbidity of the flow, the ability to measure size-velocity correlation in high number density two phase flows and the independence of the theoretically calculated calibration curve to the conditions during the measurement (such as beams passing through optical windows or the power of incident laser beams). The only disadvantage is its limitation to the sizing of spherical particles.

The effects of the beam intersection angle, the collection angle and particle refractive index have been quantified. The collection optics were positioned at an angle of 30° off axis in the forward direction for the applications presented here, which was ideal for detection of the refraction part of the scattered light, although collection in the backscatter and sidescatter direction was examined as well. Finally, it has been shown that the technique can be used to measure the gas phase in the presence of glass beads, although with a cross talk from the beads, which was quantified as around 7% of the total measurements of beads during the sampling time.

The phase-Doppler technique has been used here for the measurement of simple laboratory particle-laden gas flows, but it has the potential to measure particle size and velocity under difficult conditions in industrial applications.

b) Physics of two phase flows.

Experiments have been carried out in a particle-laden free jet and round sudden step expansion using the phase-Doppler instrument. The parameters of interest for the aerodynamic behaviour of the beads are the particle size and the mass loading. Both parameters influence the velocity characteristics of the beads and the gas phase in the presence of the beads. Measurements of the mean and variance of the axial and radial velocity and the correlation coefficient were taken for the single phase fluid and the 40, 80 and 200 μm beads at various mass loadings, while the gas phase was measured only in the presence of the 80 μm beads.

The behaviour of the beads has been analysed in terms of the Stokes number, which is defined as the ratio of the relevant gas flow timescale to the particle relaxation time. It was found that for small values of the turbulent Stokes number of the flow, entailing a very small response of the beads to the gas phase turbulence, a large anisotropy exists between the velocity r.m.s. fluctuation of the beads in

the axial and the radial direction. The initial conditions of the beads were found to be very important for the development of the beads' velocity characteristics downstream, as their inertia makes them maintain their conditions for longer periods of time than the gas. A "fan spreading" model for the dispersion of the beads explains how small response of the beads to the gas phase turbulence can result in large axial r.m.s. fluctuations of the beads, while their radial r.m.s. fluctuation remains very small. This interpretation is important to those trying to evaluate complicated models for the prediction of the behaviour of the dispersed phase in situations where this complexity is not needed and their models are not properly validated.

In the round sudden step expansion, the influence of the expansion ratio has been examined in addition to the particle size and mass loading parameters. The modification of the expansion ratio changes the timescales of the flow and this is important for the dispersion of the beads in the reverse flow region. Both the 40 and 80 μm beads enter the recirculation zone existing downstream of the step in the expansion flow with ratio of 5, while the 80 μm beads do not enter the recirculation zone when the expansion ratio is 3.33. The 200 μm beads do not enter the reverse flow region in either expansion ratio flow. The relative importance of three processes, namely transit time of the beads along the reattachment length, the centrifugal forces on the beads due to the streamline curvature and the turbulent timescale of the flow, has been found to be responsible for the dispersion of the particles in the recirculation zone. The "fan spreading" model is valid here also and explains the large anisotropy existing between the axial and radial r.m.s. fluctuation of the beads at the neighbourhood of the separation streamline.

The effect of the particles on the gas phase is more pronounced as the mass loading increases and the interaction between the gas and the particles becomes "two way". The mean axial velocity of the gas phase is modified due to the momentum transfered from the particles to the gas and is larger relative to the single phase at the centre and lower at the edge of the jet or close to the wall of the downstream tube at the expansion flow. The gas turbulence characteristics are modified and the influence varies at different locations in the flow and turbulence is reduced close to the nozzle and increased farther downstream for both examined flows.

The experimental results are valuable for comparison to the predictions of the flows as there are only few measurements available in two phase flows and especially in recirculating flows. The fan spreading model suggested for the dispersion of the particles and the modification of the gas phase characteristics may have implications for the two phase flow modelling.

5.2 Recommendations for further work.

The need for reliable instrumentation for simultaneous size-velocity measurements in two phase flows has always been a drawback to the understanding of the physics of two phase flows. The contribution of this thesis on the instrumentation opens possibilities for research in two phase flows, with the limitation that the particles involved should be spherical. Some practical applications ideal for the technique are the liquid fuel gas turbine combustors or the Diesel and petrol injection internal combustion engines where it can provide results to check the performance of the injectors, to establish the aerodynamic behaviour of droplets in complex flows and to study the droplet evaporation and combustion.

Further information about the performance of the technique in the backscatter direction is required, in order to measure in flows where access in the forward direction is impossible, e.g. measurements in the flame of a large furnace. Also, the extension of the technique to size spherical particles using the reflection part of scattered light by collecting light at sidescatter direction is useful for many applications. For example, bubbles scatter mainly reflected light from their surface and their size is important for cavitation studies and for chemical processes studies (electrolysis).

The measurement of the flux and concentration of the dispersed phase is important and its accuracy when measured by the phase-Doppler technique should be evaluated. However, zero-crossing counters reject noisy signals due to the frequency validation scheme and this can affect the accuracy of the flux and concentration measurements. For this reason, instruments measuring the frequency and the phase by fast Fourier transform techniques, which can measure in low signal-to-noise ratio situations (Lading et al, 1988), may be useful if they can measure fast enough. Further research is

needed on the development of such instruments and their performance to be evaluated.

The technique might be extended to size non-spherical particles by collecting light in forward direction close to the axis, where the diffraction part of the scattered light, which is independent of the shape of the particles, is dominant. The phase Doppler technique can be thought as an extension of the visibility technique (Bachalo, 1980). The visibility technique based on diffraction is valid in forward scatter (Farmer, 1972), so that the phase of the diffraction part of the scattered light (Jones, 1974), which is either 0° or 180°, is related to particle size and the 'mask-space ratio' pattern might give information on the size of the particles. The only question is whether the number of photodetectors needed to resolve the spatial pattern of phase (0° or 180°) is sufficiently small to be realistic.

Turning to the physics of two phase flows, the limitations of the "fan spreading" model should be established and requires an experimental investigation of jet flows with exit mean Stokes number of the order of unity and turbulent Stokes number around unity. The application of the model to more complicated flows and its application to the prediction of the behaviour of the particles there should be examined.

The velocity characteristics of the particles at the exit of the upstream pipe were found to be important for their behaviour downstream. It is unlikely that in any practical application the initial conditions will be known and it is quite common for the dispersed phase to be injected into the flow from a pipe. The understanding of the flow of particles within a pipe flow would be important for the prediction of the pipe exit flow and hence for the flow downstream. It has been argued in chapters 3 and 4 that the beads acquire similar radial r.m.s. fluctuations, v'_b, to the gas at the exit of the upstream pipe due to their bouncing on the wall of the pipe rather than response to the gas turbulence. Investigations in pipe flows, such as Tsuji et al (1982) & (1984) and Govan et al (1989), support the above arguments. However, the effect of the flow Reynolds number, the length and the diameter of the pipe on the behaviour of the particles is not clear and should be investigated in the future.

In the discussion of chapter 4 it was argued that the bimodality of the velocity p.d.f. of the beads in regions of the sudden step

expansion flow is due to the presence of large scale structures in the shear layer and in the vicinity of the stagnation point and the existence of such structures in the neighbourhood of recirculating flows has been reported by many workers (e.g. Schefer et al, 1987 for a bluff body combustor). This behaviour of the particles should be examined in other recirculating flows, such as swirl stabilised burner arrangements. Since the dispersion of particles into the recirculation zone is important for stable combustion of liquid and solid fuels and is sometimes due to the larger scales of the flow (Chung and Troutt, 1988 and Kamalu et al, 1989), the turbulent length scales of the gas flow in the vicinity of the recirculation zone and the stagnation point should be investigated by two point correlation measurements because this will lead to better modelling of the continuous phase.

For flows with mean exit Stokes number smaller than unity a mean slip exists between the gas and the particles, so that the modification of the gas mean axial velocity influences the gas phase turbulence and it is difficult to show the influence of the presence of the particles on the gas turbulence. It has been argued here that the increase of the gas phase turbulence far from the jet nozzle was because of the production of turbulence by the increased mean rate of strain, $\frac{\partial U_f}{\partial r}$. In order to avoid this effect and establish the net influence of the presence of the particles on the turbulence of the continuous phase, measurements are needed in jets where there is no mean slip between the particles and the continuous phase. This seems possible only in dispersed two phase flows with exit mean Stokes number around unity which affects also the turbulent Stokes number and it can be found by using equation (B.8) in Appendix 3.B that an exit mean Stokes number $S_e \approx 2$ gives a turbulent Stokes number S_t around unity at a distance of 10 nozzle diameters from the exit of the jet. However, such an experiment should be carefully planned so that the upstream pipe is long enough to avoid a lag between the particles and the continuous phase at the nozzle of the jet.

The suggestions for further work, as well as the work of this thesis, reflect the opinion that carefully selected instrumentation for experiments in simple flow configurations can achieve an engineering understanding of turbulent flows and suggest ways for better mathematical modelling.

LIST OF REFERENCES

ABBOTT D.E., KLINE S.J., 1962
Experimental investigation of subsonic turbulent flow over single and double backward facing steps.
J. Basic Engineering, 84, 317 - 325.

Al-CHALABI S.A.M., HARDALUPAS Y., JONES A.R., TAYLOR A.M.K.P., 1987
Calculation of calibration curves for the phase Doppler technique: comparison between Mie theory and geometrical optics.
In Optical particle sizing. Theory and practice (ed. G. Gouesbet and G. Grehan), 107 - 120, New York : Plenum Press.

AL TAWEEL A.M., LANDAU J., 1977
Turbulence modulation in two-phase jets.
Int. J. Multiphase Flow, 3, 341 - 351.

ALIOD R., DOPAZO C., 1987
Modelling and numerical computation of turbulent axisymmetric jets containing dilute suspensions of solid particles.
In Proceedings of the sixth International Symposium on Turbulent Shear Flows, paper 21.2, Toulouse.

ALLANO D., GOUESBET G., GREHAN G., LISIECKI D., 1984
Droplet sizing using a top-hat laser beam technique.
J. Phys. D: Appl. Phys., 17, 43-58.

ALTGELD H., SCHNETTLER A., STEHMEIER D., 1980
Spark discharge particle generator for laser Doppler anemometry.
J. Phys. E: Sci. Instrum., 13, 437 - 441.

ARMALY B.F., DURST F., PEREIRA J.C.F., SCHONUNG B., 1983
Experimental and theoretical investigation of backward-facing step flow.
J. Fluid Mech., 127, 473 - 496.

BACHALO W.D., HESS C.F., HARTWELL C.A., 1979
An instrument for spray droplet size and velocity measurements.
ASME paper no. 79-WA/GT-13, Gas Turbine Division, Winter Annual Meeting, New York, Dec. 2-7, 1979.

BACHALO W.D., 1980
Method for measuring the size and velocity of spheres by dual-beam light scatter interferometry.
Appl. Opt., 19, 363 - 370.

BACHALO W.D., HOUSER M.J., 1984
Phase/Doppler spray analyser for simultaneous measurements of drop size and velocity distributions.
Optical Eng., 23, 583 - 590.

BACHALO W.D., HOUSER M.J., SMITH J.N., 1986
Evolutionary behaviour of sprays produced by pressure atomisers.
AIAA paper no. 86-0296, 24th Aerospace Sciences Meeting, Jan. 6-9, Reno, Nevada.

BACHALO W.D., 1987
The evolution of particle size and velocity measurement technology.
Proceedings of 2nd International Conference on Laser Anemometry - Advances and Applications, Paper I4, Sept. 21-23, Strathclyde, UK.

BACHALO W.D., RUDOFF R.C., BRENA DE LA ROSA A., 1988
Mass flux measurements of a high number density spray system using the phase Doppler particle analyser.
AIAA paper no. 88-0236, 26th Aerospace Sciences Meeting, Jan. 11-14, Reno, Nevada.

BACHALO W.D., SANKAR S.V., 1988
Analysis of the light scattering interferometry for spheres larger than the light wavelength.
Proceedings of the Fourth International Symposium on Applications of Laser Anemometry to Fluid Mechanics, paper 1.8, Lisbon.

BATCHELOR G.K., 1971
The stress generated in a non-dilute suspension of elongated particles by pure straining motion.
J. Fluid Mech., 46, 813 - 829.

BATCHELOR G.K., 1982
The theory of homogeneous turbulence.
Cambridge University Press, paperback edition.

BAUCKHAGE K., FLOEGEL H.H., 1984
Simultaneous measurement of droplet size and velocity in nozzle sprays.
Proceedings of the Second International Symposium on Applications of Laser Anemometry to Fluid Mechanics, paper 18.1, Lisbon.

BOERNER Th., DURST F., MANERO E., 1986
LDV measurements of gas-particle confined jet flow and digital processing.
Proceedings of the Third International Symposium on Applications of Laser Anemometry to Fluid Mechanics, paper 4.5, Lisbon.

BOOTHROYD R.G., 1967
Turbulence characteristics of the gaseous phase in duct flow of a suspension of fine particles.
Trans. Instn. Chem. Engrs., 45, T297 - T310.

BOOTHROYD R.G., 1971
Flowing gas-solids suspensions.
Chapman and Hall, London.

BRADSHAW P., WONG F.Y.F., 1972
The reattachment and ralaxation of a turbulent shear layer.
J. Fluid Mech., 52, 113 - 135.

BUCHHAVE P., GEORGE Jr. W.K., LUMLEY J.L., 1979
The measurement of turbulence with the Laser-Doppler Anemometer.
Annual Review Fluid Mechanics, 11, 443 - 503.

CALABRESE R.V., MIDDLEMAN S., 1979
The dispersion of discrete particles in a turbulent fluid field.
AIChE J., 25, 1025 - 1035.

CAPP S.P., 1983
Experimental investigation of the turbulent axisymmetric jet.
PhD Dissertation, University of Buffalo, State University of New York.

CARLSON C.R., PESKIN R.L., 1975
One dimensional particle velocity probability densities measured in turbulent gas-particle duct flow.
Int. J. Multiphase Flow, 2, 67 - 78.

CHAO B.T., 1964
Turbulent transport behaviour of small particles in dilute suspension.
Osterreichisches Ingenieur-Archiv., 18, 7 - 21.

CHERDRON W., DURST F., WHITELAW J.H., 1978
Asymmetric flows and instabilities in symmetric ducts with sudden expansions.
J. Fluid Mech., 84, 13 - 31.

CHUNG J.N., TROUTT T.R., 1988
Simulation of particle dispersion in an axisymmetric jet.
J. Fluid Mech., 186, 199 - 222.

CLIFT R., GRACE J.R., WEBER M.E., 1978
Bubbles, Drops and Particles.
Academic Press, London.

CSANADY G.T., 1963
Turbulent diffusion of heavy particles in the atmosphere.
J. Atmos. Sci., 20, 201 - 208.

DODGE L.G., RHODES D.J., REITZ R.D., 1987
Drop-size measurement techniques for sprays : comparison of Malvern laser-diffraction and Aerometrics phase/Doppler.
Appl. Opt., 26, 2144 - 2154.

DRING R.P., SUO M., 1978
Particle trajectories in swirling flows.
J. Energy, 2, 232 - 237.

DURST F., 1973
Scattering phenomena and their application in optical anemometry.
J. Appl. Math. and Phys. (ZAMP), 24, 619 - 643.

DURST F., ELIASSON B., 1974
Properties of laser Doppler signals and their exploitation for particle size measurements.
In The Accuracy of flow measurements by Laser Doppler methods, 457 - 477. Skovlunde: Proceedings LDA Symposium, Copenhagen.

DURST F., ZARE M., 1975
Laser Doppler measurements in two phase flows.
In The Accuracy of flow measurements by Laser Doppler methods, 403 - 429. Skovlunde: Proceedings LDA Symposium, Copenhagen.

DURST F., UMHAUER H., 1975
Local measurements of particle velocity, size distribution and concentration with a combined laser Doppler particle sizing system.
In The Accuracy of flow measurements by Laser Doppler methods, 430 - 456. Skovlunde: Proceedings LDA Symposium, Copenhagen.

DURST F., 1978
Studies of particle motion by laser Doppler techniques.
In Dynamic Measurements in Unsteady Flows, 345 - 372. Proceedings of the Dynamic Flow Conference, Marseille, Sept. 11-14, Baltimore, Sept. 18-21, 1978.

DURST F., MELLING A., WHITELAW J.H., 1981
Principles and practice of Laser-Doppler anemometry.
2nd edition, London: Academic Press.

DURST F., MILOJEVIC D., SCHONUNG B., 1984
Eulerian and Lagrangian predictions of particulate two-phase flows : a numerical study.
Appl. Math. Modelling, 8, 101 - 115.

ETHERIDGE D.W., KEMP P.H., 1978
Measurements of turbulent flow downstream of a rearward-facing step.
J. Fluid Mech., 86, 545 - 566.

FARMER M.W., 1972
Measurement of particle size, number density and velocity using a laser interferometer.
Appl. Opt., 11, 2603 - 2612.

FARMER M.W., 1974
Observation of large particles with a laser interferometer.
Appl. Opt., 13, 610 - 622.

FARMER M.W., 1976
Sample space for particle size and velocity measuring interferometers.
Appl. Opt., 15, 1984 - 1989.

FARMER M.W., 1978
Measurement of particle size and concentrations using LDV techniques.
In Dynamic Measurements in Unsteady Flows, 373 - 396. Proceedings of the Dynamic Flow Conference, Sept. 11-14, Marseille, Sept. 18-21, Baltimore.

FARMER M.W., 1980
Visibility of large spheres observed with a laser velocimeter : a simple model.
Appl. Opt., 19, 3660 - 3667.

FRISTROM R.M., JONES A.R., SCHWAR M.J.R., WEINBERG F.J., 1973
Particle sizing by interference fringes and signal coherence in Doppler velocimetry.
Faraday Symposia of the Chemical Society, 7, 183 - 197.

FUCHS N.A., 1964
The Mechanics of Aerosols.
Oxford: Pergamon Press. Revised and Enlarged Edition.

GLANTSCHNIG W.J., CHEN S.H., 1982
Light scattering from water droplets in the geometrical optics approximation.
Appl. Opt., 20, 2499 - 2509.

GLASS M., KENNEDY I.M., 1977
An improved seeding method for high temperature laser Doppler velocimetry.
Comb. and Flame, 29, 333 - 335.

GIBSON M.M., 1963
Spectra of turbulence in a round jet.
J. Fluid Mech., 15, 161 - 173.

GOLDSCHMIDT V.W., ESKINAZI S., 1966
Two-phase turbulent flow in a plane jet.
ASME, J. Appl. Mech., 33, 735 - 747.

GOLDSCHMIDT V.W., HOUSEHOLDER M.K., AHMADI G., CHUANG S.C., 1972
Turbulent diffusion of small particles suspended in turbulent jets.
Progr. in Heat and Mass Transfer, 6, 487 - 508.

GOSMAN A.D., IOANNIDES E., 1983
Aspects of computer simulation of liquid fueled combustors.
AIAA J. Energy, 7, 482 - 490.

GOVAN A.H., HEWITT G.F., NGAN C.F., 1989
Particle motion in a turbulent pipe flow.
Int. J. Multiphase Flow, 15, 471 - 481.

GREHAN G., GOUESBET G., RABASSE C., 1981
Monotonic relationships between scattered powers and diameters in Lorentz-Mie theory for simultaneous velocimetry and sizing of single particles.
Appl. Opt., 20, 796 - 799.

HAGHGOOIE M., KENT J.C., TABACZYNSKI R.J., 1986
Verification of LDA and seed generator performance.
Exp. in Fluids, 4, 27 - 32.

HARDALUPAS Y., 1986
Phase-Doppler anemometry for simultaneous particle size and velocity measurements.
Report FS/86/14, Fluids Section, Department of Mechanical Engineering, Imperial College, London.

HARDALUPAS Y., TAYLOR A.M.K.P., WHITELAW J.H., 1986a
Depth of field considerations in particle sizing using the phase-Doppler technique.
Proceedings of the Third International Symposium on Applications of Laser Anemometry to Fluid Mechanics, paper 18.4, Lisbon.

HARDALUPAS Y., TAYLOR A.M.K.P., WHITELAW J.H., 1986b
Two phase annular flow.
9th Australasian Fluid Mechanics Conference, 238 - 242, Auckland, New Zealand, Dec. 8-12, 1986.

HARDALUPAS Y., TAYLOR A.M.K.P., WHITELAW J.H., 1988
Measurements in heavily-laden dusty jets with phase-Doppler anemometry.
In Transport phenomena in Turbulent Flows - Theory, Experiment and Numerical simulation (ed. M. Hirata and N. Kasagi), 821 - 835. Washington D.C.: Hemisphere Publishing Corporation.

HARDALUPAS Y., TAYLOR A.M.K.P., 1989
On the measurement of particle concentration near a stagnation point.
Exp. in Fluids (in the press).

HEITOR M.V., LAKER J.R., TAYLOR A.M.K.P., VAFIDIS C., 1984
Instruction manual for the FS "model 2" Doppler-frequency counter.
Report FS/84/10, Fluids Section, Department of Mechanical Engineering, Imperial College, London.

HESS C.F., 1984a
Nonintrusive optical single-particle counter for measuring the size and velocity of droplets in a spray.
Appl. Opt., 23, 4375 - 4382.

HESS C.F., ESPINOSA V.E., 1984
Spray characterisation with a nonintrusive technique using absolute scattered light.
Optical Eng., 23, 604 - 609.

HESS C.F., 1984b
A technique combining the visibility of a Doppler signal with the peak intensity of the pedestal to measure the size and velocity of droplets in a spray.
AIAA paper no. 84-0203, AIAA 22nd Aerospace Sciences Meeting, Reno, Nevada, January 9-12, 1984.

HESS C.F., LI F., 1986
Particle sizing with intensity ratioing in laser velocimetry.
Proceedings of the Third International Symposium on Applications of Laser Anemometry to Fluid Mechanics, paper 22.2, Lisbon.

HIRLEMAN E.D., 1978
Laser techniques for simultaneous particle-size and velocity measurements.
Optics Letters, 3, 19 - 21.

HIRLEMAN E.D., MOON H.K., 1982
Response characteristics of the Multiple-Ratio Single-Particle Counter.
J. Colloid and Interf. Sci., 87, 124 - 139.

HIRLEMAN E.D., OECHSLE V., CHIGIER N.A., 1984
Response characteristics of laser diffraction particle size analysers : optical sample volume extent and lens effect.
Optical Eng., 23, 610 - 619.

HISHIDA K., MAEDA M., IMARU J., HIRONAGA K., KANO H., 1982
Measurements of size and velocity of particle in two-phase flow by a three beam LDA system.
Proceedings of the First International Symposium on Applications of Laser Anemometry to Fluid Mechanics, paper 5.6, Lisbon.

HOLVE D., SELF S.A., 1979a
Optical particle sizing for in situ measurements. Part 1.
Appl. Opt., 18, 1632 - 1645.

HOLVE D., SELF S.A., 1979b
Optical particle sizing for in situ measurements. Part 2.
Appl. Opt., 18, 1646 - 1652.

HOLVE D., 1986
In situ measurements of flyash formation from pulverised coal.
Comb. Sci. and Tech., 44, 269 - 288.

HONG N.S., JONES A.R., 1976
A light scattering technique for particle sizing based on laser fringe anemometry.
J. Phys. D: Appl. Phys., 9, 1839 - 1848.

HOUSEHOLDER M.K., GOLDSCHMIDT V.W., 1969
Turbulent diffusion and Schmidt number of particles.
J. Engineering Mechanics Division, ASCE, EM6, 1345-1367.

HOUSER M.J., 1980
Particle field diagnostics : applications of intensity ratioing, interferometry and holography.
Optical Eng., 19, 873 - 877.

HUMPHRIES W., VINCENT J.H., 1976
An experimental investigation of the detention of airborne smoke in the wake bubble behind a disk.
J. Fluid Mech., 73, 453 - 464.

HUMPHRIES W., VINCENT J.H., 1978
The transport of airborne dusts in the near wakes of bluff bodies.
Chemical Engineering Science, 33, 1141 - 1146.

JONES A.R., 1974
Light scattering by a sphere situated in an interference pattern, with relevance to fringe anemometry and particle sizing.
J. Phys. D: Appl. Phys., 7, 1369 - 1376.

JONES A.R., 1987
Fraunhofer diffraction by random irregular particles.
In Optical particle sizing. Theory and practice (ed. G. Gouesbet and G. Grehan), New York : Plenum Press.

KAMALU N., TANG L., TROUTT T.R, CHUNG J.N., CROWE C.T., 1989
Particle dispersion in developing shear layers.
In the proceedings of the International Conference on Mechanics of Two-Phase Flows, (ed. Lee S.L., Durst F.), 199 - 202, National Taiwan University, Taipei, Taiwan, June 12 - 15, 1989.

KLIAFAS Y., TAYLOR A.M.K.P., WHITELAW J.H., 1986
Errors due to turbidity in particle sizing using laser Doppler velocimetry.
In Gas-Solid Flows (ed. J.T. Jurewicz), 41 - 52. Fluids Engineering Division, ASME vol 35: AIAA/ASME 4th Fluid Mechanics, Plasma Dynamics and Lasers conference, Atlanta, Georgia.

KLIAFAS Y., TAYLOR A.M.K.P., WHITELAW J.H., 1987
Errors in particle sizing by LDA due to turbidity in the incident beams.
Exp. in Fluids, 5, 159 - 176.

KRIEBEL A.R., 1961
Particle trajectories in a gas centrifuge.
J. Basic Engineering, September 1961, 333 - 340.

LAATS M.L., FRISHMAN F.A., 1970
Scattering of an inert admixture of different grain size in a two-phase axisymmetric jet.
Heat Transfer - Soviet Res., 2, 7.

LADING L., ANDERSEN K., 1988
A covariance processor for velocity and size measurements.
Proceedings of the Fourth International Symposium on Applications of Laser Anemometry to Fluid Mechanics, paper 4.8, Lisbon.

LEVY Y., LOCKWOOD F.C., 1981
Velocity measurements in a particle laden turbulent free jet.
Comb. and Flame, 40, 333 - 339.

LIGHTFOOT N.S., NEGUS C.R., 1986
Comparison of the visibility and phase particle sizing techniques and their applications to fuel sprays.
Proceedings of the Third International Symposium on Applications of Laser Anemometry to Fluid Mechanics, paper 20.4, Lisbon.

LILLY G.P., 1973
Effect of particle size on particle eddy diffusivity.
Ind. Eng. Chem. Fundam., 12, 268 - 275.

LUMLEY J.L., 1978
Two phase and non-newtonian flows.
In Turbulence (ed. P. Bradshaw), 289 - 324. Berlin: Springer Verlag. Second Edition.

MAEDA M., HISHIDA K., SEKINE M., WATANABE N., 1986
Measurements of spray jet using LDV system with particle size discrimination.
Proceedings of the Third International Symposium on Applications of Laser Anemometry to Fluid Mechanics, paper 20.3, Lisbon.

MARTIN W.M., ADBELMESSIH A.H., LISKA J.J., DURST F., 1981
Characteristics of laser-Doppler signals from bubbles.
Int. J. Multiphase Flow, 7, 439 - 460.

McCOMP W.D., SALIH S.M., 1977
Measurement of normalised radial concentration profiles in a turbulent aerosol jet, using a laser Doppler anemometry.
J. Aerosol Sci., 8, 171 - 181.

McCOMP W.D., SALIH S.M., 1978
Comparison of some theoretical concentration profiles for solid particles in a turbulent jet with the results of measurements using a laser Doppler anemometry.
J. Aerosol Sci., 9, 299 - 313.

McCREATH C.G., CHIGIER N.A., 1973
Liquid-spray burning in the wake of a stabiliser disc.
In Fourteenth Symposium (International) on Combustion, 1355 - 1363. The Combustion Institute.

McDONELL V.G., WOOD C.P., SAMUELSEN G.S., 1986
A comparison of spatially resolved drop size and drop velocity measurements in an isothermal chamber and a swirl-stabilised combustor.
In Twenty-first Symposium (International) on Combustion, 685 - 694. The Combustion Institute.

McLAUGHLIN D.K., TIEDERMAN W.G., 1973
Biasing correcting for individual realisation of laser anemometer measurements in turbulent flows.
Phys. Fluids, 16, 2082 - 2088.

MEEK C.C., JONES B.G., 1973
Studies of the behaviour of heavy particles in a turbulent fluid flow.
J. Atmos. Sci., 30, 239 - 244.

MELLING A., WHITELAW J.H., 1975
Turbulent flow in a rectangular duct.
J. Fluid Mech., 78, 289 - 315.

MELVILLE W.K., BRAY K.N.C., 1979a
The two phase turbulent jet.
Int. J. Heat Mass Transfer, 22, 279 - 287.

MELVILLE W.K., BRAY K.N.C., 1979b
A model of the two phase turbulent jet.
Int. J. Heat Mass Transfer, 22, 647 - 656.

MEN A., KRIMERMAN Y., ADLER D., 1981
A new method of simultaneous particle sizing and two-component velocity measurement.
J. Phys. E: Sci. Instrum., 14, 747 - 751.

MIZUTANI Y., KODAMA H., MIYASAKA K., 1982
Doppler-Mie combination technique for determination of size-velocity correlation of spray droplets.
Comb. and Flame, 44, 85 - 95.

MODARRESS D., WUERER J., ELGHOBASHI S., 1982
An experimental study of a turbulent round two-phase jet.
AIAA paper no. 82-0964, AIAA/ASME 3rd Joint Thermophysics Fluids, Plasma and Heat Transfer Conference, St. Louis, Missouri, June 7 - 11 1982.

MODARRESS D., TAN H., 1983
LDA signal discrimination in two phase flows.
Exp. in Fluids, 1, 1 - 6.

MODARRESS D., TAN H., ELGHOBASHI S., 1984
Two component LDA measurement in a two-phase turbulent jet.
AIAA J., 22, 624 - 630.

MOSTAFA A.A., MONGIA H.C., McDONELL V.G., SAMUELSEN G.S., 1987
On the evolution of particle-laden jet flows : A theoretical and experimental study.
AIAA paper no. 87-2181. AIAA/SAE/ASME/ASEE 23rd Joint Propulsion Conference, San Diego, California, Jun. 29 - Jul. 2.

NAKATANI N., KOHRI S., YAMADA T., SAKABE T., 1987
Particle size and velocity measurements by the laser multifocus method using a phase-diffraction grating.
Proceedings of the 4th symposium on Flow Measurements, Osaka, 91 - 97.

NAKATANI N., KOHRI S., YAMADA T., 1987
Private communication on Particle size and velocity measurements by the phase LMF (Laser Multifocus) method, Nov. 7, 1987.

NEGUS C.R., DRAIN L.E, 1982
Mie calculations of the scattered light from a spherical particle traversing a fringe pattern produced by two intersecting laser beams.
J. Phys. D: Appl. Phys., 15, 375 - 402.

NIR A., PISMEN L.M., 1979
The effect of steady drift on the dispersion of a particle in turbulent fluid.
J. Fluid Mech., 94, 369 - 381.

OWEN P.R., 1969
Pneumatic Transport.
J. Fluid Mech., 39, 407 - 432.

PENDLETON J.D., 1982
Mie and refraction theory comparison for particle sizing with the laser velocimetry.
Appl. Opt., 21, 684 - 688.

PISMEN L.M., NIR A., 1978
On the motion of suspended particles in stationary homogeneous turbulence.
J. Fluid Mech., 84, 193 - 206.

POPPER J., ABUAF N., HETSRONI G., 1974
Velocity measurements in a two-phase turbulent jet.
Int. J. Multiphase Flow, 1, 715 - 726.

REEKS M.W., 1977
On the dispersion of small particles suspended in an isotropic turbulent fluid.
J. Fluid Mech., 83, 529 - 546.

RICOU F.P., SPALDING D.B., 1961
Measurements of entrainment by axi-symmetric turbulent jets.
J. Fluid Mech., 11, 21 - 32.

ROBERTS D.W., BRASIER C.W., BOMAR B.W., 1979
Use of a particle sizing interferometer to study water droplet size distribution.
Optical Eng., 18, 236 - 242.

RODI W., 1975
A review of experimental data of uniform density free turbulent boundary layers.
In Studies in Convection. Theory, Measurement and Applications, (ed. B.E. Launder), 79 - 165, Academic Press, London.

RUCK B., MAKIOLA B., 1988
Particle dispersion in a single-sided backward-facing step flow.
Int. J. Multiphase Flow, 14, 787 - 800.

SAFFMAN M., BUCHHAVE P., TANGER H., 1984
Simultaneous measurement of size, concentration and velocity of spherical particles by a laser Doppler method.
Proceedings of the Second International Symposium on Applications of Laser Anemometry to Fluid Mechanics, paper 8.1, Lisbon.

SAFFMAN M., 1986
The use of polarised light for optical particle sizing.
Proceedings of the Third International Symposium on Applications of Laser Anemometry to Fluid Mechanics, paper 18.2, Lisbon.

SAFFMAN M., 1987
Automatic calibration of LDA measurement volume size.
Appl. Opt., 26, 2592 - 2597.

SCHEFER R.W., NAMAZIAN M., KELLY J., 1987
Velocity measurements in a turbulent nonpremixed bluff-body stabilised flame.
Comb. Sci. Technol., 56, 101 - 138.

SHIH T.H., LUMLEY J.L., 1986
Second-order modelling of particle dispersion in a turbulent flow.
J. Fluid Mech., 163, 349 - 363.

SHUEN J.S., SOLOMON A.S.P., ZHANG Q.F., FAETH G.M., 1985
Structure of particle laden jets : measurements and predictions
AIAA J., 23, 396 - 404.

SHUEN J.S., SOLOMON A.S.P., FAETH G.M., 1986
Drop-turbulence interactions in a diffusion flame.
AIAA J., 24, 101 - 108.

SNYDER W.H., LUMLEY J.L., 1971
Some measurements of particle velocity autocorrelation functions in a turbulent flow.
J. Fluid Mech., 48, 41-71.

SOLOMON A.S.P., SHUEN J.S., ZHANG Q.F., FAETH G.M., 1985a
Measurements and predictions of the structure of evaporating sprays.
J. Heat Transfer, 107, 679 - 686.

SOLOMON A.S.P., SHUEN J.S., ZHANG Q.F., FAETH G.M., 1985b
Structure of nonevaporating sprays, part I : initial conditions and mean properties.
AIAA J., 23, 1548 - 1555.

SOLOMON A.S.P., SHUEN J.S., ZHANG Q.F., FAETH G.M., 1985c
Structure of nonevaporating sprays, part II : drop and turbulence properties.
AIAA J., 23, 1724 - 1730.

SOO S.L., IHRIG H.K., EL KOUH A.F., 1960
Experimental determination of statistical properties of two-phase turbulent flow.
Trans. ASME, J. Basic Engineering, 82 D, 609 - 621.

SPALDING D.B., 1979
Combustion and mass transfer.
Pergamon Press, Oxford.

STARNER S.H., BILGER R.W., 1981
Measurements of scalar-velocity correlations in a turbulent diffusion flame.
In Eighteenth Symposium (International) on Combustion, 921 - 930.
Pittsburgh: The Combustion Institute.

STEWART R.W., TOWNSEND A.A., 1951
Similarity and self-preservation in isotropic turbulence.
Philos. Trans. A, 243, 359.

SWITHENBANK J., BEER J.M., TAYLOR D.S., ABBOT D., McCREATH G.C., 1977
A laser diagnostic technique for the measurement of droplet and particle size distribution.
AIAA paper no. AIAA-79-69, 14th Aerospace Sciences Meeting, Jan. 26-28.

TAYLOR, G.I., 1921
Diffusion by continuous movements.
Proc. London Math. Soc., Ser. 2, 20, 196.

TENNEKES H. and LUMLEY J.L., 1972
A first course in turbulence.
The MIT Press, Cambridge, Ma.

TOWNSEND A.A., 1979
Flow patterns of large eddies in a wake and in a boundary layer.
J. Fluid Mech., 95, 515 - 537.

TROLINGER J.D., HEAP M.P., 1979
Coal particle combustion studied by holography.
Appl. Opt., 18, 1757 - 1762.

TSUJI Y., MORIKAWA Y., 1982
LDV measurements of an air-solid two-phase flow in a horizontal pipe.
J. Fluid Mech., 120, 385 - 409.

TSUJI Y., MORIKAWA Y., SHIOMI H., 1984
LDV measurements of an air-solid two-phase flow in a vertical pipe.
J. Fluid Mech., 139, 417 - 434.

VAMES J.S., HANRATTY T.J., 1988
Turbulent dispersion of droplets for air flow in a pipe.
Exp. in Fluids, 6, 94 - 105.

VAN DE HULST, 1981
Light scattering by small particles.
2nd edition, Dover Publications Inc., New York.

WANG J.C.F., TICHENOR D.A., 1981
Particle size measurements using an optical variable-frequency-grid technique.
Appl. Opt., 20, 1367 - 1373.

WANG J.C.F., HENCKEN K.R., 1986
In situ particle size measurements using a two colour laser scattering technique.
Appl. Opt., 25, 653 - 657.

WELLS M.R., STOCK D.E., 1983
The effects of crossing trajectories on the dispersion of particles in a turbulent flow.
J. Fluid Mech., 136, 31-62.

WIGLEY G., 1978
The sizing of large droplets by laser anemometry.
J. Phys. E: Sci. Instrum., 11, 639 - 642.

WILSON J.C., LIU B.Y.H., 1980
Aerodynamic particle size measurement by Laser Doppler Velocimetry.
J. Aerosol Sci., 11, 139 - 150.

WYGNANSKI I., FIEDLER H.E., 1969
Some measurements in the self-preserving jet.
J. Fluid Mech., 38, 577 - 612.

YANTA W.J., SMITH R.A., 1978
Measurements of turbulence-transport quantities with a laser-Doppler velocimeter.
AIAA paper no. 73-169, presented at 11th Aerospace Science Meeting ASME 1982, Phoenix, Atlanta.

YEOMAN M.L., AZZOPARDI B.J., WHITE H.J., BATES C.J., ROBERTS P.J., 1982
Optical development and application of a two colour LDA system for the simultaneous measurement of particle size and particle velocity.
In Engineering Applications of Laser Velocimetry, Winter Annual Meeting ASME, Phoenix, Atlanta.

YUDINE M.I., 1959
Physical considerations on heavy particle diffusion.
Adv. in Geophys., 6, 185-191.

YULE A.J., CHIGIER N.A., ATAKAN S., UNGUT A., 1977
Particle size and velocity measurement by laser anemometry.
J. Energy, 1, 220 - 228.

YUU S., YASUKOUCHI N., HIROSAWA Y., JOTAKI T., 1978
Particle turbulent diffusion in a dust laden round jet.
AIChE J., 24, 509 - 519.